TOKYO METROPOLITAN UNIVERSITY

DOCTORAL THESIS

Suzaku Study of Jovian Diffuse Hard X-ray Emission

Author:
Masaki NUMAZAWA

Supervisor:
Dr. Yuichiro EZOE

A thesis submitted in fulfillment of the requirements
for the degree of Doctor of Philosophy

in the

Department of Physics

Science and Engineering

February 18, 2020

首都大学東京　博士（理学）学位論文（課程博士）

論 文 名

「すざく」衛星による木星の広がった硬Ｘ線放射の研究（英文）

著　者　　沼澤 正樹

審査担当者

主　査

委　員

委　員

委　員

上記の論文を合格と判定する

年　　月　　日

首都大学東京大学院理工学研究科教授会

研究科長

DISSERTATION FOR A DEGREE OF
DOCTOR OF PHILOSOPHY IN SCIENCE
TOKYO METROPOLITAN UNIVERSITY

TITLE :

Suzaku Study of Jovian Diffuse Hard X-ray Emission

AUTHOR : Masaki Numazawa

EXAMINED BY

Examiner in chief

Examiner

Examiner

Examiner

QUALIFIED BY THE GRADUATE SCHOOL
OF SCIENCE AND ENGINEERING
TOKYO METROPOLITAN UNIVERSITY

Dean

Date

Abstract

Jovian diffuse hard X-ray emission had been discovered by *Suzaku* in 2006 when the solar activity went toward its minimum. The diffuse emission was spatially consistent with the Jovian inner magnetosphere and was spectrally fitted with a flat power-law function suggesting non-thermal emission. Thus, a scenario in which ultra-relativistic (tens MeV) electrons in the Jovian inner magnetosphere inverse-Comptonize solar visible photons into X-ray bands has been hypothetically proposed. In this thesis, we focused on dependence of the Jovian diffuse hard X-ray emission on solar activity to verify the hypothetical scenario. Near Jupiter within ∼2 Jovian radii (R_J), the Jovian synchrotron radio emission (JSR) has been monitored in the long-term and has been known to originate in ultra-relativistic (several MeV) electrons and vary its flux within several tens percents without simple dependence on the solar cycle. If the diffuse X-ray emission originates with such tens MeV electrons, therefore, it should show the same tendency as the JSR. Thus, we systematically analyzed the entire three X-ray data sets of Jupiter taken by *Suzaku* in 2014 and 2012, when the solar activity approximately reached its maximum, and in 2006. The phase different observations in the solar cycle enabled a discussion about the long-term variation and the solar dependence of the Jovian diffuse hard X-ray emission.

We conducted imaging and spectral analyses of the three data sets and found the diffuse emission reproductively existing through all the observations. By combining the imaging and spectral analyses, we successfully separated the contribution of the diffuse emission from the emission from Jupiter's body (i.e., the aurora and disk emission). The 1–5 keV luminosities of the diffuse emission were estimated at $(6.3 \pm 0.9) \times 10^{15}$, $(4.4 \pm 0.8) \times 10^{15}$, and $(5.6 \pm 2.2) \times 10^{15}$ erg s^{-1} in 2014, 2012, and 2006, respectively. Thus, it is thought that the diffuse emission has been stable and did not vary significantly, and did not simply depend on the solar activity, as the JSR trends. The body emission both in 0.2–1 and 1–5 keV, in contrast, probably depended on the solar activity and varied by a factor of 2–5. These results strongly supported the inverse-Compton scattering scenario by the ultra-relativistic electrons. Therefore, we estimated spatial and spectral distributions of the inverse-Compton scattering X-rays from an empirical model of high-energy electron distribution in the Jovian magnetosphere. and found a possible agreement in an inner region ($\lesssim 10\,R_J$) for the *Suzaku* X-ray observations. On contrast, we also found the model largely underestimates the density of the electrons by a factor of 10–100 in the outer region, which afresh suggested that the model incompletely describe higher energetic electrons in more distant regions. These suggestions emphasize importance of future X-ray monitoring of Jupiter and its magnetosphere.

Contents

List of Figures

List of Tables

List of Abbreviations

ATHENA	**A**dvanced **T**elescope for High **EN**ergy **A**strophysics
ARF	**A**ncillary **R**esponse **F**ile
CCD	**C**harge **C**oupled **D**evice
CMB	**C**osmic **M**icrowave **B**ackground
CTE	**C**harge **T**ransfer **E**fficiency
CX	**C**harge e**X**change
CXB	**C**osmic **X**-ray **B**ackground
EEF	**E**ncircled **E**nergy **F**unction
EOB	**E**xtensive **O**ptical **B**ench
EPIC	**E**uropean **P**hoton **I**maging **C**amera (*XMM-Newton*'s instruments)
EUV	**E**xtreme **U**ltra **V**iolet
HEW	**H**alf **E**nergy **W**idth
HPD	**H**alf **P**ower **D**iameter
HST	**H**ubble **S**pace **T**elescope
IPT	**I**o **P**lasma **T**orus
JRF	**J**upiter's **R**eference **F**rame
JSR	**J**ovian **S**ynchrotron **R**adio emission
JUXTA	**JU**piter **X**-ray **T**elescope **A**rray
NXB	**N**on **X**-ray **B**ackground
OBF	**O**ptical **B**locking **F**ilter
PSF	**P**oint **S**pread **F**unction
RMF	**R**edistribution **M**atrix **F**ile
SCI	**S**paced-row **C**harge **I**njetion
SSO	**S**olar **S**ystem **O**bject
SWCX	**S**olar **W**ind **C**harge e**X**change
UV	**U**ltra **V**iolet
XIS	**X**-ray **I**maging **S**pectrometer (*Suzaku*'s instruments)
XRS	**X**-**R**ay **S**pectrometer (*Suzaku*'s instruments)
XRT	**X**-**R**ay **T**elescope (*Suzaku*'s instruments)
XRISM	**X**-**R**ay **I**maging and **S**pectroscopy **M**ission

Physical Constants

Speed of Light in vaccum	$c_0 = 2.997\,924\,58 \times 10^{10}\,\mathrm{cm\,s^{-1}}$
Thomson scattering Cross-section	$\sigma_\mathrm{T} = 6.652\,458\,72 \times 10^{-25}\,\mathrm{cm^2}$
Solar Radius	$R_\odot = 6.957 \times 10^{10}\,\mathrm{cm}$
Solar Mass	$M_\odot = 1.9884 \times 10^{30}\,\mathrm{kg}\ (\pm\ 0.0002\,\mathrm{kg}\ )$
Solar Luminosity	$L_\odot = 3.828 \times 10^{26}\,\mathrm{W}$
	$= 3.828 \times 10^{33}\,\mathrm{erg\,s^{-1}}$
	$= 2.389\,249\,69 \times 10^{45}\,\mathrm{eV\,s^{-1}}$
Stefan-Boltzmann constant	$k_\mathrm{B} = 5.670\,367 \times 10^{-5}\,\mathrm{erg\,s^{-1}cm^{-2}K^{-4}}$
	$= 3.539\,164\,737\,760\,726 \times 10^{7}\,\mathrm{eV\,s^{-1}cm^{-2}K^{-4}}$
Classical Electron Radius	$r_\mathrm{e} = 2.817\,940\,322\,7 \times 10^{-13}\,\mathrm{cm}$
Unit conversion	
Jovian radius	$1\ \mathrm{R_J} = 7.1492 \times 10^{9}\,\mathrm{cm}$
Astronomical unit	$1\ \mathrm{AU} = 1.495\,978\,707\,00 \times 10^{13}\,\mathrm{cm}$
Energy	$1\ \mathrm{J} = 1 \times 10^{7}\,\mathrm{erg}$
	$= 6.242 \times 10^{18}\,\mathrm{eV}$
Flux density	$1\,\mathrm{Jy} = 1 \times 10^{-23}\,\mathrm{erg\,s^{-1}\,cm^{-2}\,Hz^{-1}}$

Chapter 1

Introduction

"We are just an advanced breed of monkeys on a minor planet of a very average star. But we can understand the Universe. That makes us something very special."

— Stephen William Hawking, Der Spiegel interview, 1988

The night sky is full of starlight. But we see only a small part of the universe that consists of stars, galaxies, black holes, and so on. The universe shines not only with the light visible to the human eye but also with electromagnetic waves of various wavelengths. Now, astronomers are observing the universe with a wide range of wavelengths of electromagnetic waves, as well as with gravitational waves and neutrinos. Even the same celestial body gives a completely different appearance depending on the observing wavelength. The Sun observed with visible light and with X-rays is a good example. We will be able to see the whole universe only with our "eyes wide open".

As one of the forefront of space observations, X-rays from solar system objects have been detected. The discovery of planetary X-rays was made in the 1950s from the Earth's aurora. Later, *Einstein* satellite detected X-ray emission from Jupiter in 1979, and those from the heliosphere and the Earth's upper atmosphere in the 1990s. Resent observatories such as *Chandra*, *XMM-Newton*, and *Suzaku* brought dramatic progress in the investigation of the planetary X-ray emission. *Chandra* not only provided high-resolution X-ray images of the Earth and Jupiter but also discovered X-ray emission from Venus, Mars, and Saturn. *XMM-Newton* and *Suzaku* contributed much to the elucidation of mechanisms of the X-ray emission from such planets with their spectral capabilities. Intriguingly, intrinsically "cold" objects like planets emit X-rays which are generally characteristic to extremely hot objects with temperatures often higher than 10^6 K. According to these previous observations, the origin and emission mechanism of planetary X-rays can be broadly classified into three types: (i) scattering of solar X-rays on the surface of planet, (ii) charge exchange (CX) process between heavy ions in solar winds and neutral atoms in planetary/cometary atmosphere yielding characteristic line emission, and (iii) non-thermal processes involving energetic electrons in planetary magnetosphere.

Jupiter is the largest planet and also the brightest source in the X-ray band among all the solar system objects, except for the sun. The planet has high-speed rotation with a period of ∼10 h and the largest and the most powerful magnetosphere whose size and strength are ∼100 times of Jupiter's radius (R_J) and ∼4 G at an equatorial plane. 9 spacecrafts have been put into the vicinity of Jupiter in the past, and *in-situ* measurements of its environments have been carried out. Ground-based radio observations have been also conducted to investigate Jovian environments. From these studies, it

has been recognized that electrons with energies reaching at least 50 MeV exist in Jupiter's magnetosphere. However, it has been left unclear how such energetic electrons are accelerated and release their energies. A variety of phenomena in Jupiter's system such as particle acceleration, magnetic properties, interactions between Jupiter and its moons, and Jupiter's aurora, have been the subject of investigation and results have been accumulating. As for the acceleration of energetic particles in the Jovian environment, certain scenarios have been proposed which combine several mechanisms such as betatron acceleration and wave-particle interaction. However, its applicability in wide scales of both space and energy has not been fully explored through observations. In order to obtain a "panorama" describing how and where electrons acquire and lose their energy in the Jovian magnetosphere, we need better knowledge of spatial and spectral distribution of such high-energy electrons which will enable us to look into their time variation and strength of correlation with the auroral luminescence and/or the solar activity.

After the discovery of Jupiter's X-rays by *Einstein* satellite, *Chandra* obtained the high-quality image and *XMM-Newton* played important roles in obtaining separate spectra from Jupiter's aurorae and disk. We now understand that the X-ray emission from the aurorae contains CX line emission and non-thermal bremsstrahlung, with the latter generated by ions and electrons accelerated in the Jovian magnetosphere. Emission from the disk is mainly composed of solar X-ray scattering on the planetary atmosphere. *Suzaku*, moreover, detected X-rays extending over radiation belts of Jupiter and Io's orbit ($\sim 6\,R_J$) in 1–5 keV band, characterized by a quite flat spectrum consistent with a non-thermal emission. This feature favors a hypothesis that ultra-relativistic electrons (tens MeV) energize solar visible photons through inverse Compton scattering into the X-ray band. However, we have a remaining issue that the electron density estimated from the X-ray flux is >10 times larger than the estimation from an empirical model of charged particles in the Jovian magnetosphere. The result opens an interesting possibility that an X-ray observation is likely to be a new probe in monitoring energetic activities in the radiation belt where the direct measurement is difficult with *in-situ* observatories.

In this thesis, we analyze three data sets of Jupiter observations by *Suzaku* in 2006, 2012, and 2014 in terms of a consistent procedure by focusing on the Jovian diffuse hard X-ray emission, and investigate its reproducibility, time variation, and emission mechanism. We believe that the results described in this thesis will be quite valuable for future missions of Jupiter exploration planned after the 2030s. In the following chapters, we summarize the past researches of Jupiter X-rays and the instrumentation for the present study in chapter 2 and chapter 3, respectively, describe the analysis procedure and result in chapter 4, discuss on the observed results in chapter 5, and give a conclusion in chapter 6.

Chapter 2

Review

This chapter gives a brief description of current understandings of X-ray phenomena in our solar system. The subjects dealt in this chapter are also reviewed by Bhardwaj, R. F. Elsner, Randall Gladstone, et al. (2007) and Bagenal et al. (2004).

2.1 X-rays from solar system objects

Our solar system now contains 8 planets, their ~200 satellites, and a large number of small bodies such as comets and asteroids. As a natural laboratory, they provide various phenomena and valuable knowledge on similar processes occurring somewhere else in the universe. X-ray emission from the solar system objects well characterizes physical processes in the emitting bodies. Generally, X-rays are emitted from extremely hot gas or plasma (1–100 MK) where atoms and electrons have high thermal energy (Rybicki and Lightman, 2004). We know, in the solar system, the solar corona with a high temperature of million degrees is the first in the list of X-ray producing objects. However, it was reported in the last several decades that other solar system objects also emit X-rays even they do not contain hot gases. Their atmospheres have temperatures of no more than ~1000 K much colder than the solar corona (Krankowsky et al., 1986; Schunk and Nagy, 2000). Therefore, a. study of X-ray emission from the solar system objects including the Sun is very useful in understanding various kinds of X-ray phenomena taking place in the universe. The study of the solar system objects opens an avenue for understanding the other distant X-ray objects, particularly because the solar system sources are able to be directly probed in many cases.

In the 1950s, X-rays from the auroral region of the Earth were discovered. In 1962, a rocket experiment aiming for detecting X-rays from the Moon serendipitously discovered X-rays from Scorpius X-1 and the diffuse X-ray background. This was the first detection of an extrasolar X-ray source, and the X-ray astronomy has started there (Giacconi et al., 1962). In the 1970s, fluorescent solar X-ray scattering was studied by *Apollo 15* and *16* missions. In the same period, the first X-ray satellite *Uhuru* was launched in 1970 and established the satellite-based X-ray astronomy which is the standard practice today. In 1979, the *Einstein* observatory discovered X-rays from Jupiter (Metzger et al., 1983) (more details are given in the following section). In the following decade up to 1990, X-ray emission was detected from 3 solar system objects other than the Sun, namely the Earth, the Moon, and Jupiter. In 1996, the *Röntgensatellite* (*ROSAT*) discovered X-rays from comets (Dennerl et al., 1997; Lisse, Dennerl, Englhauser, Harden, et al., 1996). Our understanding of the X-ray emission from the solar system objects was revolutionized by this epoch-making discovery. The data

provided evidence of the Solar Wind Charge eXchange (SWCX) and urged Cravens (2002, 1997) to demonstrate its mechanism as an important process of the X-ray production in the solar system.

After the appearance of the advanced X-ray observatories *Chandra*, *XMM-Newton*, and *Suzaku* in the 2000s, the study of X-ray emission from the solar system objects progressed at a quick pace. The observations successively showed X-ray emission from a number of solar system objects which contain Venus, Mars with its halo, Saturn with its rings, the Galilean satellites Io with its plasma torus, and Europa. Thanks to the good spatial and spectral resolution compared with the past X-ray observatories, the physical mechanism of the production of X-rays from the solar system objects was significantly better understood. Bhardwaj, R. F. Elsner, Randall Gladstone, et al. (2007) reviewed and summarized recent results of X-ray observations of the solar system objects, and gave an overview of the X-ray production mechanisms in the solar system. Ezoe, Fujimoto, et al. (2012) and Ezoe, Ishikawa, Ohashi, Yamasaki, et al. (2011) summarized the subsequent comprehension of X-rays from the solar system objects observed with *Suzaku*.

X-rays are a part of electromagnetic radiation with wavelengths of 0.01–10 nm in general terms, whose corresponding photon energies range from ~100 eV to tens of keV. In this paper, we define soft and hard X-rays as energy ranges below and above 1 keV, respectively. As energy goes further lower, the electromagnetic wave becomes extreme ultraviolet (EUV), ultraviolet (UV), visible light, infrared (IR) and radio waves. In the planetary science, observations with other wavelengths than X-rays are also quite useful. For Jupiter, we give a review later in section 2.2.

Bhardwaj, R. F. Elsner, Randall Gladstone, et al. (2007) briefly described a variety of physical mechanisms responsible for X-ray production from the solar system objects, by summarizing the main mechanisms to be the following 5 processes:

1. Collisional excitation of neutral species and ions by an impact of charged particles (particularly electrons) followed by line emission.

2. Electron collisions with neutrals and ions producing continuum bremsstrahlung.

3. Solar photon scattering from neutrals in planetary atmospheres—both elastic scattering and K-shell fluorescent emission.

4. Charge exchange (CX) of solar wind ions having energies of ~1 keV u^{-1} with neutrals, followed by line emission.

5. CX of energetic heavy ions of planetary magnetospheric origin with energies of MeV u^{-1} impacting neutrals—or of directly excited ions in collisions with neutrals.

X-ray emission from the solar system objects mainly shows phenomena involving highly excited neutrals and ions. The Bohr energy expression:

$$E_n = -Z^2\ 13.6\,\mathrm{eV}/n^2, \tag{2.1}$$

gives energies for a species with nuclear charge Z, and the principal quantum number n for one electron. According to the equation, the ground-state energy for atomic hydrogen, i.e., $Z = 1$, is −13.6 eV, which is also the ionization potential. On the other hand, for O^{7+} ions ($Z = 8$), the ground-state energy is 64 times this value, −870 eV. In the case of an atom/ion with multiple electrons,

the energy levels are not so simply expressed but the X-ray emission process reflects the transition between energy levels which can be bound or free. There are broadly 3 types of transitions, namely bound–bound, bound–free, and free–free, respectively denoted as *b*–*b*, *b*–*f*, and *f*–*f*. Once an atom is excited from the ground state to a higher level by collisions with fast electrons, then the de-excitation will be line emission of one (or more) photons by the excited electrons falling to lower states. Considering the $n = 2 \rightarrow 1$ transition for example, H Lyman alpha photons with an energy of 10.2 eV correspond to UV radiation, whereas for O^{7+} ions 653 eV photons are produced and they are soft X-rays.

We consider in more detail each of the above-listed 5 mechanisms of the X-ray production in connection with the solar system objects or its surrounding regions. We will classify these mechanisms into 3 categories as follows, and describe them in the later sections one by one;

1. Solar X-rays and their scattering on the surfaces of the objects (→ subsection 2.1.1).
2. Line emission from charge exchange processes by heavy ions contained in solar winds or interplanetary plasma sources (→ subsection 2.1.2).
3. Non-thermal emission in the planetary magnetosphere (→ subsection 2.1.3).

2.1.1 Solar X-rays and its scattering

Needless to say, the Sun is the source of energy for all life on the Earth. The source of the solar energy is a nuclear fusion reaction that occurs in the stellar interior where hydrogen is converted to helium. Davis (1969) conducted an experiment to detect evidence of solar neutrinos in order to confirm that the nuclear fusion actually took place in the center of the Sun. Another method of exploring the internal structure of the Sun is helioseismology, namely the study of the structure and dynamics of the Sun through its oscillations. The study to clarify the stellar interior by investigating the Sun's vibration began in the early 1960s with the discovery of steady solar vibration by Leighton et al. (1962). In the old days in the 17th century, Galilei discovered sunspots in the Sun using a telescope that was just invented. In the 20th century, Hale and Nicholson (1925) found the magnetic field of thousands of gauss at the sunspot and signaled the beginning of the solar physics. Later, solar observations using not only white light but also Hα monochromatic light (656.3 nm wavelength), radio waves, X-rays, etc., proved that the Sun is an active celestial body with many explosive processes.

Most of the solar activities are caused by magnetic fields. In the middle of the 20th century, it was found that solar corona seen during a total solar eclipse actually showed an extremely high temperature of ~1 MK. Later, it was found that this corona phenomenon was also caused by magnetic fields, but the specific mechanism remained still as a mystery. From the corona, it was found that plasma was constantly flowing out into the interplanetary space at a speed of 400–800 km s^{-1}. This is the solar wind which was theoretically expected by Parker (1965). It can be said that the solar wind is a result of the ultra-high temperature corona originated by the solar magnetic activity. The solar winds always collide with solar system objects including the Earth. In the planetary magnetospheres and upper atmospheres, the effects of the interaction with the solar winds appear clearly. For example, when a large amount of plasma is ejected with flares (called as coronal mass ejection), magnetic storms and aurora occur on the Earth. In this way, the solar physics itself is a very interesting topic,

and it contains various aspects of fundamental physics, but here we would like to focus on it from the viewpoint of "effect on X-ray emission from solar system objects".

Solar X-rays

Solar X-rays and UV photons are mainly produced in the solar corona rather than the surface. This is because the X-ray and UV continuum represent much higher temperature than the visible light, and the opacity of the medium increases as the wavelength becomes shorter in these bands. Thus, the emission corresponds to a phenomenon occurring in the upper layer of the solar atmosphere. In the range of EUV where the wavelength is 100 nm or less, *b–f* and *f–f* emission from abundant elements such as hydrogen and helium are the main component. In the wavelength range below 10 nm (0.1 keV), the *b–f* and *f–f* emission from low Z species increases, and a continuum component to 1 nm or less (1 keV or more) is formed. In the shorter wavelength range, the radiation from the corona of 1 MK becomes weaker, and the main components are the emission lines and continuous components from high-temperature plasmas over 10 MK heated by solar flares.

X-rays are generated when electrons collide with neutral or ionized atoms. Fast electrons collide with atoms and excite them into a higher bound state or further ionize them. The former is found in the solar corona as line emission in the range of X-ray and UV. Electrons whose kinetic energy is high enough (about the temperature of the coronal plasma) can excite ions of high Z species to such as He-like oxygen (O^{6+}) or Ne-like iron (Fe^{16+}), and produce X-rays. When the plasma is in thermal equilibrium, the radiative recombination balances the collisional excitation to a certain energy levels. Here, the radiative recombination (simply the reverse process of photo-ionization) occurs when an electron in a free state falls into a bound state. This is the so-called *b–f* transition. In the case when the bound state is not a ground state, then an X-ray line is produced with an energy corresponding to the difference of energy levels. In a hot plasma, dielectronic recombination is often more important than the simple radiative recombination in high Z species since several electrons are orbiting in an atom (Mewe, 1990). There are two electrons involved in this recombination process: the colliding electron and the electron inside the atom. The colliding electron and the atom stay for a long time keeping a short distance as a temporarily trapped state, and it raises the probability of the dielectronic recombination.

When the energy of the electron is significantly higher, a continuum component is generated by the *f–f* transition. This process is called as bremsstrahlung and can be considered as electromagnetic radiation in the classical description. It is emitted by the acceleration of electrons caused by Coulomb interaction with a charged nucleus. In a high-temperature plasma such as the solar corona, the electron energy distribution is Maxwellian, and thus the emission is thermal bremsstrahlung. This radiation is one of the main components of solar X-rays (Zirin, 1988), and is also considered to be produced in high-temperature plasma in Io Plasma Torus (IPT) (R. F. Elsner, Gladstone, et al., 2002).

Radiation from the solar corona (the temperatures between ~1 MK in coronal holes and 3 MK in active regions) mainly consists of the above mechanisms 1 and 2. The heavy ions (O^{6+}, O^{7+}, Fe^{14+}, Si^{12+}, etc.) in the solar corona are highly ionized, and they generate many X-ray emission lines through the processes described above. Moreover, the solar corona containing these heavy ions is also the source of solar winds.

Solar X-ray scattering on solar system objects

X-rays are characterized by being easily absorbed by atoms and molecules in the atmosphere and subject to Thomson scattering (Chantler, 1995). When applied to the solar system objects, it corresponds to the scattering of solar X-rays in the atmosphere of planets and satellites, which works like a frosted glass mirror. The balance between the scattering and the absorption cross sections is important. In the soft X-ray band, the former is much smaller than the latter, and the solar X-rays are only slightly rebounded in the target atmosphere. Nevertheless, radiation from this process is seen in the planetary X-ray spectrum. For example, in the case of the Earth, scattered X-rays are observed not only when a large flare occurs but also in the quiet state. Maurellis et al. (2000) first calculated the scattering of solar X-rays on Jupiter's disk. Cravens, Clark, et al. (2006) showed that the scattering albedo of stellar X-rays is very small in the exoplanet system (1×10^{-3} at 3 nm wavelength). The X-ray spectrum in this process is basically that of solar X-rays, but emission lines from highly ionized elements in the corona are broadened in energy by an albedo function that depends on the scattering process in the planetary atmosphere.

When an atom is irradiated by X-rays, its inner electrons are either excited or emitted, creating vacancies in the inner shell. When outer shell electrons make transition to the inner shell vacancies, the energy corresponding to the energy level difference is emitted as an electromagnetic wave (characteristic X-rays) in the X-ray region. This is called fluorescent X-ray emission.

The energy of the incident X-rays to ionize an atom needs to be higher than the absorption edge energy of the target element. The absorption edge energy of inner-shell electrons is in the wavelength region of X-rays for many elements. X-ray fluorescence is caused by an electron transition to a lower vacant level, and the fluorescent X-rays from solar system objects are mainly from Kα and Kβ transitions. L-shell fluorescence from heavy elements can also occur, but the fluorescence yields are much lower than for the K-shell. Since the energy of the fluorescent X-rays is unique to the element, the target composition can be identified from the observed spectrum (referred to as qualitative analysis). Further, the X-ray fluorescence intensity is proportional to the number of the target element, the density of each element can be measured (referred to as quantitative analysis).

Carbon is contained in Jupiter's atmospheric methane, and as carbon dioxide in Venus', and Mars' atmosphere. Fluorescent X-rays from carbon have little contribution to disk X-rays from planets like Jupiter, but are dominant in Venus and Mars, where carbon dioxide is the main component in the atmosphere. Krasnopolsky et al. (2004) showed that the contribution of solar X-ray scattering and K-shell fluorescence was small in the X-ray emission of comets because their atmosphere does not provide the neutral column density of $\sim 1 \times 10^{20}\,\mathrm{cm}^{-2}$ required for this process (it is easy on the Earth). Fluorescence processes occur not only in the atmosphere, but also by the absorption of solar X-rays on solid surfaces such as the Moon, Galileo moons, and Saturn's rings. It can be said that X-rays emitted from the solar system objects with relatively low surface temperatures are ultimately induced by the solar radiation (and the solar corona).

2.1.2 Charge exchange

One of the most important X-ray production mechanisms for many solar system environments is the solar wind charge exchange (SWCX) mechanism (review articles can be found in Cravens, 2002;

Krasnopolsky et al., 2004; Lisse, Cravens, et al., 2004). Charge exchange (or charge transfer; CX) is a fundamental process in atomic physics, which is accompanied by characteristic line emission. This process has been investigated in various contexts for a long time. The main feature of CX is a significantly large cross section of $\sim 1 \times 10^{-15}$ cm^2 (Lisse, Dennerl, Englhauser, Trümper, et al., 1997), which is several orders of magnitude larger than those of other processes of electron collisional excitation (Cravens, 2002; Krasnopolsky et al., 2004). In recent X-ray astrophysics, the CX process has attracted attention as a new type of emission from a variety of X-ray sources such as solar system objects, starburst galaxies and supernova remnants, where ionized particles or hot plasmas interact with near-neutral low-density gas. This section briefly describes the principle and historical study of the CX process.

Principle of charge exchange

In the CX process, one or more electrons transfer from an atom or molecule to an ion, entering to certain excited states, and the ion which captured the electrons is de-excited by releasing emission lines as the electrons cascade down to the ground state. The CX reaction is generally described by

$$A^{q+} + B \rightarrow A^{(q-r)+*} + B^{r+} \tag{2.2}$$

$$\rightarrow A^{(q-r)+} + B^{r+} + h\nu, \tag{2.3}$$

where A denotes the colliding ion (e.g., O, C, Fe, etc) with a charge q (e.g., 5, 6, or 7), and r electrons are captured from a neutral target B (an atom or molecule; e.g., H, O, H_2O, etc). Consequently, the ion A is de-excited through line emission with an energy $h\nu$. The CX process can be intuitively understood by the following "Classical over-Barrier Model". As shown in Figure 2.1, when the two particles are separated, there is a barrier between the Coulomb potentials created by each particle, and electrons are bound to each particle. As the incident ion approaches and the distance between the potentials decreases, the barrier energy becomes lower. As the distance becomes very short and the barrier level drops to lower than the binding energy of the target neutral's electrons, the electrons bound to the target neutral can move to the other ion.

When the ionization degree of the colliding particle is high, the energy level of the ground state is much lower than that of the neutral particle, and the moved electron will go to the excited level of the colliding particle. In Figure 2.2, we consider a highly-ionized heavy atom, namely fully-stripped carbon, contained in the solar winds as colliding particles. They interact with neutral hydrogen atoms and molecules around comets or the Earth's atmosphere. When the colliding particles have the velocity comparable to the solar wind, a single electron is usually transferred. Equation 2.2 are thus specifically written as,

$$C^{6+} + H \rightarrow C^{5+*} + H^{+}. \tag{2.4}$$

The electron is thought to enter into the $n = 4$ level of carbon. The electron in the excited level will cascade down to the ground level by emitting photons with energies corresponding to the difference of the energy levels. In the case of ions which are either fully ionized or with one electron, the K-shell has a vacancy and the electron makes transition from the higher level to the ground level. X-rays

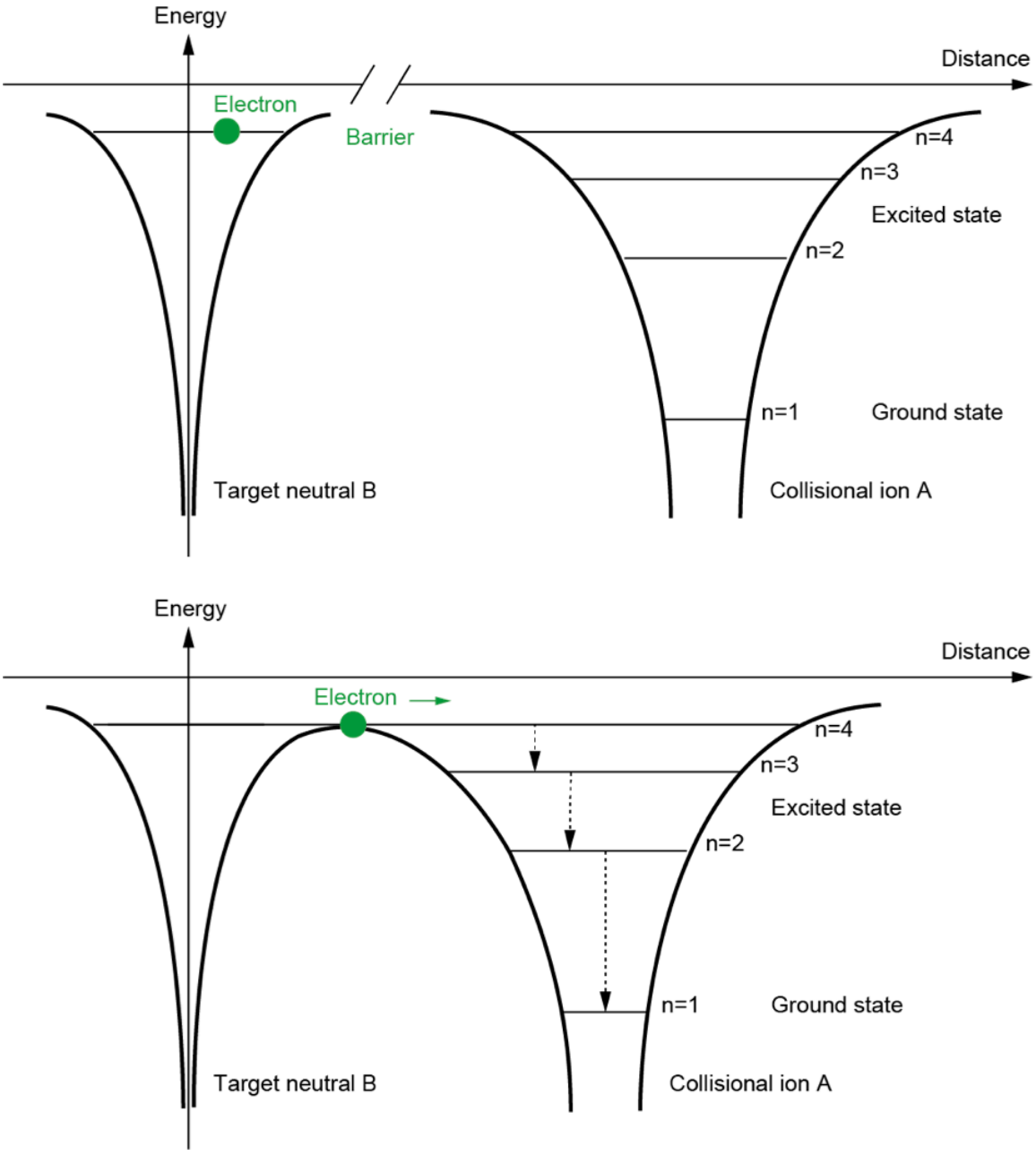

FIGURE 2.1: Schematic views of potential energies in the charge exchange process based on the Classical over-Barrier Model. In the upper panel, the collisional ion A and the target neutral B are separated, and there is a potential barrier between them so that no electron moves from B to A. On the other hand, in the lower panel under a lower separation, the potential barrier is lower and the electron can transfer. The electron transits to the ground state through X-ray line emission since the ground state energy level of the highly-ionized A is lower than that of the neutral B.

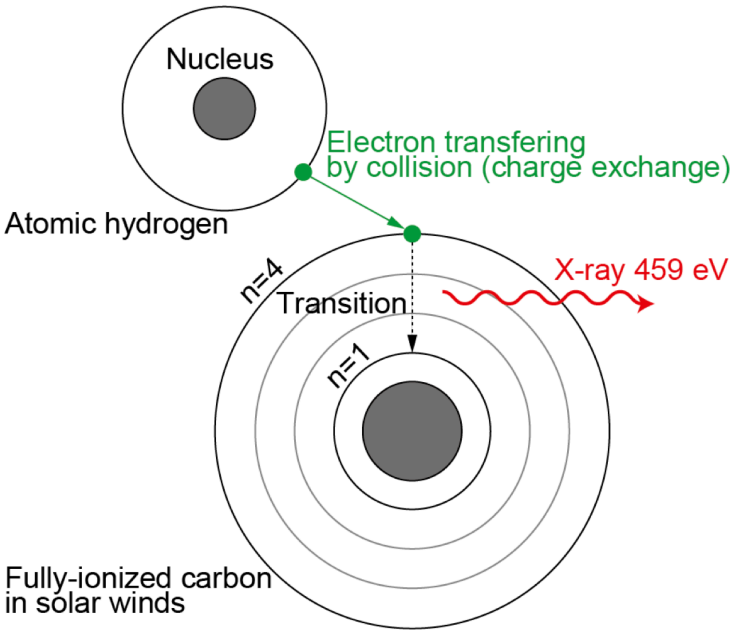

FIGURE 2.2: A schematic view of the CX process in which an electron is transferred and an X-ray line emission is produced. This is an example process between fully-ionized carbon in solar winds and atomic hydrogen. The electron is transferred to the excited level ($n = 4$) of the carbon from the hydrogen and falls down to the ground state ($n = 1$) through X-ray emission with a fixed energy of 459 eV.

emitted from the electron has a certain energy specific to the ion species. X-rays radiated by the CX reaction are exclusively emission lines specific to each ion, and no continuum is emitted. This is greatly different from the other emission processes such as bremsstrahlung.

According to quantum mechanics, each electron orbit defined by the principal quantum number n is further divided into orbits with different angular momentum. When the relative velocity at the time of collision is large, the probability of entering to a state with different angular momentum is determined by the degree of degeneracy, and the larger the degree, the easier for the electron to enter the state. According to the selection rule, the angular momentum quantum number l should change by 1 in a transition emitting a photon, and many electrons eventually fall to the ground state by making transition to the inner states step by step. On the other hand, when the relative speed of the initial collision is small, the electron is more likely to enter into a state with a small angular momentum. When the electron is in the orbit with the angular momentum quantum number $l = 1$ (p orbital), it is possible to make an immediate transition to the ground state. Therefore, the transition from the second shell ($n = 2$) to the ground state (2p $\rightarrow$ 1s transition) occurs when the relative velocity is low, and the outer orbits such as the third, fourth, and fifth are involved when the relative velocity is large. For example, in the case of fully-ionized carbon, X-rays of 367 eV correspond to 2p $\rightarrow$ 1s transition in the former case and the energy is 459 eV for 4p $\rightarrow$ 1s transition in the latter case.

Solar wind charge exchange

The SWCX mechanism was first proposed (Cravens, 1997) to explain the surprising *ROSAT* observations of soft X-ray and EUV emission from the Comet Hyakutake in 1996 (Lisse, Dennerl, Englhauser,

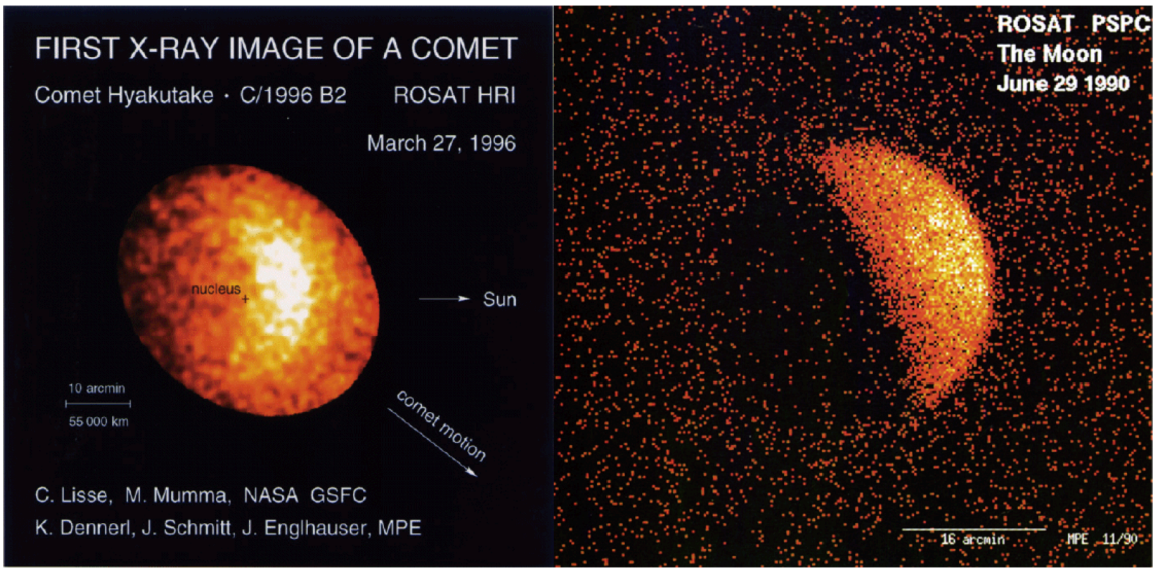

FIGURE 2.3: Historical *ROSAT* images of X-ray emission from solar system objects.[1] The left panel shows X-rays from the Comet Hyakutake which is the first detection of the SWCX process in the solar system. The right image shows X-rays from the Moon where the solar X-ray scattering occurs in the right side brighter area. A decade-long mystery about the origin of X-rays from the dark moon (the left side dark area) is solved by *Chandra*'s observation. This is the Earth's geocoronal SWCX X-ray emission as a "foreground" to the spacecraft observation.

Harden, et al., 1996), as shown in Figure 2.3. Since then, the mechanism has also been shown to operate in the heliosphere, in the terrestrial magnetosheath (geocoronal emission; as shown in Figure 2.3), and at Mars (halo emission). For the species and charge states relevant to the actual SWCX process in comets and planets, the principal quantum number of the ion $A^{(q-1)+}$ is usually in the range $n = 4, 5$, or 6. The most significant lines in the measured cometary spectra are the He-like transitions of O^{6+}, produced by the CX of solar wind O^{7+} ions with neutral targets. In particular, the lines with energies 561, 568, and 574 eV are very strong (Krasnopolsky et al., 2004; Lisse, Cravens, et al., 2004).

Highly-charged ions are essential for the X-ray production in the CX process, and the solar winds contain a small amount of such ions. Schwadron and Cravens (2000) and Steiger et al. (2000) found that 0.1% of the solar winds comprise such highly charged heavy ions such as O^{7+}, O^{6+}, C^{6+}, C^{5+}, N^{6+}, Ne^{8+}, Si^{9+}, and Fe^{12+}. Their composition and abundance are variable and largely depend on the solar activity, which strongly affects the condition of the solar corona as the origin of the solar winds. Schwadron and Cravens (2000) and Steiger et al. (2000) further suggested that the slower solar winds originated from the hotter corona and contained more abundant highly charged ions.

X-ray production from the CX process can be expressed by the following relatively simple equation:

$$P_{\mathrm{sqjn}}(\mathbf{r}) = n_{\mathrm{sq}}(\mathbf{r}) n_{\mathrm{n}}(\mathbf{r}) \langle g \rangle f_{\mathrm{sqj}} \sigma_{\mathrm{sqn}}(g). \tag{2.5}$$

[1] These images are credited by C. Lisse, M. Mumma (NASA/GSFC), K. Dennerl, J. Schmidt, and J. Englhauser (MPE): https://apod.nasa.gov/apod/image/hyakutake_rosat_big.gif (left), and by *ROSAT*/J. Schmitt et al.: https://chandra.harvard.edu/photo/2003/moon/moon_rosat.jpg (right), respectively.

Here, $P_{\mathrm{sqjn}}(\mathbf{r})$ is the photon volume emission rate in units of photons $\mathrm{cm}^{-3}\mathrm{s}^{-1}$ at a position vector $\mathbf{r}$, in the solar system environment. $n_{\mathrm{sq}}(\mathbf{r})$ is the number density of the solar wind, with s denoting the ion species and q the charge-state, and $n_{\mathrm{n}}(\mathbf{r})$ is the number density of target neutral species, n. $\langle g \rangle$ is the average collision velocity which is almost equal to the solar wind speed, u_{SW}, for most of the locations. $\sigma_{\mathrm{sqn}}(g)$ is the total charge transfer cross-section at the collision velocity g for the designated ion and neutral species. f_{sqj} is the probability of occurrence of the specific transition, j, after the charge-exchange collision.

Equation 2.5 has to be applied to all the solar wind species with all charge states, all target neutral species, and all the relevant transitions to obtain the complete spectrum of the SWCX X-ray emission. In a collisionally thin regime where the neutral density is low, n_{sq} is just the static solar wind density. On the other hand, in the vicinity of the object, the original solar wind flux of a particular ion species may be attenuated due to the CX collisions or the density can be altered by dynamical processes such as the bow shock caused by the supersonic solar wind flow around the object. This implies that it is difficult to completely estimate where and how much the X-rays are generated by the SWCX process.

On planets with a magnetosphere, the CX mechanism can be modified considerably. In the example case of Jupiter, as described later in section 2.2, heavy ions come not only from solar winds but also from planetary plasma sources. They all cause the CX process and give the X-ray line emission. It explains a part of soft X-rays observed in Jupiter's aurora. The presence of strong magnetic fields deflects and accelerates the heavy ions. The energetic heavy ions descend to the planetary neutral atmosphere, where they collide with atoms and molecules and lose the transition energy. This will increase the fraction of highly excited ions. Therefore, the ionization degree of precipitating ions can be both increased and decreased many times through continuous collisions with the atmospheric gas. The basic mechanism is the same as the above described SWCX process, however especially the ion species in the magnetosphere can be different from the solar winds and the emitted X-ray spectrum would thus be different and strongly dependent on the kinetic energy of the ions (Kharchenko et al., 2008). Although such an effect is expected to be present in all magnetic planets, currently it has only been confirmed in Jupiter.

Charge exchange in X-ray astrophysics

When the X-ray radiation from the comet was recognized as being caused by the CX process, it was suggested that part of the diffuse soft X-ray background was also due to the CX process with solar winds interacting with the geocorona and with neutral materials in the heliosphere. The "mysterious X-ray brightening" observed during the *ROSAT* all-sky survey was shown to correlate with the solar wind flux, and its origin was also interpreted as the CX process between the solar winds and the geocoronal neutral hydrogen (Cravens, 2000). Therefore, the SWCX process provides a means for observational investigations of low-density neutral matter in the geocorona, outer planetary atmosphere, and around comets, as well as the elemental composition of the solar winds (Dennerl, 2010). On the other hand, in the observation of the diffuse soft X-ray background, separation of the X-ray radiation from the high-temperature interstellar medium from the CX X-rays is difficult in both spatially and spectrally when the resolution is not good enough. In this view, the SWCX process can be a troublesome existence. Especially in the low energy side, there is an indication that X-rays produced by the SWCX process in the heliosphere account for a large proportion of the stationary component

(Lallement, 2004). It is an important issue to be fully resolved for the study of hot interstellar and intergalactic materials.

2.1.3 Non-thermal emission

In this section, we will summarize radiation processes which are relevant to high energy electrons. These are formulated as non-thermal radiation processes, and three types, including the bremsstrahlung already mentioned above, are important for the X-ray emission. The non-thermal radiation is important in understanding the acceleration process of high energy electrons, which is a universal phenomenon taking place in the universe on various different scales. Such non-thermal radiation has also been observed in our solar system, indicating that electrons are accelerated to very high energies of the order of keV–MeV. In this thesis, we study the possibility of particle acceleration in the magnetosphere, especially based on X-ray observations of Jupiter. In this relatively "close" region within the solar system, it would be possible to obtain detailed properties of the particles as the seed particles and the resultant X-rays emitted from the system. Our study will be a step forward in solving the fundamental and common problems about the particle acceleration in the universe.

Bremsstrahlung

Free electrons are deflected by the Coulomb force of the nuclei (mainly protons), and this acceleration causes emission of electromagnetic waves. Situations of electron–electron or proton–proton encounters do not cause acceleration of dipole moments, and no bremsstrahlung radiation is resulted. In addition, since protons are much heavier than electrons, only electrons should be considered for the bremsstrahlung process in which the acceleration strength is essential.

When the motion of a single electron is deflected by a single nucleus, the emitted energy per frequency is given by

$$\frac{\mathrm{d}W(b)}{\mathrm{d}\omega} = \frac{8\pi}{3c^3}\omega^4 |\mathscr{F}[\mathrm{d}(\omega)]|^2. \tag{2.6}$$

When the single electron with a velocity of v and a charge of $-e$ paths near the single nucleus with a charge of $-Ze$ with an impact parameter of b, and is slightly made a turn by the Coulomb force, Equation 2.6 becomes with a function of b given by

$$\frac{\mathrm{d}W(b)}{\mathrm{d}\omega} \approx \begin{cases} \frac{8Z^2e^6}{3\pi c^3 m^2 v^2 b^2} & (b \ll v/\omega), \\ 0 & (b \gg v/\omega). \end{cases} \tag{2.7}$$

Equation 2.7 diverges when $b \to 0$ and $v \to 0$, so in fact, their minimum limitations should be set by realistic values.

Electrons with a uniform velocity of v in a certain plasma with electron and ion density of n_e and n_i, respectively, emit the power per unit volume and unit time given by

$$\frac{dW(b)}{d\omega dV dt} = n_e n_i 2\pi v \int_{b_{min}}^{\infty} \frac{dW(b)}{d\omega} b db \tag{2.8}$$

$$\approx n_e n_i 2\pi v \int_{b_{min}}^{b_{max}} \frac{8Z^2 e^6}{3\pi c^3 m^2 v^2 b^2} \tag{2.9}$$

$$= \frac{16e^6}{3c^3 m^2 v} n_e n_i Z^2 \log \frac{b_{max}}{b_{min}} \tag{2.10}$$

$$= \frac{16\pi e^6}{3\sqrt{3}c^3 m^2 v} n_e n_i Z^2 \frac{\sqrt{3}}{\pi} \log\left(\frac{b_{max}}{b_{min}}\right) \tag{2.11}$$

$$= \frac{16\pi e^6}{3\sqrt{3}c^3 m^2 v} n_e n_i Z^2 g_{ff}(v, \omega), \tag{2.12}$$

which considers electron number pathing between b to $b+db$ per unit time for a single ion is described by $2\pi b db v n_e$. Here, $g_{ff}(v, \omega) = \sqrt{3}/\pi \log(b_{max}/b_{min})$ is called "Gaunt factor" with a function of the electron energy and the emitted frequency in the bremsstrahlung and roughly values an order of ~1.

Equation 2.12 is based on an assumption that electrons have a certain velocity (v). Then, we obtain the energy spectrum of the bremsstrahlung to fold with an actual distribution of the electron velocity. The bremsstrahlung can occur in both thermal and non-thermal regimes. The thermal bremsstrahlung is called as *f–f* emission, as mentioned already, and observed as a continuum emission from optically thin hot plasmas such as the solar corona. Depending on whether the electron distribution is Maxwellian or power-law, it becomes thermal or non-thermal bremsstrahlung, respectively. The former produces a spectrum with a certain cut-off energy of ~kT corresponding to the electron temperature, while the latter does a power-law spectrum. In both mechanisms, such continuum is accompanied with X-ray line emission in various astrophysical contexts (e.g., Porquet et al., 2001; Tatischeff, 2003).

Synchrotron radiation

Electrons accelerated by a magnetic field B will produce synchrotron radiation, in which electromagnetic waves are emitted because the Lorentz force by the magnetic field causes deflection of the electron path. It is one of the most important radiation mechanisms in high energy astrophysics. Supernova remnants are the representative sources of synchrotron radiation emitted usually in the radio wavelength (even up to X-ray band). Another source in our solar system is the Jovian synchrotron radio emission. It is produced near Jupiter (~2 R_J) where the magnetic field is very strong (~1.2 G; Bolton, Janssen, et al., 2002), and has been intensely monitored for a long time. Here we briefly describe the general scheme of the synchrotron radiation (for more details, see e.g., Rybicki and Lightman, 2004).

An electron with energy $E = \gamma m_e c^2$ gyrates around a magnetic field line with an angular frequency (Larmor frequency)

$$\Omega_{Le} = \frac{eB}{\gamma m_e c}, \tag{2.13}$$

and the associated radius of gyration orbit (Larmor radius) with a pitch angle θ is,

$$r_{\rm Le} = \frac{v_\perp}{\Omega_{\rm Le}} = \frac{\gamma m_{\rm e} c v \sin\theta}{eB} \simeq \frac{\gamma m_{\rm e} c^2}{eB}, \tag{2.14}$$

which is numerically given as

$$r_{\rm Le} \simeq 1.7 \times 10^3 \gamma \left(\frac{1{\rm G}}{B}\right) \ {\rm cm}. \tag{2.15}$$

The total power of the synchrotron radiation is given by

$$P_{\rm syn} = \frac{4}{3} c \sigma_{\rm T} \beta^2 \gamma^2 U_{\rm B}, \tag{2.16}$$

where $U_{\rm B}$ is the energy density of the magnetic field ($= B^2/(8\pi)$). The power emitted by an electron as a function of photon energy ϵ is given by,

$$P_{\rm syn}(\epsilon) = \frac{\sqrt{3} e^3 B \sin\theta}{2\pi m_{\rm e} c} F\left(\frac{\epsilon}{\epsilon_{\rm c}}\right) \tag{2.17}$$

$$\epsilon_{\rm c} = \frac{3\hbar\gamma^2 eB \sin\theta}{2 m_{\rm e} c} \tag{2.18}$$

$$F(x) \equiv x \int_x^\infty K_{5/3}(\xi)\, d\xi. \tag{2.19}$$

Here, $\epsilon_{\rm c}$ denotes the characteristic synchrotron photon energy, and $F(x)$ gives the spectral energy distribution from a single electron in terms of the modified Bessel function $K_{5/3}$ (Ginzburg and Syrovatskii, 1964).

The spectrum of the synchrotron radiation for given energy distribution of electrons can be obtained by integrating the above photon spectrum generated by a single electron. The energy spectrum of the accelerated electrons is generally described by a power-law function, and the number density spectrum as a function of energy E is described by,

$$N(E) = C E^{-p}. \tag{2.20}$$

The resultant photon energy spectrum (not the number spectrum) can also be described by a power-law with a spectral index s,

$$P(\epsilon) \propto \epsilon^{-s}. \tag{2.21}$$

The total power radiated per unit volume per unit photon energy ϵ by such an electron distribution is given by integrating over the entire electron energy as,

$$P_{{\rm tot}_{\rm syn}}(\epsilon) = \int {\rm d}E\, N(E) P_{\rm syn}(\epsilon) \tag{2.22}$$

$$= \frac{\sqrt{3} e^3 B \sin\theta}{2\pi m_{\rm e} c} \frac{C}{p+1} \Gamma\left(\frac{p}{4} + \frac{19}{12}\right) \Gamma\left(\frac{p}{4} - \frac{1}{12}\right) \left(\frac{m_{\rm e} c \epsilon}{3\hbar\gamma^2 eB \sin\theta}\right)^{-(p-1)/2} \tag{2.23}$$

$$\propto C B^{(p+1)/2} \epsilon^{-(p-1)/2}, \tag{2.24}$$

where Γ denotes the gamma function. According to this formula, when the electron energy density

spectrum has a power-law index p, the energy spectral index of the synchrotron emission becomes $(p-1)/2$. In the X-ray observation, the photon number spectrum is often used and it is given by $I_{\mathrm{tot_{syn}}}(\epsilon) = P_{\mathrm{tot_{syn}}}(\epsilon)/\epsilon$. So, the photon index Γ of the power-law is given by

$$I_{\mathrm{tot_{syn}}} \propto \epsilon^{-\Gamma} \tag{2.25}$$

$$\Gamma = \frac{p+1}{2}. \tag{2.26}$$

Note that the spectral index Γ is defined by the electron distribution rather than by the single-electron emission spectrum. The characteristic synchrotron photon energy ϵ_c strongly depends on the electron energy as $\epsilon_c \propto \gamma^2 \propto E^2$. This difference in the dependence on the power index accounts for the slope difference between the spectra of emitted photons and parent electrons. The emitted photon energy spectrum has a peak at $\epsilon_{\mathrm{peak}} = 0.29\epsilon_c$, whose numerical values are given below.

$$\epsilon_{\mathrm{peak}} = 0.29\epsilon_c \simeq 0.29\frac{3\hbar\gamma^2 eB}{2m_e c} = 0.29\times 3\gamma^2 B\frac{\hbar e}{2m_e c} \tag{2.27}$$

$$= 0.87\times\left(2\times10^7\frac{E_e}{10\,\mathrm{TeV}}\right)^2\left(\frac{B}{1\,\mathrm{mG}}\right)\times 1\,\mathrm{mG}\times 9.3\times10^{-21}\,\mathrm{erg/G} \tag{2.28}$$

$$= 3.2\times10^{-9}\left(\frac{E_e}{10\,\mathrm{TeV}}\right)^2\left(\frac{B}{1\,\mathrm{mG}}\right)\mathrm{erg} \tag{2.29}$$

$$\approx 2\,\mathrm{keV}\left(\frac{E_e}{10\,\mathrm{TeV}}\right)^2\left(\frac{B}{1\,\mathrm{mG}}\right). \tag{2.30}$$

Inverse Compton scattering

Inverse Compton scattering is an important mechanism in producing high-energy photons in diverse astrophysical settings. In this process, low energy photons (seed photons or soft photons) are scattered by high energy electrons to higher energies.

The total power radiated by a single high energy electron is given by

$$P_{\mathrm{IC}} = \frac{4}{3}c\sigma_T\beta^2\gamma^2 U_{\mathrm{ph}}, \tag{2.31}$$

where U_{ph} is the energy density of seed photons ($= n_{\mathrm{ph}}(\epsilon_0)\epsilon_0$). Note that this is the same formula as for the synchrotron radiation, Equation 2.16, with U_B replaced by U_{ph}. This formula is valid as long as the Thomson scattering holds, namely $\epsilon_0 \ll m_e c^2$.

The number of photons scattered per unit time is $c\sigma_T n_{\mathrm{ph}}$. Dividing Equation 2.31 by this, one can obtain the average energy of the scattered photons:

$$\epsilon = \frac{4}{3}\gamma^2\epsilon_0, \tag{2.32}$$

where the value of β is near unity ($\gamma \gg 1$).

Assuming that the electron distribution takes the form of Equation 2.20, the spectra for single scattering, namely the total scattered power per volume per energy, is given by

$$P_{\mathrm{tot_{IC}}}(\epsilon) = \pi c r_0^2 C A(p) \epsilon^{-(p-1)/2} \int \mathrm{d}\epsilon_0 \, \epsilon_0^{(p-1)/2} n_{\mathrm{ph}}(\epsilon_0) \tag{2.33}$$

$$A(p) \equiv 2^{p+1} \int_0^\infty \mathrm{d}x \, x^{(p-1)/2} f(x) \tag{2.34}$$

$$= 2^{p+3} \frac{p^2 + 4p + 11}{(p+3)^2(p+5)(p+1)}, \tag{2.35}$$

which is valid in the isotropic approximation. When the photon spectrum $n_{\mathrm{ph}}(\epsilon_0)$ is given by the blackbody radiation,

$$n_{\mathrm{ph}}(\epsilon_0) = \frac{8\pi\epsilon_0}{h^3 c^3} \frac{1}{e^{\epsilon_0/kT} - 1}, \tag{2.36}$$

we obtain from Equation 2.34

$$P_{\mathrm{tot_{IC}}}(\epsilon) = \frac{8\pi^2 r_0^2 C}{h^3 c^2} (kT)^{(p+5)/2} F(p) \epsilon^{-(p-1)/2} \tag{2.37}$$

$$F(p) \equiv A(p) \Gamma\left(\frac{p+5}{2}\right) \zeta\left(\frac{p+5}{2}\right) \tag{2.38}$$

$$\zeta(s) \equiv \sum_{k=1}^{\infty} k^{-s}, \tag{2.39}$$

where ζ denotes the Riemann zeta function. Note that the photon index of the inverse Compton scattering spectrum has a dependence on the electron energy distribution in the same manner as Equation 2.26.

The inverse Compton scattering is an efficient process of producing X-ray and γ-ray emission in various astrophysical contexts. For instance, Sunyaev-Zel'dovich effect is the most important phenomenon produced by this process. Photons of Cosmic Microwave Background radiation (CMB) passing through clusters of galaxies are scattered off by high energy electrons whose energy is typically several keV, and the 2.7 K blackbody spectrum is shifted up to slightly higher energy. Far-infrared photons, that are powerfully emitted by some galaxies, also become hard X-rays of several hundred keV when scattered by high energy electrons with energy 10 GeV.

2.2 Jupiter system

Jupiter which is the largest planet in our solar system has a period of rotation of 9 h 55 min 29.37 s, a radius of 71 492 km (traditionally defined as 1 $\mathrm{R_J}$), a period and a radius of revolution of 11.86 years and ~5.2 AU (~7.8×10^8 km), respectively. Jupiter's magnetic field is ~4.2 G on the equatorial surface. Since the Earth's surface magnetic field is ~0.35 G, it is more than 10 times stronger.

Evidence of Jupiter's magnetic field was obtained in the mid-1950s when a ground radio telescope accidentally detected radio emission from this planet. This intensely changing radio emission was interpreted as synchrotron radiation from high energy particles interacting with the magnetic field around the planet. Since then, Jupiter's magnetic field and its radiation belt have been studied directly by *Pioneer* and *Voyager* spacecrafts, and are one of the most active research subjects for up

to today's *JUNO* satellite. *Pioneer 10* also measured Saturn's magnetic field directly in September 1979.

If we can take the Earth's magnetic field, the most well-studied case of the planetary magnetic field, as a model, its origin is considered to be inside the core of the planet. A dynamo is a common and simple mechanism for creating the magnetic field. The dynamo is a mechanism that converts mechanical energy into electric or magnetic field energy. Usually, a dynamo has a built-in permanent magnet that creates the field. However, it is also possible to consider a dynamo that creates a magnetic field as a result of its own action. Such a dynamo is called as a self-excited dynamo and is thought to be the simplest mechanism in explaining the planetary magnetic field. Necessary elements for its operation are a good electrical conductor and a mechanical energy source to drive the dynamo.

Jupiter's magnetic field is tilted by ~11° relatively to its axis of rotation (similar situation as the Earth). It has a more complicated magnetic structure than the Earth, but its essence can be considered basically the same. It is clear that the origin of Jupiter's magnetic field is closely related to the internal structure of the planet. The presence of the magnetic field around Jupiter and Saturn can be seen as indirect evidence that these planets have liquid domains inside. According to one theory, Jupiter's conductive core may reach 0.7–0.8 R_J.

Based on the basic principle of the dynamo action described above, Jupiter's 10-hour high-speed rotation produces a convective system with a ring current. This current creates a magnetic field that affects the strength of the original ring current. In fact, the magnetic field generated in this way works in the direction that reduces the original force driving the ring current. In this way, the system limits the strength of the magnetic field and prevents it from increasing to infinity.

2.2.1 Magnetosphere

Jupiter's magnetic field extends out of the surface beyond its atmospheric layer and regulates the behavior of charged particles which are far from Jupiter itself. A magnetosphere is defined as the region where the influence of magnetic fields on charged particles is significant. The shape of the planetary magnetosphere generally is not a simple sphere. The Jovian magnetosphere has a long magnetotail that extends nearly to 7.5×10^8 km ($\approx 1 \times 10^4$ R_J, even to Saturn's orbit) in the opposite direction of the Sun. The Earth's magnetosphere is similar in basic structure, but it is much smaller in size. Jupiter's magnetosphere is overwhelmingly huge and powerful, and its size is variable in the range of 50–100 R_J in the solar direction.

Jupiter's magnetosphere changes its size by interactions with the solar winds. The solar wind is composed of protons, electrons, and heavy ions, with its intensity depending on the average solar activity characterized by the 11-year solar cycle. When the solar winds collide into Jupiter's magnetic field, a bow shock is formed. The inner region of the shock bounded by the surface of a magnetopause is called as a magnetosheath, and the magnetic field is disturbed there. It was precisely in this region where *Voyager* recorded the highest temperature in the solar system, reaching ~300 MK (Krimigis, 1981).

The shape of the magnetosphere is determined by the balance between the external pressure (ram pressure) exerted by the solar wind and the internal pressure (magnetic pressure) of the magnetosphere, but it is sensitive to changes in the intensity of the solar wind. If the solar wind is strong, the Sun side of the magnetosphere will be compressed accordingly. One of the reasons why

the Earth's magnetosphere is much smaller than Jupiter's is that the Earth is closer to the Sun, and the solar wind's ram pressure is higher (actually 25 times stronger). But it is also related to the fact that the Earth's magnetic field is much weaker than that of Jupiter.

In the outer region of Jupiter's magnetosphere beyond 20 R_J, the magnetic field is mostly confined to a plane which is the extension of the planet's equator. In this disk-like region, there is a current flow carried by a low energy plasma confined in the magnetic field. This region, called as the plasma sheet, is twisted to opposite directions in the dawn and dusk spheres of the planet. Thus, if the sheet is above the equator on one side, it is lower on the other side. The plasma sheet behaves like a rigid body, rotating in synchronization with the planetary rotation with up and down movements.

Jupiter's magnetosphere is classified into 3 regions according to the convention of previous research; (i) inner (<6 R_J), (ii) middle (6-50R_J), and (iii) outer (>50 R_J) regions. With one exception of *Cassini*, which mainly skimmed the dusk boundary region in December 2000, 6 spacecrafts have so far explored the magnetosphere of Jupiter. *Pioneer 10* flew by Jupiter in December 1973 along a low inclination trajectory (S Ⅲ[2] latitude <15°) and approached within 2.8 R_J from Jupiter's center. This satellite confirmed the strong magnetic field of Jupiter and its very large spatial size. *Pioneer 11* arrived at Jupiter in December 1974 on a highly-inclined trajectory (maximum S Ⅲ latitude 52°) and approached within 1.6 R_J of Jupiter's center. Because of its retrograde orbit and its high inclination, *Pioneer 11* provided the best description of the internal field so far. *Voyager 1* and *2* visited Jupiter in March and July 1979 on nearly equatorial trajectories, with closest distances of 4.9 R_J and 10.1 R_J, respectively. *Voyager 1* discovered a dense plasma torus of heavy ions near Io's orbit, whereas *Voyager 2* revealed the equatorial current sheet of Jupiter in detail. *Ulysses* flew by Jupiter in February 1992 on a mid-latitude trajectory with the closest distance of 6.3 R_J from Jupiter's center. This was the first spacecraft to explore the dusk high-latitude region of Jupiter. Finally, *Galileo* has been orbiting Jupiter since December 1995. After exploring the magnetotail as its prime mission, the spacecraft has now completed its investigation of the dusk and post-noon sectors of Jupiter's magnetosphere. In this way, the 6 spacecrafts have jointly performed complete mapping of the low-latitude regions of the magnetosphere over the entire local time. In the following, we mainly describe the interiors of the inner magnetosphere which is relevant to Jupiter's X-ray emission. As for the middle and outer magnetosphere, see Bagenal et al., 2004 (in particular Chapter 24) and Khurana et al., 2004) for their detailed accounts.

Particle distribution

The Jovian magnetosphere is normally described in terms of three major regions (Dessler, 1983)

1. The inner magnetosphere extends to the orbit of Io at a distance of ~6 R_J. This is the region where the principal magnetic field is created by the origin internal to the planet itself. Outside of this region, the effect of the azimuthal current sheet in the equatorial plane produces significant perturbation, leading to the stretching of the magnetic field lines in the radial direction.

[2]The Jupiter system Ⅲ (1965) coordinate system follows the definition in Appendix B of Dessler, 1983. This coordinate system is the accepted standard for analysis of data from the Jupiter system. System Ⅲ is a spherical, planetographic coordinate system where the planetary rotation rate of (9 h, 55 min, 29.71 s) is based on the rate of rotation of Jupiter's magnetic field. The prime meridian is defined as the sub-Earth meridian at 00:00:00 UT on Jan 1, 1965. Range is measured from Jupiter center of mass. Longitude for standard System Ⅲ is measured west. This direction choice causes the coordinate system to be left-handed and to a stationary or distant observer, longitude increases with time.

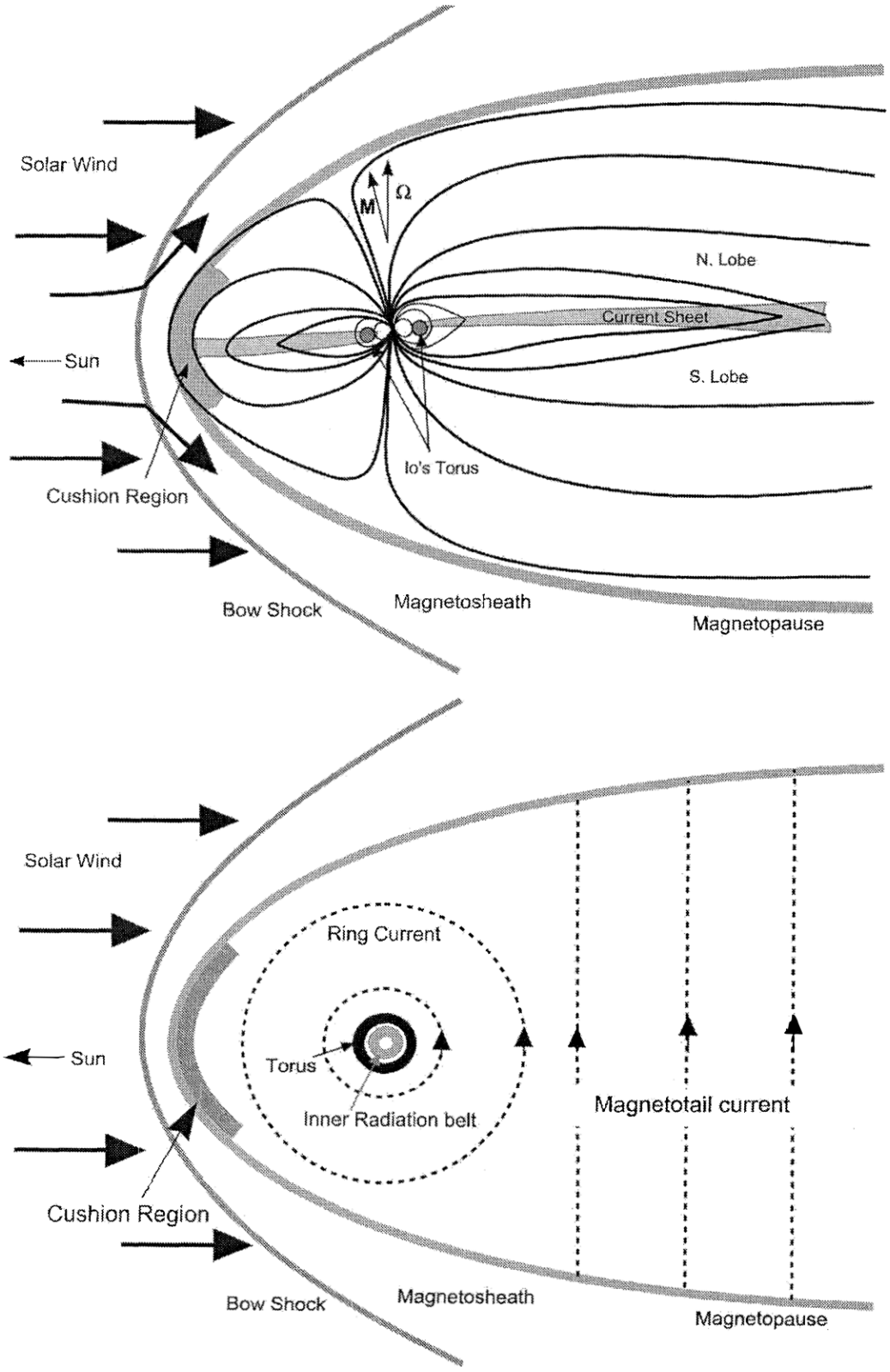

FIGURE 2.4: A schematic picture of Jupiter's magnetosphere showing the noon–midnight meridian (top) and the equatorial cross section (bottom) (Fig. 24.1 in Bagenal et al., 2004).

2. The middle magnetosphere is located between ~6 R_J and 30–50 R_J, and this is where the equatorial currents flow.

3. The outer magnetosphere extends from 30–50 R_J to the magnetopause. In this region, the magnetic field has a large southward component, and changes in the solar wind pressure can cause large temporal and spatial variations both in magnitude and direction.

In the Jovian radiation belts, trapped particles are about 10 times more energetic than their counterparts in the Earth. In addition, the particles are several orders of magnitude more abundant since Jupiter's magnetosphere has major internal sources of material. It is now understood that most of the particles come from Io and the IPT. As a result, the densest part of the magnetosphere is the IPT situated at 5.5–10 R_J (Rogers, 1995).

The model developed by Divine and Garrett (1983) is the only global model available today and is based on data obtained by the series of *Pioneer* and *Voyager* fly-bys combined with those by Earth-based observations (Divine and Garrett, 1983). For the electrons, the model covers the whole range from the surface of Jupiter to the magnetotail, while for the protons it is applicable from the surface to the magnetic shell parameter[3] $L = 12$. As for the energy spectra, minimum energies of the model are 0.06 and 0.6 MeV for electrons and protons, respectively.

The magnetic field used in the model is based on the D4 model derived from the *Pioneer* Helium vector magnetometer data (Smith et al., 1976), and is given by

$$B = \left(\frac{M}{r_m}\right)\sqrt{1 + 3(\sin\lambda_m)^2}, \tag{2.40}$$

where M is the magnetic dipole moment of Jupiter (4.225 G R_J^3; Smith et al., 1976), r_m and λ_m are distance and latitude in the S III coordinate. The magnetic shell parameter is given by

$$L = \left(\frac{r_m}{R_J}\right)(\cos\lambda_m)^{-2}, \tag{2.41}$$

where R_J is the Jovian equatorial radius (7.1492×10^9 cm).

The actual model formulas are given here, showing the fluxes of the charged particles (both electrons and protons) for the 4π direction as follows:

$$J = 4\pi \int_0^{\frac{\pi}{2}} I \sin\alpha \, d\alpha \tag{2.42}$$

$$\log I = A_0 - A_1 \log E + \frac{A_1 - A_2}{2}\log\{1 + (E/D_2)^2\} + \frac{A_2 - A_3}{3}\log\{1 + (E/D_3)^3\} \tag{2.43}$$

$$A_n \equiv a_n + (b_n - a_n)\frac{3(c_n - 1)^2 x + 3c_n(c_n - 1)x^2 + c_n^2 x^3}{3 - 9c_n + 7c_n^2} \tag{2.44}$$

$$x \equiv \frac{\log(B_m/B_e)}{\log(B_c/B_e)}, \tag{2.45}$$

[3]The magnetic shell parameter L (L-value) had been first proposed by McIlwain (1961) for the Earth's magnetosphere. Now, it is widely used to describe a particular set of planetary magnetic field lines. Colloquially, the L-value often describes the set of magnetic field lines which cross the planet's magnetic equator at a number of planet-radii equal to the L-value.

TABLE 2.1: Parameters of the Divine&Garrett model for electrons, taken from Divine and Garrett, 1983.

L	a_0	a_1	a_2	a_3	b_0	b_1	b_2	b_3	c_0	c_1	c_2	c_3	D_2	D_3
1.089	6.06	0.0	0.0	4.7	6.06	0.0	0.0	4.7	0.0	0.0	0.81	0.5	2.0	30.0
1.55	6.9	0.0	0.3	4.3	6.06	0.0	0.0	4.7	0.0	0.0	0.81	0.5	2.0	30.0
1.75	7.34	0.0	0.57	3.98	6.06	0.0	0.0	4.7	0.0	0.0	0.81	0.5	2.0	30.0
1.9	7.0	0.0	0.47	4.38	6.51	0.0	0.0	5.42	0.0	0.0	0.83	0.5	2.0	30.0
2.0	7.36	0.0	0.75	3.65	6.26	0.0	0.0	4.76	0.0	0.0	0.68	0.5	2.0	30.0
2.1	7.29	0.0	0.69	3.41	6.33	0.0	0.0	4.79	0.0	0.0	0.7	0.5	2.0	30.0
2.4	7.31	0.72	0.67	4.15	5.91	0.0	0.0	5.21	0.0	0.58	0.14	0.18	0.7	26.0
2.6	7.33	0.96	0.69	4.24	5.79	0.0	0.0	4.85	0.0	0.55	0.06	0.0	0.7	26.0
2.8	7.39	0.76	0.59	2.65	5.86	0.0	0.0	6.09	0.0	0.56	0.36	0.35	0.2	22.0
2.85	7.44	0.8	0.6	2.65	5.8	0.0	0.0	6.09	0.0	0.56	0.37	0.35	0.2	22.0
3.2	7.0	1.32	0.53	2.65	5.89	0.0	0.0	6.09	0.0	0.49	0.4	0.35	0.2	22.0
3.6	6.91	1.37	0.51	3.51	5.75	0.0	0.0	6.7	0.0	0.58	0.49	0.35	0.2	22.0
5.2	6.21	1.7	0.48	4.93	5.8	0.0	0.34	4.28	0.0	0.56	0.0	0.5	0.2	22.0
6.2	6.37	1.33	0.0	2.27	6.33	0.0	1.66	3.07	0.0	0.56	0.13	0.4	1.0	10.0
7.2	6.39	1.07	0.02	3.02	6.12	0.0	1.82	3.56	0.0	0.32	0.06	0.4	1.0	10.0
9.0	6.6	0.65	0.54	3.6	5.63	0.65	2.07	2.0	0.0	0.0	0.59	0.47	1.0	10.0
10.5	7.23	0.59	1.95	2.23	5.73	0.93	2.71	2.0	0.55	0.0	0.62	0.56	1.0	10.0
11.0	7.07	0.92	2.0	2.0	5.56	0.82	2.82	2.0	0.56	0.57	0.47	0.0	1.0	10.0
12.0	6.76	0.95	2.13	2.0	5.0	1.2	2.99	2.0	0.58	0.26	0.37	0.0	1.0	10.0
14.0	6.67	0.2	2.9	2.0	3.34	2.86	1.01	2.0	0.62	0.65	0.0	0.0	1.0	10.0
16.0	4.44	0.89	0.9	2.0	5.86	0.76	7.95	2.0	0.0	0.26	0.7	0.0	1.0	10.0

where E is the energy of the charged particles and x is the intermediate variable where $0 \leq x \leq 1$. B_m represents the mirror point field strength given by $B_m = B(\sin\alpha)^{-2}$, B_c does the upper cutoff field strength along the L-value for stable charged particle trajectories, which is calculated from the O4 model (Acuna and Ness, 1976) and is described as the dashed curve in figure 1 in Divine and Garrett, 1983, and B_e does the minimum field strength along the L-value given by $B_e = M(LR_J)^{-3}$. Table 2.1 summarizes a_n, b_n, c_n and D_n parameters in Equation 2.43 and Equation 2.44 for electrons (for protons, see table 5 in Divine and Garrett, 1983), and the resultant distributions are shown in Figure 2.5 (for protons, also see figure 3 in Divine and Garrett, 1983).

Inner radiation belts

Plasmas are energized by various electric fields and directed inwards, creating radiation belts in the inner magnetosphere of Jupiter. N. Brice and Mcdonough (1973) and Schardt and Goertz (1983) described that this radial diffusion was driven by the ionospheric dynamo fields produced by the winds in Jupiter's atmosphere. Based on the *Pioneer* observations, the electron distribution in the

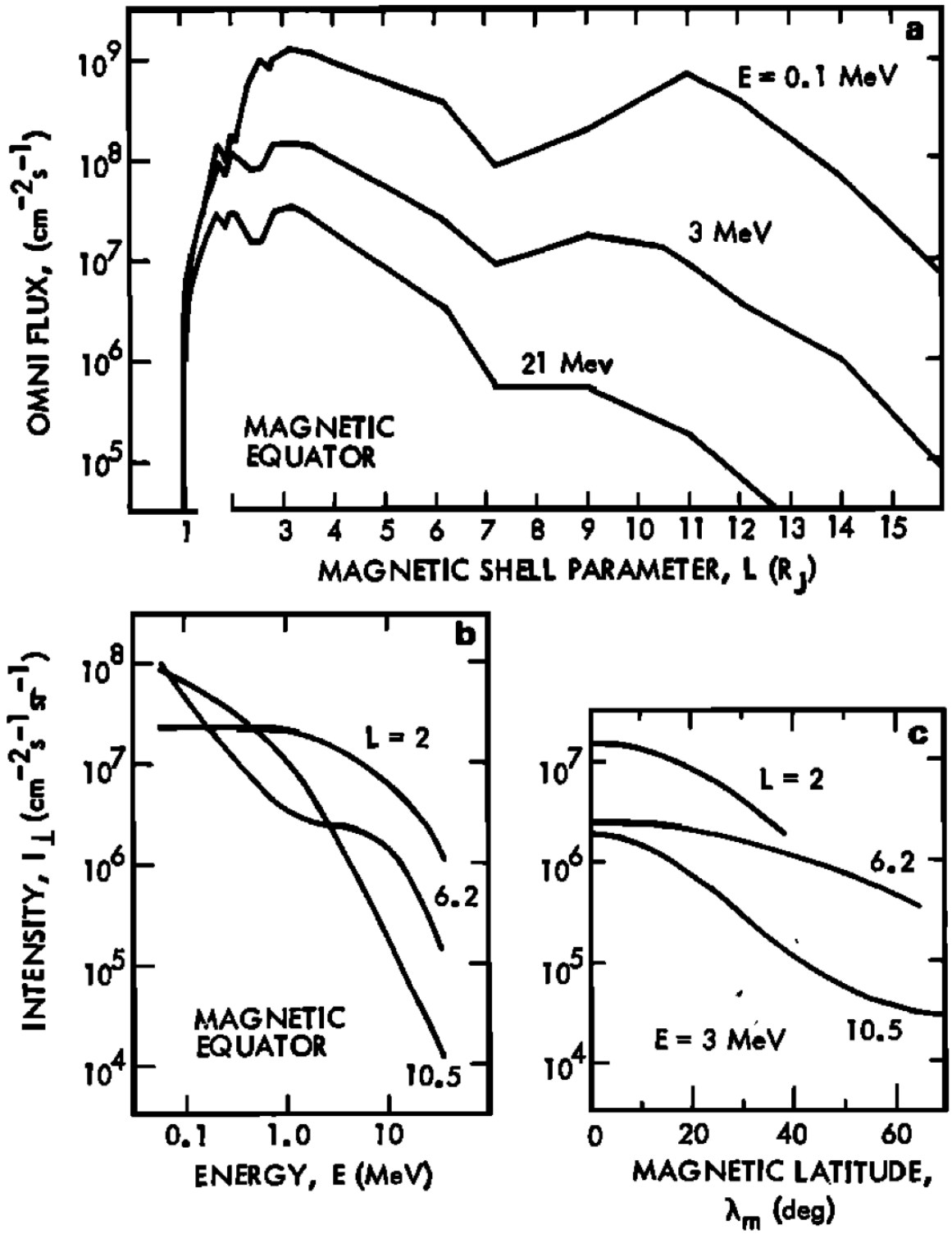

FIGURE 2.5: Sample dependences for electron distribution model in the Jovian magnetosphere, taken from Divine and Garrett, 1983. (a) Omnidirectional integral flux at three energies as a function of L-shell parameter. (b) Integral intensity at 90° pitch angle at the equator and for three L-shell values as a function of energy. (c) Integral (E = 3 MeV) intensity at 90° pitch angle for different L-shells as a function magnetic latitude.

inner (and middle) magnetosphere was modeled by Divine and Garrett (1983), the details of which will be shown later.

The Divine&Garrett (D&G) model reproduces the *in-situ* observed data quite well, with deviations limited to a range which might be expected from dynamics and time variability. The electrons could be strongly absorbed by Galilean moons, Io at 5.9 R_J and Europa at 9.5 R_J. However, the observed effects of the absorption are small and no large density drops are observed near the orbits of these moons. Inside of distance ~2 R_J, electrons are further lost due to interaction with other minor satellites and the rings of Jupiter. The *Galileo* satellite observed that the energy spectra of electrons became softer as the satellite approached Jupiter (<2 R_J), presumably because energetic electrons experienced stronger interaction in Jupiter's atmosphere.

However, the D&G model provides a relatively poor fit to the observed features of the synchrotron emission, including the overall intensity, spectrum of the radio emission, and the beaming curve variation over Jupiter's rotation. Bolton, Levin, et al. (2001) have inverted the observed synchrotron emission to relativistic electrons and looked into the spatial distribution of electrons in the radiation belts, and indicated that the D&G model significantly underestimated the number density of relativistic electrons by as much as a factor of 5–10. The pitch-angle distribution was also not consistent with the synchrotron emission images. Near Jupiter (<3 R_J), the relativistic electrons lose their energy via the synchrotron radiation in the decimetric radio band, which was first discovered from Earth-based observations by Sloanaker (1959).

The Jovian synchrotron emission has been observed in decimetric radio bands corresponding to frequencies between hundreds MHz to several GHz. Figure 2.6 shows a color map of the 13.8 GHz synchrotron emission taken by the *Cassini* spacecraft (Bolton, Janssen, et al., 2002). This observation provides unambiguous evidence for the presence of ultra-relativistic electrons with energies up to tens MeV. The brightest regions near 1.4 R_J shows peak emission by electrons with an average energy of ~50 MeV gyrating in a background magnetic field of empirically ~1.2 G. In regions showing significant emission at radial distances >2 R_J, it is probably suggested that much higher energy (~100 MeV) electrons at the larger radial distances due to the weaker magnetic field strength. Including ground-based observations with different wavelengths (e.g., 0.333, 2.3, and 5 GHz), a spectrum of the Jovian synchrotron emission has been obtained as shown in Figure 2.7 which indicates energy indexes roughly estimated with ~0.15 and ~2, whose corresponding photon indexes are ~1.15 and ~3, in lower and higher frequencies than 5 GHz, respectively.

Bolton, Janssen, et al. (2002), Klein et al. (2001), and Santos-Costa et al. (2008) reported both long and short term variations of the synchrotron emission (Figure 2.8). Given the strength of Jupiter's magnetic field and the relevant energies of the electrons responsible for the synchrotron emission, it was difficult for theorists to explain even a 10–20% variability in the synchrotron range. On the other hand, a correlation between the long-term variation of the synchrotron flux and the solar wind intensity has been reported by Bolton, Gulkis, et al. (1989) with a lag time of 1–2 years, consistent with the diffusion coefficients suggested by N. M. Brice and Ioannidis (1970). Miyoshi, Misawa, et al. (1999) have reported that some short-term variation of the synchrotron radiation was correlated with the solar F10.7 flux enhancements, and suggested that this may be due to enhanced radial diffusion as a result of atmospheric heating associated with the increase of the solar UV/EUV flux. The characteristic timescale for relativistic electrons for the radial diffusion and the resultant

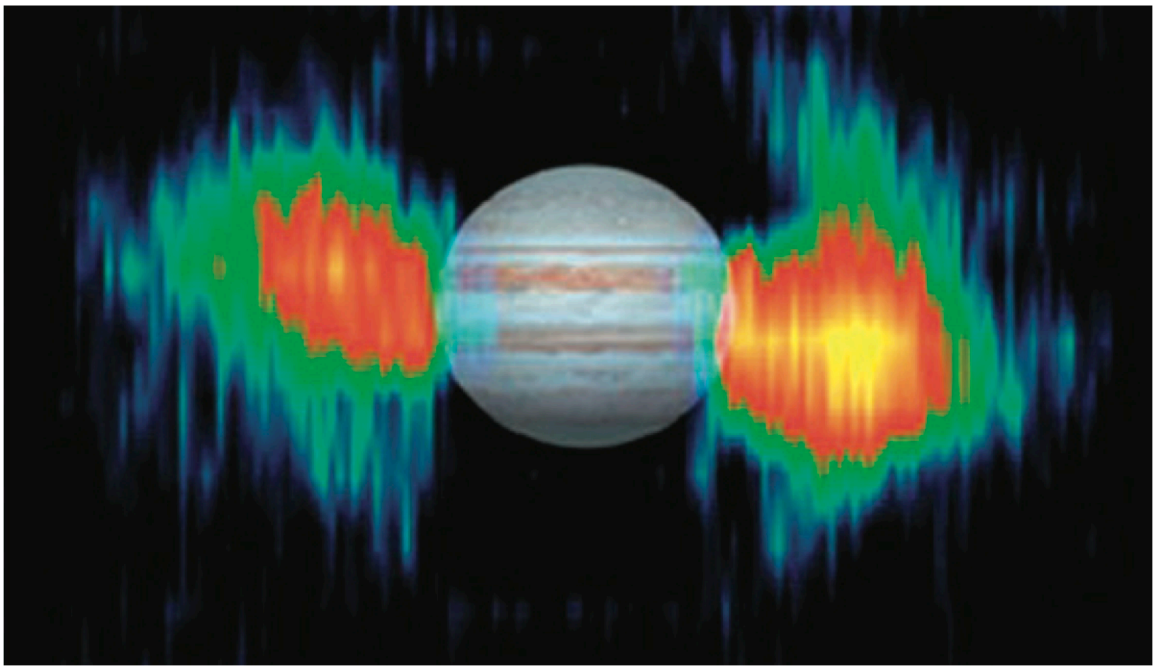

FIGURE 2.6: *Galileo* Color maps of Jupiter's synchrotron emission at 2.2 cm wavelength (13.8 GHz) obtained with the *Cassini* Radar instrument during Jupiter flyby in 2001 (after figure 27.15 in Bagenal et al., 2004). A visible image constructed from *Hubble Space Telescope* and *Voyager* data is shown superimposed for context. Thermal emission from the atmosphere has been subtracted.

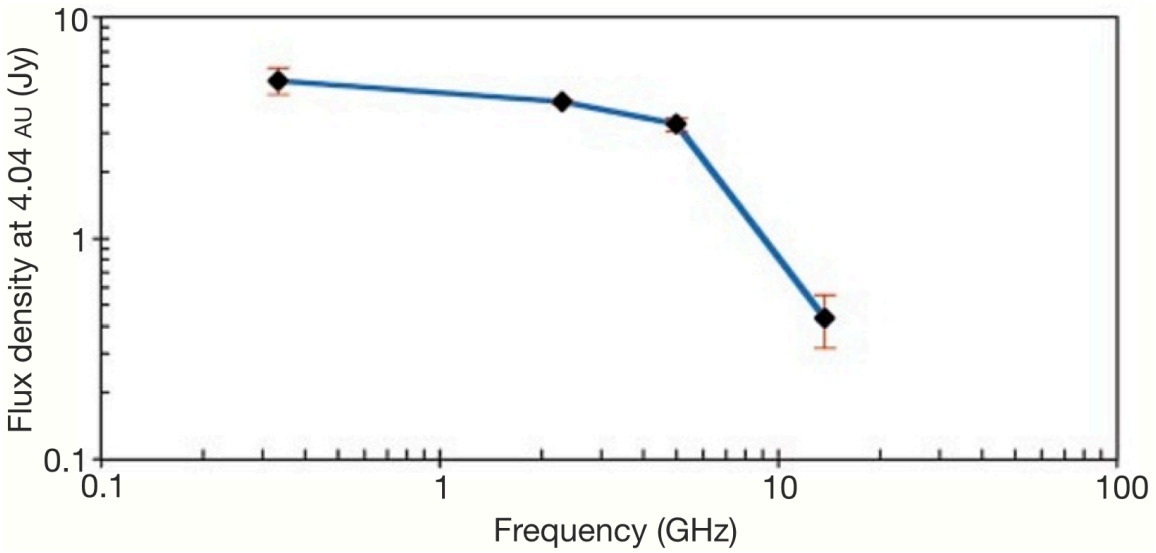

FIGURE 2.7: Jupiter's non-thermal radio spectrum, taken from Bolton, Janssen, et al., 2002. The flux density of Jupiter's synchrotron emission simultaneously observed with *Cassini* (13.8 GHz), the DSN (2.3 GHz), and the VLA (0.333 GHz) from January 2001. Previous measurements at 6 cm (5 GHz) from 1994 are also shown for completeness.

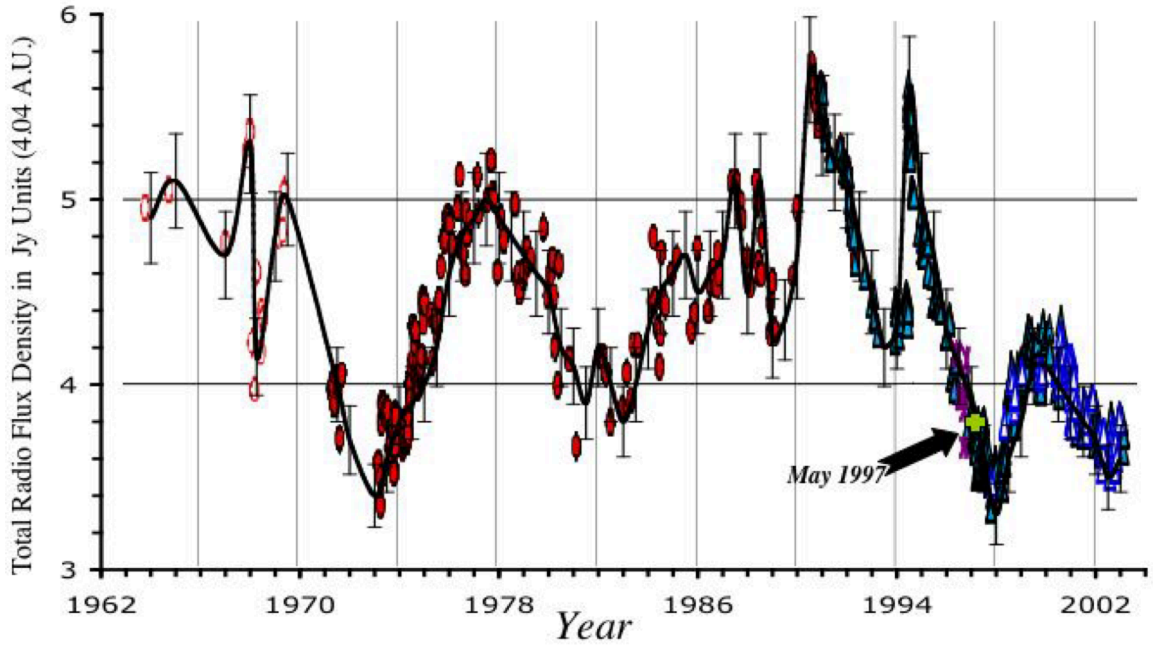

FIGURE 2.8: History of long-term variations in the flux density of Jupiter's synchrotron radio emission at 13 cm wavelength. The DSN and GAVRT data (open and filled triangles) were merged with the ongoing NASA/JPL Jupiter Patrol (filled circles), and observations made with Parkes and Nancay radio telescopes (open circles) (after Bolton, Janssen, et al. (2002)). The black curve depicts the general temporal variation of the decimetric emission.

synchrotron radiation is approximately a year. Because of the great complexity of the Jupiter system (rings, dust, and satellites) and the strength of the Jovian magnetic field (~10 times stronger than the Earth's), Jupiter's radiation belts are very energetic and have a wide variety of processes going on.

Io Plasma Torus

Io has the orbit closest to Jupiter (5.9 R_J) among the four Galilean satellites, with the orbital period of 42.46 h. The most important factors that make Io's electrodynamic interaction unique in our solar system are Jupiter's strong magnetic field, its fast rotation, and Io's volcanic activity. Io and the other Galilean satellites are located deep within Jupiter's magnetosphere. In contrast, for example, the Earth's moon passes through the tail of the Earth's magnetosphere once per month. Io is also the most volcanically active body in our solar system with more than 100 known active volcanoes. These volcanoes create a tenuous and patchy atmosphere on Io that is thought to consist mainly of SO_2.

Through several processes, Io's atmosphere loses matter into the Jovian magnetosphere where the mass arrives in both ionized and neutral forms. Saur et al. (2003) estimated that <20% is locally ionized. A mechanism of the neutral mass loss could be sputtering by torus ions (Johnson, 2013; Smyth, 1998). The neutrals are then ionized by UV radiation or by electron impact ionization. The new ions and electrons accumulate around the orbit of Io and form the Io plasma torus as shown in Figure 2.9. The total mass loss rate from Io, which maintains the torus, is thought to be ~1000 kg s^{-1}.

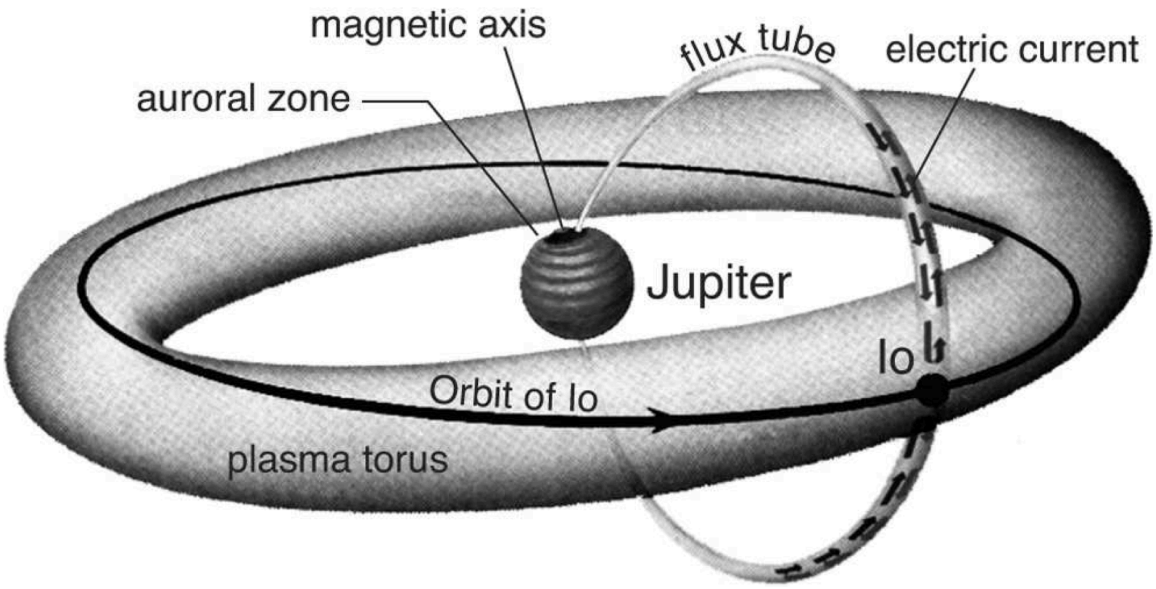

FIGURE 2.9: A sketch of the Io plasma torus and the general geometrical setup, after Audouze and Israel (1988).

Upstream of Io the plasma nearly fully co-rotates with Jupiter, i.e., with the same angular velocity as Jupiter, whose rotation period of ~10 h makes the IPT rotate with a velocity of ~74 km s^{-1}. The torus plasma overtakes Io with a relative velocity of ~57 km s^{-1}. The plasma of the torus consists mostly of the ions of SO_2, i.e., S^+, S^{2+}, O^+, O^{2+}, etc., which eventually populate the whole magnetosphere of Jupiter. Therefore, the plasma of the Jovian magnetosphere, in contrast to that of the Earth, contains mostly heavy ions. Outside of Io's ionosphere in the IPT, the plasma density varied for different fly-by measurements as ~1000 cm^{-3} to ~3600 cm^{-3} (Gurnett et al., 1996), which is comparable to the maximum density of 2000 cm^{-3} observed by *Voyager 1* (Frank and Paterson, 2000, 2001, 2002; Frank, Paterson, et al., 1996).

Aurora

Auroral processes are exhibited by planets and satellites which have a collisionally thick atmosphere and an internal magnetic field sufficiently strong to stand against the solar wind or plasma flow. This auroral activity is manifested as emission produced by the impact of high-energy charged particles with the planet's upper atmosphere. Thus, auroras reflect the magnetospheric processes and show us the global scale of the magnetosphere.

Jupiter's aurora is one of the most powerful region (~1×10^3 W in radiation; 100 times stronger than that of the Earth) over all planets in the solar system, and has been observed in a wide range of wavelengths from infra-red to X-ray. Several phenomena have been confirmed through UV and IR observations, such as the main oval surrounding Jupiter's magnetic pole, the satellite's footprint through their own flux tube, and the polar emission connecting to the magnetotail (Bagenal et al., 2004; e.g., figure 26.1).

Regarding Jupiter's aurora, an interaction of Io with Jupiter's magnetic field is of particular interest, with no equivalent phenomenon at the Earth. Io is electrically connected, due to its ionosphere, with Jupiter's magnetic field and with the co-rotating IPT.

Particle acceleration

The following scenarios are considered for acceleration mechanisms of the high energy particles in Jupiter magnetosphere. At first, plasmas, which are thought to mainly originate in the IPT (in part from solar winds) and to be transported outward via several transient processes (see detail, e.g., chapter 25 in Bagenal et al., 2004), are provided by magnetic reconnections in the magnetotail, trapped in Jupiter's magnetic field and transported inward across the field lines. Then, in the inward transport process, the plasma particles are accelerated by a betatron acceleration based on the conservation of the first adiabatic invariant of themselves in the magnetic field, i.e.,

$$\mu = \frac{p_\perp}{2m_0 B} = \frac{E_\mathrm{k}}{B}\left(1 + \frac{E_\mathrm{k}}{E_0}\right) \tag{2.46}$$

should be conserved. Here, $p_\perp$ is the momentum of the charged particle perpendicular to the magnetic field direction, m_0 is the rest mass of the particle, B is the magnetic field magnitude (at the mirror point), E_k is the kinetic energy of the particles, and E_0 is the rest energy of the particles. For simplicity, the pitch angle of the particles is assumed to be 90°. When the particles conserving μ are transported from regions with relatively weak magnetic fields (distant from the planet) into regions with strong magnetic fields (vicinity of the planet), the energy of the particles increases in response to the change in the magnetic field strength.

However, it was also known that the radial diffusion process could not completely explain densities of ultra-relativistic (several tens MeV) particles in the inner radiation belts, which suggested a necessity of non-adiabatic accelerations until the particles approaching the Io (Sicard and Bourdarie, 2004). The wave-particle interaction by the whistler-mode chorus waves has been focused as one candidate for the non-adiabatic accelerations (Horne et al., 2008; Miyoshi, Morioka, et al., 2003). The whistler-mode chorus waves are plasma waves generated in the inner magnetosphere and observed in 0.2–0.8 times wavelength bands of the characteristic cyclotron frequency of electrons (Santolík et al., 2004). Ratcliffe and Storey (1953) discovered the whistler-mode chorus waves from the Earth's magnetospheric observations (they called "whistlers") and Katoh and Omura (2007) and Omura et al. (2008) conducted the simulated experiments and reproduced that in part high-energy electrons are accelerated with high efficiency by nonlinear interaction with the generated chorus waves. The chorus waves, whose amplitude is $\sim 10^{-3}$ times the background magnetic field strength, are coherent waves, and the (in part) resonant electrons are trapped by the potential created by the wave electromagnetic field component, resulting in efficient acceleration. Figure 2.10 shows spatial distributions of the chorus waves observed by the *Galileo* probe (Katoh, Tsuchiya, et al., 2011). The chorus waves have been observed in regions between Io ($\sim 6\,\mathrm{R_J}$) to Ganymede ($\sim 15\,\mathrm{R_J}$) along the probe trajectories. It remains necessary to directly observe the chorus waves with high-resolution for more detail discussion about its physical processes.

These accelerated particles lose their energies by colliding with the moons, dusts, and rings, by generating synchrotron radiations in the vicinity of Jupiter, and by precipitating into the ionosphere followed by the aurora emission. As for the acceleration and disappearance of particles in Jupiter magnetosphere, theoretical scenarios based on *in-situ* and remote observations of high energy particles and the aurora emission are being constructed. However, many phenomena remain that have

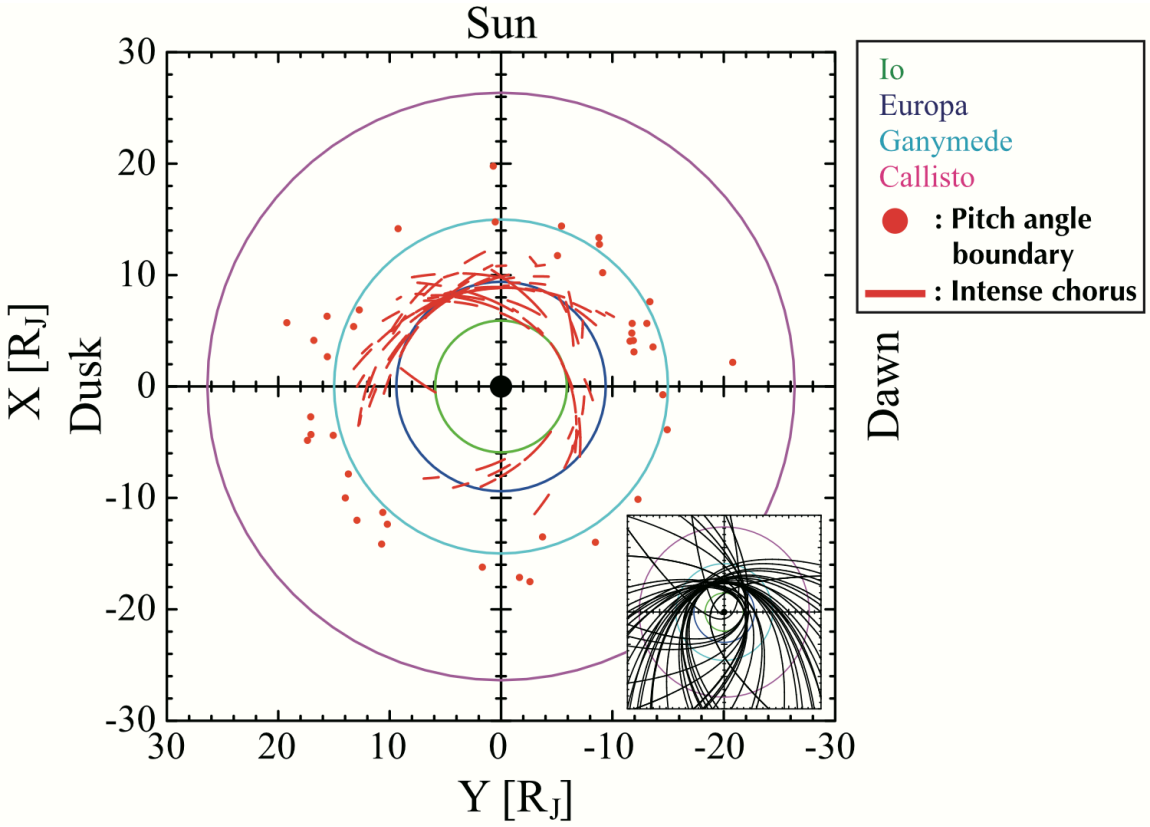

FIGURE 2.10: Spatial distributions of the whistler-mode chorus waves observed by *Galileo* probe, taken from Katoh, Tsuchiya, et al., 2011.

not been sufficiently elucidated by observations, such as the magnetosphere-ionosphere coupling, non-adiabatic accelerations near Io, acceleration by field-aligned currents and so on. In order to entirely describe the mechanism of the generation and extinction of high-energy particles in Jupiter magnetosphere, It is necessary to obtain the spectra of high-energy particles at each location, the maximum energy of particles, the aurora emission, etc. spatially and temporally.

2.2.2 X-ray emission

The *Einstein* observatory first detected Jupiter's X-ray emission on April 13, 1979 (Metzger et al., 1983). In the same period, Jupiter's ultraviolet auroral emission was also first detected by the *International Ultraviolet Explorer* (*IUE*) and subsequently observed by the *Voyager 1* Ultraviolet Spectrometer which was passing through the Jupiter system. The spatial resolution of the instruments in this era was not enough to identify that the emission is connected anywhere in the Jovian magnetosphere, and even related with the Io torus or larger radial distances from the planet. Nevertheless, the *Einstein* spectrum provided a view that Jupiter's auroral emission is not due to electron bremsstrahlung as on the Earth, but is likely line emission from energetic oxygen and sulfur ions (0.03–4.0 MeV/nucleon) precipitating just outside of the Io plasma torus (IPT). This view indicated by Metzger et al. (1983) was followed by observations by Gehrels and Stone (1983), showing a large decrease in the radial distribution of these ions at 6–8 R_J. The effect on Jupiter's upper atmosphere by energetic electrons and ion precipitation was modeled by Horanyi et al. (1988) and Waite Jr.,

Cravens, et al. (1983), respectively. The models aimed at distinguishing the electrons from the ion precipitation, and suggested that most of the effects were similar, but that both ultraviolet and X-ray emissions from the energetic oxygen and sulfur were the observable sign of the ion precipitation.

Searches for these auroral emission lines were carried out in UV (Waite Jr., Clarke, et al., 1988) X-ray wavelengths (Waite Jr., Bagenal, et al., 1994; Waite Jr., Gladstone, et al., 1997) based on the *IUE* and *ROSAT* observations, respectively. No clear signatures, however, were obtained for sulfur near 1256 Å or for oxygen at 1304 Å.

Auroral emission: *Chandra* & *XMM-Newton*

Chandra carried out the first observations of Jupiter's X-ray aurora. Surprisingly, the emission was not located in the ultraviolet auroral zone at all (Gladstone et al., 2002), and the X-rays came from higher latitudes near Jupiter's pole—regions that were mapped to the outer boundary of Jupiter's magnetosphere. Furthermore, the emission was pulsing regularly with a 40-min period. The periodicity was reminiscent of Jupiter's radio emission known as quasi-periodic radio bursts, which had been observed by *Ulysses* in conjunction with energetic electron acceleration in Jupiter's outer magnetosphere (MacDowall et al., 1993). However, the 40-minute periodicity was not present during a latter observational sequence (R. F. Elsner, Lugaz, et al., 2005). Variability at similar time scales was seen, but the occurrence was in a more random way. Simultaneous radio observations by *Ulysses* indicated that the variation had no strong periodic feature as seen in the past occasions, and statistical correlation between the X-ray and radio variations could not be found. A *Chandra* time-tagged observation coordinated with UV observation by *Hubble Space Telescope (HST)*, in addition, allowed identification of a Jovian polar cap auroral flare, although spatial correlation between X-ray and UV was not confirmed. The X-rays increased in time in a consistent way with the UV flare, but the location of the X-ray peak was not morphologically associated with the UV flare location (R. F. Elsner, Lugaz, et al., 2005). This morphological inconsistency between X-ray and UV has been left unsolved up to date.

Chandra showed a clear spectral signature of oxygen line emission and the location to be a high-latitude region that could be mapped to near the magnetopause boundary as shown in Figure 2.11. These results presented the following difficulties. If X-ray aurora was observed at low latitudes, this region could be connected to the middle magnetosphere where there was sufficient phase space density of energetic sulfur and oxygen ions to account for the X-ray emission. However, the high aurora latitudes were connected to the outer magnetosphere which lacked the density of energetic heavy ions to provide the measured X-ray intensity. Horanyi et al. (1988) suggested firstly that acceleration of energetic ions could be invoked to increase the phase space distribution, and the question was whether the acceleration involved magnetospheric heavy ions or solar wind heavy ions. This acceleration process for both sources was soon demonstrated, and megavolt accelerations were required. Such acceleration may also explain the quasi-periodic radio emissions (Cravens, Waite, et al., 2003).

Subsequent spectral observations were conducted from *XMM-Newton* whose X-ray detector had medium and high energy resolution (Branduardi-Raymont, Bhardwaj, R. F. Elsner, et al., 2007; Branduardi-Raymont, R. F. Elsner, Galand, et al., 2008; Branduardi-Raymont, R. F. Elsner, Gladstone, et al., 2004). The observations showed very strong emission lines of He-like oxygen from

Jupiter's aurora as shown in Figure 2.12. In addition, *XMM-Newton*, for the first time, identified a higher energy component in the auroral spectra which was variable on a time scale of days as shown in Figure 2.13 (Branduardi-Raymont, Bhardwaj, R. F. Elsner, et al., 2007). The spectral shape of the high-energy component is consistent to be bremsstrahlung of energetic electrons precipitating from the magnetosphere (Singhal et al., 1992). The variability of the bremsstrahlung spectrum was caused by a change of energy distribution of electrons in the Jovian magnetosphere or by an increase of the solar activity during the observation period, November 2003. Kharchenko et al. (2008) have calculated the X-ray spectrum produced by precipitating sulfur and oxygen ions in the auroral atmosphere of Jupiter, and compared it with the results by *Chandra* and *XMM-Newton*. They found a reasonable agreement between the observed and model spectra if equal abundance of sulfur and oxygen ions with energies of ~1–2 MeV u^{-1} exist in the emitting region.

The above-mentioned question whether the acceleration involved magnetospheric heavy ions or solar wind heavy ions may now be answered: both of them are likely to contribute equally. Bunce et al. (2004) suggested that magnetic reconnection near the cusp of Jupiter's magnetosphere might be responsible for the acceleration of heavy ions, and from an analogy with the Earth, both solar winds and magnetospheric plasmas could be accelerated.

Disk emission: *Chandra* & *XMM-Newton*

Waite Jr., Gladstone, et al. (1997) first recognized the low-latitude disk X-ray emission (i.e., near Jupiter's equator) from *ROSAT* observations, and suggested a correlation between low magnetic field regions and X-ray bright regions. This supported a view that the X-rays were generated as a result of precipitation of energetic sulfur and oxygen ions originating Jupiter's inner radiation belts into its atmosphere. Maurellis et al. (2000) proposed two alternative mechanisms, which could account for the low-latitude *ROSAT* measurements well. One is an elastic scattering of solar X-rays by atmospheric neutrals, and the other is a fluorescence from carbon K-shell caused by X-ray scattering of methane molecules located below the Jovian homopause.

In the 2000s, a *Chandra* HRC-I observation gave the high-resolution image of Jupiter's X-rays (Gladstone et al., 2002), with no information on the X-ray spectrum. It resolved two auroral hot spots in the polar regions, and, in addition, displayed a relatively uniform distribution of X-rays covering the whole Jupiter's disk at low latitude.

Observations by *XMM-Newton* in April and November 2003 clearly showed a difference in spectral shape between the disk and auroral emission as shown in Figure 2.12 (Branduardi-Raymont, Bhardwaj, R. F. Elsner, et al., 2007). The disk spectrum (Figure 2.13) peaked at higher energies (0.7–0.8 keV) than the aurora (0.5–0.6 keV) and lacked the high energy component (>3 keV) which was present in the latter. Based on the observation in November 2003, *XMM-Newton* EPIC images were shown in narrow spectral bands centered on the O^{6+}, O^{7+}, Fe^{16+} and Mg^{10+} emission lines (Branduardi-Raymont, Bhardwaj, R. F. Elsner, et al., 2007).

The disk X-ray spectrum measured with *XMM-Newton* was well fitted by a coronal plasma model with a temperature in the range 0.4–0.5 keV and solar abundance, by including additional Mg^{10+} and Si^{12+} emission lines at 1.35 and 1.86 keV, respectively. These lines in the spectra were likely to be caused by the solar activity which was enhanced at the time of observation. The *XMM-Newton* spectral data strongly supported the view that Jupiter's disk X-rays were scattered solar radiation

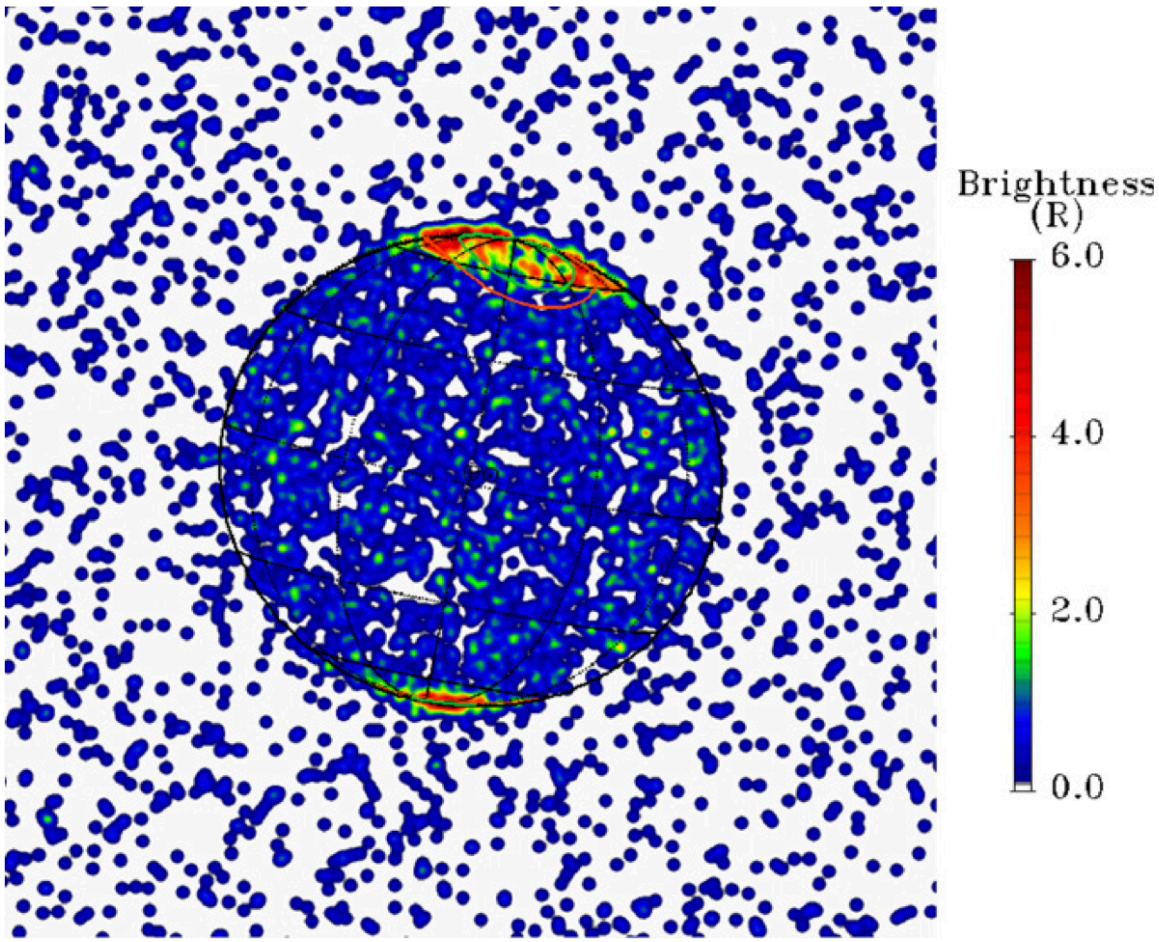

FIGURE 2.11: *Chandra* HRC images of Jupiter's X-rays showing bright X-ray emission from Jupiter's aurorae at the high-latitude position and uniform distribution from the low-latitude disk regions, taken from Bhardwaj, R. F. Elsner, Randall Gladstone, et al., 2007.

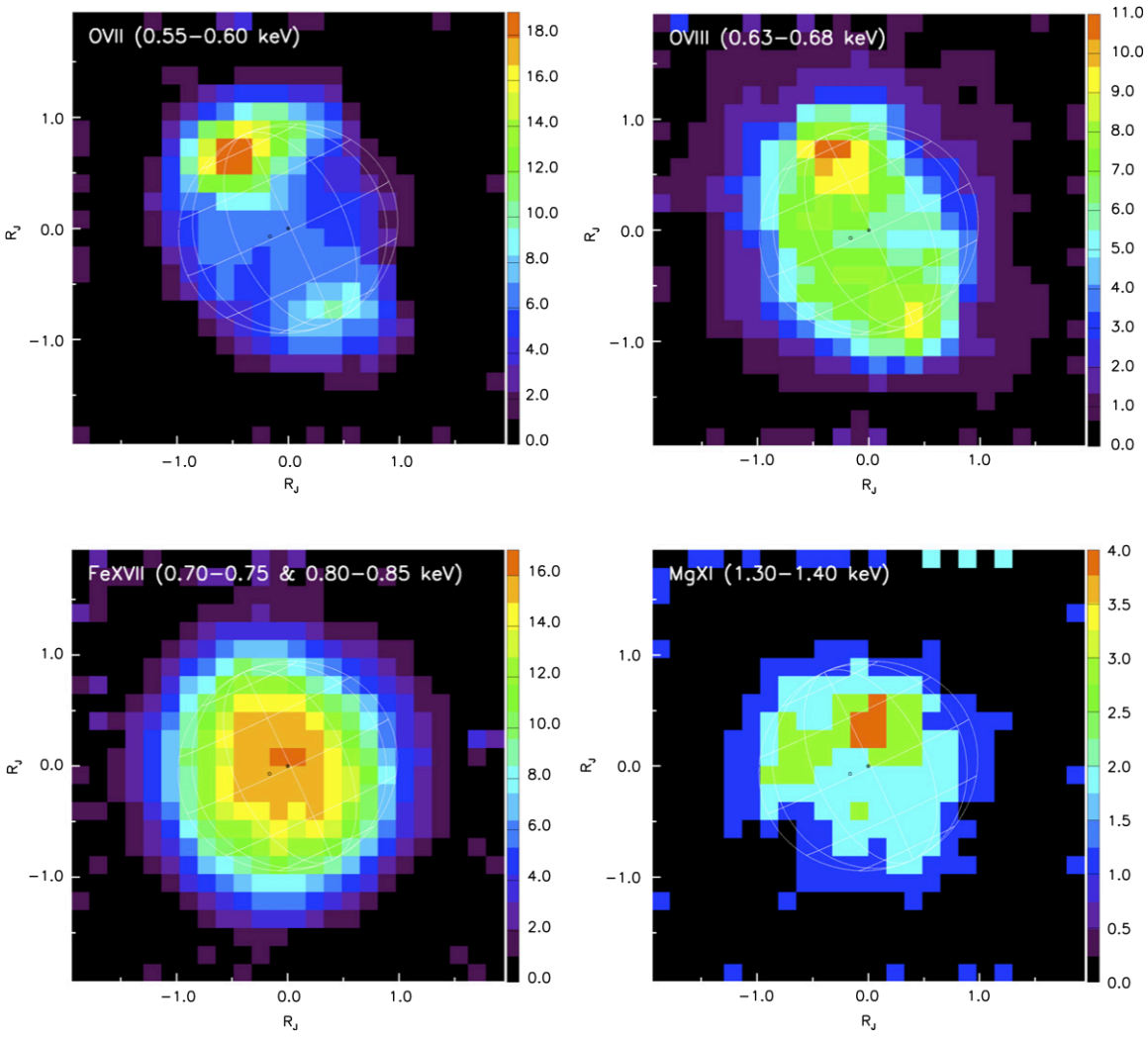

FIGURE 2.12: *XMM-Newton* EPIC images of Jupiter's X-rays in 4 sets of energy bands (taken from Branduardi-Raymont, Bhardwaj, R. Elsner, et al., 2007): (upper left) 0.55–0.60 keV for O^{6+}, (upper right) 0.63–0.68 keV for O^{7+}, (lower left) 0.70–0.75 and 0.80–0.85 keV for Fe^{16+}, (lower right) 1.30–1.40 keV for Mg^{10+}. The O^{6+} emission peaks clearly at the North and (more weakly) South auroral spots, and O^{7+} extends to lower latitudes, with enhancement at the North spot, while Mg^{10+} and especially Fe^{16+} display a more uniform distribution over the planet's disk.

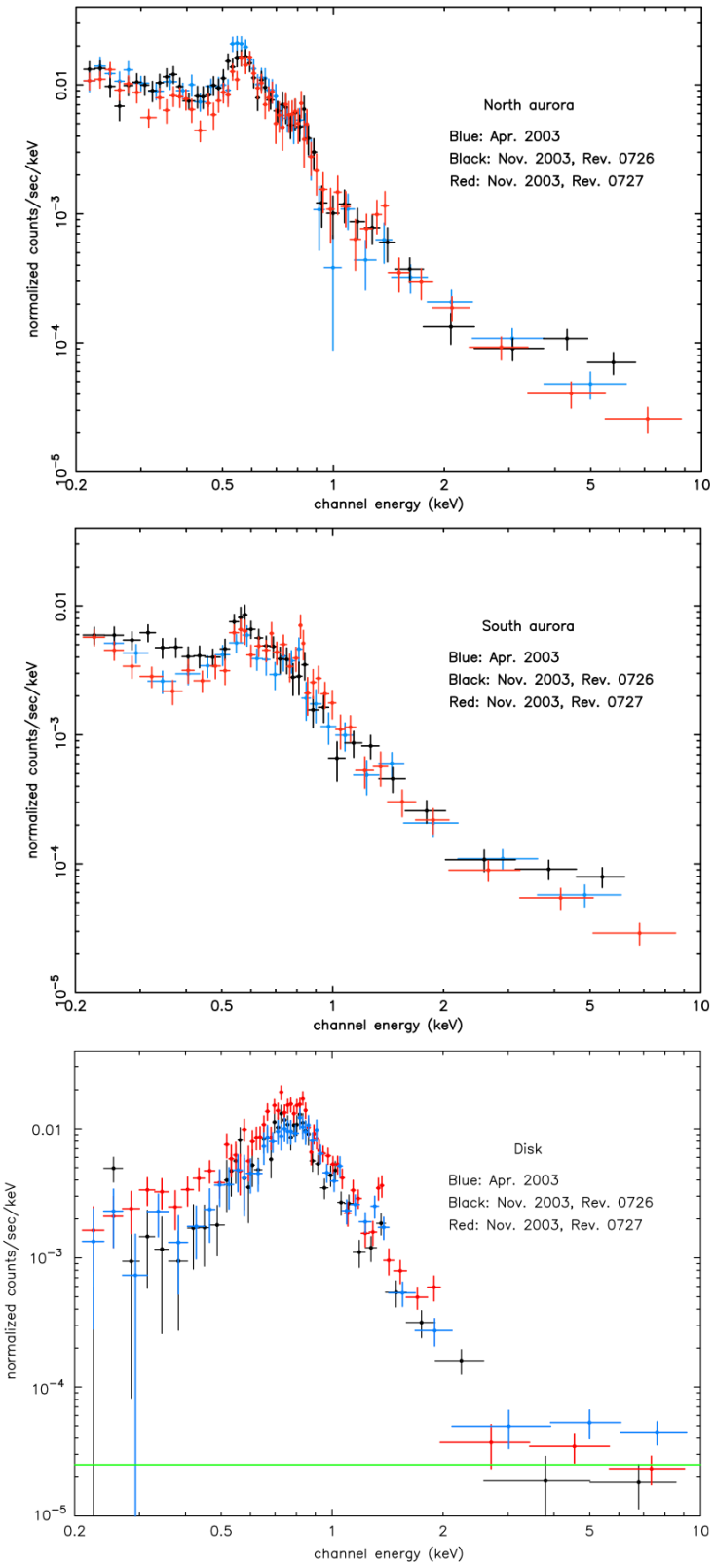

FIGURE 2.13: *XMM-Newton* EPIC spectra of Jupiter's X-rays from (top) north and (middle) south aurora, and (bottom) disk regions, respectively (taken from Branduardi-Raymont, Bhardwaj, R. F. Elsner, et al., 2007).

(Branduardi-Raymont, Bhardwaj, R. F. Elsner, et al., 2007). A *Chandra* ACIS-S observation in February 2003 indicated a similar result that the disk emission was harder than the auroral emission (Bhardwaj, 2006; Bhardwaj, R. F. Elsner, J. Hunter Waite, et al., 2005). *Chandra* observations also confirmed the correlation between the regions of low magnetic field and slightly higher soft X-ray count rate, suggesting a possibility of a secondary component in addition to the scattered solar X-rays. Unlike the auroral X-ray emission, the disk emission did not show any variability on timescales from 10 to 100 min.

The conclusions obtained from the spectral studies of Jupiter were strengthened by the observation, again in November 2003 by *XMM-Newton*, of similar day-to-day variability in the solar and Jovian equatorial X-ray fluxes. A large solar X-ray flare, occurred on Jupiter-facing side of the Sun, was accompanied by a corresponding feature in Jupiter's disk X-ray lightcurve (see Figure 30, taken from Bhardwaj, R. F. Elsner, Randall Gladstone, et al., 2007). This finding supported the view that indeed Jupiter's low latitude X-rays were mostly scattered radiation of solar origin. Recent calculation of the albedo effect (Cravens, Clark, et al., 2006) could explain the observed flux, under the hypothesis that both elastic scattering and fluorescence were the origin of the observed emission. These results, however, do not rule out the presence of other sources for the low-latitude X-ray emission, e.g., precipitation of energetic oxygen and sulfur ions from Jupiter's radiation belts, especially into the regions of low magnetic field.

Emission from Jupiter's inner radiation belts: *Suzaku*

There are so many high-energy electrons in Jupiter's radiation belts. The magnetic field is strong within ~6 R_J from Jupiter (~1.2 G and ~0.01 G at ~1.5 R_J and ~6.0 R_J, respectively), and three exploration satellites (*Pioneer 10*, *Pioneer 11*, and *Galileo*) discovered high-energy electrons from keV reaching up to several tens of MeV. Synchrotron radiation from these electrons has been monitored in radio wavelengths by ground-based telescopes and *Cassini* satellite. In short, Jupiter's internal radiation belts are the strongest particle acceleration site in the solar system. However, since the environment is occupied by plasmas with energetic particles, it is difficult for exploration satellites to directly enter the region and only limited information can be obtained. Also, the remote observation of the Jovian synchrotron radio emission is biased to the region where the magnetic field is very strong (~2 R_J). Thus, a precise and global view of the energy and spatial distribution of electrons in the inner radiation belts has not yet been obtained. Understanding the distribution of such high-energy electrons is very important in clarifying the acceleration mechanism.

Suzaku observed Jupiter for ~160 ks in February 2006 and discovered extended X-ray emission in 1–5 keV around Jupiter (Ezoe, Ishikawa, Ohashi, Miyoshi, et al., 2010). The *Suzaku* XIS instrument could detect relatively weak emission as shown in Figure 2.14 (top), since, comparing with other X-ray observatories, the detector background was low and the satellite orbit had a low altitude of about 550 km (Mitsuda et al., 2007). The spatial distribution of the extended emission also shown in Figure 2.14 (bottom) was roughly approximated by an ellipse-like shape with a size of 16 R_J × 8 R_J, indicating an association with Jupiter's inner radiation belts where the relativistic electrons existed. The spectrum was well fitted by a flat power-law with a photon index ~1.4, which strongly suggested non-thermal emission. The luminosity estimated from the power-law spectral fit in 1–5 keV was 3.3×10^{15} erg s^{-1}, which was as large as that of the auroral emission within a factor of 2–3.

Ezoe, Ishikawa, Ohashi, Miyoshi, et al. (2010) discussed a possibility that the emission was produced via an inverse Compton scattering process in which the relativistic electrons in the inner radiation belts amplified the energy of visible photons coming from the Sun. However, the electron density in the inner radiation belts modeled from the past *in-situ* measurements could not account for the level needed to explain the observed X-ray luminosity by a factor of 7–50.

Table 2.2 summarized the above-mentioned comprehension of Jupiter's X-rays. It indicates that we have not completely understood the mechanisms of Jupiter's X-ray emission other than from the aurora region. On the other hand, the fact that X-rays are emitted from Jupiter suggests that X-ray observations can be established as a new probe to monitor high-energy particles that reach keV to MeV.

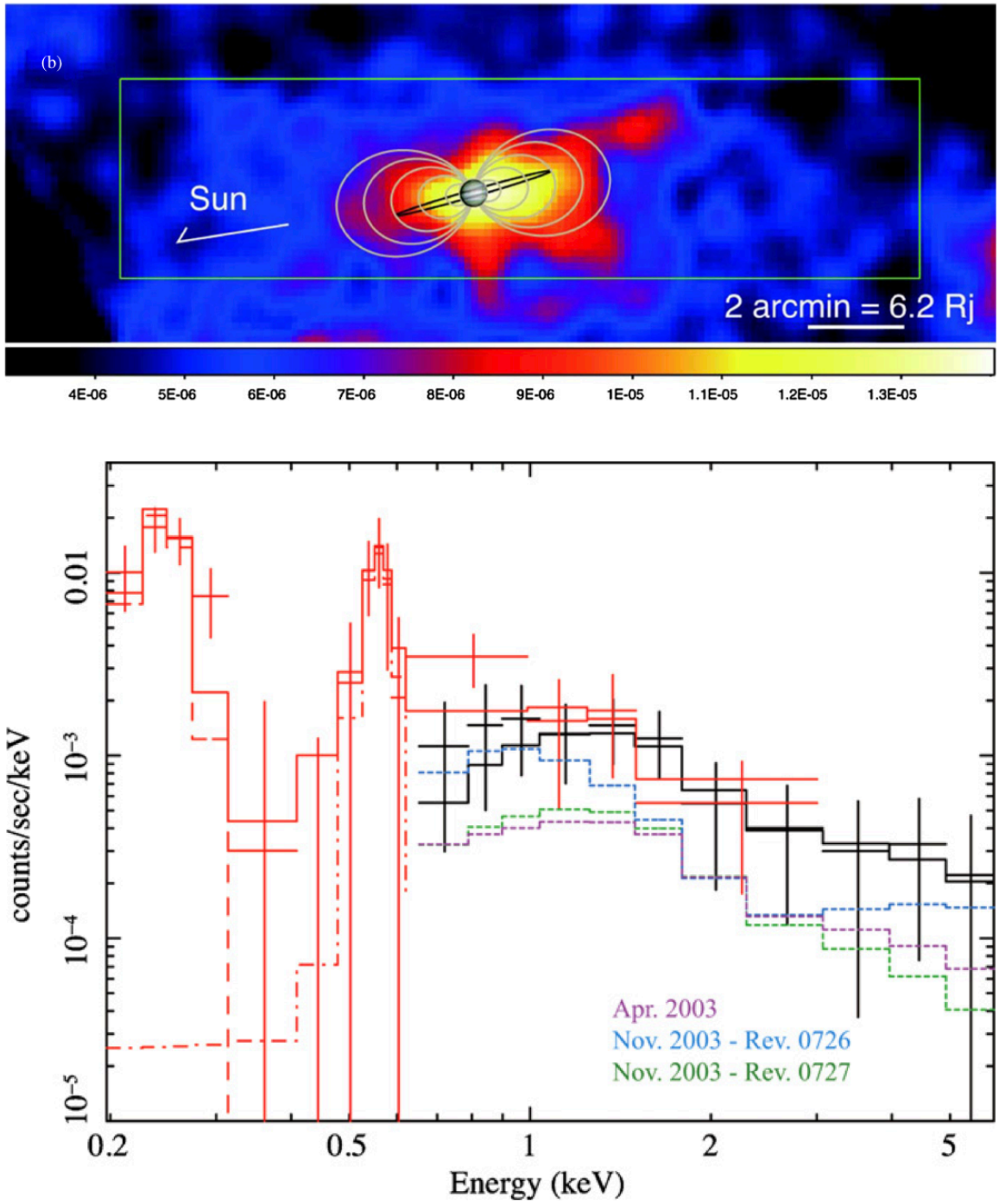

FIGURE 2.14: *Suzaku* XIS (top) image (1–5 keV) and (bottom) spectra of Jupiter's X-rays from an extended region over the Jovian magnetosphere (taken from Ezoe, Ishikawa, Ohashi, Miyoshi, et al., 2010).

TABLE 2.2: A comprehension of X-ray emission from the Jupiter system and its mechanisms.

Region (object)	Energy range (keV)	Luminosity (erg s^{-1})	Mechanism
Aurora	0.1–10	$\sim 1 \times 10^{16}$	Charge exchange process of MeV ions + Bremsstrahlung by keV electrons
Disk	0.1–10	$\sim 3 \times 10^{15}$	Solar X-ray scattering + Magnetospheric particle precipitation(?)
Radiation belts(?)	1–5	$\sim 3 \times 10^{15}$	Inverse Compton scattering of solar photons by tens MeV electrons(?)
Galilean moons	0.5–0.7	$\sim 2 \times 10^{13}$	Collision of ions to its surface(?)
Io plasma torus	0.25–2	$\sim 1 \times 10^{14}$	Line emissions from highly-ionized particles + Bremsstrahlung by keV electrons(?)

Chapter 3

Instrumentation

X-rays from astronomical objects can only be measured from space because the terrestrial atmosphere is opaque to this wavelength regime. X-ray astronomy has advanced through launching a number of rockets and astronomical satellites. At present, there are two large X-ray observatories operating in Earth orbit, *Chandra*, and *XMM-Newton*, over about 20 years. Japanese *Suzaku*, operated in 2005–2015, was characterized by a very low background. The National Aeronautics and Space Administration (NASA)'s mission *Chandra* achieves the best angular resolution (0.5″) and provides us with spectacular X-ray images of all categories of objects. On the other hand, *Chandra* is not so suitable to observe extended X-ray sources, because its instrumental background is high due to its high-altitude orbit. The European mission *XMM-Newton* is unique with its large effective area, which gives us X-ray spectra with good statistics. However, *XMM-Newton* also shows a relatively high detector background, as compared with *Suzaku*, and is not perfect for the study of Jovian diffuse hard X-ray emission. This satellite has a highly elliptical orbit, with an apogee of about 115 000 km and a perigee of about 6000 km. The high orbits of *Chandra* and *XMM-Newton* enable long continuous observations, however their trajectories pass through the Earth's radiation belts and cause a significant increase of the detector background. On the other hand, *Suzaku* orbited around the Earth at a low altitude of ~500 km, and the onboard instrument showed stable and low background. In fact, *Suzaku* was the only observatory which detected Jupiter's diffuse hard X-ray emission in 1–5 keV at this time (Ezoe, Ishikawa, Ohashi, Miyoshi, et al., 2010). On the contrary, *Suzaku* had a disadvantage in the angular resolution in spatially distinguishing the diffuse emission from Jupiter's auroral emission, which was dominant in the similar energy range of >1 keV. The auroral emission is thought to be emitted via bremsstrahlung and was intermittently observed by *XMM-Newton* (Branduardi-Raymont, Bhardwaj, R. F. Elsner, et al., 2007; Branduardi-Raymont, R. F. Elsner, Galand, et al., 2008; Branduardi-Raymont, R. F. Elsner, Gladstone, et al., 2004). Based on these characteristics of the satellites, in this paper, we will mainly utilize *Suzaku* data, and also adopt *XMM-Newton* data which were taken in coordinated observations with *Suzaku*. Details about *Suzaku* and *XMM-Newton* are described in the following sections.

3.1 *Suzaku* observatory

Suzaku is the 5th Japanese X-ray astronomy satellite, launched in July 2005 (Mitsuda et al., 2007) and operated in the orbit till 2015. The orbit was near-circular with an apogee of 568 km, an inclination of 31.9°, and an orbital period of about 96 minutes. Three scientific payloads were onboard

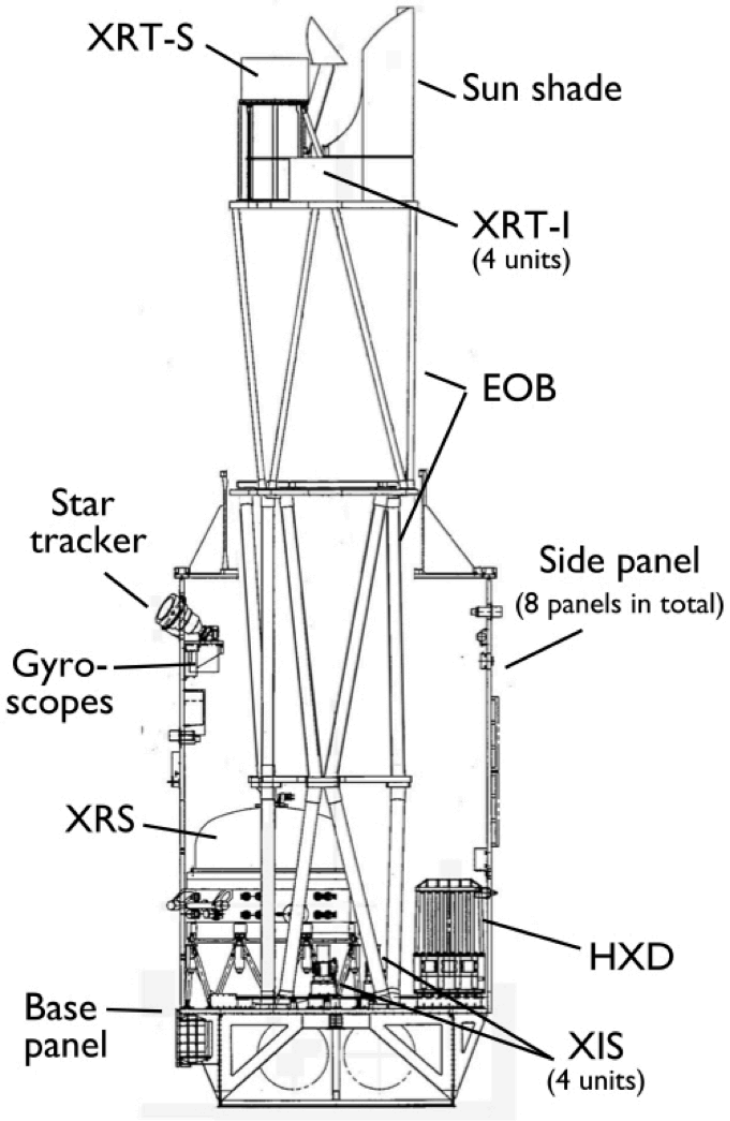

FIGURE 3.1: Side view of *Suzaku* with the internal structures after deployment of the Extensible Optical Bench (EOB), quoted from Mitsuda et al., 2007.

on *Suzaku*. The first instrument is the X-ray Imaging Spectrometer (XIS), which covers the energy range of 0.2–12 keV (Koyama et al., 2007). The second one is the non-imaging, collimated Hard X-ray Detector (HXD), with the bandpass extending to very high energies of 10–600 keV (Takahashi et al., 2007). The HXD is equipped with an all-sky monitor, the Wide-band All-sky Monitor, which can detect Gamma Ray Bursts and other transient sources. The third one is an X-ray microcalorimeter (X-Ray Spectrometer; XRS, Kelley et al., 2007). Although XRS has superior energy resolution than XIS in the energy range 0.3–12 keV, the loss of liquid helium in the very early phase hampered its operation in the orbit. A configuration of these payloads is shown in Figure 3.1, and their parameters are summarized in Table 3.1.

3.1.1 X-ray Telescope

Suzaku has five light-weight thin-foil X-Ray Telescopes (XRTs, Serlemitsos et al., 2007). Four of them are used for XIS, and the remaining one is for XRS. The external dimensions of the four XRTs for XIS

TABLE 3.1: Overview of *Suzaku* capabilities (after Mitsuda et al., 2007).

S/C	Orbit apogee	568 km
	Orbital period	96 min
	Observing efficiency	~43 %
XRT	Focal length	4.75 m
	Field of view	17′ at 1.5 keV
		13′ at 8 keV
	Plate scale	0.724′ mm^{-1}
	Effective area	440 cm^2 at 1.5 keV
		250 cm^2 at 8 keV
	Angular resolution	2′ (HPD; Half Power Diameter)
XIS	Field of view	17.8′ × 17.8′
	Bandpass	0.2–12 keV
	Pixel grid	1024 × 1024
	Pixel size	24 μm × 24 μm
	Energy resolution	~130 eV at 6 keV (FWHM)
		~60 eV at 1.5 keV (FWHM)
	Effective area (incl. XRT)	330 cm^2 (at 1.5 keV) / 160 cm^2 (at 8 keV) (FI)
		370 cm^2 (at 1.5 keV) / 110 cm^2 (at 8 keV) (BI)
	Time resolution	8 s (normal mode)
		7.8 ms (P-sum mode)

are the same.

The XRTs consist of closely nested thin-foil plates, reflecting X-rays at small grazing angles, and are mounted on the Extensible Optical Bench (EOB) to the spacecraft. The XRT has a cylindrical shape with the following components:

1. a thermal shield at the entrance aperture to help maintain a uniform temperature;
2. a pre-collimator mounted on metal rings for stray light elimination;
3. a primary stage for the first X-ray reflection;
4. a secondary stage for the second X-ray reflection;
5. a base ring for structural integrity and for interfacing the EOB of the spacecraft.

All these components, except for the base rings, are constructed in segments with an azimuthal angle 90° and called as quadrants. Four quadrants are coupled together with interconnect-couplers and also by the top and base rings. The telescope housings are made of aluminum to keep the lightweight. Each reflector consists of a substrate also made of aluminum and an epoxy layer working as adhesive to bond the reflecting gold surface to the substrate. Because the substrates have a thickness of 0.152 mm, they allow high-density nesting and thus provide a large collecting area with a moderate angular resolution in the energy range 0.2–12 keV. Each telescope unit weighs less than 20 kg.

Performance of XRT was confirmed with XIS in orbit. Imaging capability of XRT was confirmed by observing SS Cyg in quiescence in November 2005 for a total exposure time 41.3 ks. This is a point source and moderately bright (3.5–5.9 count s^{-1} for XIS0 through XIS3), with no pile-up even at the image core. Figure 3.2 shows the images and point spread functions (PSFs) for all the XRT modules. The HPD (half power diameter), which is the diameter enclosing half of the focused X-rays, was obtained as 1.8′, 2.3′, 2.0′, and 2.0′ for XRT0, 1, 2 and 3, respectively.

Figure 3.3 shows focal positions of XRT when the satellite is pointed to a source at the XIS aim point. The data were taken with a point-like active galaxy, MCG6-30-15, in August 2005. The focal positions are located close to the detector center with deviations 0.3 mm from each other.

Therefore, the field of views of the XIS sensors overlap well.

A series of observations of the Crab Nebula was conducted in August 2005 and August 2006 at off-axis angles 0′, 3.5′, and 5.7′. Based on the data, the vignetting of the four XRT telescopes were studied in two energy bands, 3–6 keV and 8–10 keV. Figure 3.4 shows the observed vignetting data of the Crab compared with calculated curves by a ray-tracing simulator. The results allow us to obtain the effective area within 10% accuracy over the XIS field of view.

3.1.2 X-ray Imaging Spectrometer (XIS)

The XIS instrument consists of four sensors: XIS 0, 1, 2, and 3. Each sensor is an X-ray sensitive charge coupled device (CCD), in which incident X-ray photons are converted to a number of electron-hole pairs via photoelectric absorption and subsequent ionization by photoelectrons and by secondary electrons. The incident X-ray position is recorded as the pixel position, and the number of pairs tells us the energy. Each XIS is located in the focal plane of the XRT. The imaging area of each CCD has

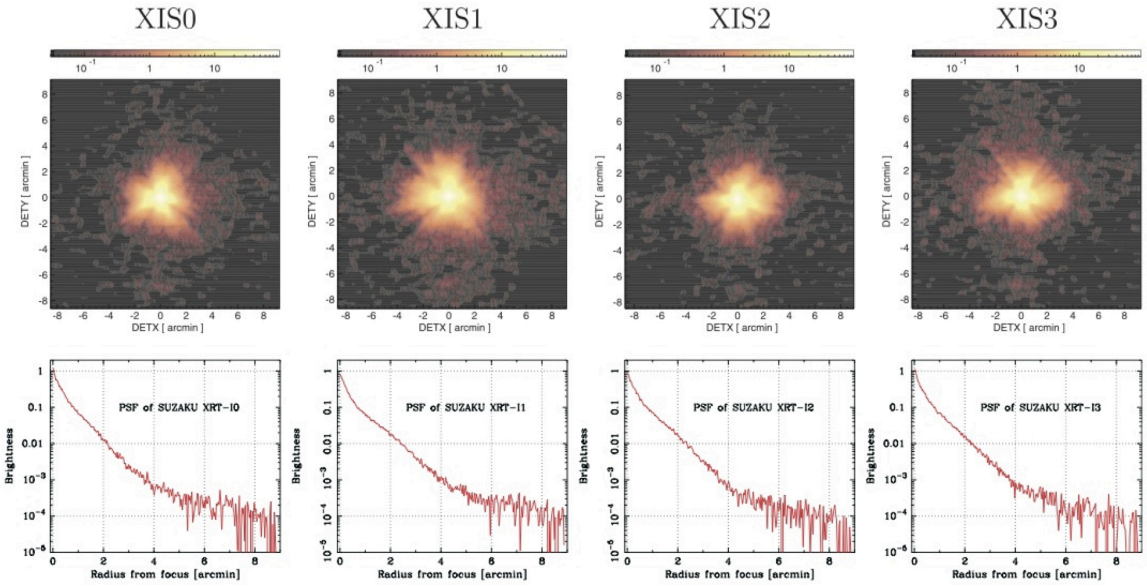

FIGURE 3.2: Image and Point-Spread Function (PSF) of four XRT modules taken from Serlemitsos et al., 2007. All of the images are binned with 2×2 pixels, followed by smoothing with a Gaussian profile with a sigma of 3 pixels, where the pixel size is 24 μm.

1024×1024 pixels, and covers a $17.8' \times 17.8'$ region on the sky. The specification of the XIS is summarized in Table 3.1. The angular resolution is $\sim 2'$ defined by HPD of the XRT.

The CCD chip has a gate structure on one surface to transfer the charge packets to the readout gate. The surface of the chip with the gate structure is defined as "front side". A front-side illuminated CCD (FI CCD) detects X-ray photons on this side, and photons penetrate the gate structure. The photoelectric absorption by the gate structure reduces the low energy quantum detection efficiency (QDE) for the FI CCD. On the other hand, a back-side illuminated CCD (BI CCD) detects photons from the "back side", which has no gate structure. The BI CCD gives a high QDE below 1 keV, but the electrons have to drift to the gate structure on the other side. This gives somewhat worse energy resolution than the FI CCD because of the diffusive spread of the electron cloud. The XIS instrument consists of three FI CCD (XIS 0, 2, 3) and one BI CCD (XIS 1) sensors. A comparison of the effective area between the FI and BI CCDs combined with the XRT efficiency is shown in Figure 3.5. This figure shows spectral features due to the elemental composition of XIS and XRT. K-shell absorption edges of oxygen (0.54 keV) and aluminum (1.56 keV) in the blocking filters are present, as well as a number of weak M-shell features between 2–3 keV arising from the gold on the XRT. According to this figure, the BI CCD has an advantage in the soft X-rays detection below 1 keV. To minimize thermal noise, the sensors are operated at about $-90\,^{\circ}$C in the orbit.

X-ray CCDs are also sensitive to UV and optical photons. To suppress such signals, an optical blocking filter (OBF) is installed in front of each XIS sensor. The OBF is made of polyimide with a thickness of 1000 Å, which is coated with 1200 Å-thick aluminum (with 400 Å and 800 Å on different sides). To calibrate the XIS energy scale in the orbit, three ^{55}Fe isotopes with a half-life of 2.73 years are mounted in each XIS sensor. The isotopes emit strong Mn Kα and Kβ lines at 5.9 keV and 6.5 keV, respectively. Two sources are attached on the sidewall of the housing and illuminate two corners of the CCD chip, and the other one is installed on the door of the housing to illuminate the entire chip.

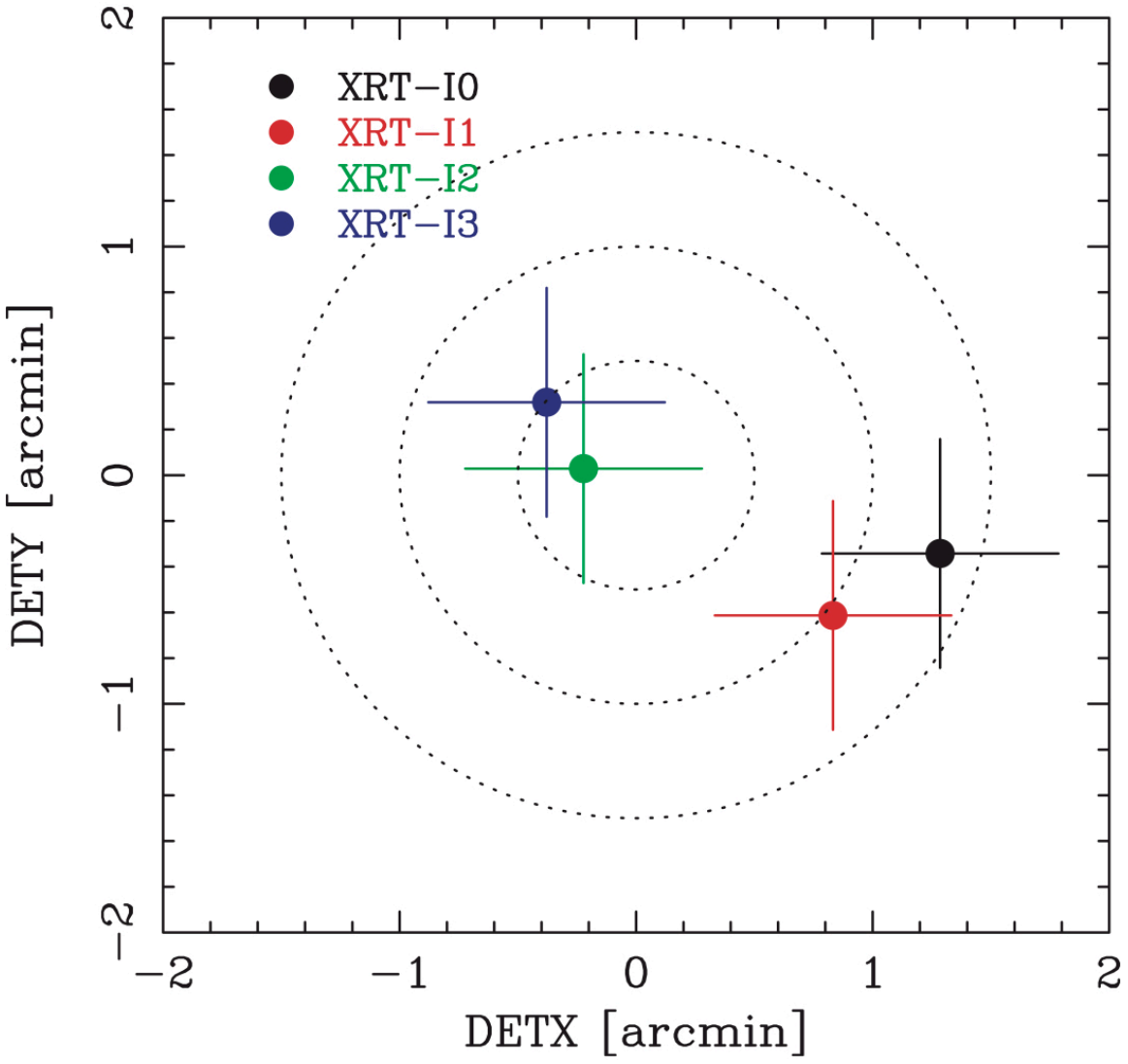

FIGURE 3.3: Focal positions of the four XIS sensors when the satellite was pointed to the Crab Nebula in August–September 2005 at the XIS aimpoint, taken from Serlemitsos et al., 2007. DETX and DETY indicate the detector coordinates.

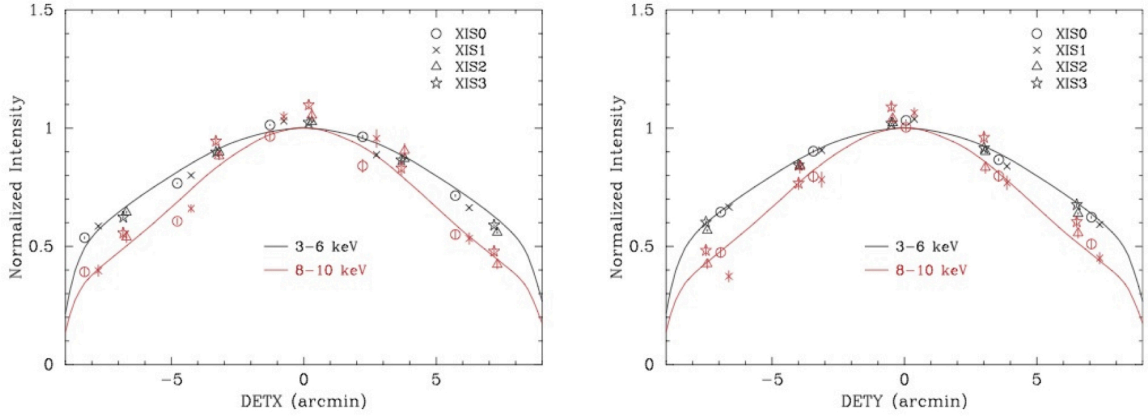

FIGURE 3.4: Vignetting curves of the four XRT telescopes using the Crab Nebula taken during August 2005, taken from Serlemitsos et al., 2007. The model curves were calculated with ray-tracing simulator with spectral parameters of $N_{\rm H} = 0.33 \times 10^{22}$ cm^{-2}, photon index 2.09, and normalization 9.845 photons cm^{-2}s^{-1}keV^{-1}, respectively.

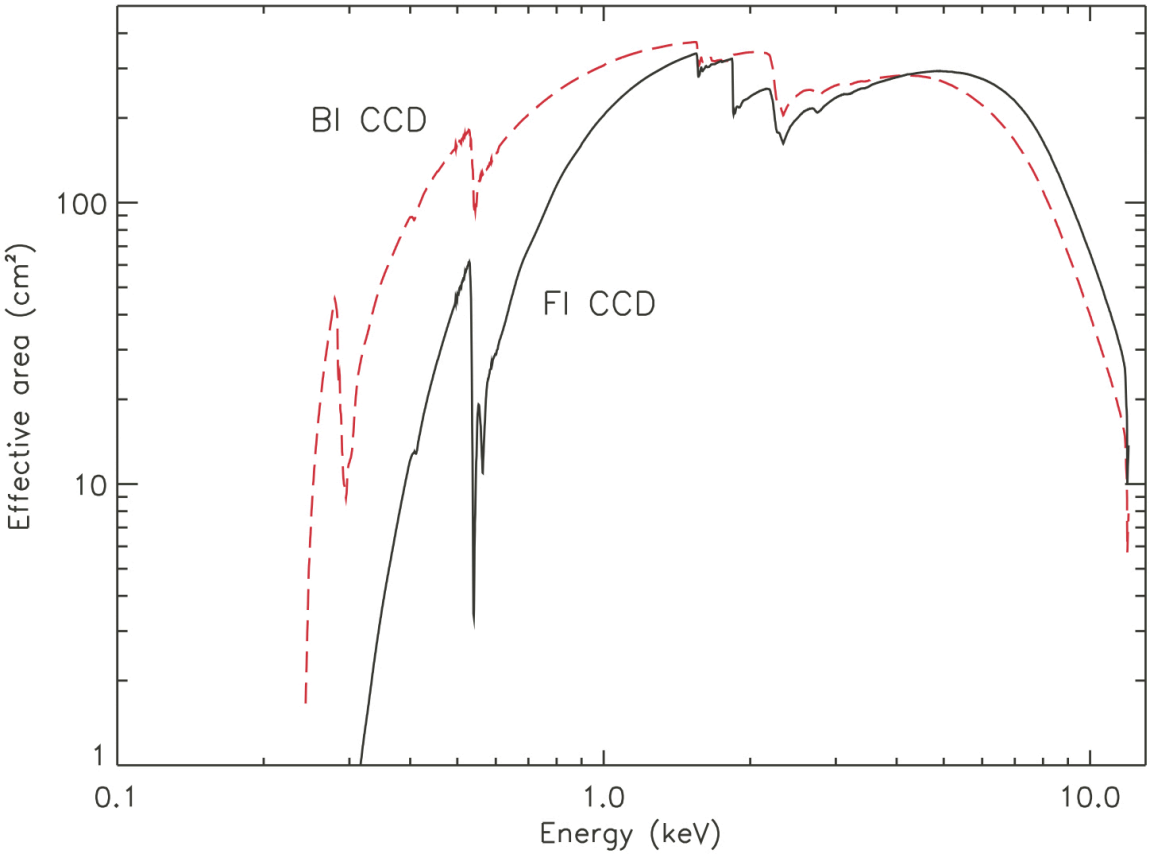

FIGURE 3.5: XIS effective area for a combination of XRT and XIS, for both FI and BI CCDs, taken from Mitsuda et al., 2007.

The source at the door is used for the initial calibration only, before the opening of the door.

XIS background

Background of the XIS mainly consists of the following three components: (i) Non X-ray Background (NXB), (ii) diffuse X-rays from hot interstellar medium, such as local hot bubble and milky-way halo, and cosmic X-ray background (CXB) of extragalactic origin, and (iii) solar system emission, consisting of SWCX emission from terrestrial atmosphere and heliosphere and reflection of solar X-rays.

NXB is originated from cosmic ray incidence, and the spectrum comprises continuum and several emission lines. The continuum component is produced when the cosmic rays directly deposit their energy on the CCD chip, while fluorescent X-rays are emitted when the cosmic rays hit the spacecraft body. The diffuse X-rays from the local hot bubble are dominant below 1 keV, and the intensity depends on the direction in the sky with no time variation. The CXB comes from all directions of sky and its spectrum is approximated by a power-law function with a photon index ~1.4 in the energy band 2–10 keV (Kushino et al., 2002). It is uniform over the sky with small local fluctuations. The solar system component is mostly emission lines from both SWCX and fluorescence lines of nitrogen and oxygen originated from solar X-ray scattering at the terrestrial atmosphere. The intensity depends on the solar activity and on the elevation angle from the sunlit Earth rim. The atmospheric scattering component can be minimized by screening the data with the elevation angle. The screening criteria for the XIS data are described in the following chapters.

These background events also affect the *Chandra* and *XMM-Newton* data, even more severely. Figure 3.6 shows the XIS background count rate as a function of energy, together with those of *ASCA*, *Chandra*, and *XMM-Newton*. This plot indicates that *Suzaku* XIS, in particular FI, shows the background level significantly lower than other instruments by a factor of >2. *Suzaku*'s low-Earth orbit gives the NXB of the XIS to be very stable on time scales of months, and thus the NXB spectrum can be constructed from the data obtained when the spacecraft is pointed to the night Earth. The background rate in the energy range 0.4–12 keV is 0.1–0.2 count s^{-1} for the XIS FI and 0.3–0.6 count s^{-1} for the BI after grade selection.

Filters

The quantum efficiency below 2 keV decreases in the orbit due to accumulation of contaminating material on the optical blocking filter (OBF) of the XIS sensors. The OBF is subject to radiation cooling, and its low temperature causes the accumulation of contamination material. The contamination source is thought to be outgassing from the satellite, and consists of several different materials with time-varying composition. The thickness and the chemical composition of the contaminant at the XIS nominal position are monitored by observing standard cosmic X-ray sources.

Sudden anomalies caused putatively by micro-meteorite hits affect the XIS sensors. A drastic anomaly of XIS 2 occurred in November 2006, and the entire sensor was lost then. In June 2009, 1/8 of the XIS 0 area became noisy and the region was masked by area discrimination since then. For XIS 1, it is speculated that a small hole was punched on the OBF in December 2009. Diagnostic observations showed that the scientific impact of this anomaly was minimal, and the sensor was operated in the same way as before the anomaly.

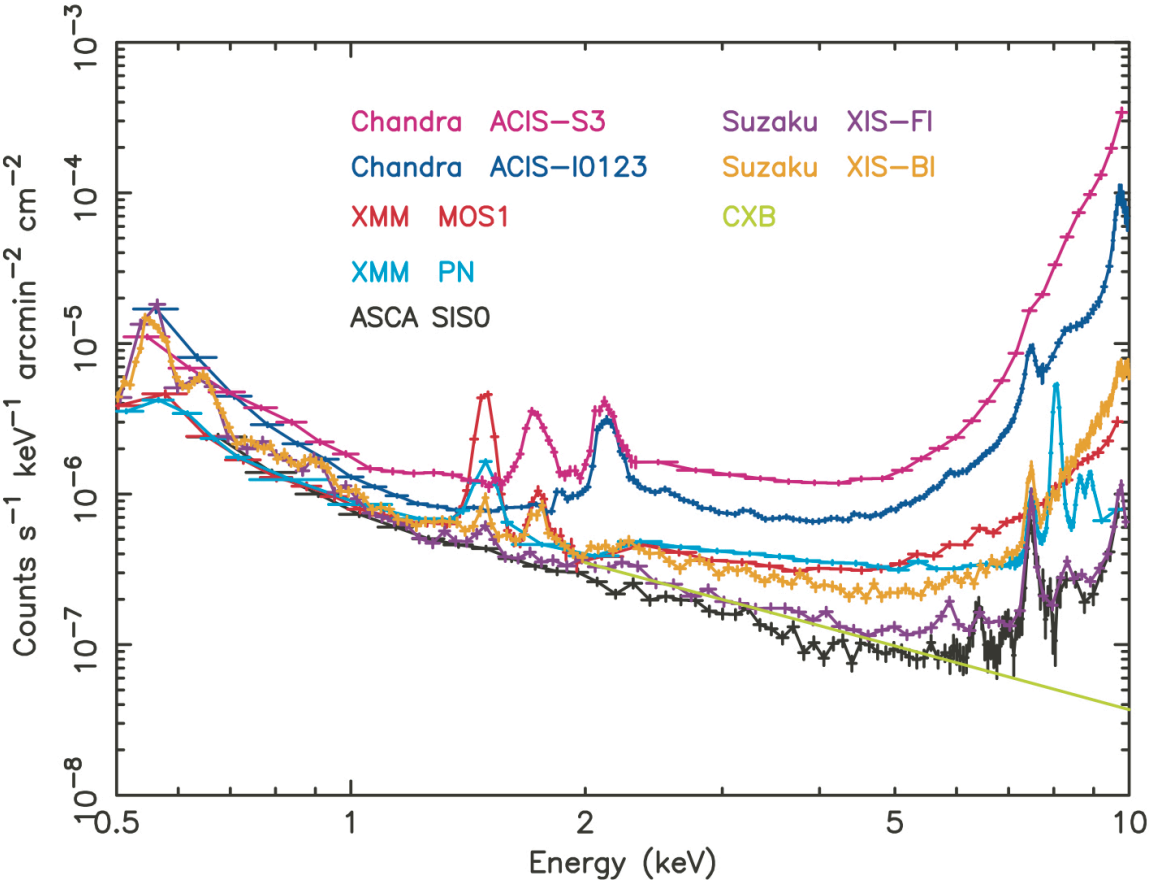

FIGURE 3.6: XIS background count rate as a function of energy, along with those of *ASCA*, *Chandra*, and *XMM-Newton*, taken from Mitsuda et al., 2007. The rate is normalized with the effective area and the field of view, which is a good measure of the sensitivity determined by the background for spatially extended sources.

Radiation damage

The performance of X-ray CCDs gradually degrades in the space environment due to the radiation damage. This generally causes an increase in the dark current and a decrease of the charge transfer efficiency (CTE). For XIS, the dark current is expected to show a small increase because of the low ($\sim -90\,^{\circ}$C) operating temperature. However, the decrease of CTE is unavoidable, and continuous calibration of CCD on orbit is essential to keep the good performance of the XIS. The CTE calibration uses the radioisotope, and charge injection is performed with the following procedure: (i) The ^{55}Fe sources near the two corners of the chip enable us to monitor the charge loss in the transfer by the gain comparison. (ii) the CCD chips are equipped with charge injection capability, which can be used to recover the CTE. To raise the CTE, the XIS sensors employ spaced-row charge injection (SCI). In this operation, periodically injected artificial charges fill radiation-induced traps and prevent electrons produced by X-rays from being captured by the charge traps. The SCI was successfully demonstrated in 2006, and the energy resolution was improved.

In the standard processing of the XIS data, flickering pixels have to be removed. These are pixels which produce false signals above the threshold in a given period of time, thus the number of flickering pixels depends on how long the data are integrated. In producing the NXB database, a very long integration time was used (19 months), whereas individual observations are much shorter. Because of this, the NXB spectra generated using `xisnxbgen` have many flickering pixels removed and are systematically weaker than the actual background spectra. This was not a problem in the early phase of the mission when the fraction of flickering pixels was tiny. However, as the fraction increased, the discrepancy became noticeable in the later phase of the mission. We apply a method to cope with this problem. A cumulative flickering pixel map ("noisy pixel map"; the map of the pixels that have shown flickering more than once throughout the mission in the past) is provided in the CALDB. This map can be applied for observation data to better match the background spectra generated by `xisnxbgen` at a sacrifice of an effective area up to 6.5%. See details of this procedure in `http://www.astro.isas.jaxa.jp/suzaku/analysis/xis/nxb_new2/`.

3.2 *XMM-Newton* observatory

The European Space Agency (ESA)'s X-ray satellite *XMM-Newton* was launched on December 10, 1999, from Kourou (French Guiana) by the Ariane-V rocket (Jansen et al., 2001). It was placed into a highly eccentric orbit, with an apogee about 115 000 km and a perigee about 6000 km, and an orbital inclination of 33°, which provides good visibility over the celestial sky. Although the orbital period is 48 hours, the exposure available for scientific data analysis is limited to 39 hours (~140 ks) per orbit. This is because observations are not carried out when the satellite altitude is less than 46 000 km, where the radiation background related to the Earth's magnetosphere is severe. *XMM-Newton* carries the following three instruments: (i) European Photon Imaging Camera (EPIC), (ii) Reflection Grating Spectrometer (RGS), and (iii) Optical Monitor (OM).

The three EPIC cameras consist of two different types of CCD cameras, MOS and pn, and two systems with MOS sensors have the RGS spectrometers in the X-ray path under the X-ray telescopes. The OM has its own telescope. A sketch of the *XMM-Newton* payload is shown in Figure 3.7. There

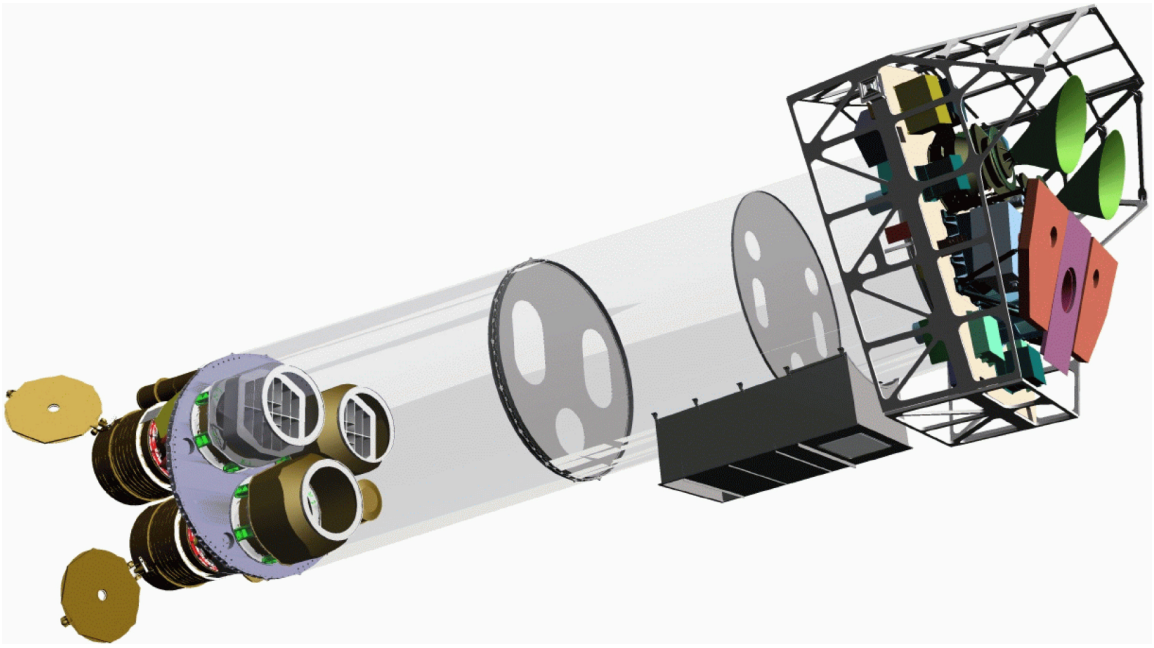

FIGURE 3.7: A sketch of the *XMM-Newton* payload taken from Jansen et al., 2001. The three mirror modules, two of which are equipped with Reflection Grating Arrays, are visible at the lower left. At the right end of the assembly, the focal plane instruments are shown: EPIC MOS cameras with their radiators (black/green horns), radiator of the EPIC pn camera (violet) and those of the (light blue) MOS detectors (in red). The OM telescope is obscured by the lower mirror module.

are in total six science instruments (2 MOS, 1 pn, 2 RGS, and 1 OM) on board *XMM-Newton*, which are operated simultaneously. The instruments can be operated independently and in different modes of data acquisition.

In the following sections, we describe the X-ray telescopes and EPIC cameras, which are used in this study. We summarize the basic parameters of the EPIC cameras in Table 3.2.

3.2.1 X-ray Telescope

XMM-Newton's three XRTs are co-aligned with an accuracy of better than 1–2″. Each telescope consists of 58 Wolter type-I mirror shells, and the grazing incidence angle ranges between 17′ and 42′. The focal length is 7.5 m and the diameter of the outermost mirror is 70 cm. One telescope equipped with the pn camera at the focal plane has a simple light path with double reflection by the first and second mirror modules. The other two telescopes, combined with MOS detectors, have the RGS assembly in their light path, and part of the incoming X-rays are reflected to a secondary focal plane. About 44% of the incoming light is focused onto the MOS camera at the prime focus, while 40% is dispersed by RGS to a linear strip of CCDs. The remaining light is absorbed by the support structures of the RGA.

The first critical parameter which determines the quality of an X-ray mirror module is its ability to focus photons. One of *XMM-Newton*'s strong points is that the core of its on-axis point-spread function (PSF) is narrow and varies little over a wide energy range (0.1–6 keV). Above 6 keV, the PSF becomes only slightly more energy-dependent. PSF determines the imaging quality of XRT, and Figure 3.8 shows the in-orbit on-axis images obtained by each detector. The radial substructures

TABLE 3.2: Basic performance of the EPIC detectors (after ESA: XMM-Newton SOC, 2019; Jansen et al., 2001).

	EPIC-MOS	EPIC-pn
Illumination method	Front illuminated	Back illuminated
Pixel size	40 μm	150 μm
	1.1″	4.1″
Field of View	30′	30′
PSF (FWHM/HEW)	5″ / 14″	5″ / 14″
Spectral resolution	~70 eV	~80 eV
Time resolution	1.5 ms	0.03 ms
Band pass	0.15–12 keV	0.15–15 keV

TABLE 3.3: The on-axis in orbit and on ground 1.5 keV HEW of the different XRT (after ESA: XMM-Newton SOC, 2019; Jansen et al., 2001).

Instr.	MOS1	MOS2	pn
HEW (orb./grd.) (arcsec)	15.2/15.2	13.8 / 13.6	13.0/12.8

are caused by the spiders holding the mirror shells. The encircled energy function (EEF) of each detector is shown in the bottom of Figure 3.8 as a function of radius from the center of the PSF for several different energies. For an on-axis source, high energy photons are reflected and focused predominantly by the inner shells of the XRTs. The inner shells have small curvature and apparently give better focus than the average of all shells, hence the EEF increases for higher photon energy. A half energy width (HEW), which means the angular width encircling half of all the reflected photons, can be derived from EEF. Table 3.3 lists the on-axis HEW for the different XRTs measured in orbit and on ground. The PSF depends on the off-axis angle of the source, and as it increases the HEW becomes larger.

XMM-Newton's XRT has the largest effective area of focusing telescope so far. The effective area at 1.5 keV is about 1550 cm^2 for each telescope, i.e., 4650 cm^2 in total. Figure 3.9 shows the on-axis effective area of all XRTs. The two MOS cameras have lower area than pn, because incoming photons are partially reflected by the RGS and the remaining photons fall onto the MOS detectors. The shape of the X-ray PSF and the effective area are both a function of off-axis angle within the field of view. As the off-axis angle increases, the XRT effective area decreases. This effect is called "vignetting". Figure 3.10 displays the vignetting curves as a function of off-axis angle for several different energies. The vertical axis is normalized by the on-axis effective area.

The off-axis vignetting for the two telescopes equipped with the RGS has a directional dependence according to the RGS's dispersion direction. As shown in Figure 3.10 left panel, a source at an off-axis position in the dispersion direction will be vignetted either largely (0°) or little (180°) since the reflection surface is inclined by 1.58° from the X-ray path.

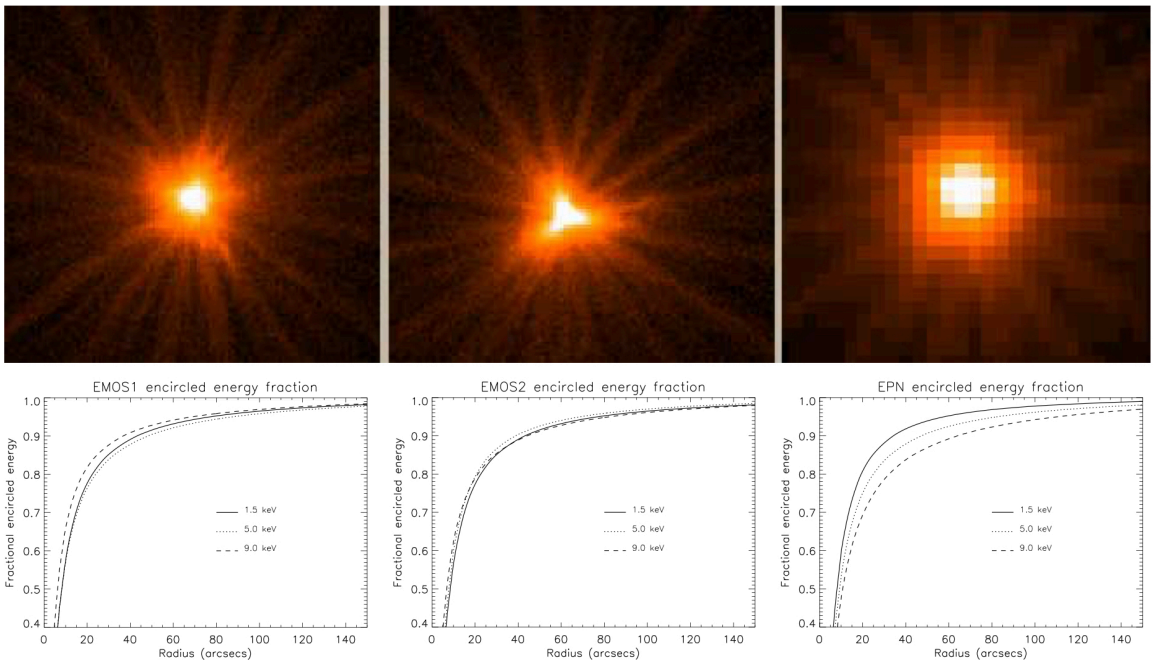

FIGURE 3.8: (top) On-axis images of the MOS1, MOS2 and pn detectors (left to right). The images are 110 arcsec wide and a logarithmic scale is used to visualize the wings of the PSF. (bottom) The encircled energy function as a function of angular radius (on-axis) at different energies. The curves are calculated assuming a fractional encircled energy of 100% at a radial distance of 5′. These figures are after ESA: XMM-Newton SOC, 2019.

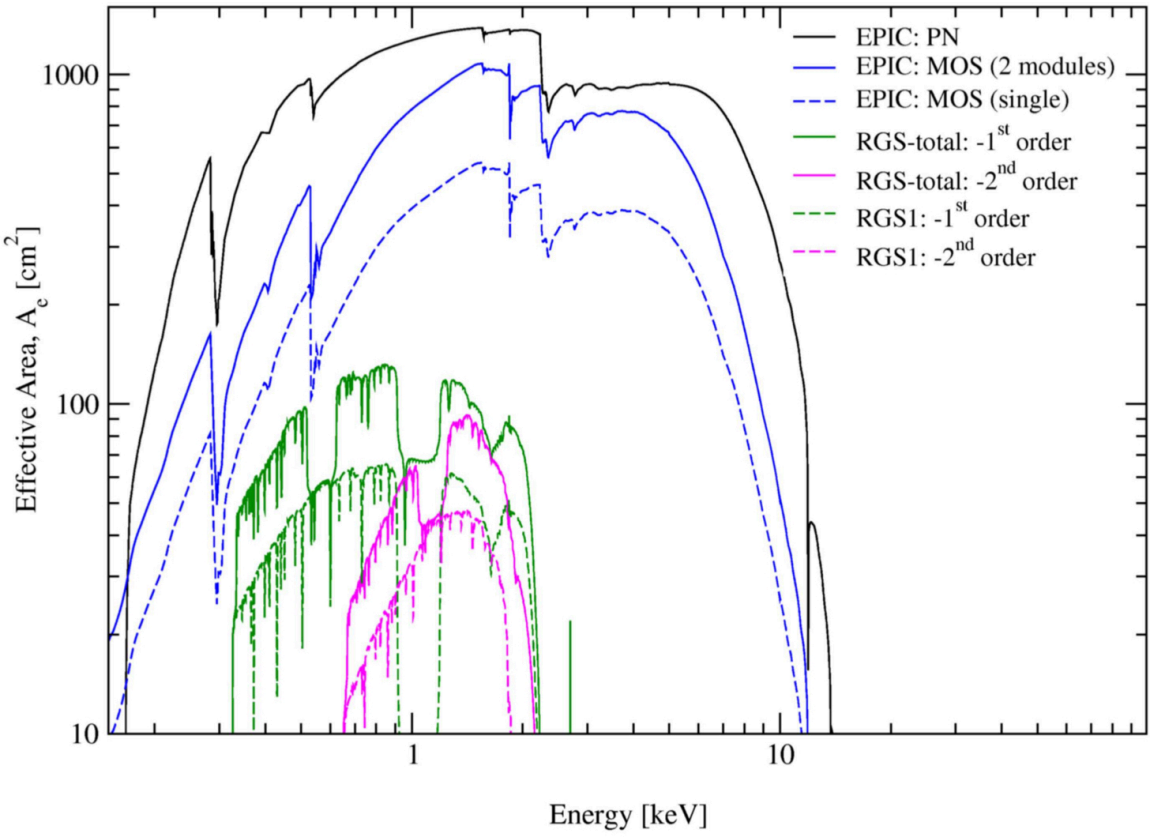

FIGURE 3.9: The net effective area of all XRTs, combined with the response characteristics of the focal plane detectors, taken from ESA: XMM-Newton SOC, 2019.

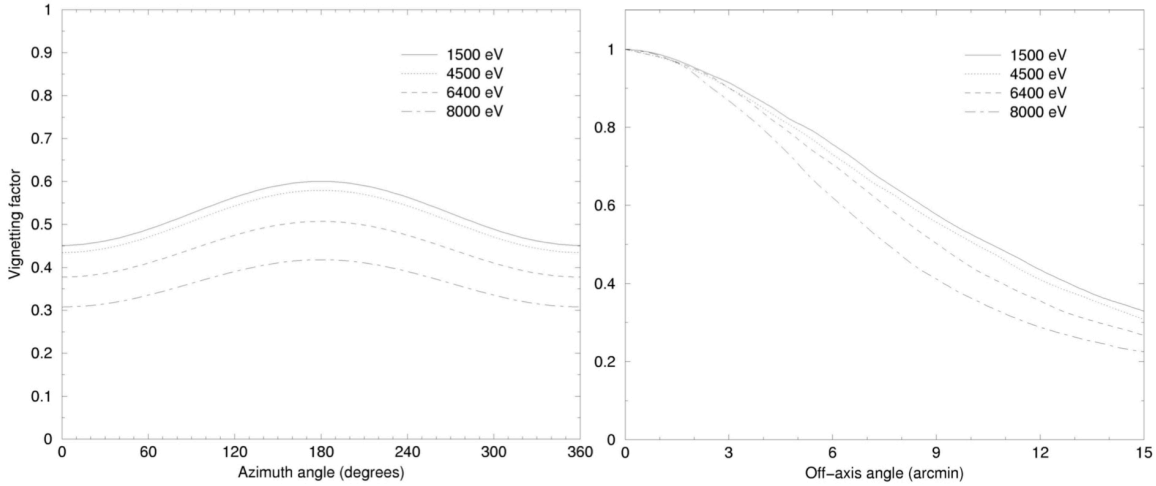

FIGURE 3.10: (left) Vignetting factor as a function of azimuthal angle of the X-ray telescope in front of the MOS1 camera. The curves are given for an off-axis angle of 10′. (right) Vignetting curve as a function of off-axis angle (0–15′ based on simulations) for several different energies for the X-ray telescope equipped with the pn camera. These figures were taken from ESA: XMM-Newton SOC, 2019.

3.2.2 European Photon Imaging Camera (EPIC)

The EPIC MOS and pn cameras have pixel sizes of 40 μm and 150 μm, respectively. For the focal length of the X-ray telescopes (7.5 m), these pixel size corresponds to 1.1″ and 4.1″ on the sky. Since they are smaller than the HEW of XRT (∼15″), EPIC's angular resolution is basically determined by the PSF of the mirror modules.

The energy resolution of EPIC cameras is determined by the intrinsic performance of the CCD instruments. The measured in-flight FWHM of the Al Kα (1.4 keV) and Mn Kα (5.89 keV), which are the on-board calibration lines. It is well known that the energy resolution of the MOS cameras has been gradually decreasing due to the charge transfer inefficiency (CTI) effect, which means the imperfect transfer of charge during the transportation through the CCD to the output amplifiers. The latest calibration status is found at *XMM-Newton* Science Operation Centre.[1] The accuracy of the energy determination is about 10 eV over the full energy range and for all modes except for MOS timing mode.

EPIC background

The EPIC background can be divided into two parts: background due to X-ray incidence, and instrumental background. The latter component may be further divided into a detector noise component, which becomes important at low energies (i.e., <300 eV), and a second component which is caused by particles. The instrumental background is characterized by a flat spectrum and is particularly important in high energies (i.e., > a few keV).

The particle-induced background can be divided into two components: an external "flaring" component, characterized by strong and rapid variability which is totally absent for most of the time, and a second more stable internal component. The flaring component is currently attributed

[1] http://xmm.vilspa.esa.es/external/xmm_sw_cal/calib/documentation.shtml#EPIC

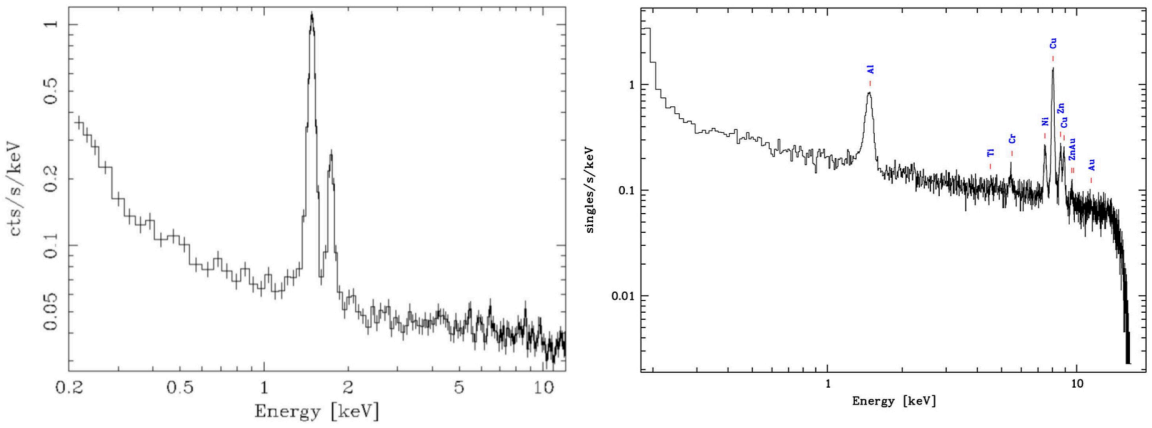

FIGURE 3.11: (left) Background spectrum for the MOS1 camera during an observation with the filter wheel in the closed position. The prominent features around 1.5 and 1.7 keV are respectively Al K and Si K fluorescence lines. The rise of the spectrum below 0.5 keV is due to the detector noise. (right) That for the pn camera. The rise of the spectrum below 0.3 keV is due to the detector noise. The relative line strengths depend on the (variable) incident particle spectrum. These figures are after ESA: XMM-Newton SOC, 2019.

to soft protons, which are presumably funneled toward the detectors by the X-ray mirrors. The stable component is due to the interaction of high-energy particles with the spacecraft structure surrounding the detectors and possibly the detectors themselves. All these background components are summarized as follows:

1. Background by the X-ray incidence
2. Instrumental Background
   (a) detector noise (<300 eV)
   (b) particle induced background (> a few keV)
      - flaring component: due to soft protons (< a few 100 keV)
      - stable component: due to high-energy particles (>100 MeV)

Current understanding is that soft protons are most likely distributing in clouds which populate the Earth's magnetosphere. The number of such clouds encountered by *XMM-Newton* in its orbit depends upon many factors, such as the altitude of the satellite, its position in the magnetosphere, and the level of solar activity.

The intensity of the stable background is monitored regularly for both MOS and pn cameras during closed filter observations. This component shows only a little intensity variation in time which are typically observed on long time-scales. The intensity of this component during any given observation is within ~10% of the mean. The intensity observed in a MOS camera is usually well correlated with the intensity measured in the other, although some exceptions have been seen. In Figure 3.11 we show the observed spectra of the stable component for the MOS1 and pn camera, respectively.

Average count rates due to the internal "quiescent" background, for both MOS and pn, depend on different modes and filters, as well as energy ranges and pattern selection. For example, the

background count rate of MOS camera with the "thin" filter is ~0.3–2 count s^{-1} in 0.2–1 keV, and ~1–3 count s^{-1} in 1–5 keV, while that of pn camera is ~3–20 count s^{-1} in 0.2–5 keV. Further details are given in http://www.cosmos.esa.int/web/xmm-newton/bs-countrate.

Filters

The EPIC CCDs are also sensitive to IR, visible and UV light. Therefore, if an astronomical target has a high optical to X-ray flux ratio, there is a possibility that the X-ray signal is contaminated by non X-ray photons. To prevent such a contribution, each EPIC camera is equipped with a set of 3 separate aluminized optical blocking filters, named as "thick", "medium" and "thin" filters. The thick filter should be used for all point source targets up to 1–4 m_V (MOS) or 0–3 m_V (pn). The medium filter is about 10^3 times less efficient than the thick filter, therefore, it is useful for preventing optical contamination from point sources as bright as 8–10 m_V. The thin filter is about 10^5 less efficient than the thick filter, so the use of this filter will be limited to point sources with optical brightness m_V about 14 magnitudes fainter than the corresponding thick filter limitations.

3.3 Strategy of the present thesis

Suzaku observed Jupiter three times in February 2006, January 2012, and April 2014 with the XIS instrument. As already shown in Figure 3.6, the low-Earth orbit of *Suzaku* and the large effective area of XIS FI gives the lowest particle background among all X-ray CCDs which have been used for X-ray observatories. The Jovian diffuse hard X-ray emission was seen in 1–5 keV. In this band, the XIS FI has good sensitivity for spatially extended sources due to the low background. Therefore, in this thesis, we utilize only the XIS FI data for the hard diffuse emission, with the BI data used for the soft emission only.

Since the *Suzaku* observation in 2014 was coordinated with *XMM-Newton*, we also use the *XMM-Newton*'s EPIC camera to look into the emission from Jupiter's body. The angular resolution of *XMM-Newton* is much better than that of *Suzaku*, so it is able to separate the body emission. The body emission contains strong non-thermal bremsstrahlung in >2 keV from Jupiter's aurorae, which needs to be separated from the extended hard emission from the *Suzaku* data.

Chapter 4

Observations and analysis

This chapter describes X-ray observations of Jupiter from *Suzaku* and *XMM-Newton* and results of the data analysis. Table 4.1 summarizes parameters of the *Suzaku* observations. Observations from *Suzaku* have been carried out in three separate periods, which are February 24–28, 2006, January 3–13, 2012, and April 15–21, 2014, with net exposure times of 159, 165, and 160 ks, respectively. Numazawa et al. (2019) reported results of the *Suzaku* observation in 2014, but analytical processes had been changed in this thesis. Figure 4.1 shows relative positions of Jupiter by fixing the positions of the Sun and the Earth (i.e., the observatory). Distances to Jupiter from the Earth are ∼5.0, 4.7, and 5.4 AU, and opening angles of the line connecting Sun–Jupiter–Earth are ∼9.9°, 11.0° and 10.7°, for the 2006, 2012, and 2014 observations, respectively. These parameters are taken from NASA's Jet Propulsion Laboratory HORIZONS Web-Interface.[1]

Solar activity, indicated by sunspot number, showed significant variation over a period of 2002–2016 as shown in Figure 4.2, whose data were taken from Sunspot Index and Long-term Solar Observations (Silso) web site.[2] During the first *Suzaku* observation in 2006, the activity was approaching the solar minimum when the 23rd solar cycle was near the end. On the other hand, in the second and the third observations in 2012 and 2014, the activity was near the solar maximum of the 24th cycle.

First of all, we mainly utilized `HEASoft` version 6.21 (released on April 5, 2017) and `CALDB` version 2016-06-07 for all the analysis of the *Suzaku* data described in this chapter. In addition, we used `XMMSAS` version 1.2 (`xmmsas_20160201_1833-15.0.0`) for the *XMM-Newton* data analysis.

The entire *Suzaku* data were reprocessed after the termination of the satellite operation and online-released on October 24, 2016. We adopted the newly reprocessed cleaned event files with processing version 3.0.22.43 and 3.0.22.44. Here, we briefly describe the analysis flow of the Jupiter data;

1. Create mosaic images from XIS BI for a soft band (0.2–1 keV) and XIS FI for a hard band (1–5 keV) from the screened event files, for which exposure corrections were made by dividing the image with exposure map generated by `xisexpmapgen` (version 2015-01-07).

2. Identify bright point sources in the hard band mosaic image using `wavdetect` in `CIAO` package (version 4.11), 3XMM-DR8 Catalog (2014 only), and/or visual detection, and exclude them from the event files to obtain contamination-free images.

[1] https://ssd.jpl.nasa.gov/horizons.cgi
[2] http://www.sidc.be/silso/monthlyssnplot

TABLE 4.1: Specifications of the *Suzaku* observations of Jupiter.

Year		2006	2012	2014
Date		Feb. 24–28	Jan. 3–13	Apr. 15–21
Line of sight	(α, δ)	~226.6, −16.2	~28.9, 10.6	~104.2, 23.1
	(hh:mm:ss)	15h 06m 24s, −16°12′0″	1h 55m 36s, 10°36′0″	6h 56m 48s, 23°6′0″
	(b, l)	344.0°, 35.7°	147.5°, −49.2°	192.7°, 11.4°
Maneuver		4	5	14
Motion velocity		~3.3″ h^{-1}	~7.3″ h^{-1}	~19.9″ h^{-1}
Exposure		159 ks	165 ks	160 ks
Distance		~5.0 AU	~4.7 AU	~5.4 AU
Angle (Sun-Jupiter-Earth)		~9.9°	~11.0°	~10.7°

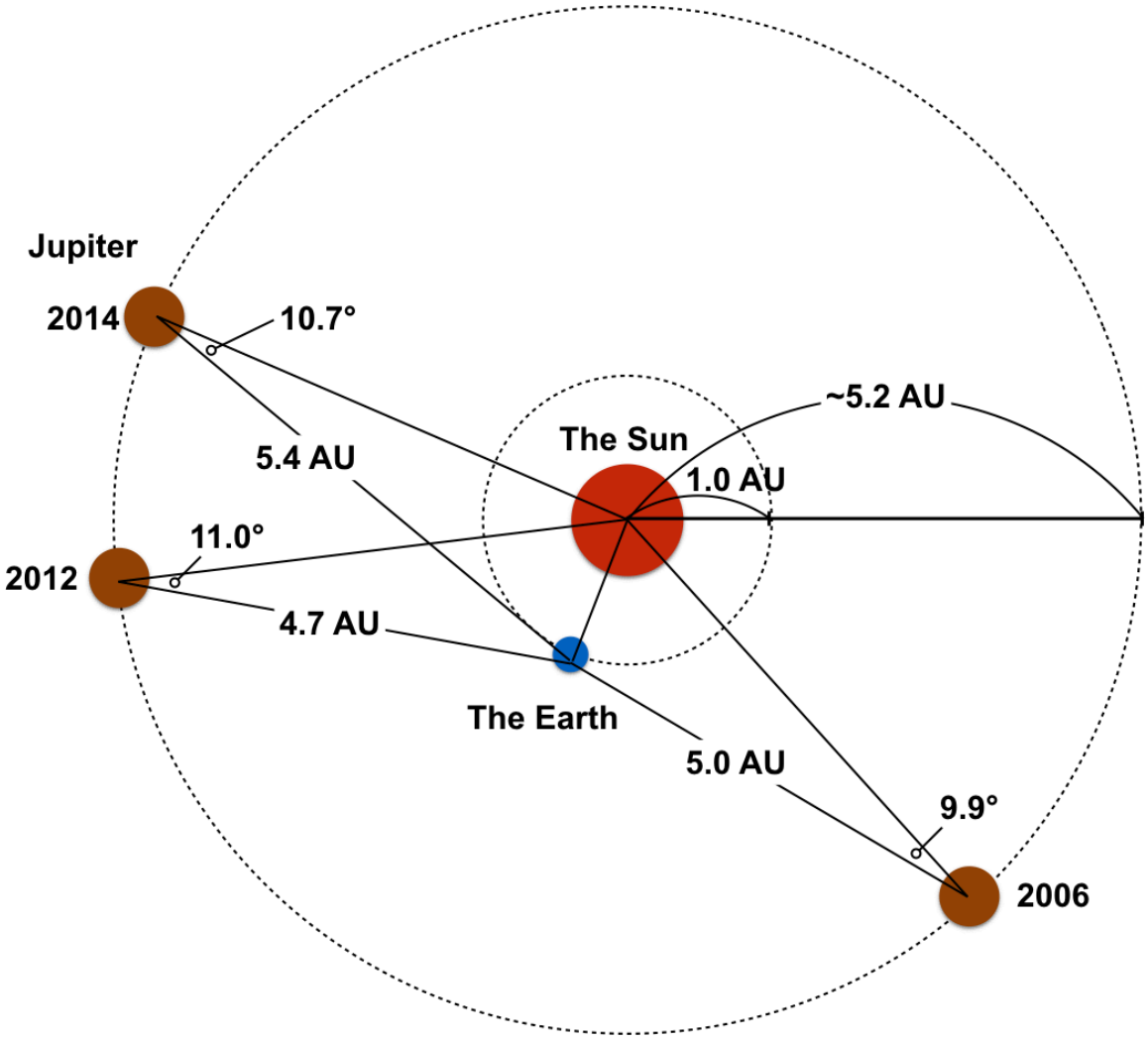

FIGURE 4.1: Relative positions of Jupiter with respect to the Sun and the Earth.

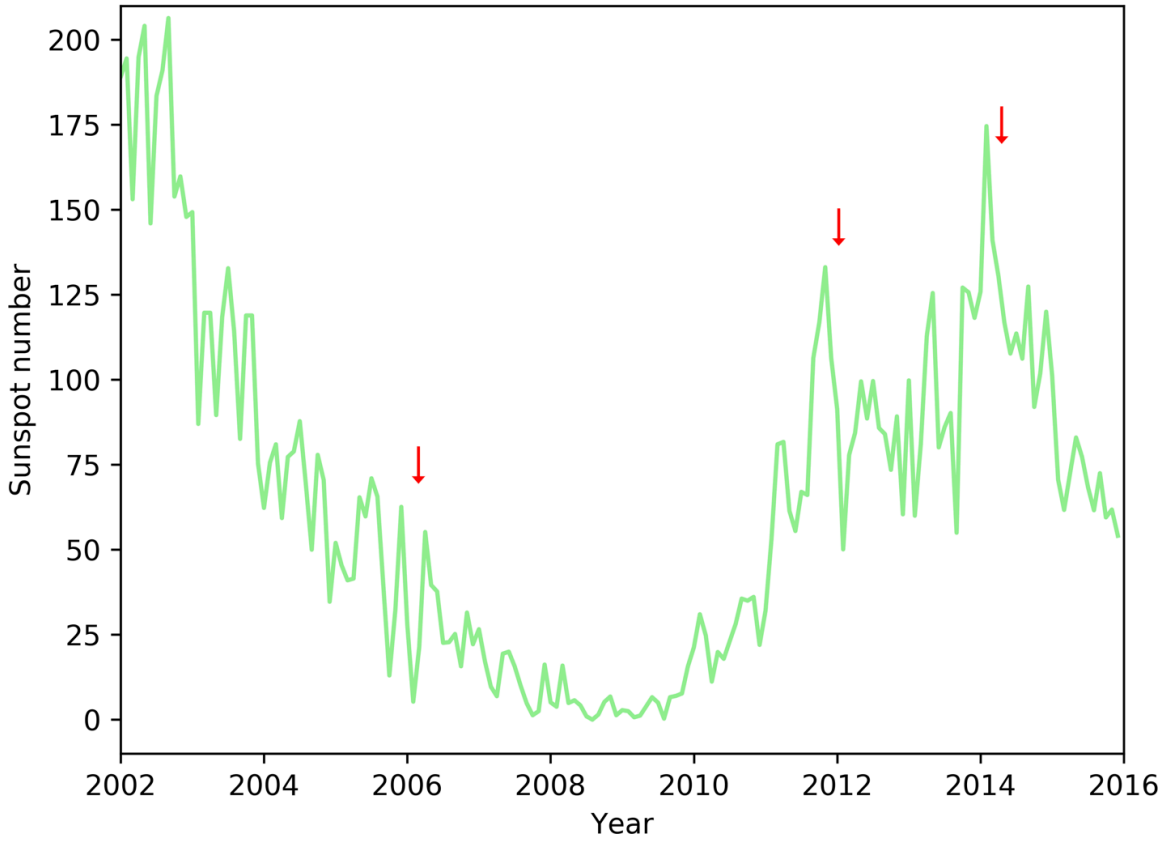

FIGURE 4.2: Variation of solar activity shown by the sunspot number. Red arrows indicate the period of *Suzaku* observations of Jupiter. Data are taken from Sunspot Index and Long-term Solar Observations (Silso) web site.

3. Convert the sky coordinate of the image after the point-source exclusion into Jupiter's reference frame (JRF) coordinate (see Appendix A).

4. Create images in the JRF coordinate for the two energy bands, using the event files processed in step 3.

5. Make projection profiles from the JRF images and estimate the size of diffuse emission around Jupiter assuming an ellipsoidal shape. A ratio of diffuse to point-like emission (i.e., from Jupiter itself) is calculated.

6. Extract spectra from a circular (for source) and a surrounding annular (for background) regions both centered at the origin of the JRF coordinate, using the event files processed in step 3.

7. Generate the Redistribution Matrix File (RMF) for the epoch of the Jupiter observation using `xisrmfgen` (version 2012-04-21), and the Ancillary Response Files (ARFs) for the circular and ellipsoidal regions are produced using `xissimarfgen` (version 2010-11-05).

8. Carry out spectral fits using `Xspec` (version 12.10.1) with the models describing Jupiter's X-ray emission and a power-law function for the Jovian diffuse hard X-ray emission. The background-subtracted spectra of all detectors (XIS FI+BI) are fitted.

4.1 2014 observations by *Suzaku* and *XMM-Newton*

The log of *Suzaku* and *XMM-Newton* observations in 2014 is shown in Table 4.2. The coordinated *XMM-Newton* observations with ID revolution 2628 and 2630 approximately correspond to the *Suzaku* observation ID 508023010–508023040 and 508023110–508023120, respectively. Net exposure of the *Suzaku* observations was 161.5 ks, while the *XMM-Newton* one was 77.4 ks.

TABLE 4.2: Logs of the *Suzaku* and *XMM-Newton* observations in 2014.

Suzaku	Obs. ID	Line of Sight (R.A., Decl.)	Obs. date (start)	(end)	Exposure (ks)
	508023010	103.7993, 23.1163	2014-04-15T02:03:41	2014-04-15T09:20:12	13.1
	508023020	103.8407, 23.1129	2014-04-15T09:20:25	2014-04-15T17:20:12	15.4
	508023030	103.8837, 23.1078	2014-04-15T17:20:25	2014-04-16T01:35:11	8.9
	508023040	103.9250, 23.1078	2014-04-16T01:35:24	2014-04-16T09:20:11	15.6
	508023050	103.9685, 23.1027	2014-04-16T09:20:24	2014-04-16T17:20:11	14.3
	508023060	104.0103, 23.0994	2014-04-16T17:20:24	2014-04-17T01:30:18	8.9
	508023070	104.0402, 23.0972	2014-04-17T01:30:27	2014-04-17T04:35:18	4.6
	508023080	104.3277, 23.0738	2014-04-19T02:54:24	2014-04-19T10:45:19	16.0
	508023090	104.3715, 23.0706	2014-04-19T10:45:32	2014-04-19T18:45:13	12.0
	508023100	104.4171, 23.0664	2014-04-19T18:45:30	2014-04-20T02:45:18	9.4
	508023110	104.4639, 23.0622	2014-04-20T02:45:31	2014-04-20T10:45:18	16.7
	508023120	104.5088, 23.0594	2014-04-20T10:47:35	2014-04-20T18:45:18	11.2
	508023130	104.5549, 23.0543	2014-04-20T18:45:31	2014-04-21T02:45:18	10.1
	508023140	104.5850, 23.0530	2014-04-21T02:45:27	2014-04-21T05:23:18	5.3
XMM-Newton	rev. 2628	103.9189, 23.1029	2014-04-15T21:12:34	2014-04-16T09:06:51	42.4
	rev. 2630	104.4784, 23.0552	2014-04-20T02:28:34	2014-04-20T12:21:15	35.0

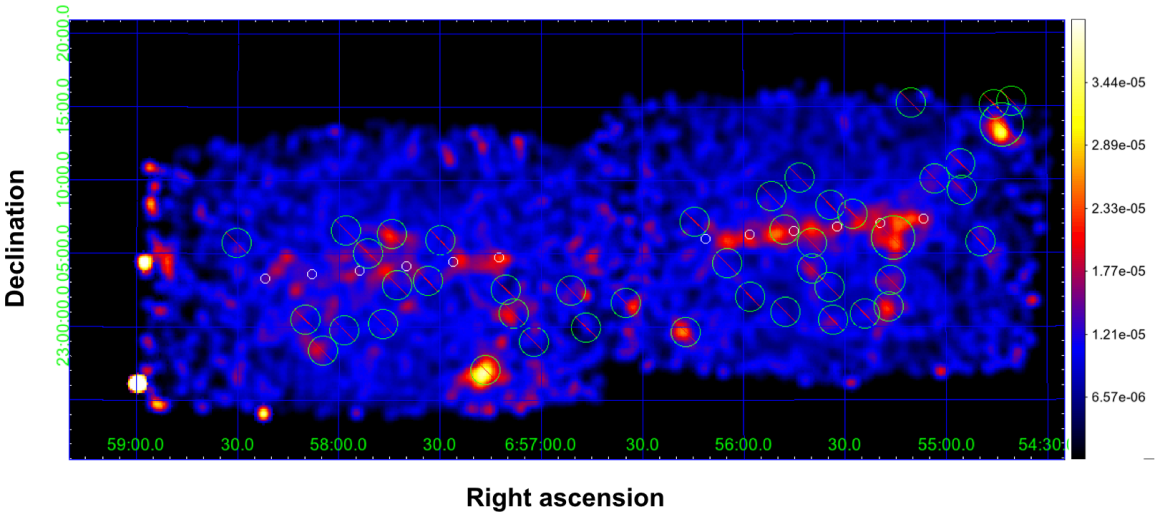

FIGURE 4.3: *Suzaku* XIS BI mosaic images of the vicinity of Jupiter in 0.2–1 keV, displayed on the J2000.0 coordinates. Exposures are corrected and the unit is counts s^{-1} binned $pixel^{-1}$. For clarity, the images are binned in 8×8 original pixels and smoothed by a Gaussian of $\sigma = 5$ pixels. White circles show the size and trajectory of Jupiter during the observations. Green circles marked with a red slash indicate point sources that are omitted when we superpose the images in Jupiter's reference frame.

4.1.1 Image analysis

Mosaic image

Since Jupiter moves fast (up to a few arcmins per day) in the field of view during the observation, we need to change the pointing direction fourteen times a day to keep the object near the field center. We will then convert all the data coordinates into Jupiter's reference frame (JRF) before we analyze the emission from Jupiter. We used Jupiter's ephemeris obtained from the Jet Propulsion Laboratory (JPL). At first, before the above-mentioned procedure, we examined X-ray images without the attitude correction. Figure 4.3 and Figure 4.4 show mosaic images of BI and FI instruments in two energy bands, 0.2–1 and 1–5 keV, respectively. The images were divided by exposure maps which were generated by the exposure map generator `xisexpmapgen`. In both images, especially in the 0.2–1 keV one, faint trails are seen along Jupiter's motion, indicating that Jupiter's X-rays are detected.

There are point sources in the image besides Jupiter's trail, and they are more noticeable in the 1–5 keV image. We used `wavdetect` (which is a point-search program in the `CIAO` package) to pick-up the sources along with their positions and compared with the *XMM-Newton* Serendipitous Source Catalog (3XMM- DR8 version). This showed a total of 44 point sources. These point sources are indicated in Figure 4.3 and Figure 4.4 by green circles marked with a red slash. We excluded circular regions centered on individual sources, with a diameter equal to the beam size, i.e., the half power diameter (HPD) of XIS (~2′). For safety, we masked these 44 point sources for both 0.2–1 and 1–5 keV images.

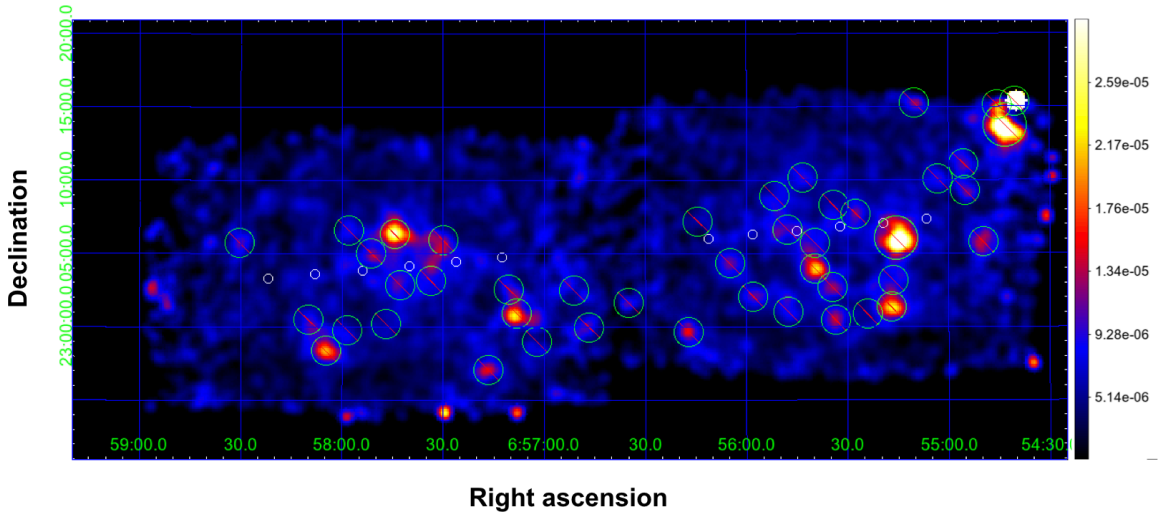

FIGURE 4.4: The same as Figure 4.3 but for XIS FI in 1–5 keV.

Jupiter's reference frame (JRF) image

We have to correct the coordinates of the event file to obtain coordinates centered at Jupiter. There is no official tool for the coordinate correction for moving targets, so we made it on our own and called it `attitune`. The `attitune` tool can correct the coordinate by taking into account both Jupiter's motion in the sky and the satellite's orbital motion around the Earth. The Earth's motion around the Sun is also considered. Parameters of the former were obtained from JPL HORIZON, while the latter ones were extracted from the *Suzaku* orbit file packaged with the event files of the respective observations. Using these information, the tool corrects the line-of-sight direction recorded in the attitude files, which are in the same package of the event files of each observation. This correction resulted that Jupiter was in the center of the field of view. The event files were re-processed by `xiscoord` (version 2009-02-28) through addressing the corrected attitude files, finally, to be converted into Jupiter's reference frame (JRF).

We created the two band images again, but in the JRF coordinate as shown in Figure 4.5 and Figure 4.6. The 44 point sources were removed from the event file before this step. Exposure maps can also be generated by `xisexpmapgen` with the corrected attitude files. In generating the exposure maps, the positions of the 44 point sources, which were no more stationary in the JRF framework, were excluded using detector masks as a parameter of `xisexpmapgen`. Jupiter's movement in the 8 s interval, which is equal to *Suzaku*'s time resolution defined by the event-by-event accumulation in CCD, corresponded to ~0.04″ as estimated from Jupiter's apparent velocity and causes a negligible image blur compared with *Suzaku*'s HPD (~2′).

The images thus obtained indicate different spatial extent between the soft and the hard energy bands as seen in Figure 4.5 and Figure 4.6. The soft X-ray image is likely to agree with the point spread function (PSF) of *Suzaku*. On the other hand, the hard X-ray one is surely more extended than the PSF and indicates a spatial extent ~6′ × ~2′ corresponding to ~20 R_J × ~8 R_J.

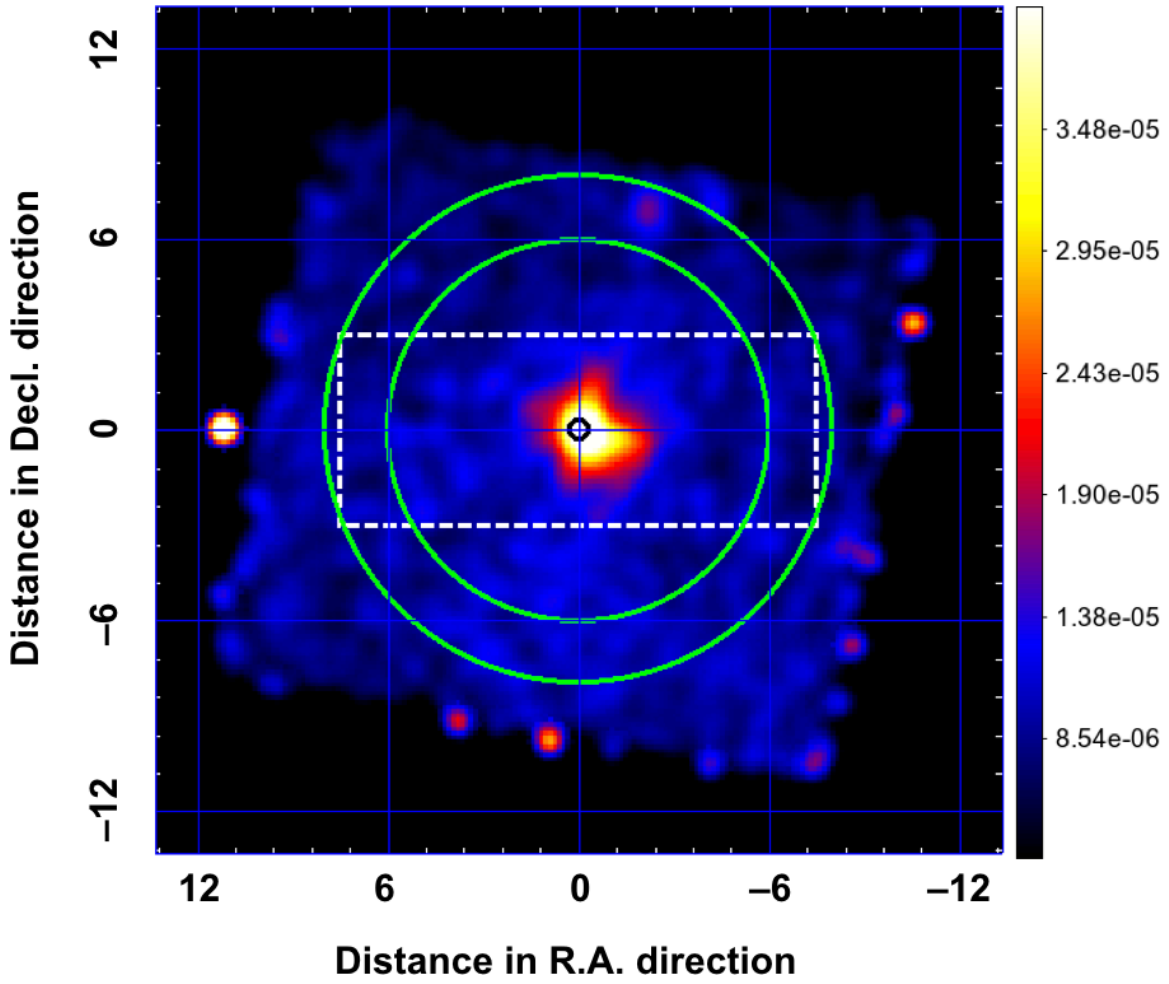

FIGURE 4.5: *Suzaku* XIS BI image after correcting for Jupiter's ephemeris and *Suzaku*'s orbital motion in 0.2–1 keV. The images are exposure-corrected, binned, and smoothed in the same way as in Figure 4.3. White dashed square shows the region used for a projection profile, with a size $15' \times 6'$. Green circles indicate the regions used for spectral analysis. The radius of the inner circle is $6'$ to extract the source and the outer radius $8'$ defines the background region.

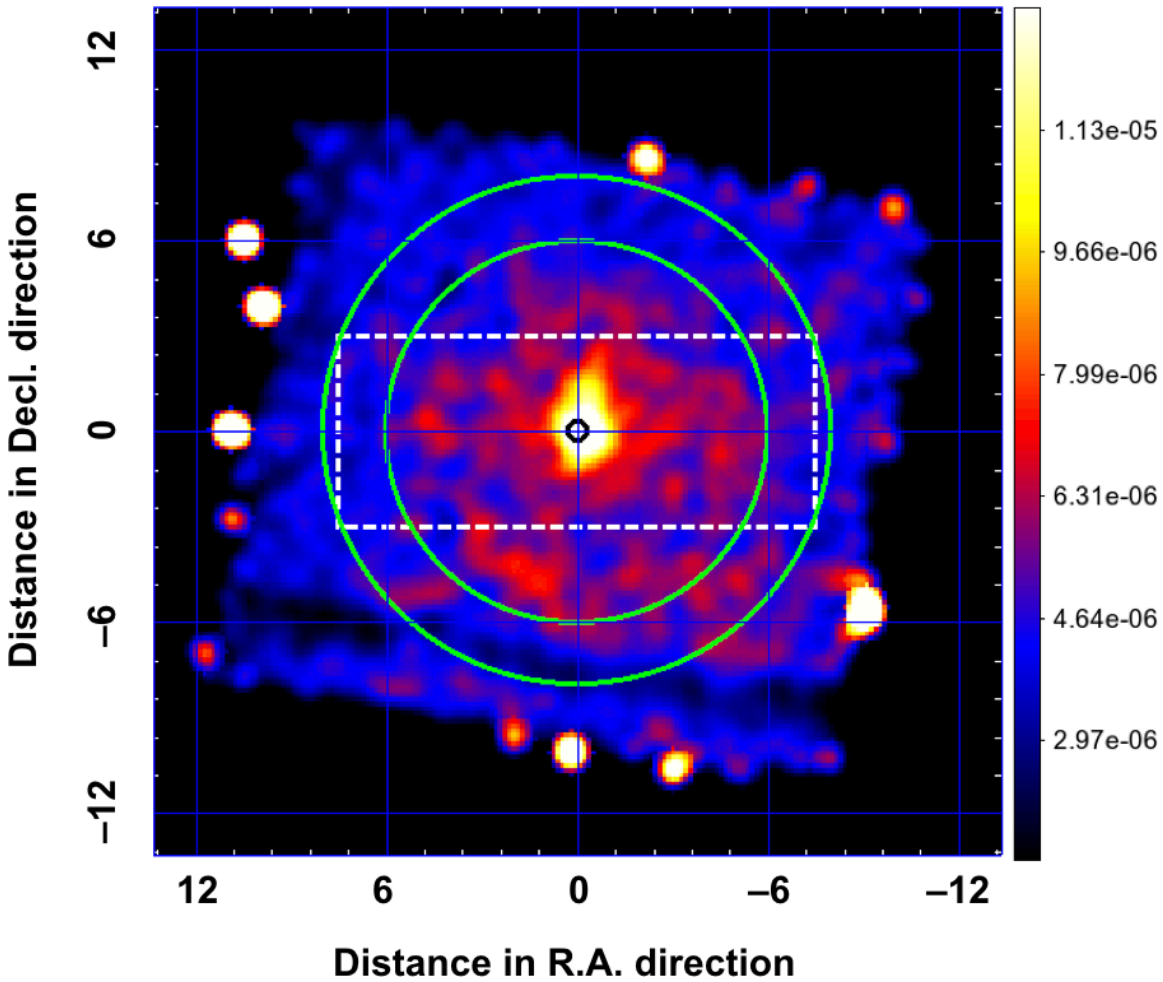

FIGURE 4.6: The same image as Figure 4.5 but for XIS FI in 1–5 keV.

Projection profile

To look into the spatial distribution of the X-ray emission, we generated projection profiles along the horizontal axis as shown in Figure 4.7 and Figure 4.8. In these plots, the data were accumulated in white dashed squares in Figure 4.5 and Figure 4.6 with a binning of 16×16 pixels without smoothing.

We produced a model profile consisting of Jupiter's body (disk and aurorae) and its surroundings, with their configurations assumed to be a small circle and an ellipse, respectively. For this modeling, we utilized `xissimarfgen` by varying parameters which described the shape of the X-ray emitting region. The size of the small circle describing Jupiter's body emission was fixed to be Jupiter's apparent size of 18.3″. The elliptical shape of the diffuse emission was changed around 6′ in horizontal (R.A.) and 2.5′ in vertical (Decl.) axes with a pitch angle 5″ in each axis. The simulated models are normalized and centered on Jupiter to be fitted with the data.

As a result, we found that the observed profile can be represented by a combination of the uniform circle and a uniform elliptical emission with semi-axes of 6.4′ and 2.5′, corresponding to 21.0 R_J and 8.2 R_J, respectively. The hard band emission is surely extended over a wide region (>6 R_J). On the other hand, the soft emission is not well-fitted by the same model and marginally consistent with the small circular emission from Jupiter's body.

We calculated a diffuse intensity ratio, defined as the intensity of the simulated elliptical emission (green curve in Figure 4.7) divided by that of the small circular emission (orange curve), by integrating counts in the respective areas in the projection profiles. The diffuse intensity ratio (D/B ratio) was evaluated as 1.91 ± 0.36 in the 2014 observation.

4.1.2 Coordinated *XMM-Newton* observations

This section describes the observed results taken in 2014 from *XMM-Newton*, which gives much better angular resolution (∼15″ in half energy width) than *Suzaku* and its simultaneous data are very useful in separating Jupiter's body and extended components. Figure 4.9 and Figure 4.10 show the EPIC images in 0.2–1 and 1–5 keV, respectively. The images are reconstructed in the JRF coordinate by using `attmove` (version 1.5) which is one of the SAS tools and has been officially developed to handle data of moving targets such as the solar system objects. The images are then generated by using ESAS tools[3] (ESA: XMM-Newton SOC, 2019). The soft X-rays contribute significantly to the aurora emission, while the hard X-rays are relatively uniform over Jupiter's body.

Here, we did not subtract the cosmic diffuse X-ray background, CXB, when produced the energy spectra because Jupiter cast a shadow to the diffuse background and the residual particle background of the detector was no more than 1% of Jupiter's flux in the band 0.2–2 keV. Note that the particle background gives significantly more contribution in higher energies. Lumb (2002) reported that the EPIC particle background was flat as a function of energy and the estimated level was 0.0210 ± 0.0022 $cm^{-2}\,s^{-1}$. Considering the size of the region for which the spectrum is produced, we estimate the level to be 9.6×10^{-5} count s^{-1} which was less than 5% of the flux integrated above 2 keV. Thus, we created the EPIC particle background spectra using `mos-`, `pn-spectra`, `mos-` and `pn-back` (from the ESAS package) and subtracted them from the source region spectra. These background spectra reproduce well the particle background component of each EPIC camera based

[3] https://heasarc.gsfc.nasa.gov/docs/xmm/esas/cookbook/xmm-esas.html

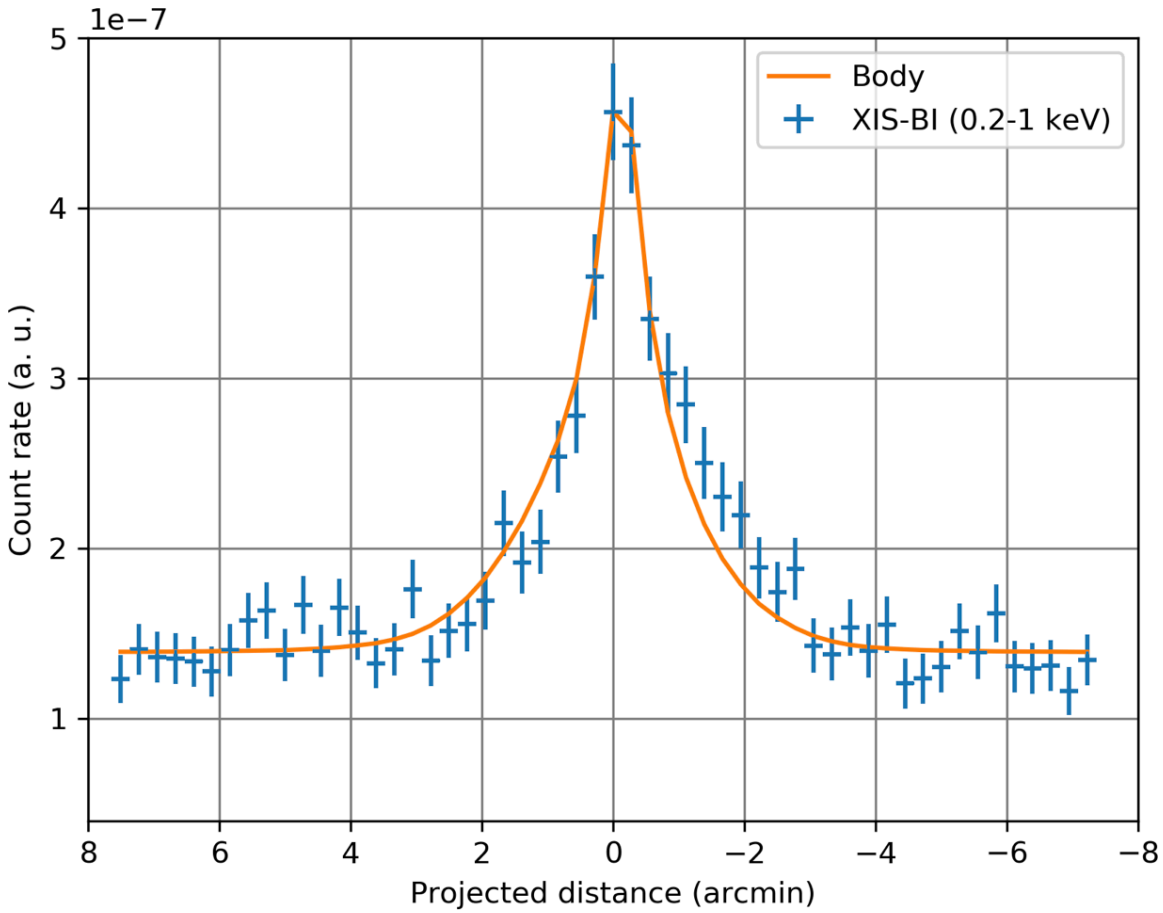

FIGURE 4.7: Projection profiles in the soft band along the horizontal axis, extracted from square regions in Figure 4.5 (0.2–1 keV). Crosses show the data. Errors are statistical 1σ ones. The orange curve shows a simplified model of X-rays from Jupiter's body (18.3 $''$ radius) in 0.2–1 keV. The normalization and offset of the curve are tuned by fitting the data with reduced χ-square of 1.10.

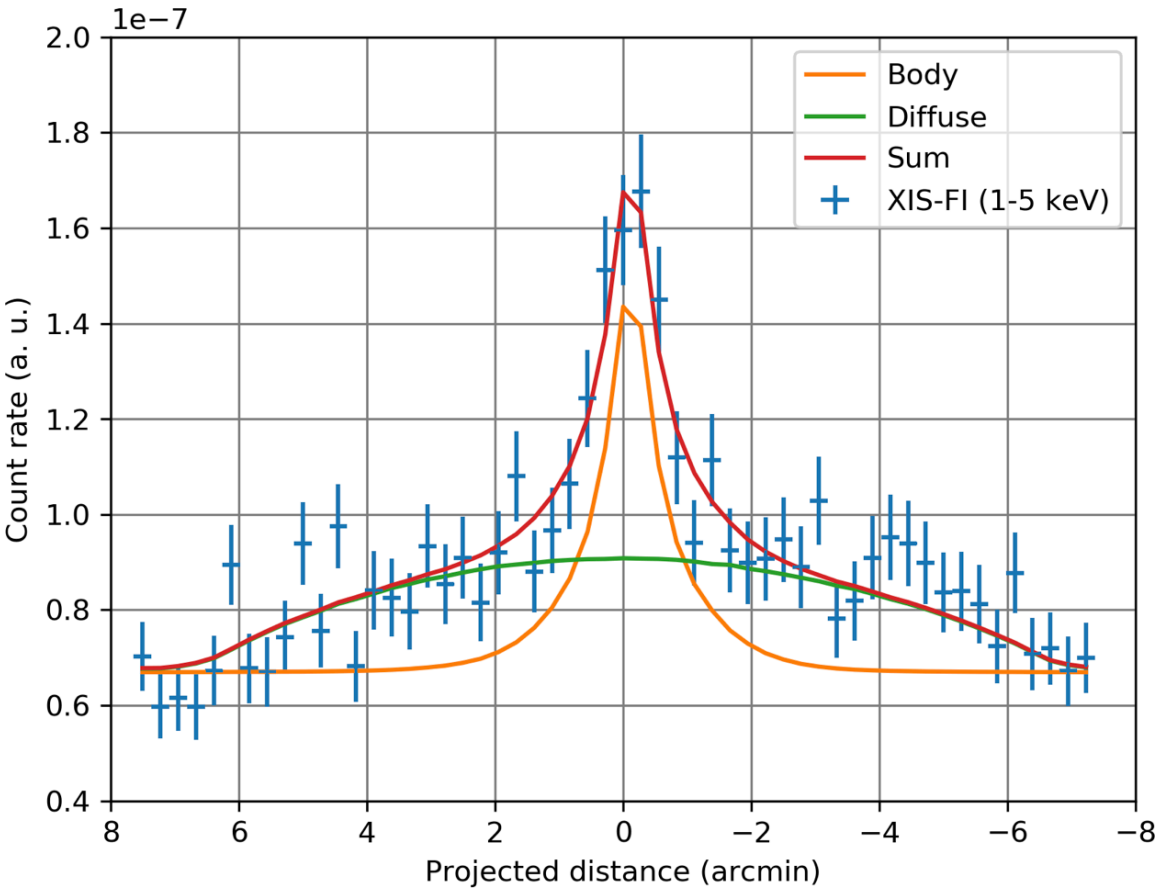

FIGURE 4.8: The same as Figure 4.7, but in Figure 4.6 (1–5 keV). The orange curve shows a simplified model of X-rays from Jupiter's body (18.3 ″ radius) in 1–5 keV. In the left panel, the green curve indicates the expected profile for a uniform elliptical region with semi-axes of 6.4 ′ and 2.5 ′, and the red line is the sum of the orange and green curves. The normalizations and offsets of these lines are tuned by fitting the data with reduced χ-square of 1.02.

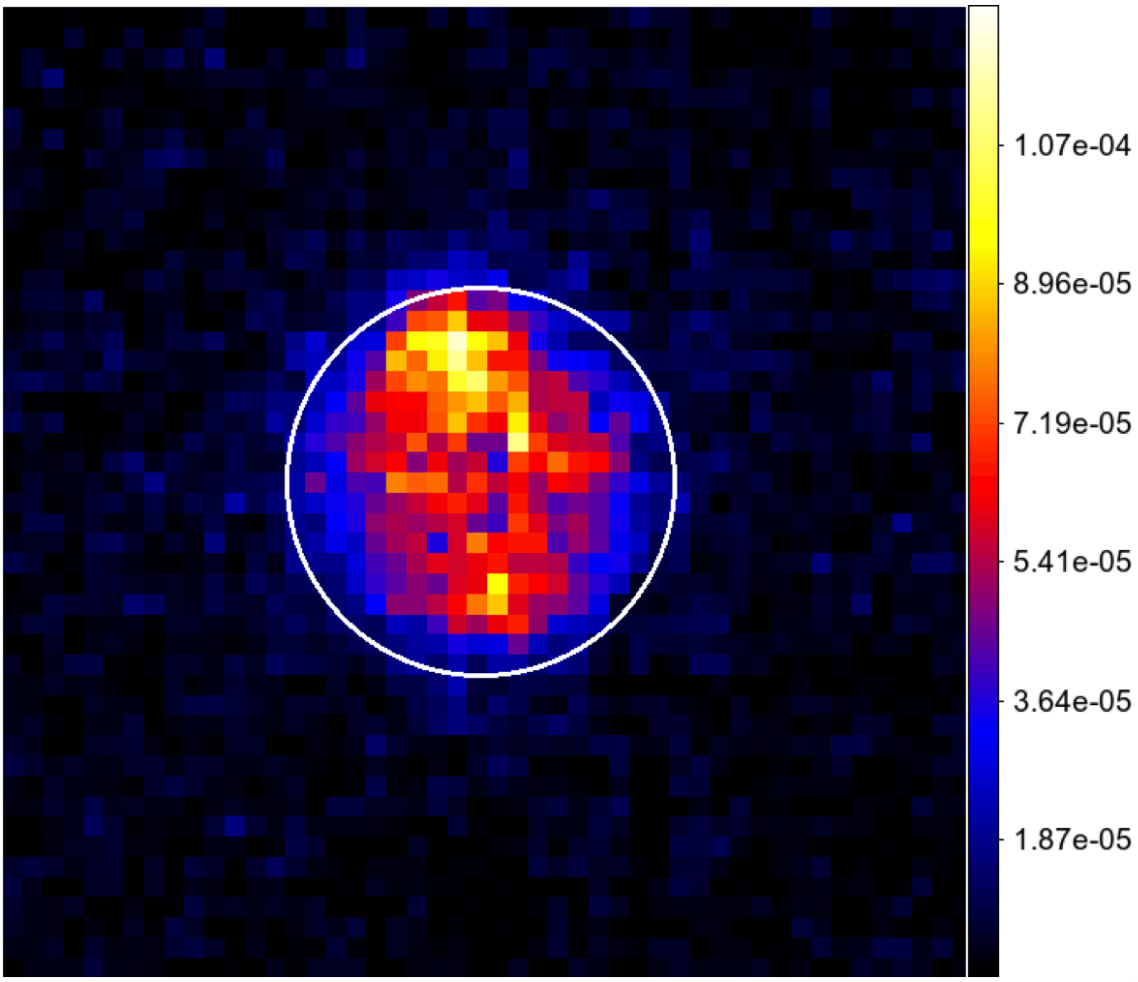

FIGURE 4.9: *XMM-Newton* cameras' combined images after correcting for Jupiter's ephemeris and *XMM-Newton*'s orbital motion in 0.2–1 keV. The white circle has a radius of 24″. Both the width and the hight of the image correspond to 2′.

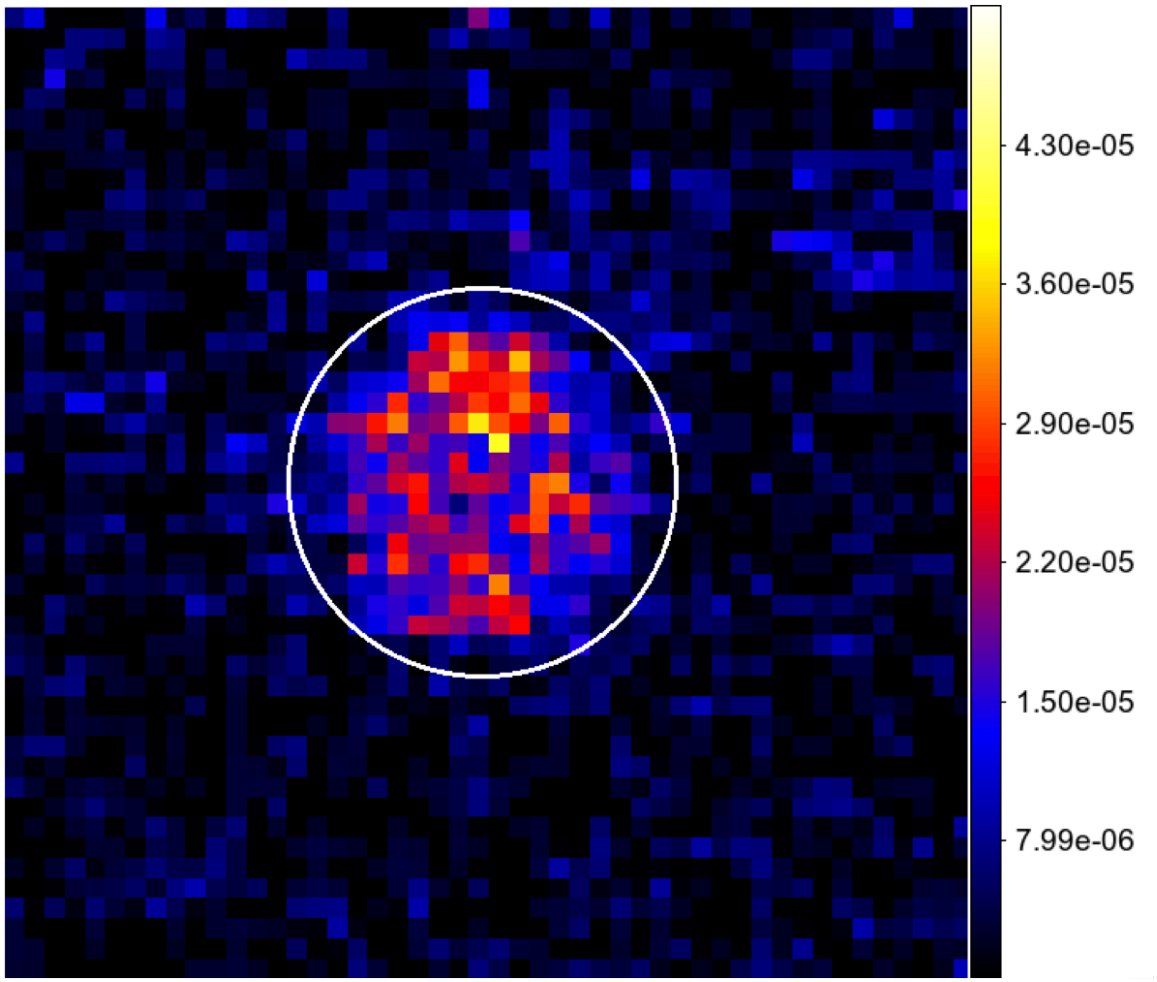

FIGURE 4.10: The same as Figure 4.9 but in 1–5 keV.

on the models calibrated by the developer team. RMFs and ARFs were generated by `rmfgen` and `arfgen` from SAS tools with the point source option, in the same manner as in Branduardi-Raymont, Bhardwaj, R. F. Elsner, et al., 2007; Branduardi-Raymont, R. F. Elsner, Gladstone, et al., 2004.

The MOS and pn spectra after the background subtraction are shown in Figure 4.11. The spectra are characterized by a thermal continuum with several emission lines in the lower energy band and also a continuum extending up to >5 keV. Following the analysis in Branduardi-Raymont, Bhardwaj, R. F. Elsner, et al., 2007, we tried to fit a model consisting of four Gaussians along with the following three continuum components: an APEC model peaked near 0.8 keV, a thermal bremsstrahlung in a range <0.5 keV, and a power-law function for the hard end of the spectrum. Here, we did not include an absorbing column in the model, because of the proximity of the object. The four Gaussians had center energies, 0.57, 0.65, 1.35, and 1.86 keV, which are the known values of O_{VII}, $O_{VIIILy\alpha}$, Mg_{XI}, and SI_{XIII} lines, respectively. Given the moderate statistical quality of the data, the higher two line energies were fixed in the spectral fits. We assumed that O_{VII} and $O_{VIIILy\alpha}$ lines were charge exchange (CX) emission from Jupiter's aurorae where the cool thermal bremsstrahlung was produced, whereas Mg_{XI} and SI_{XIII} lines were scattered solar coronal emission from Jupiter's disk which was also responsible for the thermal emission fitted by the APEC model. The power-law component represents non-thermal bremsstrahlung from keV electrons which are considered to precipitate into the aurorae.

Table 4.3 summarizes the best-fit parameters and 90% confidence errors. The temperature of the APEC model, ~0.59 keV, is consistent with the solar coronal emission (Branduardi-Raymont, Bhardwaj, R. Elsner, et al., 2007). The temperature of the cool bremsstrahlung, ~0.09 keV, also agrees with the results from the past *XMM-Newton* observations (Branduardi-Raymont, Bhardwaj, R. F. Elsner, et al., 2007). The photon index Γ and normalization of the power-law component were, however, different from the past *XMM-Newton* observations. We estimated the 2014 flux in 2–7 keV as $(4.4 \pm 0.1) \times 10^{-14}$ erg cm^{-2} s^{-1} and compared it with that in the past observations ($\sim 2.1 \times 10^{14}$ erg cm^{-2} s^{-1}; after table 1 in Branduardi-Raymont, Bhardwaj, R. F. Elsner, et al., 2007), which turned out to be a factor of ~2 increase, with the difference of the distance to Jupiter taken into account. Such a flux change seems possible, since there was a factor-of-two variation observed within several days in Nov. 2003 from *XMM-Newton* (rev. 0726 and 0727; Branduardi-Raymont, Bhardwaj, R. F. Elsner, et al., 2007).

4.1.3 Spectral analysis of *Suzaku* data

We analyzed the *Suzaku* spectrum by extracting photons from a rather wide region, in order to examine the nature of the extended emission. We used the JRF-converted event files, from which the 44 point sources were removed, and accumulated source photons from the circle with a radius of 6′ and background ones from the surrounding annulus with an outer radius of 8′ using `xselect` (version 2.4d). Both regions have the same center in the JRF coordinate. Consequently, the source region includes both Jupiter's body and the diffuse emission which cannot be spatially separated by *Suzaku*'s angular resolution (HPD of ~2′). The diffuse X-ray background was subtracted using the data taken in the outer annular region. The size of Jupiter's body (~30″ in diameter) is smaller than the source region, and we may ignore Jupiter's occultation of a small part of the diffuse X-ray background.

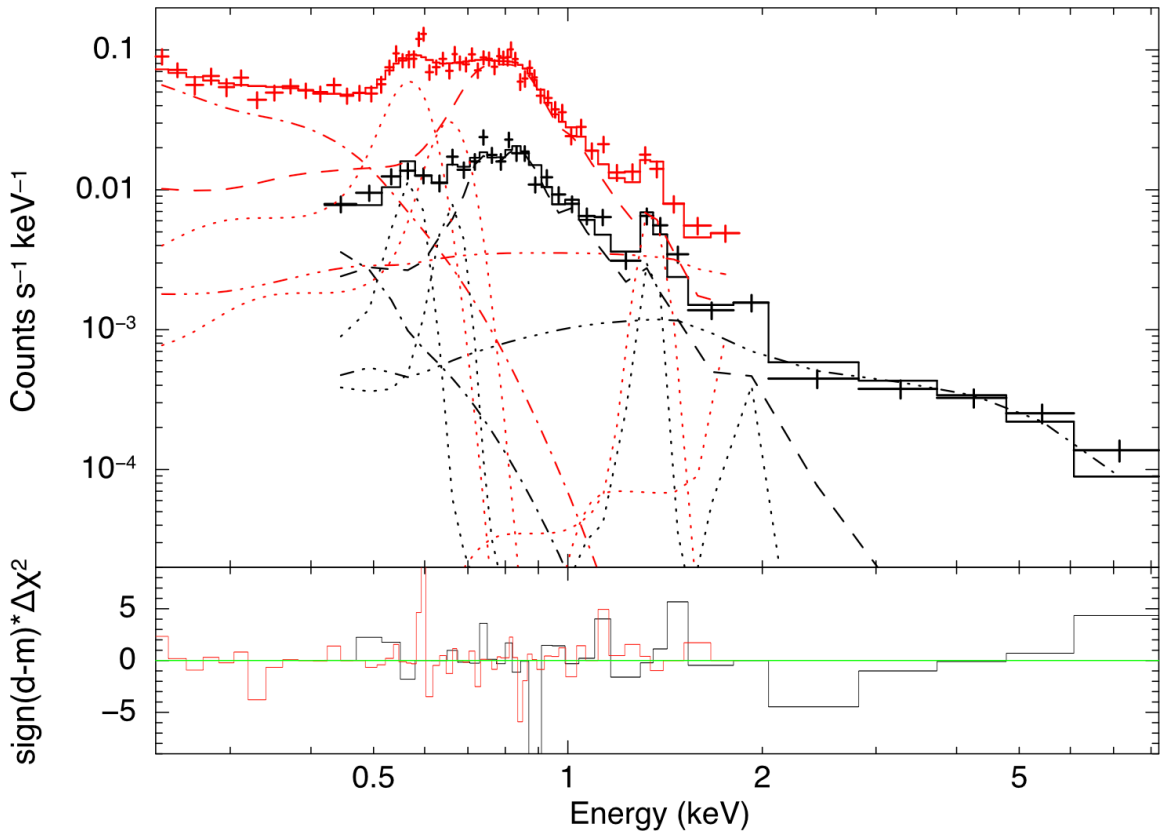

FIGURE 4.11: Background-subtracted MOS (black) and pn (red) spectra of Jupiter's body emission region, compared with the best-fit models summarized in Table 4.3 (solid lines).

TABLE 4.3: Spectral parameters (and their 90% confidence errors) for the *XMM-Newton* MOS (0.4–8 keV) and pn (0.2–2 keV) data of the point-like emission region in 2014.

APEC[a]	kT[b]	Norm.[c]
	$0.59^{+0.02}_{-0.02}$	$27.1^{+1.2}_{-1.4}$
Gaussian[d]	Line energy[e]	Flux[f]
	$0.57^{+0.002}_{-0.01}$	$17.3^{+2.1}_{-2.2}$
	$0.66^{+0.01}_{-0.01}$	$6.8^{+2.1}_{-1.4}$
	1.35 (fixed)	$1.0^{+0.3}_{-0.3}$
	1.86 (fixed)	$0.5^{+0.3}_{-0.3}$
Bremss.	kT[b]	Norm.[c]
	$0.09^{+0.02}_{-0.02}$	$1562.5^{+1585.2}_{-792.8}$
Power-law	Γ (Photon index)	Norm.[c]
	$0.85^{+0.19}_{-0.25}$	$4.3^{+1.3}_{-1.2}$
χ^2/d.o.f[g]	118.25 / 79	

[a] APEC abundance parameter is set by `aspl` (Asplund et al., 2009).
[b] APEC or bremsstrahlung temperature in keV.
[c] Normalization in units of 10^6 photons cm^{-2} s^{-1} keV^{-1}.
[d] The widths of Gaussians are fixed at 0.01 keV in the fits.
[e] Energy of the emission line features in keV.
[f] Total flux in the line in units of 10^6 photons cm^{-2} s^{-1}.
[g] χ^2 value and degrees of freedom.

Then, we generated both RMF and ARFs using `xisrmfgen` and `xissimarfgen` for each extracted spectral file, respectively. Based on the results of the profile fitting of the projected data, we prepared both point-like ARFs and elliptically extended ARFs for the emission from Jupiter's body and the diffuse emission, respectively. The total exposure time for each region was calculated from the pre-generated exposure maps in the JRF coordinate, and the *backscal* parameters of both the source and the background spectral files were over-written with these values. This procedure was necessary because `xselect` did not take into account the loss of areas of the removed point-source regions in the JRF-converted event files.

Spectral fit

The XIS spectra thus obtained are shown in Figure 4.12. A thermal emission accompanied by several lines can be seen in the low energy range, and an additional continuum extends up to >5 keV: similar to the feature seen in the EPIC spectra (Figure 4.11). We first fitted the spectra with the best-fit model from the EPIC spectral analysis by employing point-source ARFs, and found a difference around the 0.5 keV line and a large excess of the hard component. Then, we allowed the center energy of the first Gaussian at 0.57 keV to be free and added an additional power-law model for the diffuse emission, which uses the extended ARFs. We fixed the parameters of the previous power-law component at the *XMM-Newton* values, which accounted for the auroral non-thermal bremsstrahlung.

Table 4.4 summarizes the best-fit parameters and their 90% errors. Temperatures and normalizations of the APEC and the thermal bremsstrahlung models agree with the results of *XMM-Newton*'s EPIC spectral fits within their errors. Fluxes of the Gaussians centered at 1.35 and 1.86 keV are consistent within their errors. The center energy of the first Gaussian in the best-fit model is 0.53 keV, which does not directly match any likely energy resulted from the CX reaction. We consider that this feature is likely to be a mixture of oxygen and nitrogen lines whose energies are 0.57 and 0.43 keV, respectively. Significant flux increase of the line-like feature at ~0.53 keV also suggests that the condition of the CX process may have changed from that in the coordinated *XMM-Newton* observation. A flux of the second Gaussian at ~0.65 keV which increased by a factor of 2.8 ± 1.5 from the coordinated *XMM-Newton* observation was also likely caused by the change of the CX condition. In the hard energy band, we recognize an excess from the power-law fit to *XMM-Newton*'s EPIC data. This excess can be fitted by another power-law model with Γ of $1.24^{+0.49}_{-0.56}$. This rather flat power-law spectrum is likely to be the same as the non-thermal emission discovered from the past *Suzaku* observation in 2006 (Ezoe, Ishikawa, Ohashi, Miyoshi, et al., 2010).

Flux & luminosity

Finally, we calculated fluxes and estimated luminosities in 0.2–1 and 1–5 keV from the best-fit model, corrected for the distance to Jupiter at the observed epoch. The fluxes in 0.2–1 and 1–5 keV are calculated as $(25.5 \pm 1.6) \times 10^{-14}$ and $(13.2 \pm 1.1) \times 10^{-14}$ erg cm^{-2} s^{-1}, respectively. Then, the luminosities are estimated as $(21.0 \pm 1.3) \times 10^{15}$ and $(10.8 \pm 0.9) \times 10^{15}$ erg s^{-1} for 0.2–1 and 1–5 keV, respectively. As for the two hard components, which are Jupiter's body and the diffuse emission, the luminosities in 1–5 keV are separately obtained as $(4.5 \pm 0.3) \times 10^{15}$ and $(6.3 \pm 0.9) \times 10^{15}$ erg s^{-1}, respectively. We also calculate the luminosity ratio, namely the diffuse luminosity divided by that of

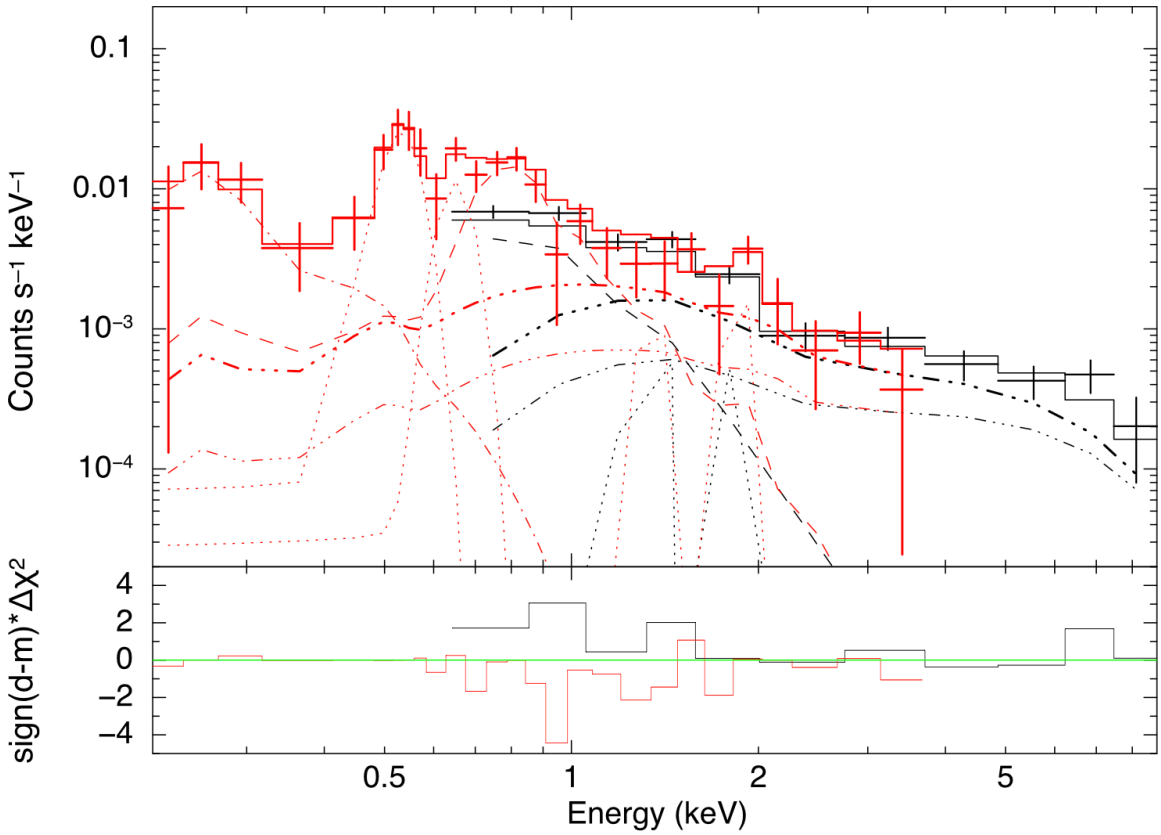

FIGURE 4.12: Background-subtracted FI (black) and BI (red) spectra of the extended emission region, compared with the best-fit models summarized in Table 4.4 (solid lines). APEC model, thermal bremsstrahlung, two power-law functions, and four Gaussians are shown in dashed, dash-dotted, dash-three-dotted, and dotted lines, respectively. Energies of the Gaussian lines (dotted curves) are 0.53 ± 0.01, 0.65, 1.35, and 1.86 keV, representing a possible N_{VII} and O_{VII} mixture, $O_{VIIILy\alpha}$, Mg_{XI}, and SI_{XIII} lines, respectively. The line energies of the last two lines are fixed in the spectral fits. The Γ and normalization of one power-law model (thin dash-three-dotted curves) are also fixed to the values from the spectral fits of *XMM-Newton*'s EPIC data.

TABLE 4.4: Best-fit parameters (and their 90% confidence errors) for the *Suzaku* XIS FI (0.65–9 keV) and BI (0.2–3.5 keV) spectra of the extended emission in 2014.

Body	APEC[a]	kT[b]	Norm.[c]
		$0.53^{+0.1}_{-0.2}$	$30.7^{+27.2}_{-3.8}$
	Gaussian[d]	Line energy[e]	Flux[f]
		$0.53^{+0.01}_{-0.01}$	$46.7^{+57.9}_{-16.2}$
		$0.65^{+0.02}_{-0.03}$	$19.1^{+9.7}_{-8.3}$
		1.35 (fixed)	$1.1^{+1.7}_{-1.1}$
		1.86 (fixed)	$2.2^{+1.7}_{-1.5}$
	Bremss.	kT[b]	Norm.[c]
		$0.08^{+0.10}_{-0.05}$	$1927.9^{+17870.1}_{-1608.0}$
	Power-law	Γ (Photon index)	Norm.[c]
		0.85 (fixed)	4.3 (fixed)
Diffuse	Power-law	Γ (Photon index)	Norm.[c]
		$1.24^{+0.49}_{-0.56}$	$15.3^{+10.9}_{-8.2}$
	χ^2/d.o.f[g]	28.84 / 26	

[a] APEC abundance parameter is set by `aspl` (Asplund et al., 2009).
[b] APEC or bremsstrahlung temperature in keV.
[c] Normalization in units of 10^6 photons cm^{-2} s^{-1} keV^{-1}.
[d] The widths of Gaussians are fixed at 0.01 keV in the fits.
[e] Energy of the emission line features in keV.
[f] Total flux in the line in units of 10^6 photons cm^{-2} s^{-1}.
[g] χ^2 value and degrees of freedom.

Jupiter's body, as 1.41 ± 0.22. This value is consistent with the D/B ratio (1.91 ± 0.36) obtained for the projection profile within the error. Based on this, we will use the D/B ratio from the projection profile when we estimate the separate luminosities from Jupiter's body and the diffuse emission in the following sections. For the other *Suzaku* observations, no coordinated observation with *XMM-Newton* was carried out and we do not have high-resolution images.

4.2 2012 observation by *Suzaku*

The 2012 observation log is summarized in Table 4.5. The net exposure was 165.8 ks. In this period, the solar activity went up to its maximum in the 24th solar cycle. Here and after, we will adopt the same analysis procedure as described for the 2014 observation. Note that there was no coordinated X-ray observation with other satellites.

TABLE 4.5: Logs of the *Suzaku* observations in 2012.

Obs. ID	Line of Sight (R.A., Decl.)	Obs. date (start)	(end)	Exposure (ks)
506006010	28.6779, 10.4549	2012-01-03T20:54:53	2012-01-04T19:47:07	33.5
506006020	28.7092, 10.4688	2012-01-04T19:47:23	2012-01-05T20:25:14	35.5
506006030	28.9811, 10.6021	2012-01-11T04:53:35	2012-01-12T05:00:23	34.9
506006040	29.0345, 10.6283	2012-01-12T05:00:40	2012-01-13T05:57:24	38.6
506006050	29.0829, 10.6504	2012-01-13T05:57:41	2012-01-13T20:43:24	23.3

4.2.1 Image analysis

Mosaic image

Mosaic images in 0.2–1 and 1–5 keV in the J2000.0 coordinate are shown in Figure 4.13 and Figure 4.14, respectively. These are divided by exposure maps which are generated by `xisexpmapgen`. Jupiter moved from right to left and a faint X-ray trail was recognized along Jupiter's motion (especially in the soft band image).

The point sources were searched for in the hard band image using `wavdetect`, and a total of 28 sources were identified. The sources are shown by green circles with red slashes in Figure 4.13 and Figure 4.14. We removed X-ray photons from these 28 sources using circular masks with a diameter of >2 (approximating *Suzaku*'s HPD).

JRF image

We converted the events into the JRF coordinate using `attitune` and `aeattcor` in the same way as for the 2014 observation. Figure 4.15 and Figure 4.16 show the two band images in the JRF coordinate, which are also exposure-corrected. In this observation, Jupiter's movement in the 8 s interval was ~0.02″.

The hard X-ray emission is extended around Jupiter, while the soft X-ray emission corresponds to the PSF of *Suzaku*. The spatial extent of the hard X-ray image is similar to that in the 2014 observation.

Projection profile

Projection profiles are produced along the horizontal axis of the white dashed square region in the JRF image. The profiles in the soft and hard bands are shown in Figure 4.17 and Figure 4.18, respectively. The data are binned in 16×16 pixels without smoothing.

Similarly to the 2014 observation, we modeled the spatial profiles of Jupiter's body and the surrounding region. A circle with a radius of $1\,R_J = 21.1''$ was used for the body emission. An ellipse with semi-axes around $6'$ and $2.5'$ which were varied with a pitch of 5 arcsec was tested for the diffuse emission. We fitted these models to the data by adjusting the normalization, center position, and axis lengths of the ellipse.

Consequently, we found that the hard band profile was reproduced by a point-like emission overlaid by a uniform elliptical emission with semi-axes $5.6'$ and $2.4'$, corresponding to $15.9\,R_J$ and $6.9\,R_J$, respectively. In contrast, the soft band profile was inconsistent with the same model and marginally consistent with a point-like emission centered on Jupiter's body. This result is similar to that of the 2014 observation. However, the center positions of these emission are slightly shifted by $\sim -0.5'$ which corresponds to $\sim 1.4\,R_J$. This could not be a significant problem considering *Suzaku*'s angular resolution and the known pointing uncertainty (Uchiyama et al., 2008). We, then, finally obtained the D/B ratio to be 1.73 ± 0.24.

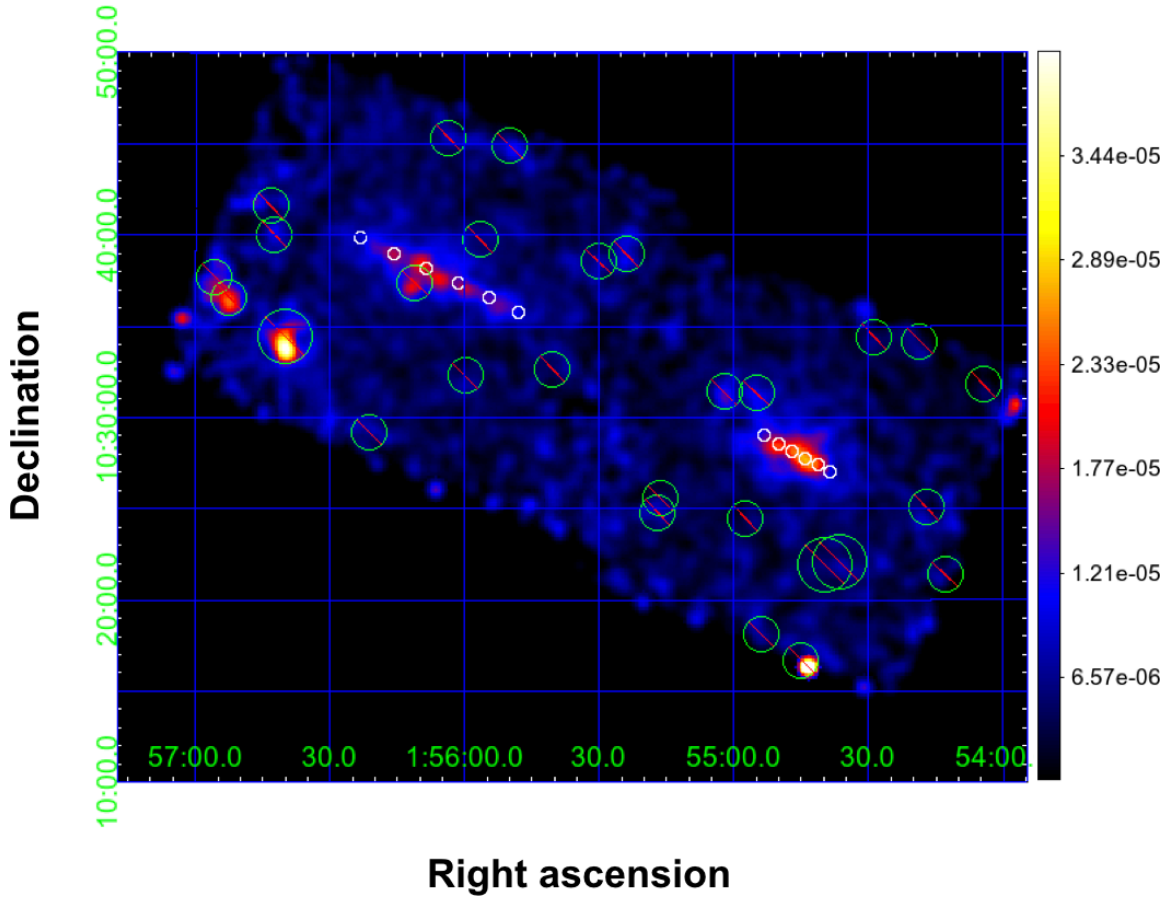

FIGURE 4.13: The same as Figure 4.3 but for the 2012 observation data.

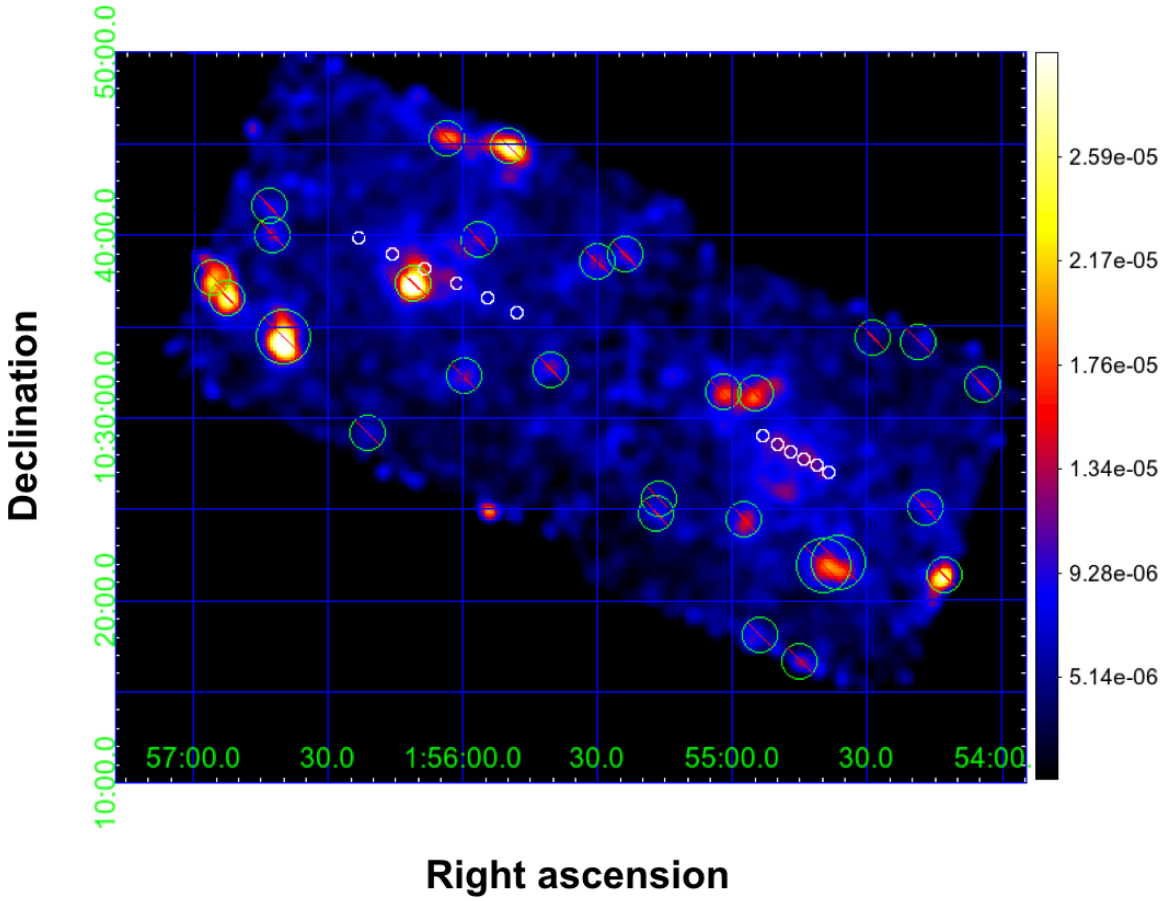

FIGURE 4.14: The same as Figure 4.4 but for the 2012 observation data.

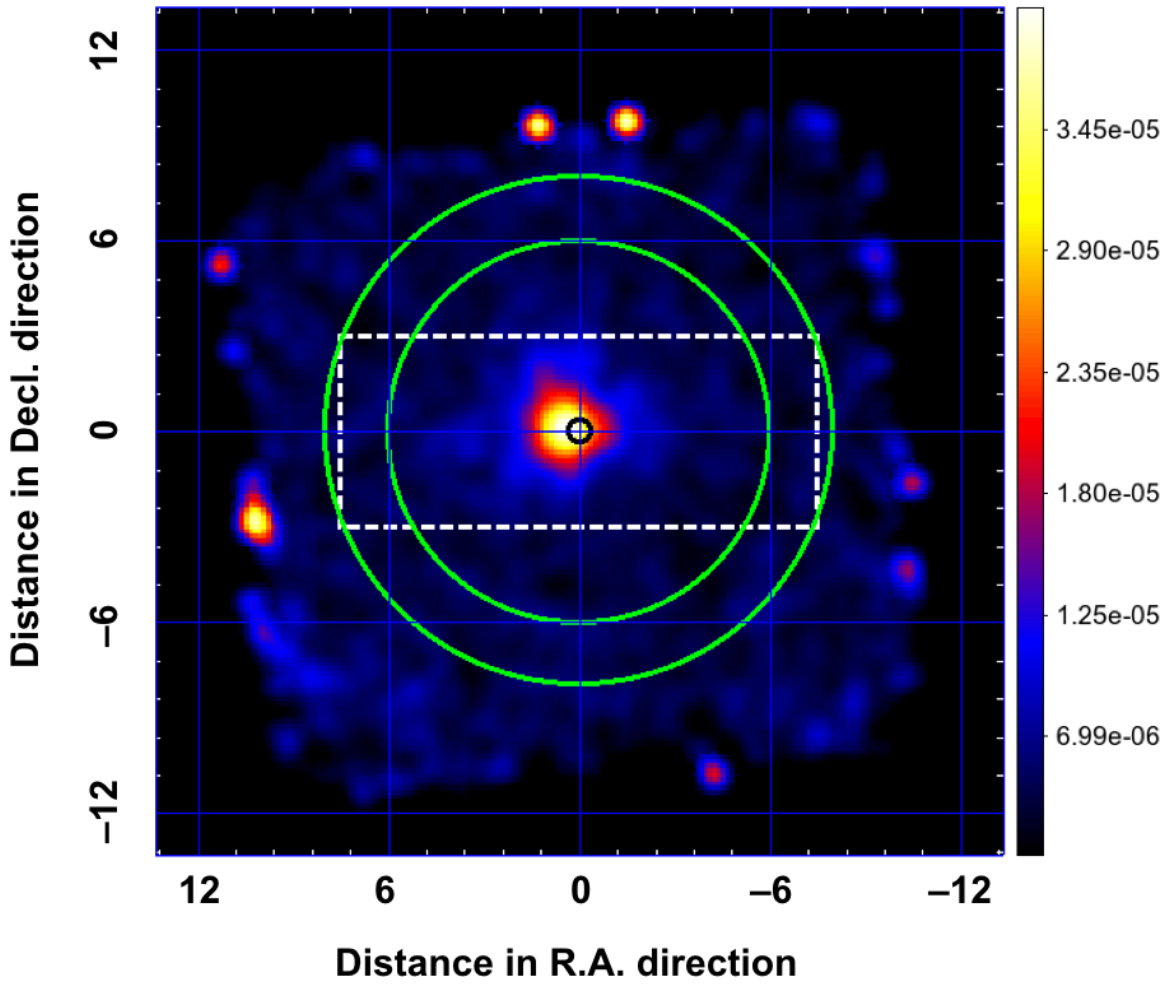

FIGURE 4.15: The same as Figure 4.5 but for the 2012 observation data.

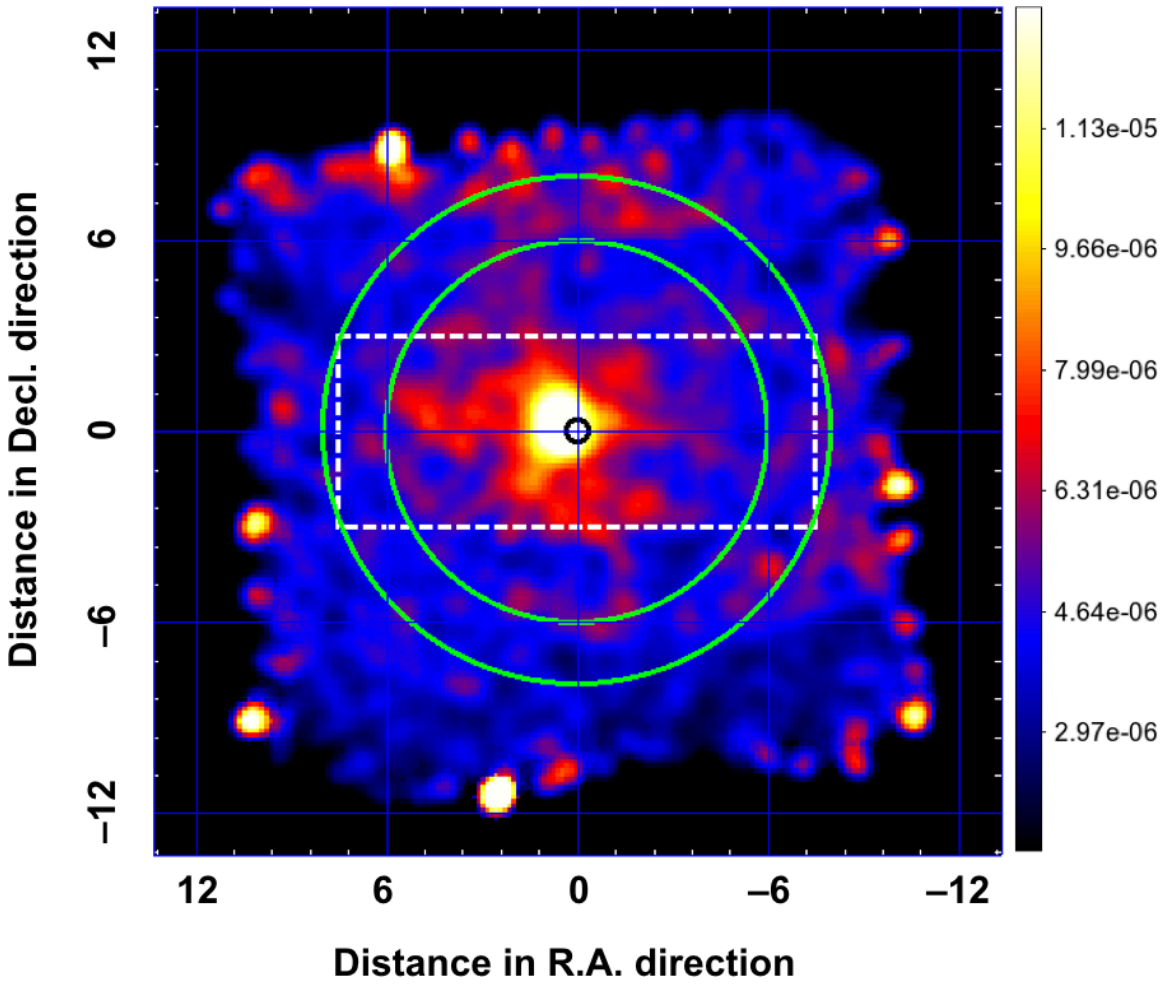

FIGURE 4.16: The same as Figure 4.6 but for the 2012 observation data.

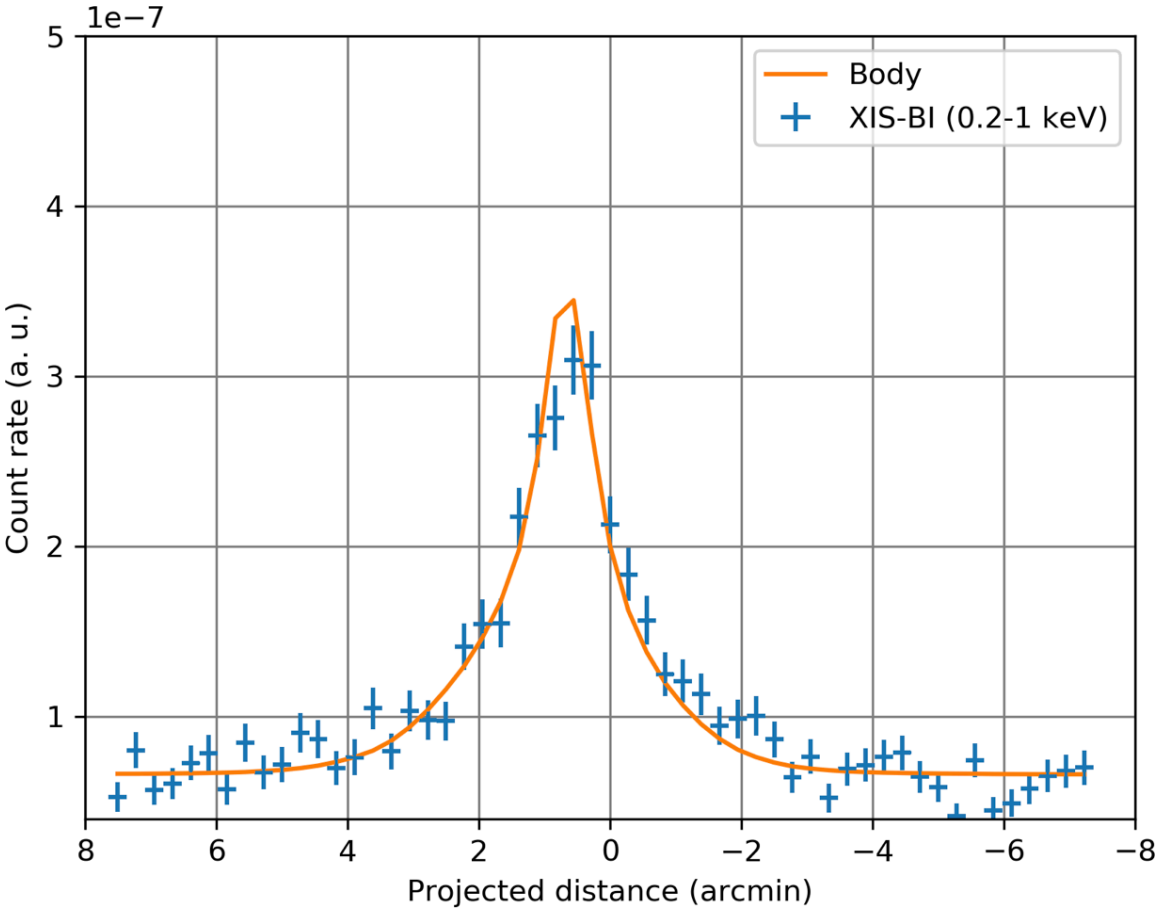

FIGURE 4.17: The same as Figure 4.7 but for the 2012 observation. Jupiter's body has a radius of 21.1 ″, while the elliptical region has semi-axes of 5.6 ′ and 2.4 ′. Reduced χ-square is 1.84.

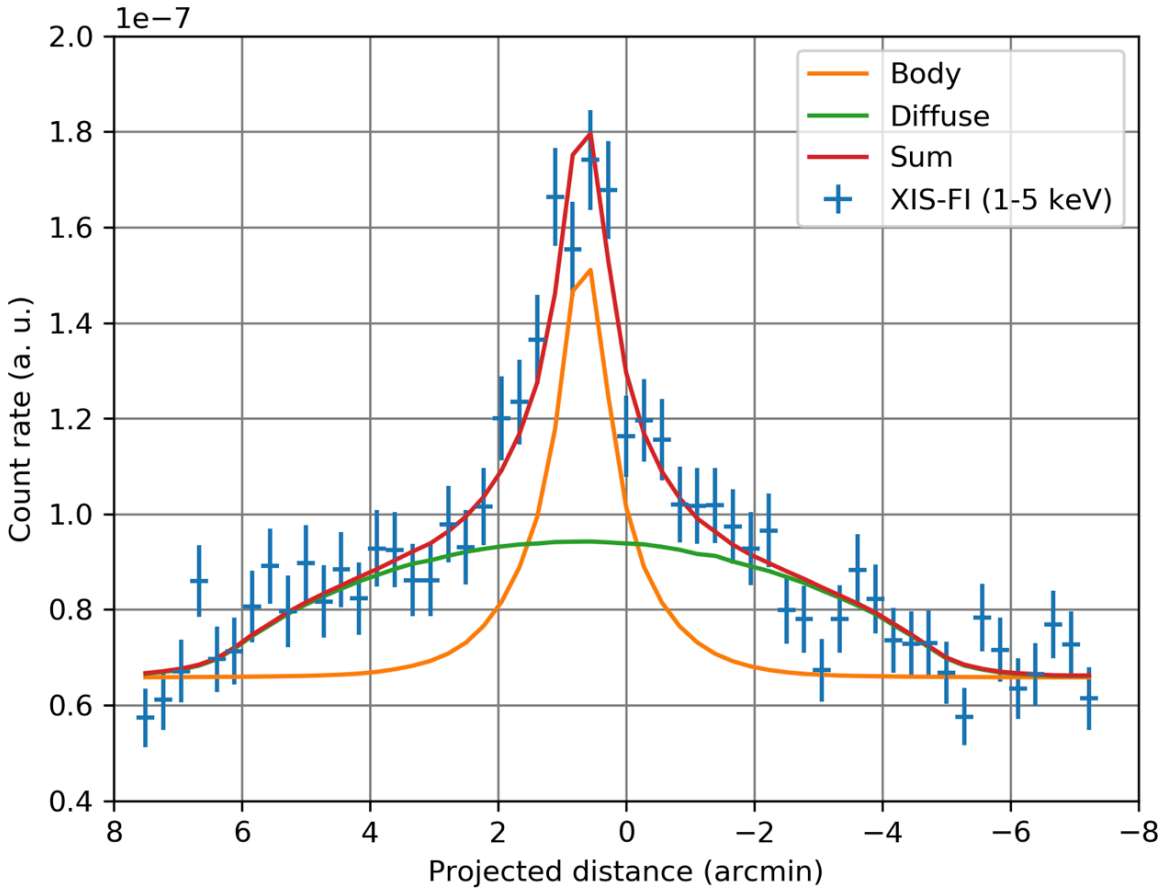

FIGURE 4.18: The same as Figure 4.8 but for the 2012 observation. Jupiter's body has a radius of 21.1 ″, while the elliptical region has semi-axes of 5.6 ′ and 2.4 ′. Reduced χ-square is 1.12.

4.2.2 Spectral analysis

Spectral analysis was carried out to the data for which the 28 point sources were removed and converted to the JRF coordinate in the same manner as for the 2014 observation. The regions used for the source and the background are also the same, namely the 6′ circular and the 6–8′ annular regions. To fit the projected profile, we used elliptically extended ARFs with semi-axes of 5.6′ and 2.4′ for the diffuse emission, with point-like circular ARFs with a radius of 21.1″ (1 R_J) for Jupiter's body.

Spectral fits

The spectra thus obtained are shown in Figure 4.19. Comparison with the XIS spectrum in 2014, the CX lines in 0.5–0.7 keV are less significant. However, this spectrum shows a thermal emission peaked around 0.8–0.9 keV with several emission lines in 1–2 keV, and also a hard continuum extending up to >5 keV. Emission below 0.5 keV is likely to be a CX component. The spectral model consists of the following components: four Gaussians, an APEC model peaked near 0.8 keV, a thermal bremsstrahlung in the range <0.5 keV, so using the point-like ARFs, and a power-law model for the hard band using the extended ARFs. The last component represents the diffuse emission including the auroral non-thermal emission. Because of the statistical quality, the four Gaussians had their center energies fixed at 0.57, 0.65, 1.35, and 1.86 keV in the same way as for the *XMM-Newton* EPIC data analysis. The former two lines represent the CX emission of O_{VII} and $O_{VIIILy\alpha}$ from Jupiter's aurorae, whereas the latter two are Mg_{XI} and Si_{XIII} lines in the scattered solar coronal emission by Jupiter's disk.

Table 4.6 summarizes the best-fit parameters and 90% confidence errors. The whole spectrum can be reproduced with similar parameters as those in 2014. The temperature of the APEC model is 0.64 keV and corresponds well with the solar coronal temperature. The APEC model shows almost the same normalization as for the 2014 *Suzaku* XIS spectrum. The bremsstrahlung temperature is also consistent with the result of the 2014 *Suzaku* XIS and *XMM-Newton* EPIC observations. The power-law slope is quite flat with $\Gamma = 0.87^{+0.30}_{-0.32}$ implying non-thermal emission as in the 2014 case.

Flux & luminosity

Similarly to the 2014 analysis, the flux and luminosity are estimated. The fluxes in 0.2–1 and 1–5 keV are $(29.3 \pm 1.6) \times 10^{-14}$ and $(11.1 \pm 0.8) \times 10^{-14}$ erg cm^{-2} s^{-1}, respectively. The corresponding luminosities are $(18.2 \pm 0.9) \times 10^{15}$ and $(6.7 \pm 0.5) \times 10^{15}$ erg s^{-1} in 0.2–1 and 1–5 keV, respectively. In the hard band, we use the D/B ratio, 1.73 ± 0.24, from the projection profile, and estimate the individual contributions from Jupiter's body and the diffuse emission as $(2.5 \pm 0.3) \times 10^{15}$ and $(4.4 \pm 0.8) \times 10^{15}$ erg s^{-1}, respectively.

4.3 2006 observation by *Suzaku*

The 2006 observation log is shown in Table 4.7. The net exposure was 158.6 ks. The solar activity was near its minimum in the 23rd solar cycle. Ezoe, Ishikawa, Ohashi, Miyoshi, et al. (2010) detected the

TABLE 4.6: Best-fit parameters (and their 90% confidence errors) for the *Suzaku* XIS FI (0.75–7 keV) and BI (0.2–3 keV) spectra of the extended emission region in 2012.

Body	APEC[a]	kT[b]	Norm.[c]
		$0.64^{+0.09}_{-0.08}$	$29.5^{+4.9}_{-5.0}$
	Gaussian[d]	Line energy[e]	Flux[f]
		0.57 (fixed)	$28.1^{+16.0}_{-16.0}$
		0.65 (fixed)	$15.2^{+7.4}_{-7.4}$
		1.35 (fixed)	$0.6^{+1.0}_{-0.6}$
		1.86 (fixed)	$0.6^{+1.2}_{-0.6}$
	Bremss.	kT[b]	Norm.[c]
		$0.09^{+0.04}_{-0.03}$	$2794.6^{+12618.8}_{-1717.1}$
Diffuse	Power-law	Γ (Photon index)	Norm.[c]
		$0.87^{+0.30}_{-0.32}$	$12.4^{+5.6}_{-4.5}$
	χ^2/d.o.f[g]	17.71 / 29	

[a] APEC abundance parameter is set by `aspl` (Asplund et al., 2009).
[b] APEC or bremsstrahlung temperature in keV.
[c] Normalization in units of 10^6 photons cm^{-2} s^{-1} keV^{-1}.
[d] The widths of Gaussians are fixed at 0.01 keV in the fits.
[e] Energy of the emission line features in keV.
[f] Total flux in the line in units of 10^6 photons cm^{-2} s^{-1}.
[g] χ^2 value and degrees of freedom.

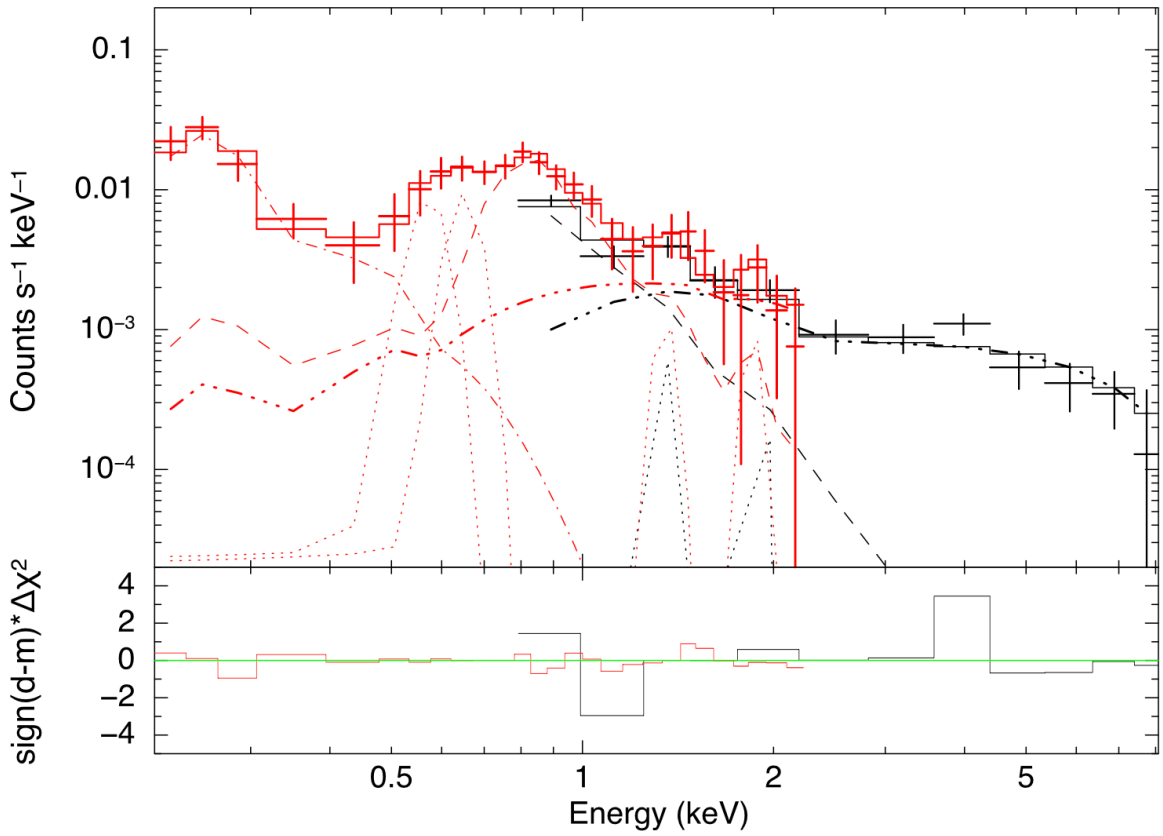

FIGURE 4.19: The same as Figure 4.12 but for the 2012 observation, compared with the best-fit models summarized in Table 4.6 (solid lines).

Jovian diffuse hard X-ray emission from this observation. In order to treat all the data in a uniform way, the data were processed again here with the same procedure as described in this chapter.

TABLE 4.7: The same as Table 4.5 but in 2006.

Obs. ID	Line of Sight (R.A., Decl.)	Obs. date (start)	(end)	Exposure (ks)
401001010	226.5694, −16.1887	2006-02-24T18:20:39	2006-02-25T19:03:24	37.8
401001020	226.5948, −16.1928	2006-02-25T19:03:33	2006-02-26T19:03:24	37.7
401001030	226.6157, −16.1957	2006-02-26T19:03:29	2006-02-27T20:38:19	40.8
401001040	226.6349, −16.1983	2006-02-27T20:38:24	2006-02-28T23:00:19	42.3

4.3.1 Image analysis

Mosaic image

Images in 0.2–1 and 1–5 keV with the J2000.0 coordinate are shown in Figure 4.20 and Figure 4.21. Since XIS 2 was still operational in this period, the hard band FI image (Figure 4.21) is based on all the FI CCDs. The exposure is corrected with exposure maps for individual detectors generated by `xisexpmapgen`. Jupiter moved from right to left and a faint trial was detected along the path (especially in the soft band).

Applying `wavdetect` and visual inspection to the hard band image, a total of 27 point sources were identified beside Jupiter's trail. The point sources are shown by green circles with a red slash in Figure 4.20 and Figure 4.21. These point sources were removed using circular regions with a diameter of $>2'$ as before.

JRF image

We converted the events into the JRF coordinate with `attitune` and `aeattcor` in the same way as for the 2014 and 2012 observations. Figure 4.22 and Figure 4.23 show the images in the JRF coordinate after the exposure correction. Jupiter's movement in the 8 s interval was only $0.007''$.

As discovered by Ezoe, Ishikawa, Ohashi, Miyoshi, et al. (2010), we confirmed the extended hard X-ray emission around Jupiter, whereas the soft X-ray emission was concentrated to *Suzaku*'s HPD. Since the JRF image is generated by a different method in Ezoe, Ishikawa, Ohashi, Miyoshi, et al., 2010, the agreement of the image indicates that the present JRF conversion method is valid. The hard band image shows that Jupiter's body gives a somewhat weaker contribution as compared with the 2014 and 2012 observations.

Projection profile

Projection profile is produced along the horizontal axis of the JRF images for the data in the white dashed square region, and contributions of the different emission components are evaluated. The profiles in the soft and hard bands are shown in Figure 4.24 and Figure 4.25, respectively. The data are binned in 16×16 pixels without smoothing.

Similarly to the 2014 and 2012 observations, the model consists of a circle with a radius of $1\,R_J = 19.9''$ for the body emission and an ellipse, for the extended emission, with semi-axes changed around $4'$ and $1'$ with a pitch of $5''$ along each axis. We fitted the model to the data by adjusting the ellipse size, normalization, and center position.

The hard band profile is marginally reproduced by this model consisting of the small circular emission and the uniform elliptical emission with semi-axes $4.2'$ and $1.2'$ corresponding to $12.6\,R_J$ and $3.5\,R_J$, respectively. The soft band profile is roughly consistent with the concentrated emission from Jupiter's body. These features are similar to those for the 2014 and 2012 observations. However, there is a small excess in the right side of the center in the soft band image. This may indicate emission from the IPT as discussed by Ezoe, Ishikawa, Ohashi, Miyoshi, et al. (2010) and reported by R. F. Elsner, Gladstone, et al. (2002). We obtained the D/B ratio to be 6.16 ± 1.78.

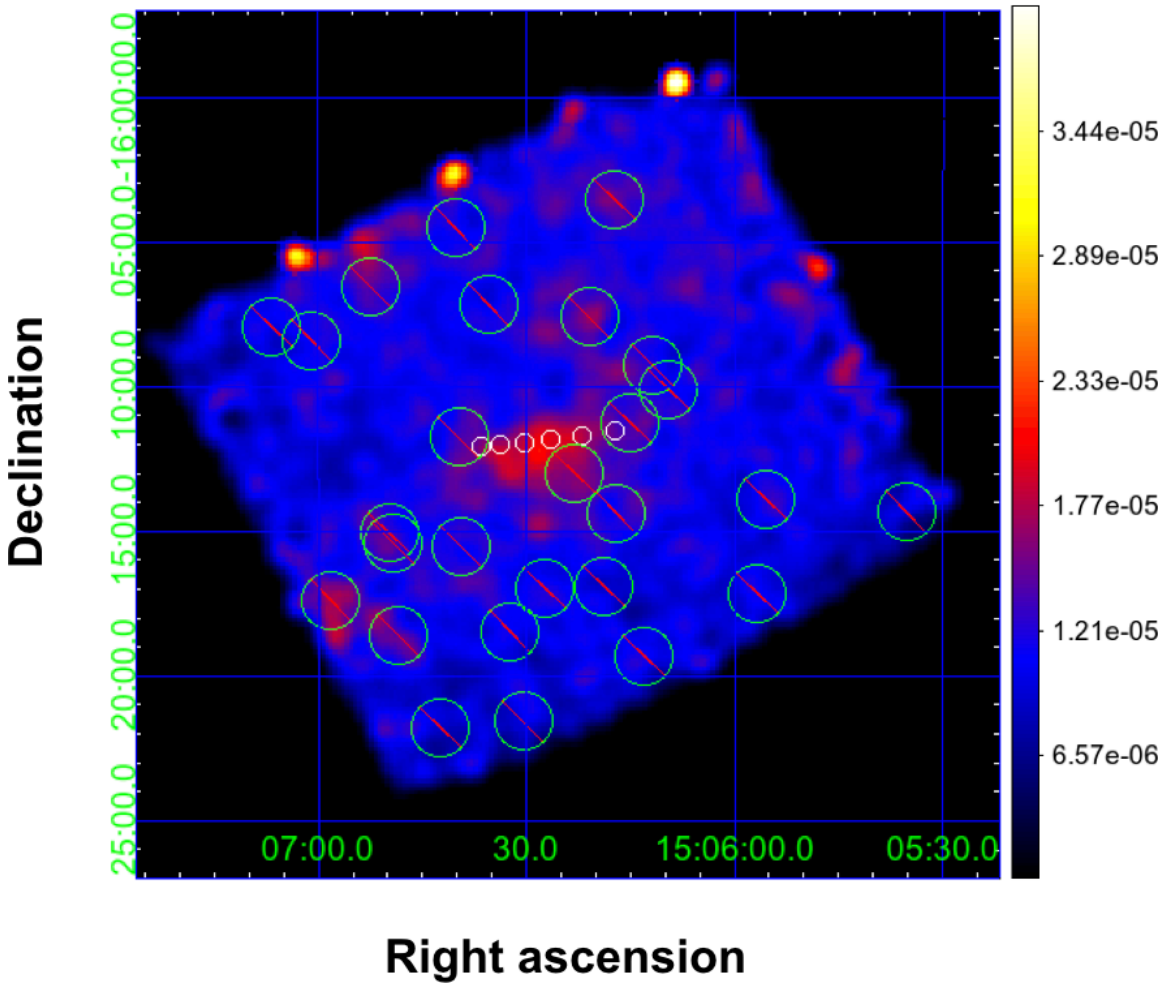

FIGURE 4.20: The same as Figure 4.3 but for the 2006 observation data.

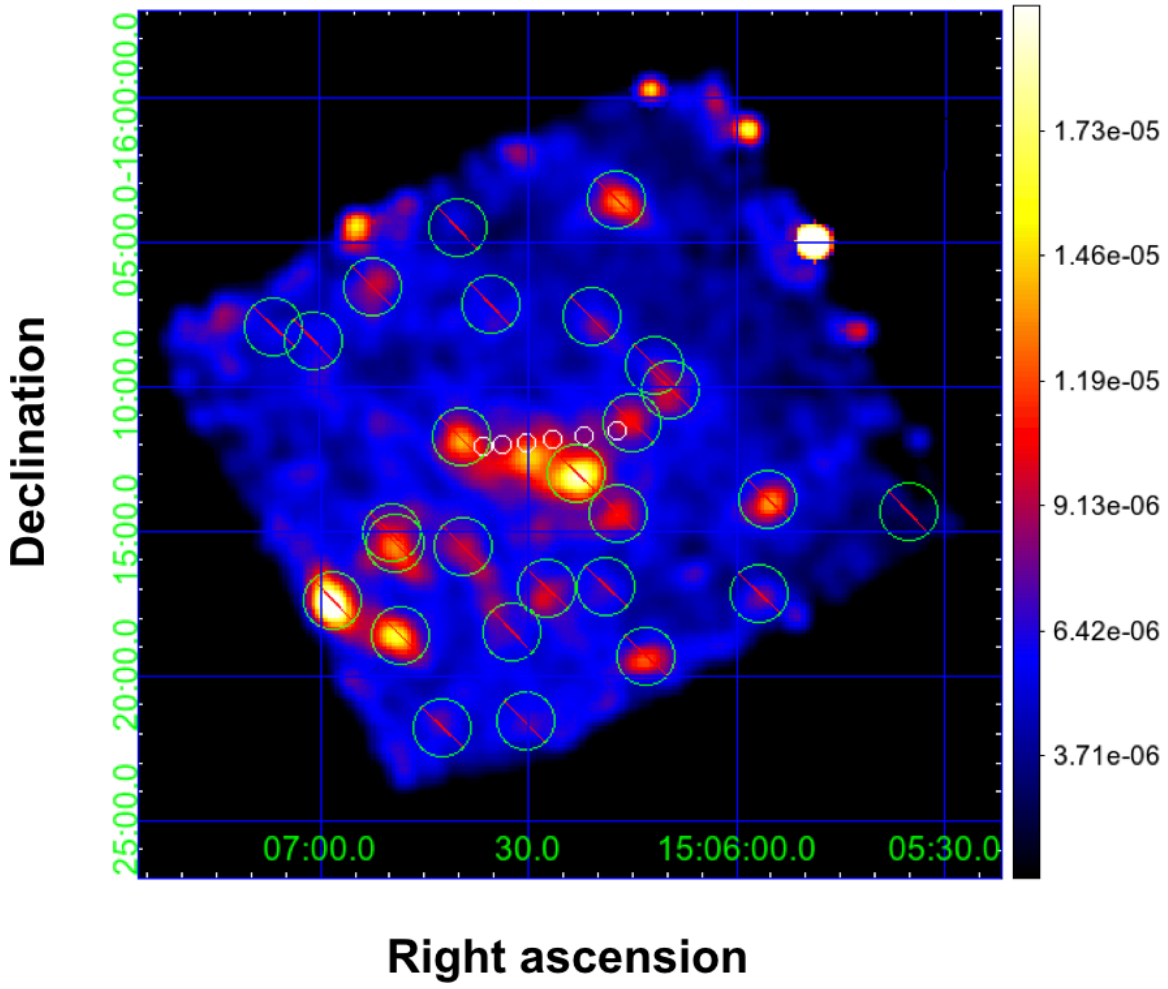

FIGURE 4.21: The same as Figure 4.4 but for the 2006 observation data.

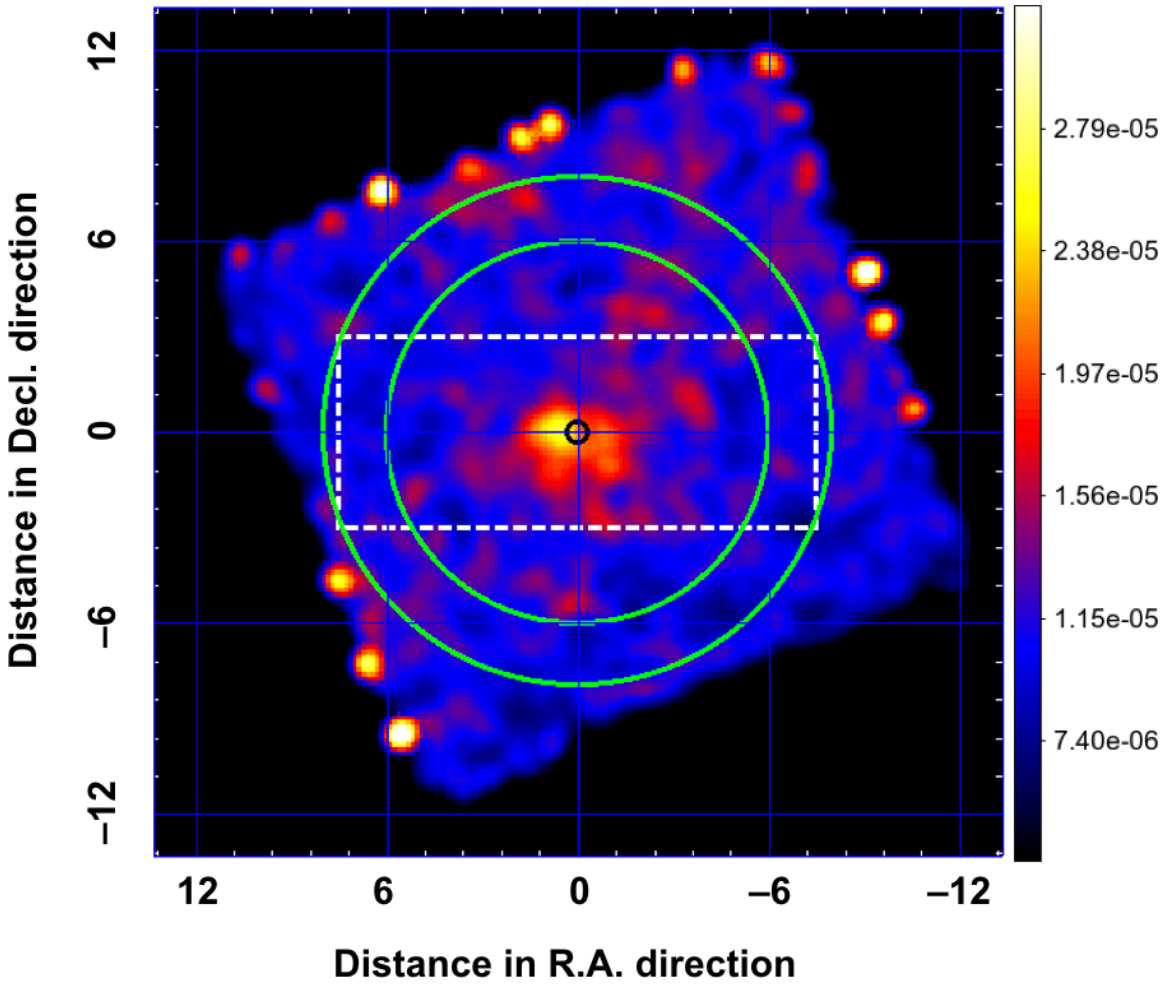

FIGURE 4.22: The same as Figure 4.5 but for the 2006 observation data.

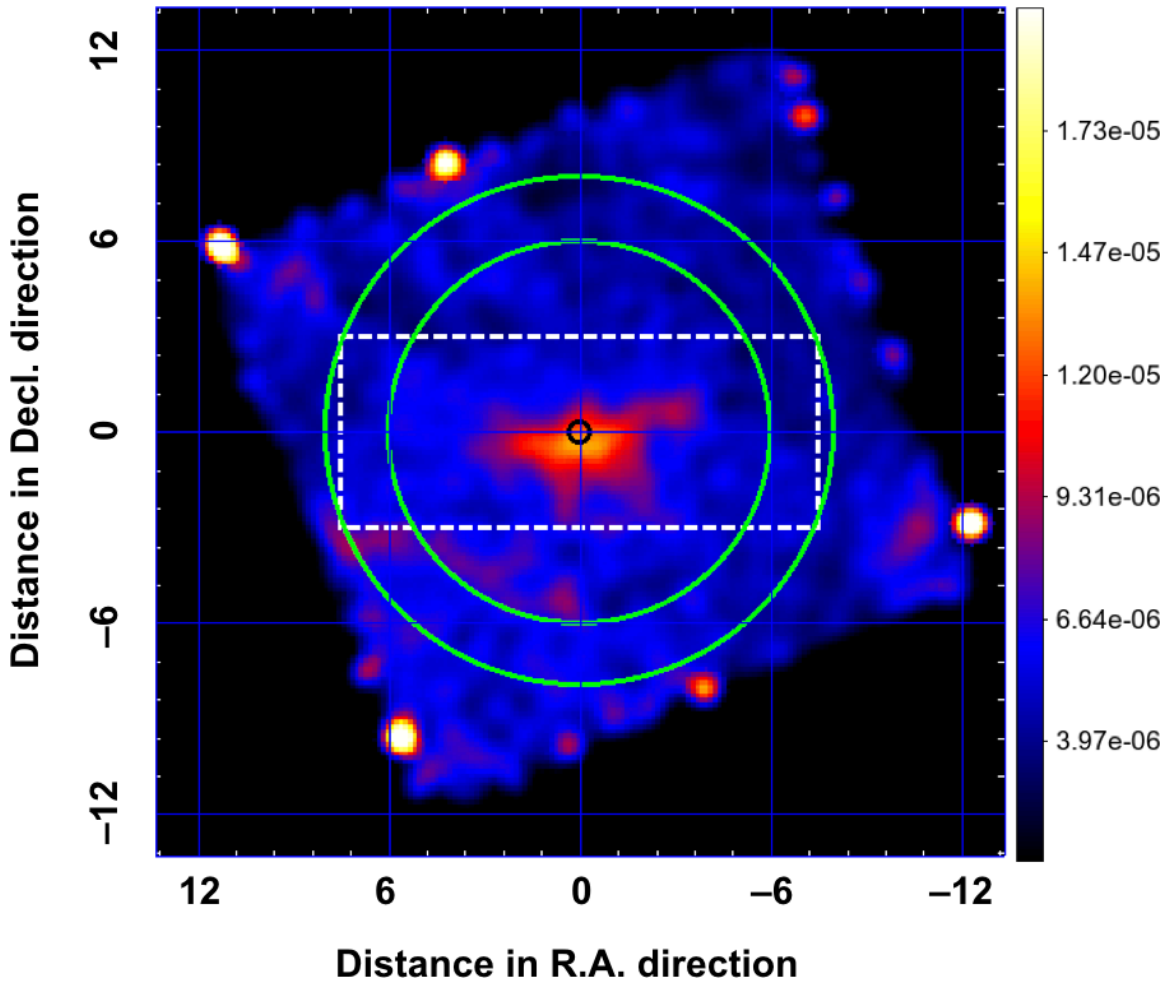

FIGURE 4.23: The same as Figure 4.6 but for the 2006 observation data.

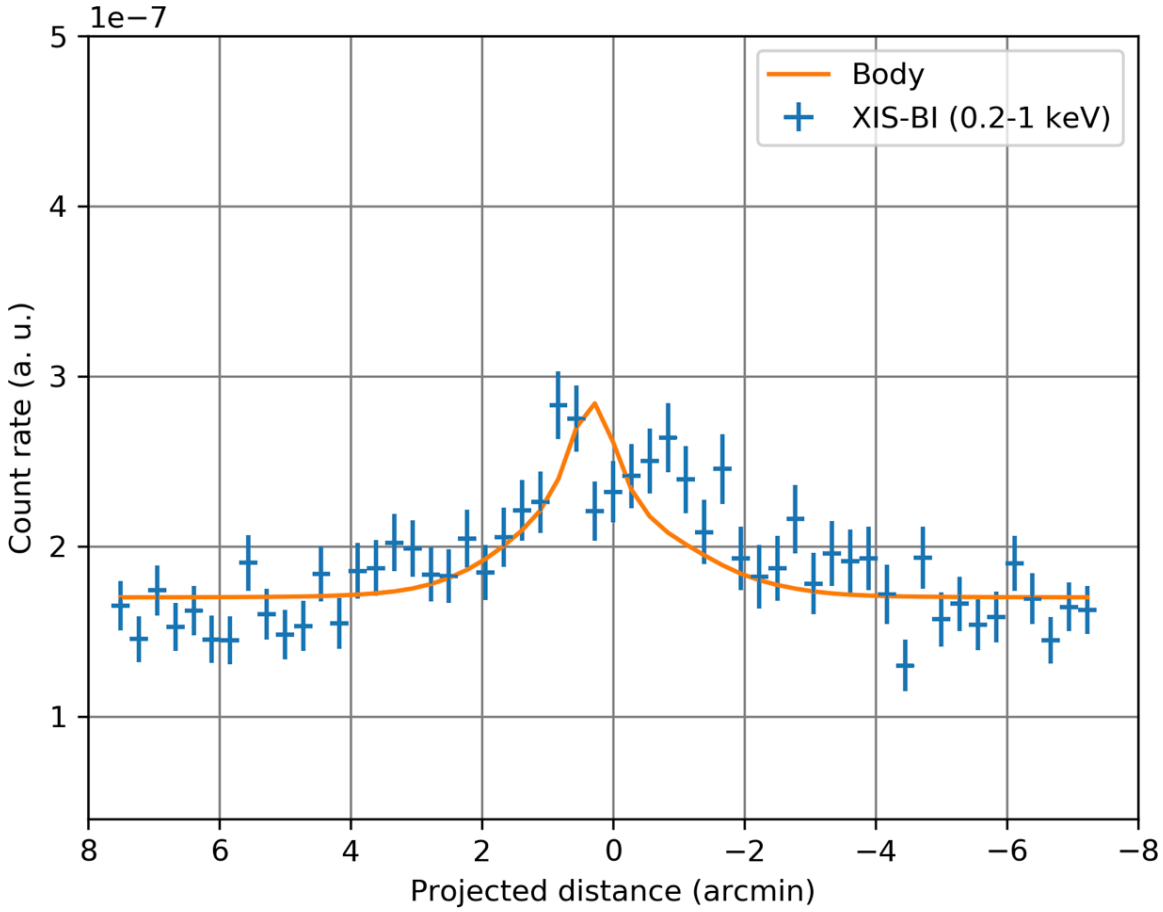

FIGURE 4.24: The same as Figure 4.7 but for the 2006 observation. Jupiter's body has a radius of 19.9″, while the elliptical region is shaped with semi-axes of 4.2′ and 1.2′. Reduced χ-square is 1.87.

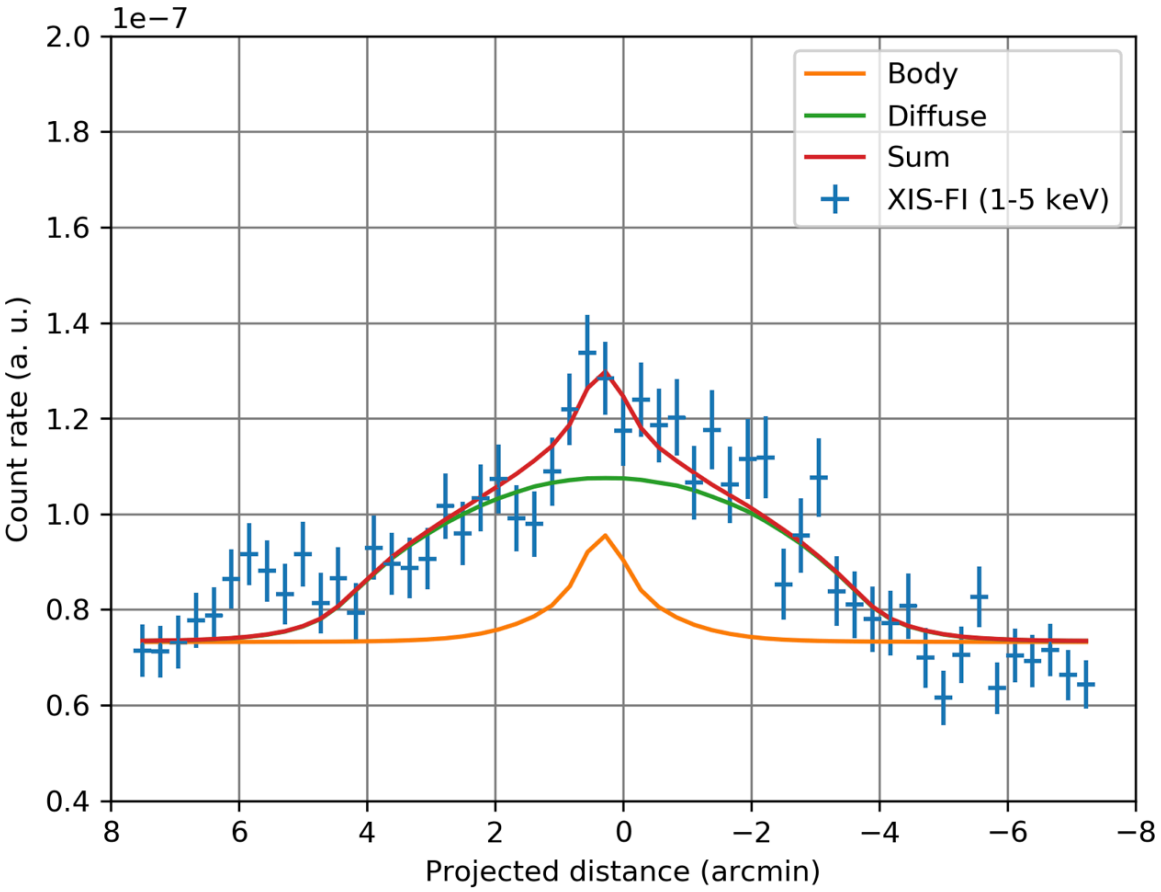

FIGURE 4.25: The same as Figure 4.8 but for the 2006 observation. Jupiter's body has a radius of 19.9″, while the elliptical region is shaped with semi-axes of 4.2′ and 1.2′. Reduced χ-square is 1.39.

4.3.2 Spectral analysis

Spectral analysis was carried out to the data for which the 27 point sources were removed and conversion to JRF coordinate was made in the same way for other observations. Extracted regions for the source and the background are also the same, i.e., 6′ circular and 6–8′ annular regions. From the projection profile fit, we use elliptically extended ARFs with semi-axes 4.2′ and 1.2′ for the diffuse emission while point-like ARFs with a radius of 19.9″ (1 R_J) for Jupiter's body.

Spectral fits

The BI and FI spectra are shown in Figure 4.26. The soft band emission is slightly weaker than those in the 2014 and 2012 observations, as indicated by the image analysis. In contrast, the hard band intensity is similar to those in the other observations. The fitted model is almost the same as the 2012 one, but the cool bremsstrahlung is replaced by a Gaussian function with a center energy 0.25 keV. This is because the spectrum does not show continuum emission below <0.5 keV. We fit with all the line energies fixed at 0.25, 0.57, 0.65, 1.35, and 1.86 keV and determined the APEC temperature. Then, we allowed the center energies of the former three lines to be free and obtained the best-fit model.

Table 4.8 summarizes the best-fit parameters and 90% confidence errors. The temperature of the APEC model is $0.73^{+0.13}_{-0.17}$ keV which is consistent with the solar coronal temperature. The normalization of the APEC model is lower than the 2014 and 2012 levels, likely to correlate with the decrease of the solar activity. The line energies are $0.25^{+0.01}_{-0.03}$, 0.55 ± 0.02, and 0.68 ± 0.02 keV, which presumably correspond to line complexes from C_{VI}, ionized Mg, Si, and S, O_{VII}, and O_{VIII} ions, respectively. The power-law slope $\Gamma = 0.65^{+0.36}_{-0.40}$, again, implies non-thermal emission.

Flux & luminosity

Fluxes in 0.2–1 and 1–5 keV are $(11.1 \pm 0.9) \times 10^{-14}$ and $(9.3 \pm 0.7) \times 10^{-14}$ erg cm^{-2} s^{-1}, respectively. Corresponding luminosities are $(7.8 \pm 0.7) \times 10^{15}$ and $(6.5 \pm 0.5) \times 10^{15}$ erg s^{-1}, respectively. In the hard band, the D/B ratio is 6.16 ± 1.78 as obtained from the projection profile and contributions of Jupiter's body and the diffuse emission are estimated as $(0.9 \pm 0.2) \times 10^{15}$ and $(5.6 \pm 2.2) \times 10^{15}$ erg s^{-1}, respectively.

4.4 Summary

The fluxes and luminosities obtained from three observations in this chapter are listed in Table 4.9. By combining the imaging and spectral analyses (and based on the coordinated observation with *XMM-Newton*), the fluxes and luminosities in the 1–5 keV of the emission from Jupiter's body and the diffuse emission are obtained separately.

Finally, we plotted a variation of each of the obtained X-ray luminosity and compared them to that of the solar activity as shown in Figure 4.27. In this figure, we described the results of the 2006 observations as unity and calculated ratios of the other results to it. As the solar activity increased from 2006 to 2012 and 2014, the soft and hard luminosities of the emission from Jupiter's body clearly increased by a factor of 2–5. The soft X-rays from Jupiter's body consist of the solar

TABLE 4.8: Best-fit parameters (and their 90% confidence errors) for the *Suzaku* XIS FI (0.7–7 keV) and BI (0.2–2 keV) spectra of the extended emission region in 2006.

Body	APEC[a]	kT[b]	Norm.[c]
		$0.73^{+0.13}_{-0.17}$	$15.4^{+4.0}_{-4.2}$
	Gaussian[d]	Line energy[e]	Flux[f]
		$0.25^{+0.01}_{-0.03}$	$96.9^{+264.4}_{-36.8}$
		$0.55^{+0.02}_{-0.02}$	$24.7^{+23.8}_{-15.7}$
		$0.68^{+0.02}_{-0.02}$	$11.9^{+6.7}_{-6.4}$
		1.35 (fixed)	$0.7^{+1.5}_{-0.7}$
		1.86 (fixed)	$1.1^{+1.4}_{-1.1}$
Diffuse	Power-law	Γ (Photon index)	Norm.[c]
		$0.65^{+0.36}_{-0.40}$	$8.4^{+5.4}_{-3.9}$
	χ^2/d.o.f[g]	29.41 / 20	

[a] APEC abundance parameter is set by `aspl` (Asplund et al., 2009).
[b] APEC temperature in keV.
[c] Normalization in units of 10^6 photons cm^{-2} s^{-1} keV^{-1}.
[d] The widths of Gaussians are fixed at 0.01 keV in the fits.
[e] Energy of the emission line features in keV.
[f] Total flux in the line in units of 10^6 photons cm^{-2} s^{-1}.
[g] χ^2 value and degrees of freedom.

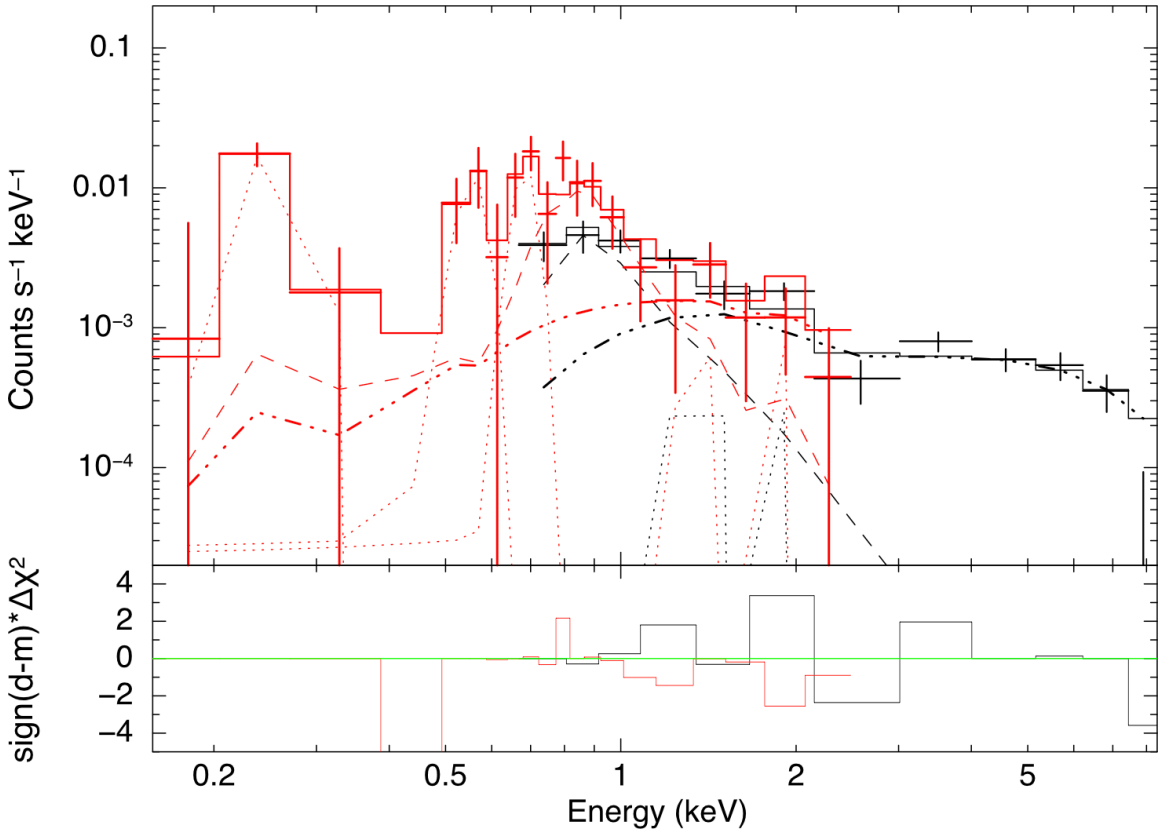

FIGURE 4.26: The same as Figure 4.12 but for the 2006 observation, compared with the best-fitting models summarized in Table 4.8 (solid lines).

X-ray scattering and the CX interaction of heavy ions which originate in not only IPT or the Jovian magnetosphere but also solar winds. Thus, we considered that it was likely to depend on the solar activity of a certain degree. The hard X-rays from Jupiter's body consist of the bremsstrahlung by energetic keV electrons in the magnetosphere. Branduardi-Raymont, Bhardwaj, R. F. Elsner, et al. (2007) have implied that the hard bremsstrahlung is maybe driven by the solar activity. We thought that our results also supported the possibility.

On the other hand, the hard luminosity of the diffuse emission was relatively stable within 20–30% at most, and did not simply depend on the solar activity. This variability was marginally consistent with that of the Jovian synchrotron radio emission which shows a tendency to be out of sync with the solar activity after 1994 when Comet Shoemaker-Levy 9 impacted on Jupiter (Bolton, Janssen, et al., 2002; Han et al., 2018; Santos-Costa et al., 2008). In the following chapter, we discuss about the diffuse hard X-ray emission, which mechanisms emit the diffuse X-rays, referring to the possibility of the inverse Compton scattering hypothesis proposed by Ezoe, Ishikawa, Ohashi, Miyoshi, et al., 2010.

TABLE 4.9: X-ray fluxes and luminosities of Jupiter's X-rays observed by *Suzaku* in 2006, 2012, and 2014. Errors are 68% confidence range.

Obs. year	Energy range[a]	Flux[b]	Luminosity[c]
2006	0.2–1.0	11.1 ± 0.9	7.8 ± 0.7
	1.0–5.0	9.3 ± 0.7	6.5 ± 0.5
	Body[d]	—	0.9 ± 0.2
	Diffuse[d]	—	5.6 ± 2.2
2012	0.2–1.0	29.3 ± 1.5	18.2 ± 0.9
	1.0–5.0	11.1 ± 0.8	6.9 ± 0.5
	Body[d]	—	2.5 ± 0.3
	Diffuse[d]	—	4.4 ± 0.8
2014	0.2–1.0	25.5 ± 1.6	21.0 ± 1.3
	1.0–5.0	13.2 ± 1.1	10.8 ± 0.9
	Body[e]	5.5 ± 0.4	4.5 ± 0.3
	Diffuse[e]	7.7 ± 1.1	6.3 ± 0.9

[a] Energy in units of keV.
[b] Flux in units of 10^{-14} erg cm^{-2} s^{-1}.
[c] Luminosity in units of 10^{15} erg s^{-1}, calculated with a distance to Jupiter listed in Table 4.1.
[d] Calculated by using the D/B ratio resulted in analyses of projection profiles.
[e] Calculated by using each model parameter of spectral fits to the *Suzaku* XIS data combining the *XMM-Newton* EPIC data.

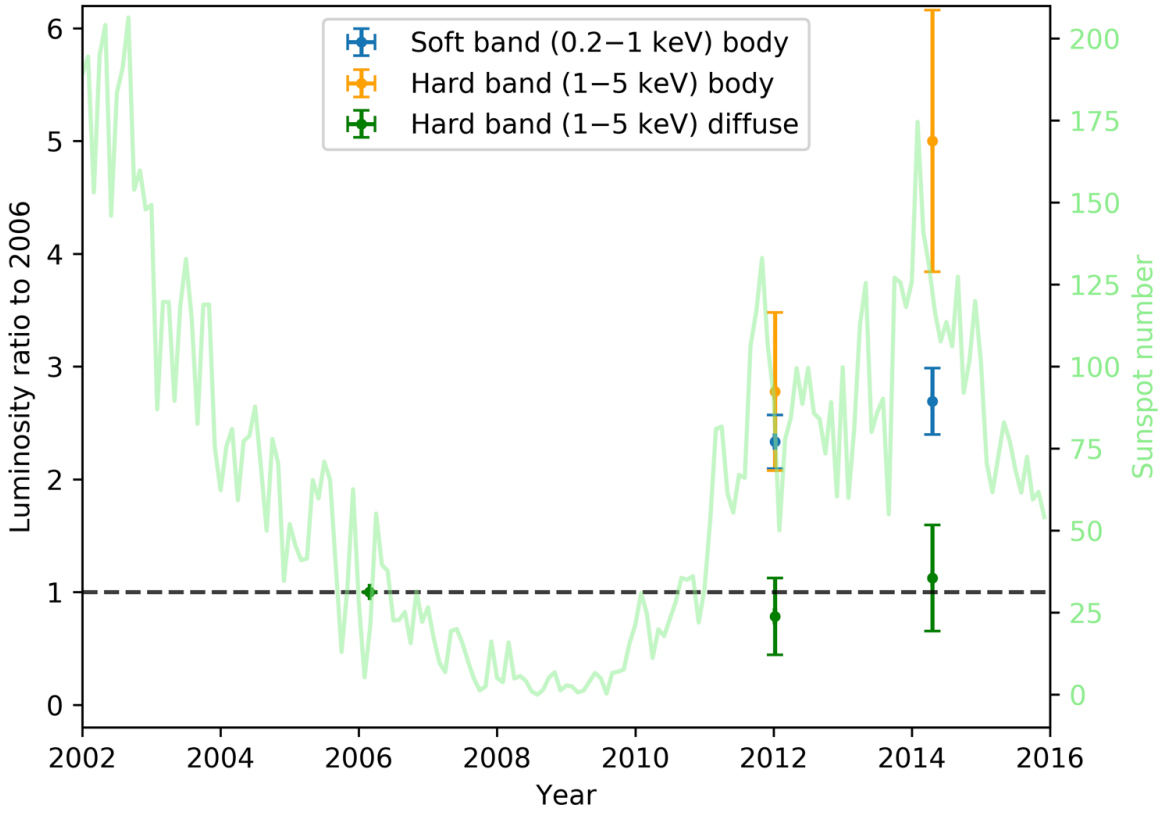

FIGURE 4.27: Variations of the *Suzaku* observed X-ray luminosities of the emission from Jupiter's body in soft (0.2–1 keV) and hard (1–5 keV) bands and of the diffuse emission in the hard band, compared to that of the solar activity. Each colored mark indicates each luminosity as shown in the legend. Vertical axes are luminosity ratios in the left side with each luminosity of the 2006 observation described as unity and sunspot number in the right side which is the same as Figure 4.2.

Chapter 5

Discussion

5.1 Origin of Jovian diffuse hard X-ray emission

In this section, we look into the origin of the Jovian diffuse hard X-ray emission. We can consider here 5 candidates for its origin as follows; (i) Cosmic X-ray Background (CXB), (ii) scattered solar X-rays, (iii) synchrotron radiation of high energy electrons in the Jovian magnetosphere, (iv) bremsstrahlung radiation by electrons which have non-thermal energy distribution, and (v) inverse Compton scattering of solar visible photons by high energy electrons. We will address each of the above possibilities in the following sections. Note that the spectrum of the extended emission could be well-fitted by the flat power-law model, suggesting that a non-thermal mechanism is working. In this view, the latter three possibilities will need closer attention.

5.1.1 Cosmic X-ray Background

In X-ray observations over a certain solid angle, the incoming photons inevitably include background radiation, consisting of origins such as Local Hot Bubble (LHB), geocoronal SWCX, Milky-Way Halo (MWH), and Cosmic X-ray Background (CXB). These radiations have spatial structures but are known to come from all directions in the sky. In the 1–5 keV band, CXB contributes most significantly among these components.

As shown in Figure 4.6, Figure 4.16, and Figure 4.23, the structure of the hard emission around Jupiter is described by a uniform elliptical shape which is extended preferentially along the horizontal axis, as seen most clearly in the 2006 observation. Such a structure is not expected if the emission is due to CXB, which should be highly uniform over the whole sky. However, since the observed data were superposed through the JRF-correction by `attitune`, we need a careful examination to see if any spurious feature might be produced. We, then, generate a simulated CXB image and compare them with the observed one to see how the uniform emission would look like. In generating the CXB image, we did not employ the known intensity and spectral parameters of CXB but the observed values from the spectral fits for the 6–8′ annular region in each observation. This should give us a realistic estimation how the actual sky background would be observed if they are spatially uniform. Even when Jupiter's extended X-rays might have been much weaker than the CXB component which takes the known spectral parameters, our estimation here can be treated as a case that Jupiter's X-rays do contribute at a certain level.

Figure 5.1 shows the XIS FI and BI spectra in the 2014, 2012, and 2006 observations, respectively. The background components, i.e., LHB, geocoronal SWCX, MWH, and CXB, were included

in the fit assuming the spectra with APEC, Gaussian function, APEC, and a power-law function, respectively. The models for MWH and CXB were multiplied by the same photoelectric absorption with $N_{\rm H}$ for the observed direction. Table 5.1 summarizes the best-fit parameters for each observation. The $N_{\rm H}$ value was fixed at the values obtained from NASA's web interface tool [1] for the line of sight direction of each observation. The photon index Γ was also fixed at 1.41 suggested by Kushino et al. (2002). We created each ARF for a circular area with a radius of 20′ which corresponded to $\sim 1.06 \times 10^{-4}$ sr. This area is larger than the *Suzaku* XIS field of view ($17.8' \times 17.8'$) and can be regarded as practically covering the field uniformly. The obtained fluxes in 2–10 keV were $(5.22 \pm 0.06) \times 10^{-8}$, $(5.43 \pm 0.09) \times 10^{-8}$ and $(4.56 \pm 0.04) \times 10^{-8}$ erg cm^{-2} s^{-1} sr^{-1} for the 2014, 2012, and 2006 observations, respectively. These values are comparable to the past results, e.g., by Kushino et al. (2002).

Using `xissim` (version 2010-11-05) along with the obtained spectral parameters and the JRF-corrected attitude files, we generated simulated CXB images in 1–5 keV in the JRF coordinate. They actually contain other components as LHB, MWH, and SWCX, but CXB is dominant in the energy range and we call it this way for convenience. We also produced a ratio image which was the observed image divided by the simulated CXB image, as shown in Figure 5.2, Figure 5.3, and Figure 5.4. All the ratio images indicate a feature extending along the horizontal axis and suggest that the observed diffuse emission is not expressed by the CXB radiation.

5.1.2 Solar X-ray scattering

It is known that all of the solar system objects basically reflect the solar photons on their surface where the particle density is high (e.g., Bhardwaj, R. F. Elsner, Randall Gladstone, et al., 2007). Actually, a part of soft X-rays from Jupiter's body is explained by the solar X-ray scattering on Jupiter's surface. We can eliminate a probability that the diffuse emission is caused by the solar X-ray scattering, based on the consideration that the efficiency of the scattering simply depends on the density of the scatterer.

According to Bagenal et al. (2004), the particle density in the Jovian magnetosphere is estimated as $\sim 2 \times 10^{3}$ cm^{-3} at IPT (maximum) and $\sim 2 \times 10^{-1}$ cm^{-3} at 35 $R_{\rm J}$, respectively. The density is significantly lower than that of Jupiter's surface which has a large density of $<1 \times 10^{20}$ cm^{-3} at 1 bar. Assuming that a scattering pass length is 10 $R_{\rm J}$ (=7.1492×10^{10} cm), the scattering column density is estimated with $\sim 1.4 \times 10^{13}$ cm^{-2} at IPT (maximum), which is sufficiently smaller than the reciprocal of the Thomson scattering cross section, $1/\sigma_{\rm T} \sim 1.5 \times 10^{24}$ cm^{-2}. Thus, we can conclude that the scattering efficiency for the solar X-ray photons is too low to explain the emission from the Jovian magnetosphere.

5.1.3 Synchrotron radiation

Synchrotron radiation occurs as a result of interactions of magnetic fields and relativistic electrons. Characteristic energy of the synchrotron radiation depends on the strength of the magnetic field and energy of the electrons. The X-ray image indicates that the hard X-rays are emitted at a distance of >6 $R_{\rm J}$. The magnetic field of the Jovian magnetosphere basically becomes weaker with the distance

[1] https://heasarc.gsfc.nasa.gov/cgi-bin/Tools/w3nh/w3nh.pl

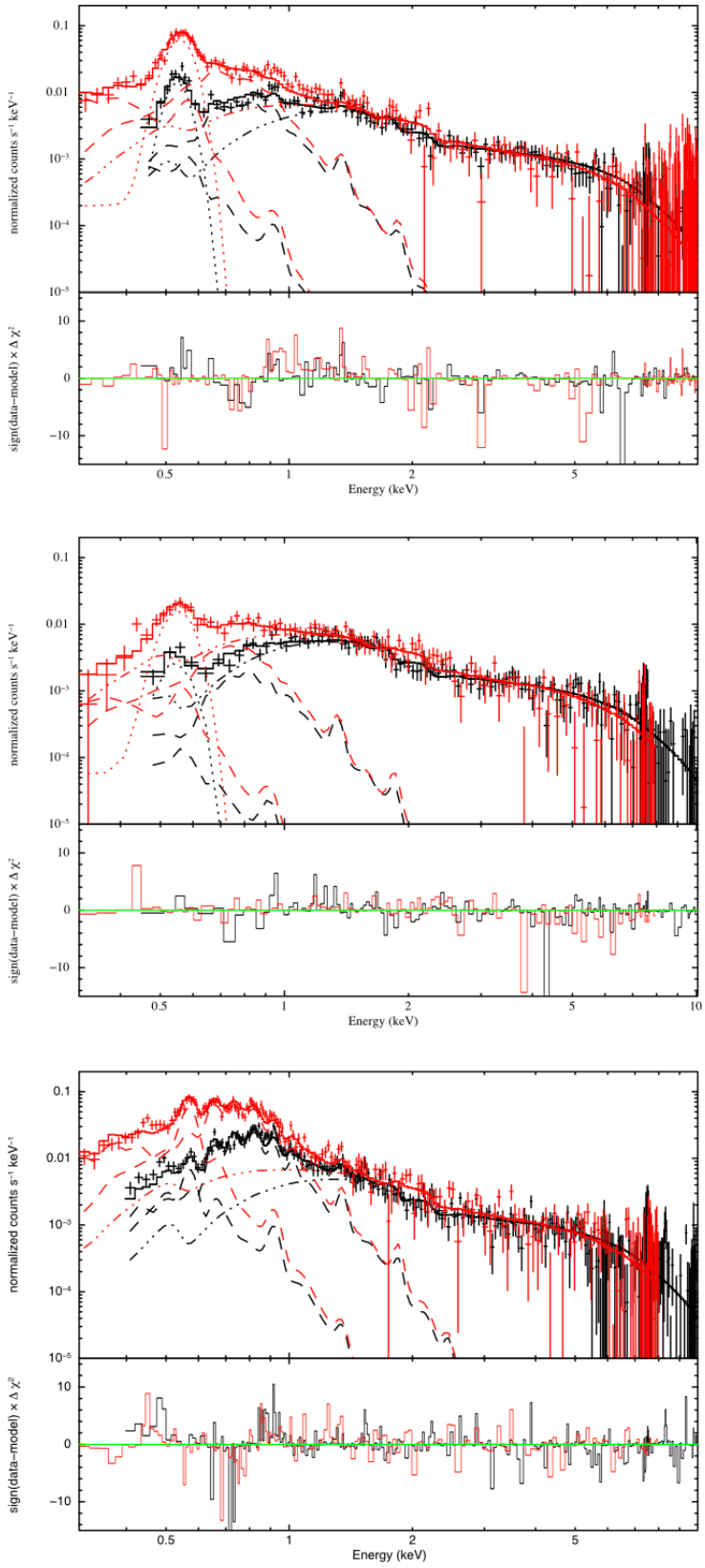

FIGURE 5.1: NXB subtracted FI (black) and BI (red) spectra of the background annular region for the 2014 (top), 2012(middle), and 2006 (bottom) observations, compared with the best-fit models summarized in Table 5.1 (solid lines). Two APEC models, Gaussian, and a power-law function are shown in dashed, dotted, and dash-three-dotted lines, respectively. Energies of the Gaussian lines (dotted curves) are around 0.54 keV, representing a possible geocoronal SWCX line from O_{VII} (not included for the 2006 spectra). Γ of the power-law function (dash-three-dotted curves) is also fixed to the known value.

TABLE 5.1: Best-fit parameters (and their 90% confidence errors) for the *Suzaku* XIS FI (0.4–10 keV) and BI (0.3–8 keV) spectra of the annulus background region in 2006, 2012, and 2014 observations. The model consists of `apec + gaussian + phabs × (apec + power-law)`, corresponding to Local Hot Bubble (LHB), geocoronal SWCX, a photoelectric absorption $N_{\rm H}$ column density, Milky-Way Halo (MWH), and Cosmic X-ray Background, respectively. The $N_{\rm H}$ is fixed at values calculated from NASA's web interface tool. Γ of the power-law function is fixed at 1.41 referring Kushino et al., 2002. The gaussian component is not included in the 2006 spectra.

Model	Parameter	2014	2012	2006
APEC[a]	kT[b]	$0.09^{+0.03}_{-0.03}$	0.1 (fixed)	$0.12^{+0.009}_{-0.007}$
	Norm.[c]	$64.0^{+23.1}_{-28.3}$	$5.6^{+9.6}_{-5.6}$	$33.5^{+5.7}_{-5.7}$
Gaussian	Line energy[d]	$0.54^{+0.003}_{-0.004}$	$0.55^{+0.006}_{-0.006}$	—
	EW[e]	$17.6^{+4.6}_{-6.2}$	$27.5^{+14.5}_{-10.0}$	—
	Flux[f]	$30.6^{+2.9}_{-4.4}$	$10.3^{+1.8}_{-2.0}$	—
Absorption	$N_{\rm H}$[g]	0.087 (fixed)	0.050 (fixed)	0.072 (fixed)
APEC[a]	kT[b]	$0.24^{+0.02}_{-0.01}$	$0.29^{+0.39}_{-0.06}$	$0.29^{+0.008}_{-0.007}$
	Norm.[c]	$29.2^{+4.4}_{-5.0}$	$4.6^{+3.6}_{-2.9}$	$29.1^{+1.7}_{-1.7}$
Power-law	Γ (Photon index)	1.41 (fixed)	1.41 (fixed)	1.41 (fixed)
	Norm.[c]	$8.6^{+0.3}_{-0.3}$	$8.9^{+0.3}_{-0.3}$	$7.5^{+0.3}_{-0.3}$
χ^2/d.o.f[h]		433.19/330	302.62/273	678.35/460

[a] APEC abundance parameter is set by `aspl` (Asplund et al., 2009).
[b] APEC or bremsstrahlung temperature in keV.
[c] Normalization in units of 10^{-4} photons cm^{-2} s^{-1} keV^{-1}.
[d] Energy of the emission line features in keV.
[e] Line equivalent width in eV.
[f] Total flux in the line in units of 10^{-4} photons cm^{-2} s^{-1}.
[g] Equivalent hydrogen column in units of 10^{22} cm^{-2}.
[h] χ^2 value and degrees of freedom.

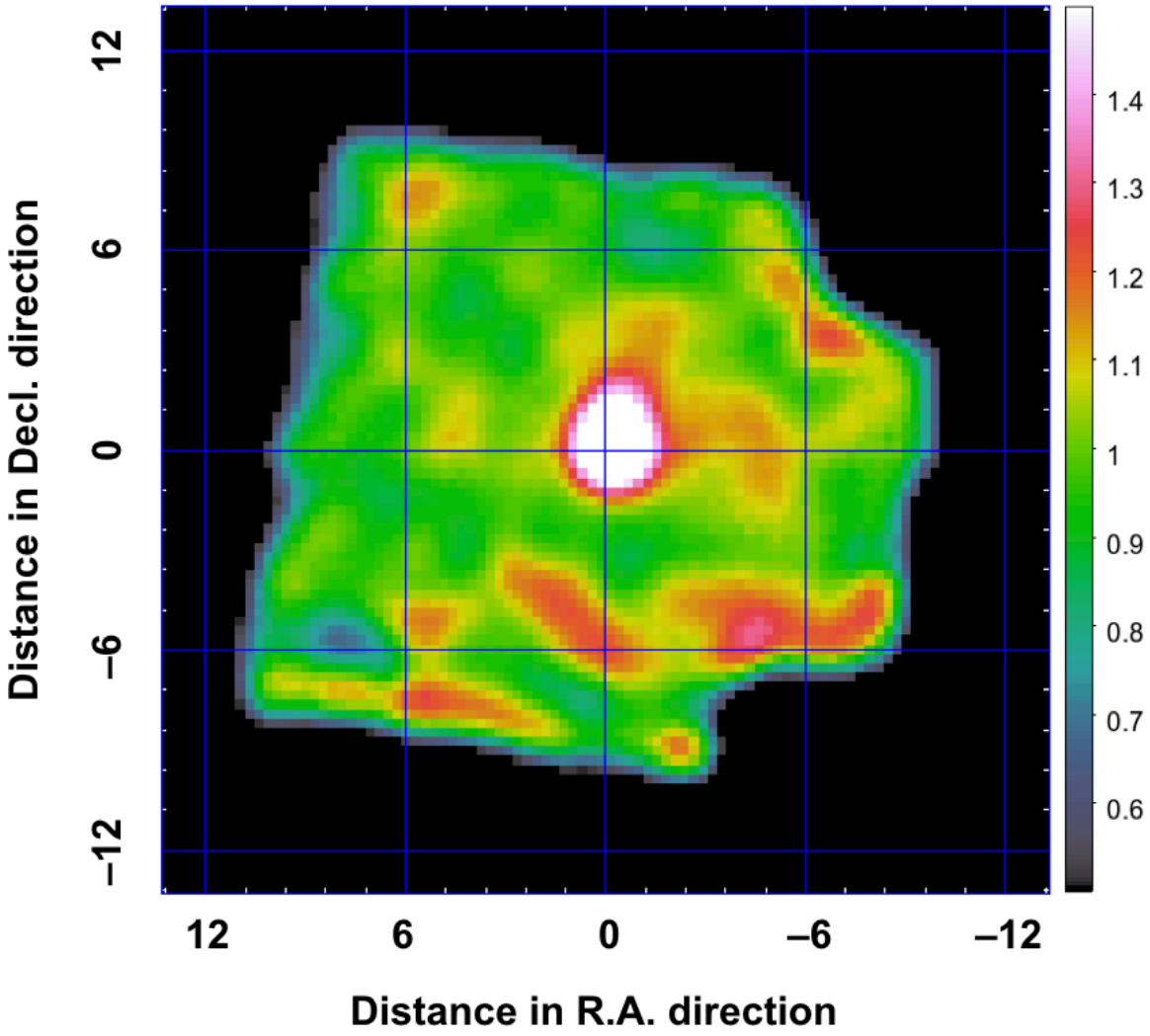

FIGURE 5.2: *Suzaku* XIS FI images in 2014 after correcting for Jupiter's ephemeris and *Suzaku*'s orbital motion in the 1–5 keV divided by CXB images in the same energy range simulated with the best-fit parameters listed in Table 5.1. The image is binned by a factor of 16 and smoothed by a Gaussian of $\sigma = 5$ pixels.

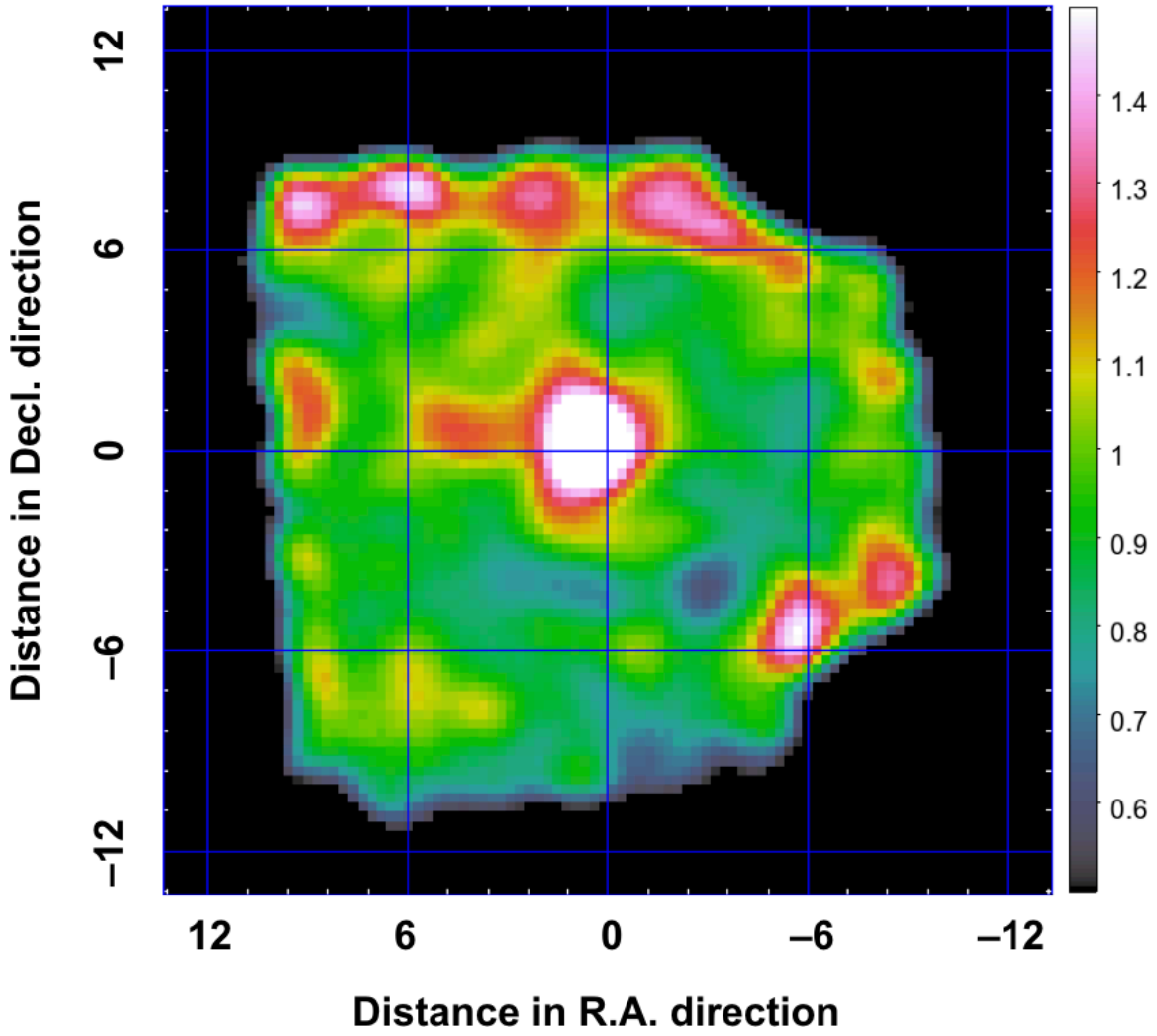

FIGURE 5.3: The same as Figure 5.2, but in 2012.

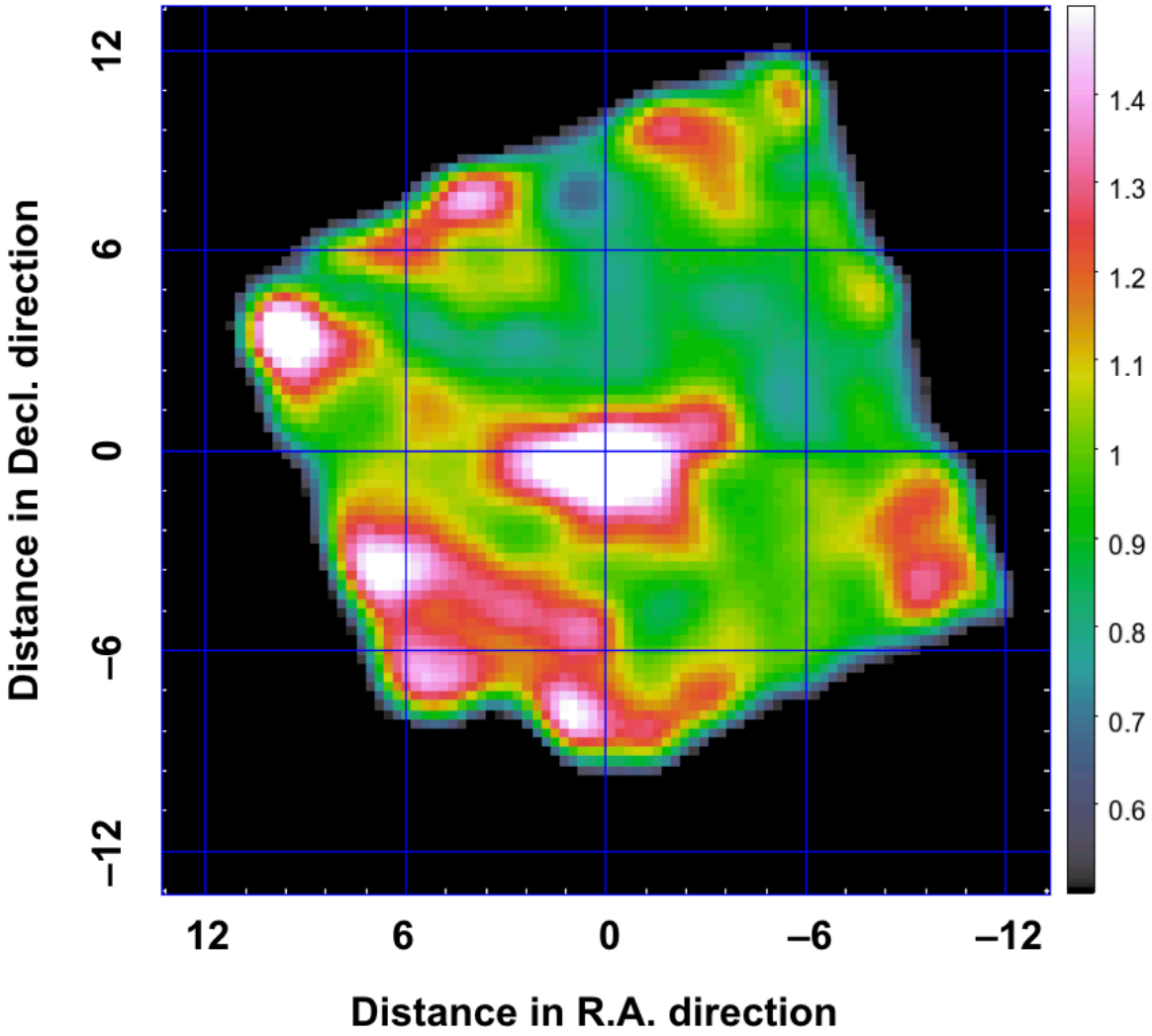

FIGURE 5.4: The same as Figure 5.2, but in 2006.

from Jupiter and is known to be on the order of 0.01 G around 6 R_J. According to Equation 2.30, when the magnetic field (B) is ~0.01 G, we need very high electron energy (E_e) of several TeV in order to produce X-ray photons. This energy is $>1 \times 10^4$ times higher than the observed maximum energy of the Jovian magnetospheric electrons ($<1 \times 10^2$ MeV; Bagenal et al., 2004).

Even in case that such very high energy electrons exist, their Larmor radius in $B = 0.01$ G is estimated to be $\sim 3 \times 10^{11}$ cm for 1 TeV electrons as given by Equation 2.15. This Larmor radius is significantly larger than the orbital radius of $\sim 6\,R_J = 4 \times 10^{10}$ cm. Such TeV electrons are unable to be trapped by the magnetic field in the Jovian magnetosphere, and, thus, will escape from the region. Therefore, we can eliminate the synchrotron radiation as a possible mechanism of the diffuse emission.

5.1.4 Bremsstrahlung

Bremsstrahlung occurs from moderately high energy electrons. We need electrons accelerated up to several keV which have been observed by past *in-situ* spacecrafts (Bagenal et al., 2004). Thus, in terms of the electron energy necessary to produce the observed emission, bremsstrahlung seems to be a reasonable mechanism. The diffuse emission may be produced by accelerated keV electrons impacting on atoms or ions present in the path of electron transport, and as the electrons lose their energies the bremsstrahlung is produced.

Electrons with Maxwellian distribution generally produce not only the bremsstrahlung continuum but also several emission lines due to interactions with atoms or ions (mainly collisional ionizations). However, we need also to assume a case of keV electrons which have non-thermal distribution (Tatischeff, 2003). The Jovian magnetosphere is known to contain high abundance of heavy ions such as oxygen and sulfur mainly originating from Io's volcano as shown in Figure 23.1 in Bagenal et al., 2004. We, therefore, would expect strong emission lines from these ions. The oxygen Kα line (0.53 keV) is also included in the spectrum of Jupiter's aurora, and it is not straightforward to tell from the oxygen line if the plasma contains Io's ejecta or not. However, sulfur Kα line (2.3 keV) is not present in the aurora so this can be a useful measure in judging the likeliness of the bremsstrahlung. By using `Xspec` for APEC model, the equivalent width of sulfur Kα line was estimated to be at least ~5 keV if the plasma contains Io's ejecta. Such a line should be observed in the XIS spectra with its energy resolution of ~130 eV at 6 keV (Koyama et al., 2007). However, we see no signature of such a line emission in Figure 4.12, Figure 4.19, and Figure 4.26. Therefore, the possibility of the bremsstrahlung can be eliminated.

5.1.5 Inverse Compton scattering

Inverse Compton scattering is the remaining possibility as a mechanism of the diffuse hard emission. Ezoe, Ishikawa, Ohashi, Miyoshi, et al. (2010) have considered the scattering of solar visible photons by ultra-relativistic electrons in the Jovian magnetosphere. Characteristic energy of the scattered photons is given by Equation 2.32 as,

$$\sim 3\,\mathrm{keV} \left(\frac{E_{\mathrm{ph}}}{1.4\,\mathrm{eV}} \right) \left(\frac{E_e}{20\,\mathrm{MeV}} \right)^2, \tag{5.1}$$

where $E_{\rm ph}$ and $E_{\rm e}$ are the energies of the solar photons and the relativistic electrons before the scattering process.

The electrons with an energy of 50 MeV were observed by *Cassini* spacecraft at 1.4 R_J (Bolton, Janssen, et al., 2002), suggesting that the inverse Compton scattering may work in a wide region in the Jovian magnetosphere. At an outer region (> several R_J), such 50 MeV electrons have not been directly observed yet, but their presence may be examined through empirical models of particle distribution in the Jovian magnetosphere (e.g., Divine and Garrett, 1983). This mechanism does not produce any line emission, which is consistent with the observed XIS spectrum. Hence, we may conclude that the most promising process for the diffuse emission is inverse Compton scattering of the solar photons by the ultra-relativistic electrons in the Jovian magnetosphere.

5.2 Particle distribution in Jovian magnetosphere

The empirical model by Divine and Garrett (1983) (D&G model) describes spatial distribution of charged particles around Jupiter. In this section, we employ this model and quantitatively examine the possibility of inverse Compton scattering. This is the first attempt of the evaluation of inverse Compton scattering based on the model of charged particle distribution in the Jovian magnetosphere. We calculate the X-ray luminosity and spectrum and compare them with the observed results from the *Suzaku* observations.

5.2.1 Charged particle model: Divine and Garrett, 1983

Although there are other models of the distribution of charged particles in the Jovian magnetosphere, we will use the D&G model because the model is most "comprehensive". The D&G model is based on the data collected during the *Pioneer* and *Voyager* flybys of Jupiter combined with earth-based observations, and is the only global model applicable from the inner to outer magnetosphere up to 16 R_J. The model also covers a wide range of electron energy higher than 0.06 MeV, and has been applied up to 35 MeV so far (Schardt and Goertz, 1983).

Our code can calculate the number density of electrons for a given energy at a given location in the Jovian magnetosphere. Figure 5.5 shows the distribution of energetic electrons in the Jovian magnetosphere reproduced by the code. Basically, as shown in Figure 2 in Divine and Garrett, 1983 and Figure 24.3 in Bagenal et al., 2004, as the electron energy becomes higher the density at a distant position from Jupiter drops quickly.

5.2.2 Inverse Compton scattering by relativistic electrons

The X-ray emission produced in the inverse Compton scattering by the ultra-relativistic electrons can be calculated in our code. Figure 5.6 describes how X-ray flux distribution is calculated. The calculation is carried out with a pitch of 2 R_J over a spatial range of <16 R_J in equatorial X- and Y-directions and <10 R_J in vertical Z-direction. The covered range of electron energy is from 0.06 to 50 MeV. The actual code adopted a python package `naima`[2] (Zabalza, 2016) to yield an X-ray differential flux or

[2] https://naima.readthedocs.io/en/latest/index.html

spectral energy distribution at a given position by taking spatial and spectral distributions of electrons given by the D&G model. We assume that the solar photons, which are subject to scattering by the electrons in this process, form a black body distribution with a temperature of 5780 K and a distance from the photon source to be 5.2 AU. They corresponded to the temperature of the Sun and the orbital radius of Jupiter, respectively. We used 170° as a scattering angle between the solar photons and the scattered X-ray photons, referring to the Sun-Jupiter-Observer angle of 10° in the *Suzaku* observations.

Figure 5.7 shows calculated results in a certain meridian surface by our code. The top two panels indicate that the L-value becomes larger at more distant from Jupiter and higher latitude, while the magnetic field B becomes isotropically smaller at more distant from Jupiter. The middle two panels indicate that the omnidirectional density of the 0.3 MeV electrons is much larger than that of the 50 MeV electrons. The 1–5 keV X-ray features calculated from such electron distributions are shown in the bottom two panels. Here, the photon indexes were estimated by fitting with a power-law function to a calculated photon spectrum at each location. In terms of the spatial distribution, the density of the higher electrons seems to be reflected in the X-ray power.

Comparison between the Divine&Garrett model to the *Suzaku* observations

We conducted a three-dimensional calculation over the magnetosphere assumed by the D&G model. The resultant images integrated along a direction of a line of sight are shown in Figure 5.8. These images indicate that the integrated density distribution of the high energy electrons is surely reflected in the integrated X-ray power distribution.

The total inverse Compton luminosity calculated from our code based on the D&G model is $\sim 5.7 \times 10^{13}$ erg s^{-1}. which is ~100 times lower than the observed value by *Suzaku* (see Table 4.9). We also estimate the count rate of the inverse Compton X-rays using the XIS FI effective area 330 cm^2 at 1.5 keV for each position and generate its projection profile along the horizontal axis. This can be compared with the observed profile. The results are shown in Figure 5.9. Results of fitting with an elliptical shape for the observed projection profiles are shown in Figure 4.8, Figure 4.18, and Figure 4.25, and are reproduced here as the observed count rates. The difference between the D&G model estimation and the observed profile is relatively small with a factor of <10 in the inner region (<10 R_J), but becomes significantly larger to factors of 10–100 in the outer region (>10 R_J). The deficiency of the model emission in the outer region is the main cause of the discrepancy with the observed results, with the proviso that it is maybe migrated, because of the CXB component which became comparable for the diffuse emission in such a region (see the background levels in Figure 4.8, Figure 4.18, and Figure 4.25) and because of unconstraint of the electron pitch angle which efficiently acts on the inverse Compton scattering.

Bagenal et al. (2004) and Bolton, Levin, et al. (2001) suggested that the D&G model probably underestimated the actual particle density in the Jovian magnetosphere by a factor of 5–10, based on a comparison of the D&G model with radio observations. The radio observations measured the Jovian synchrotron radio emission, so the data were limited in the inner region within several R_J where Jupiter's magnetic field is strong. In this regard, our result which extends further out from the inner region is consistent with their suggestion. On the other hand, our result for the outer region has no comparable observations which provide a meaningful constraint on the particle distribution.

Therefore, we have given the first observational result indicating that the D&G model underestimates the electron density by a factor of 10–100 in the distant region, where no data of such energetic particles have been obtained by *in-situ* spacecrafts.

We, additionally, estimate a photon index of the inverse Compton scattering based on the D&G model by fitting a power-law function to the spectrum in each radial position and found it to be 1.6–2.0 (lower left in Figure 5.8). The photon index expected from the D&G-model is slightly steeper as compared with the observed value. Thus, we also interpret that the D&G model underestimates preferentially the higher energy particles.

To summarize the discussion in this chapter, the most likely origin of the diffuse hard X-ray emission around Jupiter is the inverse Compton emission from the magnetosphere. In this case, electrons with energy of about 50 MeV are accelerated in a wide region in Jupiter's magnetosphere. Quantitative comparison with the D&G model showed that the electron density predicted by the model was unable to explain the observed hard X-ray luminosity by a factor of $\lesssim$100. This raises a possibility that the particle acceleration is more efficient, e.g., via the whistler-mode chorus wave-particle interactions, than the previous picture at a distant region as far as 15-20 R_J from Jupiter. The chorus waves in the Jovian magnetosphere had been observed at a region between 6 to 15 R_J by the *Galileo in-situ* measurements with constrained by its trajectories (Figure 2.10). It is possibly thought that the chorus waves are more widely distributed or other unrecognized processes exist in such distant regions. These results re-emphasize the necessity that the D&G model should be improved especially at such distant positions.

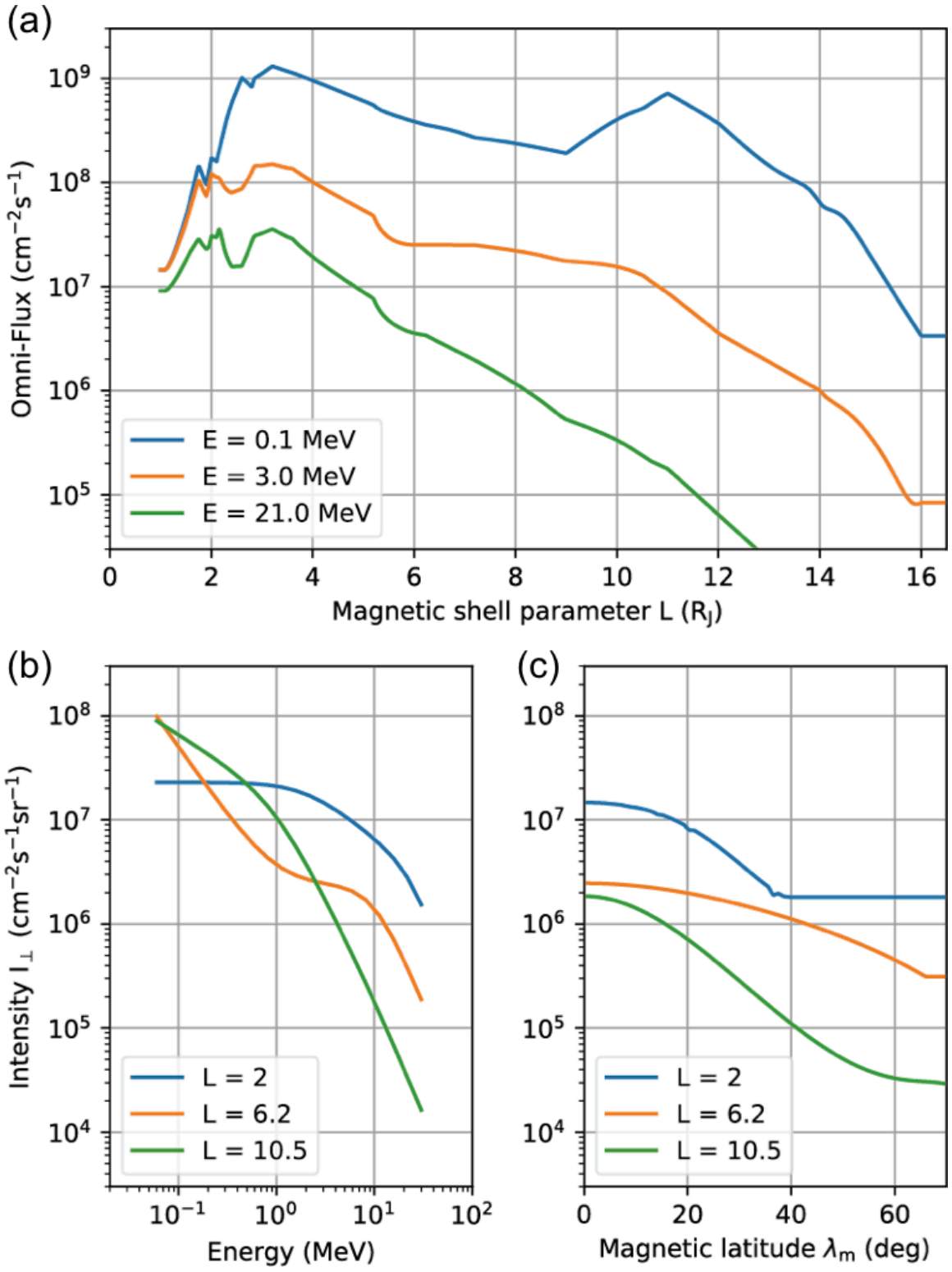

FIGURE 5.5: The electron density distribution in the Jovian magnetosphere given by the D&G model (Divine and Garrett, 1983), plotted against different parameters. (a) Omnidirectional integral flux at three energies as a function of L-shell parameter. (b) Integral intensity at a pitch angle 90°, at the equator, for three L-shell values as a function of energy. (c) Integral (E = 3 MeV) intensity at 90° pitch angle for different L-shells as a function magnetic latitude. These dependencies are all reproduced by our code and can be directly compared with Figure 2 in Divine and Garrett, 1983.

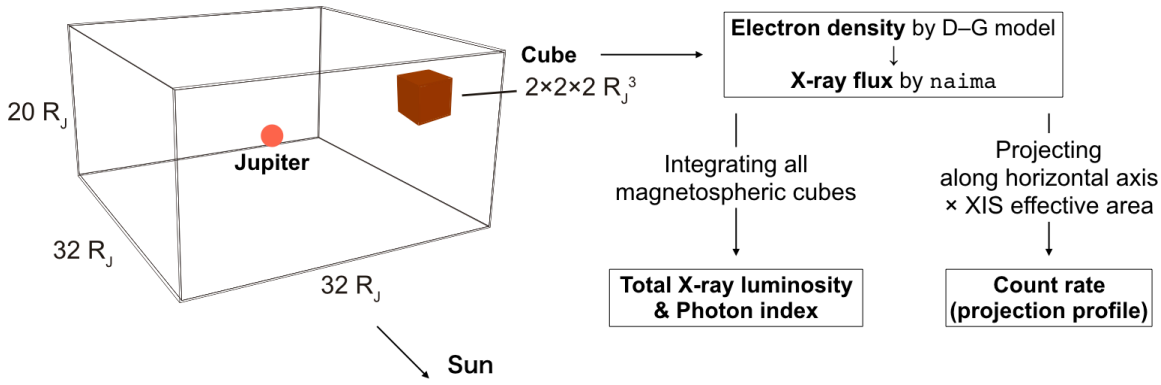

FIGURE 5.6: Schematic description of the calculation process of the inverse Compton scattering by the ultra-relativistic electrons in the Jovian magnetosphere.

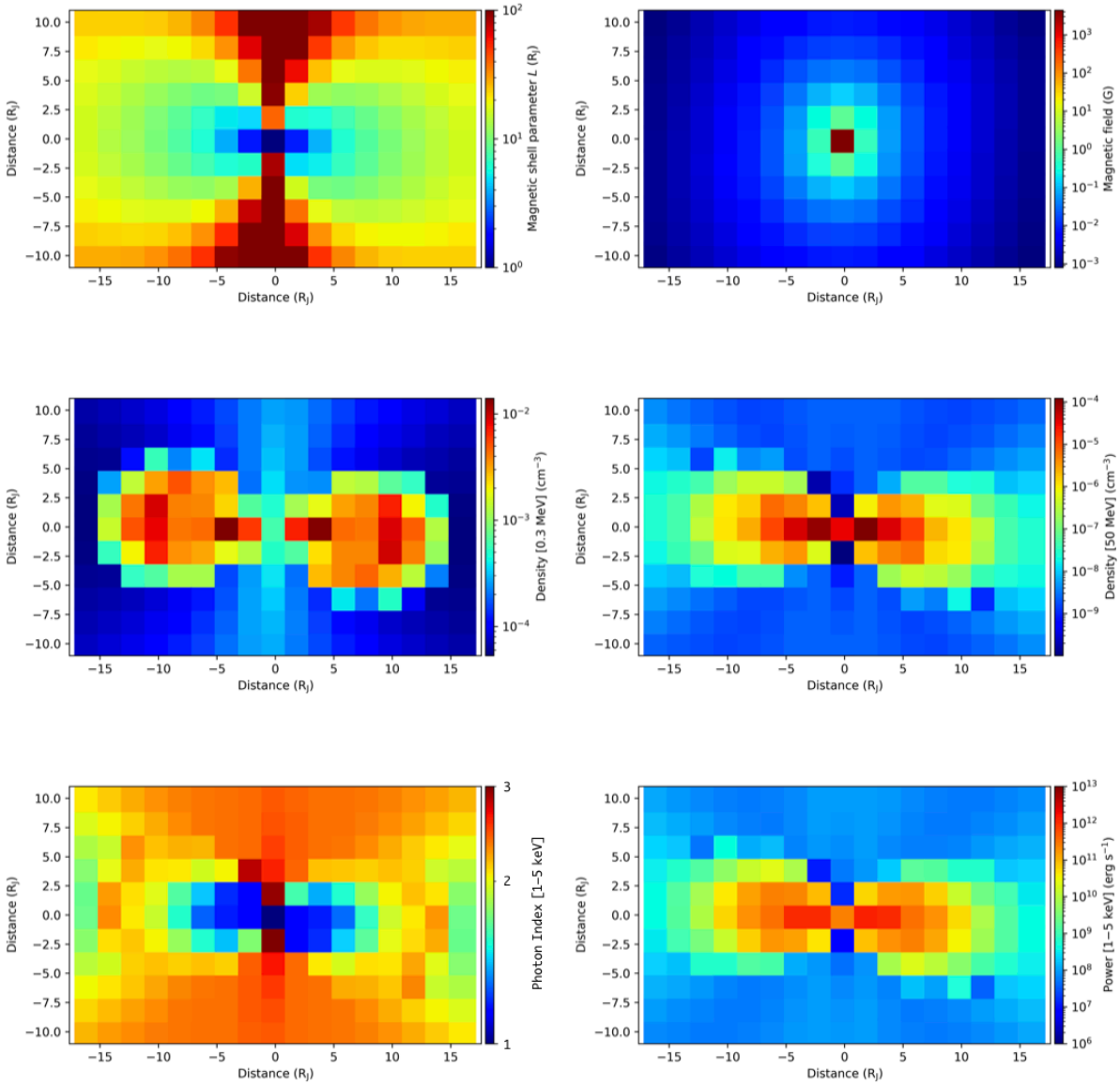

FIGURE 5.7: The D&G-model calculated color maps in a certain meridian surface of magnetic shell parameter L (top left), magnetic field B (top right), omnidirectional densities of the 0.3 MeV and 50 MeV electrons (middle left and right, respectively), photon indexes of inverse-Comptonized 1–5 keV X-ray spectra (bottom left), and powers of inverse-Comptonized 1–5 keV X-rays (bottom right). The photon indexes are obtained by fitting to the photon spectrum with a power-law function at each location.

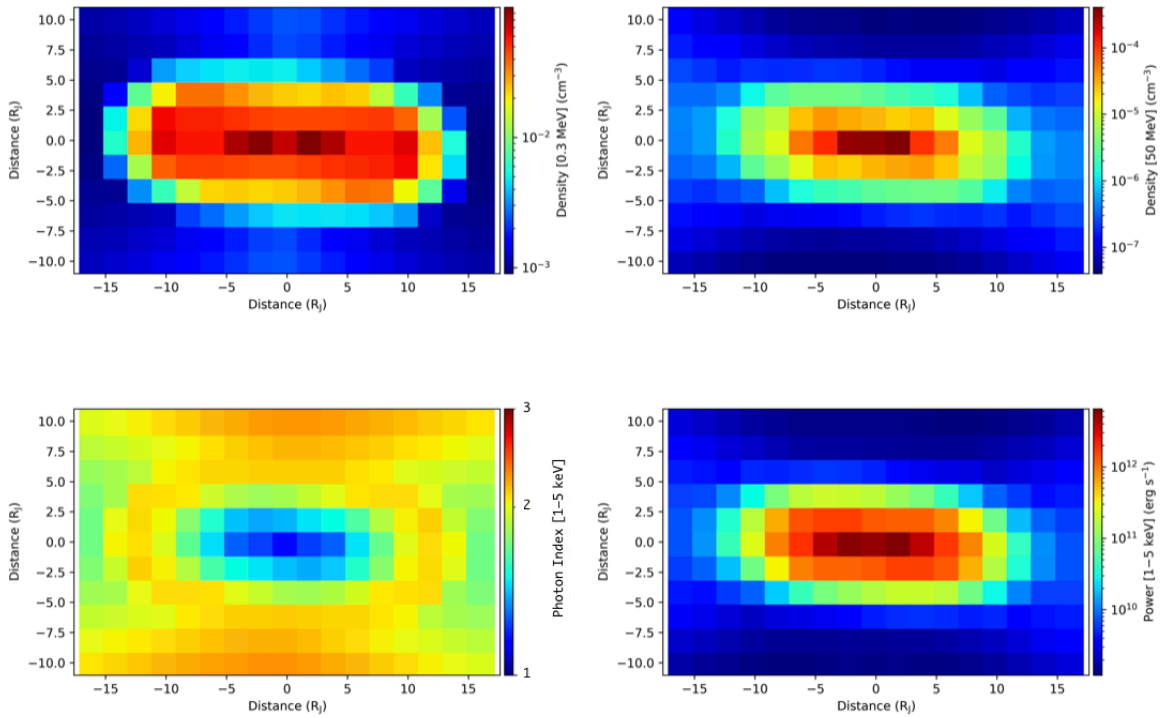

FIGURE 5.8: The three-dimensional D&G-model calculated color maps integrated in a direction of a line of sight. Omnidirectional densities of the 0.3 MeV and 50 MeV electrons (upper left and right, respectively), photon indexes of inverse-Comptonized 1–5 keV X-ray spectra (lower left), and powers of inverse-Comptonized 1–5 keV X-rays (lower right). The photon indexes are obtained by fitting to the photon spectrum with a power-law function at each location.

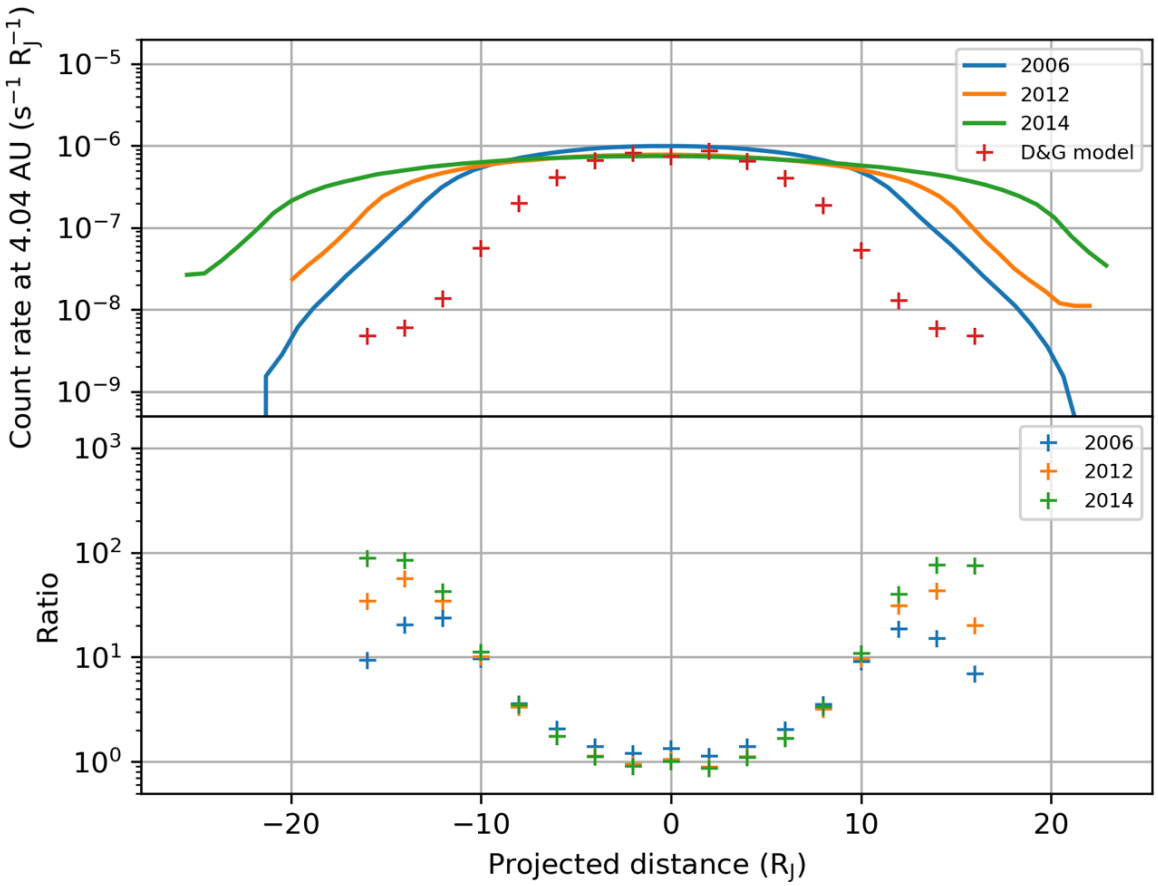

FIGURE 5.9: (Top) Intensity profiles of the extended emission modeled by the elliptical shape for the 3 *Suzaku* observations, along with the D&G model prediction. The fittings with the elliptical shape are shown in Figure 4.8, Figure 4.18, and Figure 4.25. Normalizations of these profiles are corrected so that every distance to Jupiter is 4.04 AU. (Bottom) Intensity ratio to the D&G model. Errors are not shown in the plots.

Chapter 6

Conclusion

In this thesis, we have investigated the X-ray emission in the vicinity of Jupiter using the *Suzaku* observations, combined with a coordinated *XMM-Newton* observation. We analyzed data from a total of 3 *Suzaku* XIS observations in 2006, 2012, and 2014, together with *XMM-Newton* EPIC data taken in 2014.

From the 2006 observation, Ezoe, Ishikawa, Ohashi, Miyoshi, et al. (2010) discovered hard X-ray emission extending over Jupiter's magnetosphere. They discuss that the diffuse emission is likely to be produced via inverse Compton scattering of solar visible photons by Jovian magnetospheric electrons with extremely high energies (tens of MeV). If the diffuse emission originates from such ultra-relativistic electrons, its variation amplitude should be similar to that of Jovian synchrotron radio emission (JSR) at a level of several tens of %. JSR is considered to be produced by electrons with energies of several MeV within several R_J from Jupiter, where the magnetic field is significantly strong (Bagenal et al., 2004; Bolton, Janssen, et al., 2002; Santos-Costa et al., 2008). JSR shows both short and long-term variations as shown in Fig. 2.8, but does not indicate a simple correlation with the solar activity. Variability of the Jovian diffuse X-ray emission will give a new constraint on the acceleration mechanism of high-energy electrons, independently of what can be obtained from the radio observations.

In order to verify the emission mechanism and variation of the hard X-ray emission, we looked into the *Suzaku* data from observations of Jupiter in 2012 and 2014. Here, to keep the consistency of the analysis, we addressed the 2006 data again in the same way for the other observations. Consequently, we have obtained the following results and their subsequent interpretation.

- We removed point sources from raw images in the equatorial coordinate and superposed the successively shifted images in Jupiter's reference frame coordinate in two energy bands (0.2–1 and 1–5 keV), and confirmed the hard-band X-ray emission to be extended around Jupiter for all the *Suzaku* observations in 2014, 2012, and 2006.

- We examined the spatial extent of the diffuse emission by looking into projection profiles of count rates along the R.A. directions, after accumulation of data in a square ($15' \times 6'$) region around Jupiter. Assuming point-like emission from Jupiter's body and elliptical emission around it, the projection profile in the hard band was well-fitted by the combined model, whereas the soft X-ray emission was fitted by only the point-like emission. The size of the elliptical emission is estimated as $20.0\,R_J \times 8.2\,R_J$, $15.9\,R_J \times 6.9\,R_J$, and $12.6\,R_J \times 3.5\,R_J$, and the

intensity ratio of the elliptical emission to the point-like emission (D/B ratio) was calculated ash 1.91 ± 0.36, 1.73 ± 0.24, and 6.16 ± 1.78 in 2014, 2012, and 2006, respectively.

- We extracted background-subtracted spectra from a circular source region with a radius of 6′ and an annular background region with inner and outer radii of 6′ and 8′, respectively. The spectra were fitted with a model composed of APEC, thermal bremsstrahlung, Gaussian functions, and a power-law function, which corresponded to the solar X-rays, charge exchange emission below 0.4 keV and around 0.5–0.7 keV, and the diffuse hard component. An independent fit to the coordinated *XMM-Newton*'s EPIC spectrum showed no diffuse hard emission, and we added, only in the 2014 spectrum, another power-law function describing the non-thermal bremsstrahlung in Jupiter's aurorae with fixed intensity and slope. This spectral analysis for the 2014 data provides a key result that the flux ratio of these two power-law functions in 1–5 keV was estimated as 1.41 ± 0.22 and consistent with the D/B ratio obtained from the projection profile.

- We could also separate the X-ray luminosity in the hard band into two components, namely from Jupiter's body and the diffuse emission based on the D/B ratios in 2012 and 2006. The luminosity of the diffuse emission remained stationary with no clear correlation with the variability of the solar activity. In contrast, Jupiter's body showed variability corresponding to the solar activity and indicated a relatively large enhancement in 2012 by a factor of 2–5 from the level in 2006.

- The background emission such as Cosmic X-ray Background uniformly extends over the sky, and cannot explain the anisotropic feature of this diffuse hard emission. The shape is rather consistent with a spatial extension of the Jovian magnetosphere. With the low particle density in such a distant region from Jupiter, the solar X-rays could not be simply scattered. By considering the magnetic field strength at this region (∼0.01 G), the required electron energy is too high (several TeV) to explain with the synchrotron mechanism. The obtained spectrum can exclude a non-thermal bremsstrahlung mechanism involving keV electrons, which should accompany strong fluorescent line emission from sulfur ions (2.3 keV) ejected from Io in the Jovian magnetosphere. Therefore, only the inverse Compton scattering remained plausible as a mechanism to produce the diffuse hard X-ray emission, which required tens of MeV electrons as observed by past *in-situ* measurements.

- Then, we calculated the luminosity of the inverse Compton scattering from the empirical model of charged particles in the Jovian magnetosphere (Divine and Garrett, 1983), and found it insufficient by a factor of ∼100. Moreover, projection profiles of count rates indicated that the empirical model under-estimated the electron density by factors of <10 and 10–100 in the inner (<10 R_J) and the outer (>10 R_J) regions, respectively. The result of the inner region is consistent with the result from past JSR observations (e.g., Bolton, Levin, et al., 2001), whereas the constraint on the outer region has been given by this thesis for the first time. The photon index of the model-based X-ray spectrum is slightly steeper than the observed one, and also implies that the empirical model underestimates the particle densities in the high energy side of the electron distribution.

These results raise an issue that more data are required in future, and indicate that observations of the Jovian diffuse hard X-ray emission can globally monitor the origin and behavior of ultra-relativistic electrons in the Jovian magnetosphere. Monitoring of the energetic electrons in the Jupiter system will give important clues in clarifying the mechanism of particle acceleration in the Jovian magnetosphere, whose knowledge would be further connected to our understanding of the particle acceleration phenomena occurring in stars, supernova remnants, black hole systems, and clusters of galaxies in the universe. We expect that useful data will be obtained not only from X-ray observatories which are planned for launch in the near future such as *XRISM*[1] (Tashiro et al., 2018) and *Athena*[2,3] (Barret et al., 2013), but also from Jupiter probe missions carrying small X-ray instruments (e.g., *JUXTA*; Ezoe, Kimura, et al., 2013). Such a probe mission can obtain data with high spatial resolution and high statistics since observations can be made very close to Jupiter compared with those from the Earth neighborhood.

[1] http://xrism.isas.jaxa.jp/
[2] https://www.the-athena-x-ray-observatory.eu/
[3] https://www.cosmos.esa.int/web/athena

Appendix A

Originally developed tools

A.1 `attitune`: Correction tool of reference frames of solar system objects for *Suzaku*

Unlike general X-ray celestial bodies, solar system objects (SSO) move on the sky coordinates and make a large practical part of analysis quite difficult. Although `sso_freeze` for *Chandra* and `attmove` for *XMM-Newton* are included as official tools in the packages, `CIAO` and `SAS`, respectively, no tools for *Suzaku* have been developed or released at this time. Therefore, I developed an original tool to express SSO's events in its own reference frame by editing the attitude in the observation from the orbit information of *Suzaku* and ephemerides of the objects and subsequently re-processing for the event and named it `attitune`. In this paper, it is used for Jupiter's analysis, and this makes it possible for the first time to create not only an image but also a spectrum with its reference frame. This section summarizes a concept of the tool and the debugging for use in analyses.

A.1.1 Concept

Suzaku orbits the Earth while observing a certain celestial body and stabilizes its line of sight (LoS) during the observation period. In many cases that such a celestial body is located so far away from the Earth (i.e., *Suzaku*), the motion of *Suzaku* around the Earth and the Earth itself is negligible due to its quite small parallax against the target body. However, in some cases observing nearer targets such as the SSOs, the parallax becomes larger and more effective. Additionally, to make matters worse, such near targets themselves often move in the sky in the observation period.

A near target at a certain time is positioned at a certain site in field of view (FoV) of observatories. Here, if attitude information of the observatory can be overwritten in consideration of a distance to the target from the original LoS in the sky coordinates, it will the target possible to be centered on the (replaced) FoV. Hence, based on this concept, it is possible to keep the target at the center of the FoV over the entire observation period by comprehending both the time-dependent positions of the target and *Suzaku*.

NASA's Jet Propulsion Laboratory (JPL) HORIZONS [1] provides us SSO's ephemerides by a Web-interface or an e-mail-interface. JPL HORIZONS provides solar system data and ephemeris computation for solar system objects (921 900 asteroids, 3601 comets, 209 planetary satellites, 8 planets,

[1] https://ssd.jpl.nasa.gov/horizons.cgi

the Sun, L1, L2, select spacecraft, and system barycenters). The key input parameters for the HORIZONS calculation are three: (i) target body, (ii) observer location, and (iii) time span. It outputs a lot of information about the target as a function of time, in which we mainly utilized data of J2000.0 equatorial positions (α and δ) and distances (see their web site more detail), with taking the light time to the target into account. Here, we note that `Astropy`[2] (version 3.1.2) and `Astroquery`[3] (version 0.3.10.dev0) make it seamless for scripting code to obtain and handle the ephemerides during the observation in `attitune`.

Suzaku's position on its orbit and LoS are provided as an orbit and altitude file (named as `ae‘‘OBSID’’.orb` and `ae‘‘OBSID’’xi‘‘XISID’’.att`) in its observation data sets we can handle. We derived three data from the orbit file: altitude, latitude, and longitude as a function of time, and also derived the LoS from the attitude file. By combining the *Suzaku*'s orbit information and the target's information mentioned above, we obtained distances to the target from the LoS in the equatorial coordinate with the entire range of the observation. As a result, we generated a renewal attitude file after correcting the original attitude file by the distance. Finally, *Suzaku*'s event file should be reprocessed by `xiscoord` with the renewal attitude file. Here, `xiscoord` can overwrite `SKY-X` and `-Y` columns from `DET-X` and `-Y` columns in the event file based on an input attitude file.

A.1.2 Debug by *Suzaku* observation data of the Moon

We conducted a debug of `attitune` by processing it to actual data observed by *Suzaku*. *Suzaku* had observed the Moon which is the nearest SSO from the Earth and moving with the fastest apparent velocity in the FoV in the sky coordinate. In brief, we considered that the Moon is the most suitable for debugging the tool. In the following text, we reported example results by processing to XIS 0 data.

Figure A.1 shows a XIS 0 image of the Moon in the equatorial coordinate (J2000.0). The data were taken in May 6–7 2014 with 9 maneuvers following the Moon's motion. The green circles indicate the Moon's positions at a start, center, and end time in each maneuver. Thus, the circle at the end time marginally corresponds that at the start time in the next maneuver. It is clearly shown that the Moon rapidly passed the *Suzaku*'s FoV during the single maneuver.

We firstly tried to conduct a correction with only considering the Moon's motion in the sky coordinate (i.e., without considering the *Suzaku*'s orbital motion.) to all the 9 event files by `attitune` (optional usage). The resultant image is shown in Figure A.2. The green circle centered on the FoV indicates the Moon position and size with a radius of 14.8′. We could not recognize any signature of the Lunar X-rays which likely brights on the half "dayside" disk as shown in Figure 2.3 (left).

Then, we secondary tried to conduct a full correction both with considering the Moon's motion and the *Suzaku*'s orbital motion. The resultant image is shown in Figure A.3. The green circle indicates the same as Figure A.2. We could surely recognize a typical signature of the Lunar X-rays which likely brights on the half "dayside" disk as shown in Figure 2.3 (left).

Finally, we created a spectrum in the Moon's reference frame coordinate as shown in Figure A.3. We adopted half "dayside" and "nightside" disks with a radius of 15′ as source and background regions, respectively. The background-subtracted XIS 0 spectrum is shown in Figure A.4. The spectrum

[2] https://www.astropy.org
[3] https://astroquery.readthedocs.io/en/latest/#

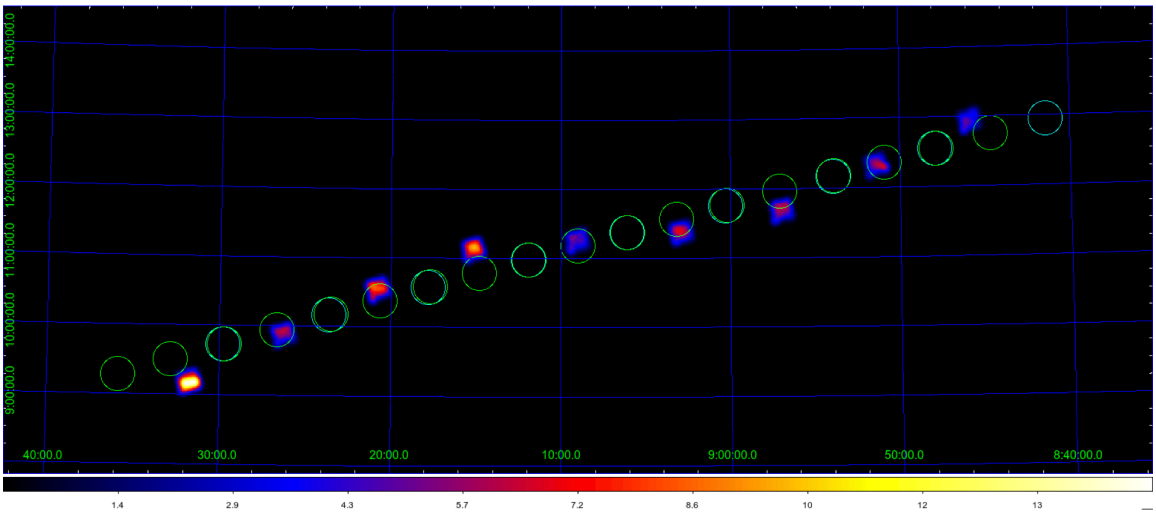

FIGURE A.1: An XIS 0 image of Lunar X-rays in the J2000.0 equatorial coordinate system. Circles show positions of start (light blue), center (green), and end (green) time of an observation in each 9 maneuver and sizes of the Moon with a radius of 14.8′. The end times approximately correspond to the start time of the next maneuvers.

shows a typical Lunar X-ray spectral feature (Wargelin et al., 2004) which consists of significant Kα fluorescent line emission of oxygen (∼0.53 keV), magnesium (∼1.25 keV), aluminum (∼1.49 keV), and silicon (∼1.74 keV). It also seems to show Kα fluorescent line emission of calcium (∼3.69 keV) and iron (∼6.41 keV) and Lα fluorescent line emission of iron (∼0.71 keV). As a result, we found the signature of the Lunar X-rays and demonstrated our original tool `attitune` successfully working for *Suzaku*'s data.

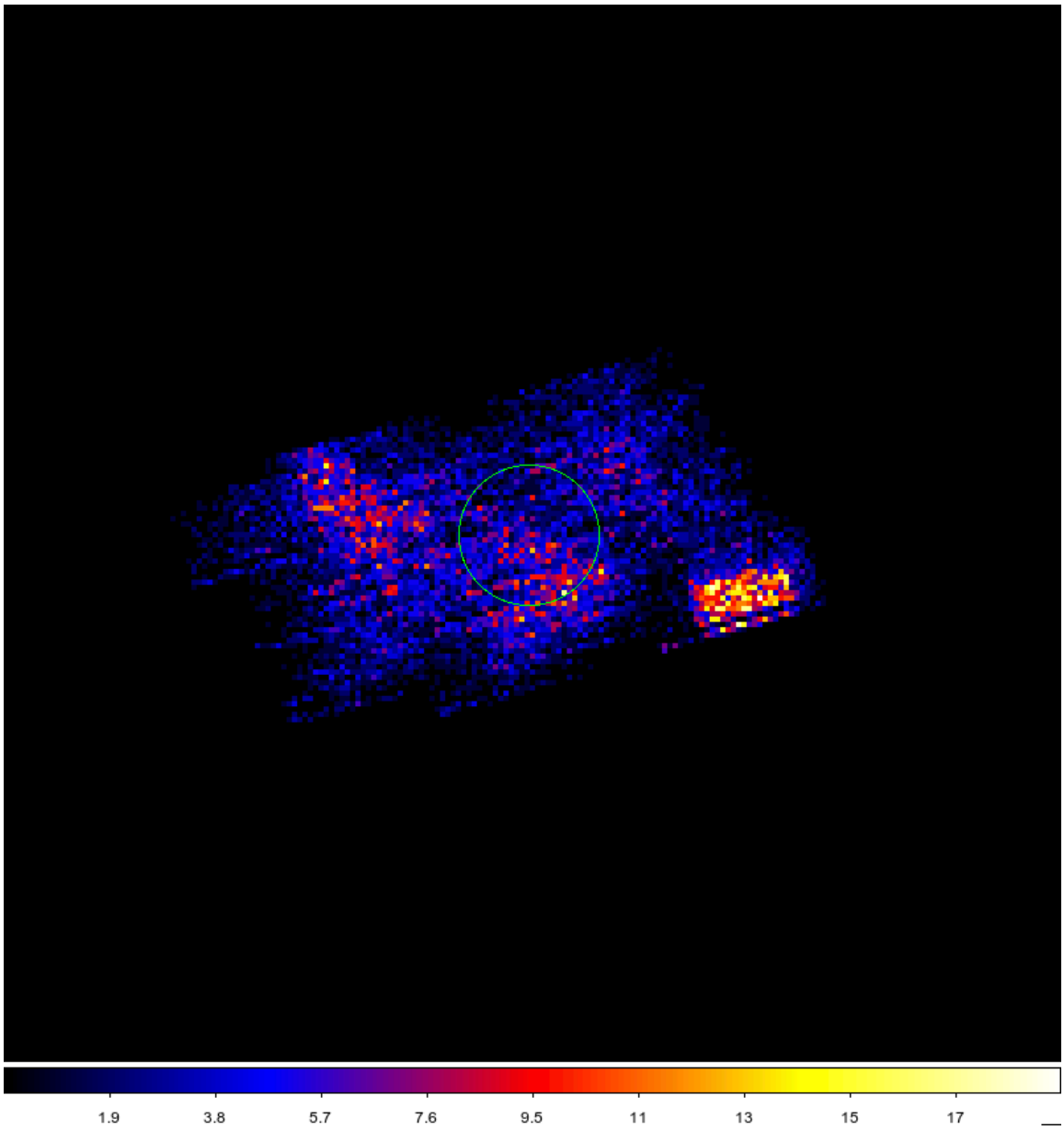

FIGURE A.2: The same as Figure A.1, but in a coordinate system corrected only ephemerides of the Moon without *Suzaku*'s orbit. A circle shows the center of the coordinate system and the size of the Moon with a radius of 14.8′.

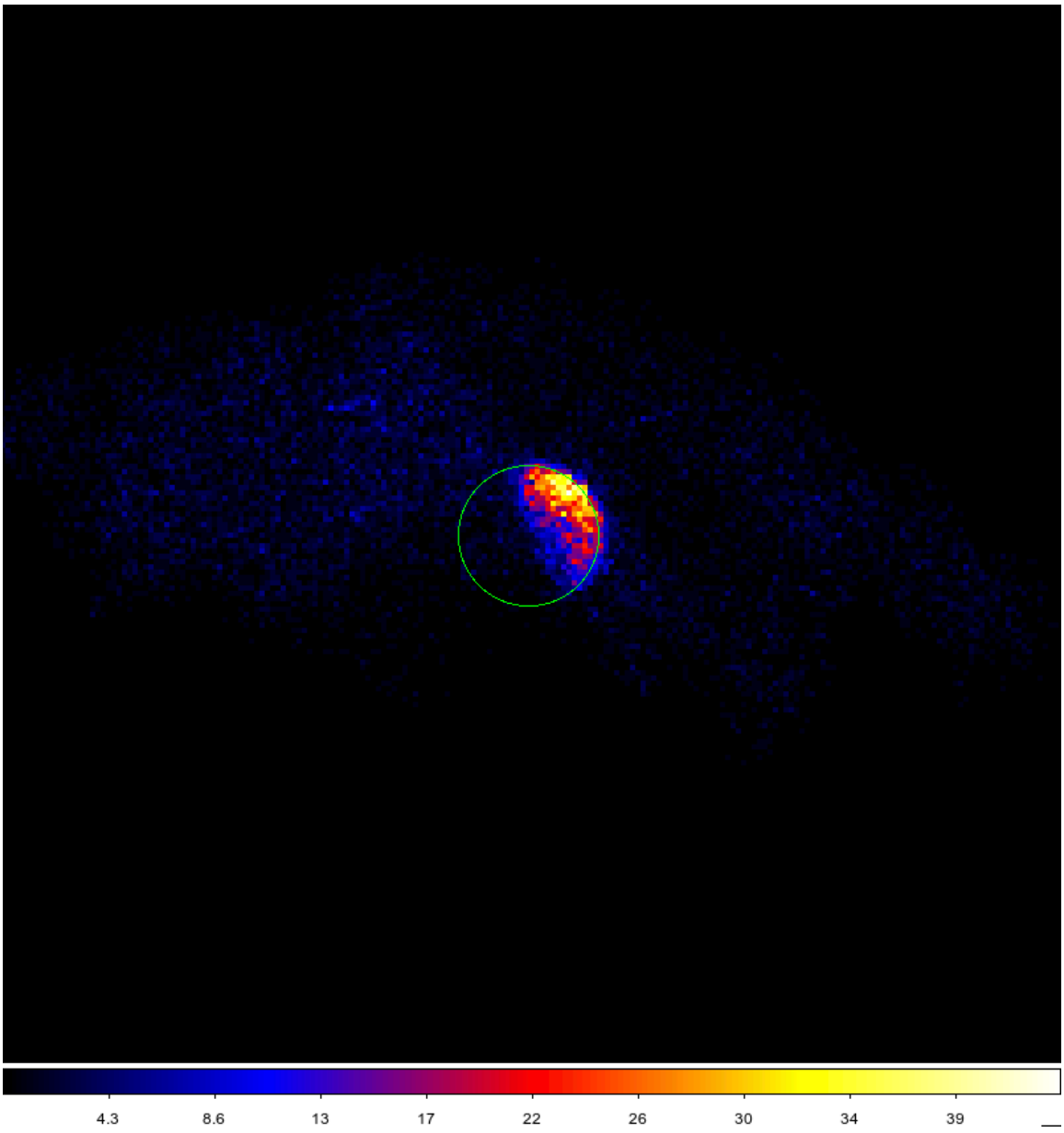

FIGURE A.3: The same as Figure A.1, but in a coordinate system corrected both ephemerides of the Moon and *Suzaku*'s orbit, i.e., in the Moon's reference frame.

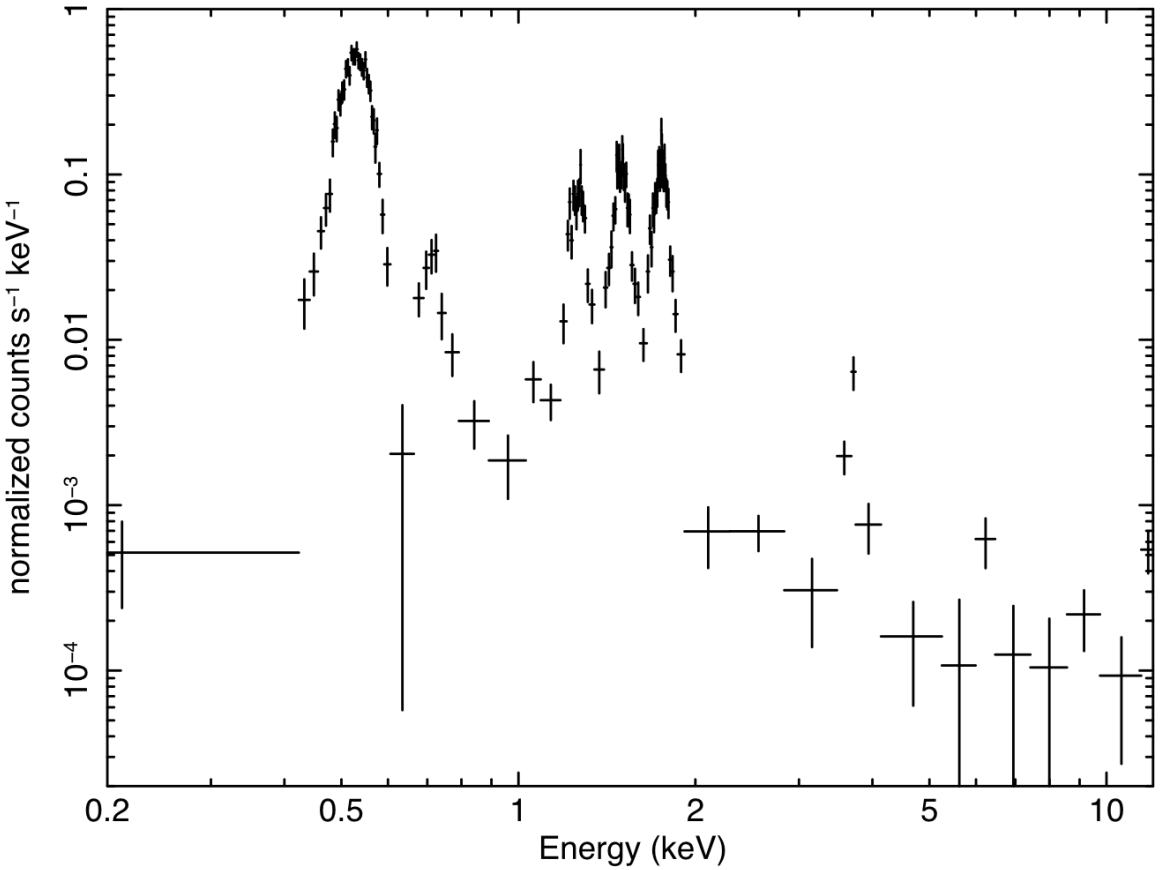

FIGURE A.4: A background-subtracted XIS 0 spectrum of Lunar X-rays. Source and background photons were extracted with the half "dayside" and "nightside" disks of the Moon, respectively.

References

[1] M. H. Acuna and N. F. Ness, “The main magnetic field of Jupiter”, Journal of Geophysical Research (1896-1977) **81**, 2917–2922 (1976).

[2] M. Asplund, N. Grevesse, A. J. Sauval, and P. Scott, “The Chemical Composition of the Sun”, ARA&A **47**, 481–522 (2009).

[3] J. Audouze and G. Israel, *The Cambridge Atlas of Astronomy* (Cambridge University Press, Oct. 27, 1988), 432 pp.

[4] F. Bagenal, T. E. Dowling, and W. B. McKinnon, eds., *Jupiter: the planet, satellites, and magnetosphere*, Cambridge Planetary Science [new ser.], 1 (Cambridge University Press, Cambridge, UK ; New York, 2004), 719 pp.

[5] D. Barret, K. Nandra, X. Barcons, A. Fabian, G. Branduardi-Raymont, M. Cappi, F. Carrera, A. Comastri, E. Costantini, A. Decourchelle, C. Done, M. Dovciak, S. Ettori, A. Finoguenov, P. Jonker, J. Kaastra, G. Matt, C. Motch, P. O’Brien, G. Pareschi, G. Pratt, G. Rauw, T. Reiprich, J. Sanders, S. Sciortino, and J. Wilms, “ATHENA+: THE FIRST DEEP UNIVERSE X-RAY OBSERVATORY”, 7 (2013).

[6] A. Bhardwaj, “X-ray emission from jupiter, saturn, and earth: a short review”, in *Advances in Geosciences*, Vol. Volume 3, 5 vols., Advances in Geosciences Volume 3 (World Scientific Publishing Company, May 1, 2006), pp. 215–230.

[7] A. Bhardwaj, R. F. Elsner, J. J. Hunter Waite, G. R. Gladstone, T. E. Cravens, and P. G. Ford, “Chandra Observation of an X-Ray Flare at Saturn: Evidence of Direct Solar Control on Saturn’s Disk X-Ray Emissions”, The Astrophysical Journal **624**, L121–L124 (2005).

[8] A. Bhardwaj, R. F. Elsner, G. Randall Gladstone, T. E. Cravens, C. M. Lisse, K. Dennerl, G. Branduardi-Raymont, B. J. Wargelin, J. Hunter Waite, I. Robertson, N. Østgaard, P. Beiersdorfer, S. L. Snowden, and V. Kharchenko, “X-rays from solar system objects”, Planetary and Space Science **55**, 1135–1189 (2007).

[9] S. J. Bolton, S. Gulkis, M. J. Klein, I. de Pater, and T. J. Thompson, “Correlation studies between solar wind parameters and the decimetric radio emission from Jupiter”, Journal of Geophysical Research **94**, 121 (1989).

[10] S. J. Bolton, M. Janssen, R. Thorne, S. Levin, M. Klein, S. Gulkis, T. Bastian, R. Sault, C. Elachi, M. Hofstadter, A. Bunker, G. Dulk, E. Gudim, G. Hamilton, W. T. K. Johnson, Y. Leblanc, O. Liepack, R. McLeod, J. Roller, L. Roth, and R. West, “Ultra-relativistic electrons in Jupiter’s radiation belts”, Nature **415**, 987–991 (2002).

[11] S. J. Bolton, S. M. Levin, S. L. Gulkis, M. J. Klein, R. J. Sault, B. Bhattacharya, R. M. Thorne, G. A. Dulk, and Y. Leblanc, "Divine-Garrett Model and Jovian synchrotron emission", Geophysical Research Letters **28**, 907–910 (2001).

[12] G. Branduardi-Raymont, A. Bhardwaj, R. F. Elsner, G. R. Gladstone, G. Ramsay, P. Rodriguez, R. Soria, J. H. Waite, Jr, and T. E. Cravens, "A study of Jupiter's aurorae with *XMM-Newton*", Astronomy & Astrophysics **463**, 761–774 (2007).

[13] G. Branduardi-Raymont, A. Bhardwaj, R. Elsner, G. Gladstone, G. Ramsay, P. Rodriguez, R. Soria, J. Waite, and T. Cravens, "Latest results on Jovian disk X-rays from XMM-Newton", Planetary and Space Science **55**, 1126–1134 (2007).

[14] G. Branduardi-Raymont, R. F. Elsner, M. Galand, D. Grodent, T. E. Cravens, P. Ford, G. R. Gladstone, and J. H. Waite, "Spectral morphology of the X-ray emission from Jupiter's aurorae", Journal of Geophysical Research: Space Physics **113** (2008).

[15] G. Branduardi-Raymont, R. F. Elsner, G. R. Gladstone, G. Ramsay, P. Rodriguez, R. Soria, and J. H. Waite, "First observation of Jupiter by *XMM-Newton*", Astronomy & Astrophysics **424**, 331–337 (2004).

[16] N. M. Brice and G. A. Ioannidis, "The magnetospheres of Jupiter and Earth", Icarus **13**, 173–183 (1970).

[17] N. Brice and T. R. Mcdonough, "Jupiter's radiation belts", Icarus **18**, 206–219 (1973).

[18] E. J. Bunce, S. W. H. Cowley, and T. K. Yeoman, "Jovian cusp processes: Implications for the polar aurora", Journal of Geophysical Research: Space Physics **109** (2004).

[19] C. T. Chantler, "Theoretical Form Factor, Attenuation, and Scattering Tabulation for Z=1–92 from E=1–10 eV to E=0.4–1.0 MeV", Journal of Physical and Chemical Reference Data **24**, 71–643 (1995).

[20] T. E. Cravens, "X-ray Emission from Comets", Science **296**, 4 (2002).

[21] T. E. Cravens, "Comet Hyakutake x-ray source: Charge transfer of solar wind heavy ions", Geophysical Research Letters **24**, 105–108 (1997).

[22] T. E. Cravens, J. Clark, A. Bhardwaj, R. Elsner, J. H. Waite, A. N. Maurellis, G. R. Gladstone, and G. Branduardi-Raymont, "X-ray emission from the outer planets: Albedo for scattering and fluorescence of solar X rays", Journal of Geophysical Research **111**, A07308 (2006).

[23] T. E. Cravens, J. H. Waite, T. I. Gombosi, N. Lugaz, G. R. Gladstone, B. H. Mauk, and R. J. MacDowall, "Implications of Jovian X-ray emission for magnetosphere-ionosphere coupling", Journal of Geophysical Research: Space Physics **108** (2003).

[24] T. E. Cravens, "Heliospheric X-ray Emission Associated with Charge Transfer of the Solar Wind with Interstellar Neutrals", The Astrophysical Journal **532**, L153–L156 (2000).

[25] R. J. Davis, *SEARCH FOR NEUTRINOS FROM THE SUN*. BNL-12981; CONF-680936-1 (Brookhaven National Lab., Upton, N. Y., Oct. 31, 1969).

[26] K. Dennerl, "Charge Transfer Reactions", Space Science Reviews **157**, 57–91 (2010).

[27] K. Dennerl, J. Englhauser, and J. Trümper, "X-ray Emissions from Comets Detected in the Röntgen X-ray Satellite All-Sky Survey", Science **277**, 1625–1630 (1997).

[28] A. J. Dessler, *Physics of the Jovian magnetosphere* (1983).

[29] N. Divine and H. B. Garrett, "Charged particle distributions in Jupiter's magnetosphere", Journal of Geophysical Research **88**, 6889 (1983).

[30] R. F. Elsner, N. Lugaz, J. H. Waite, T. E. Cravens, G. R. Gladstone, P. Ford, D. Grodent, A. Bhardwaj, R. J. MacDowall, M. D. Desch, and T. Majeed, "Simultaneous Chandra X ray, Hubble Space Telescope ultraviolet, and Ulysses radio observations of Jupiter's aurora", Journal of Geophysical Research: Space Physics **110** (2005).

[31] R. F. Elsner, G. R. Gladstone, J. H. Waite, F. J. Crary, R. R. Howell, R. E. Johnson, P. G. Ford, A. E. Metzger, K. C. Hurley, E. D. Feigelson, G. P. Garmire, A. Bhardwaj, D. C. Grodent, T. Majeed, A. F. Tennant, and M. C. Weisskopf, "Discovery of Soft X-Ray Emission from Io, Europa, and the Io Plasma Torus", The Astrophysical Journal **572**, 1077–1082 (2002).

[32] ESA: XMM-Newton SOC, *XMM-Newton Users Handbook*, Issue 2.17 (ESA, July 15, 2019).

[33] Y. Ezoe, R. Fujimoto, N. Yamasaki, K. Mitsuda, T. Ohashi, K. Ishikawa, S. Oishi, Y. Miyoshi, N. Terada, Y. Futaana, F. Porter, and G. Brown, "Suzaku observations of charge exchange emission from solar system objects: Suzaku observations of charge exchange emission from solar system objects", Astronomische Nachrichten **333**, 319–323 (2012).

[34] Y. Ezoe, K. Ishikawa, T. Ohashi, Y. Miyoshi, N. Terada, Y. Uchiyama, and H. Negoro, "DISCOVERY OF DIFFUSE HARD X-RAY EMISSION AROUND JUPITER WITH *SUZAKU*", The Astrophysical Journal **709**, L178–L182 (2010).

[35] Y. Ezoe, K. Ishikawa, T. Ohashi, N. Y. Yamasaki, K. Mitsuda, R. Fujimoto, Y. Miyoshi, N. Terada, Y. Uchiyama, and Y. Futaana, "Solar system planets observed with Suzaku", Advances in Space Research **47**, 411–418 (2011).

[36] Y. Ezoe, T. Kimura, S. Kasahara, A. Yamazaki, K. Mitsuda, M. Fujimoto, Y. Miyoshi, G. Branduardi-Raymont, K. Ishikawa, I. Mitsuishi, T. Ogawa, T. Kakiuchi, and T. Ohashi, "JUXTA: A new probe of X-ray emission from the Jupiter system", Advances in Space Research **51**, 1605–1621 (2013).

[37] L. A. Frank and W. R. Paterson, "Return to Io by the Galileo spacecraft: Plasma observations", Journal of Geophysical Research: Space Physics **105**, 25363–25378 (2000).

[38] L. A. Frank and W. R. Paterson, "Passage through lo's ionospheric plasmas by the Galileo spacecraft", Journal of Geophysical Research: Space Physics **106**, 26209–26224 (2001).

[39] L. A. Frank and W. R. Paterson, "Plasmas observed with the Galileo spacecraft during its flyby over Io's northern polar region", Journal of Geophysical Research: Space Physics **107**, SMP 31-1-SMP 31–19 (2002).

[40] L. A. Frank, W. R. Paterson, K. L. Ackerson, V. M. Vasyliunas, F. V. Coroniti, and S. J. Bolton, "Plasma Observations at Io with the Galileo Spacecraft", Science **274**, 394–395 (1996).

[41] N. Gehrels and E. C. Stone, "Energetic oxygen and sulfur ions in the Jovian magnetosphere and their contribution to the auroral excitation", Journal of Geophysical Research **88**, 5537 (1983).

[42] R. Giacconi, H. Gursky, F. R. Paolini, and B. B. Rossi, "Evidence for x Rays From Sources Outside the Solar System", Physical Review Letters **9**, 439–443 (1962).

[43] V. L. Ginzburg and S. I. Syrovatskii, *The Origin of Cosmic Rays* (Elsevier, Pergamon, 1964), 444 pp.

[44] G. R. Gladstone, J. H. Waite, D. Grodent, W. S. Lewis, F. J. Crary, R. F. Elsner, M. C. Weisskopf, T. Majeed, J.-M. Jahn, A. Bhardwaj, J. T. Clarke, D. T. Young, M. K. Dougherty, S. A. Espinosa, and T. E. Cravens, "A pulsating auroral X-ray hot spot on Jupiter", Nature **415**, 1000–1003 (2002).

[45] D. A. Gurnett, W. S. Kurth, A. Roux, S. J. Bolton, and C. F. Kennel, "Evidence for a magnetosphere at Ganymede from plasma-wave observations by the Galileo spacecraft", Nature **384**, 535–537 (1996).

[46] G. E. Hale and S. B. Nicholson, "The Law of Sun-Spot Polarity", The Astrophysical Journal **62**, 270 (1925).

[47] S. Han, G. Murakami, H. Kita, F. Tsuchiya, C. Tao, H. Misawa, A. Yamazaki, and M. Nakamura, "Investigating Solar Wind-Driven Electric Field Influence on Long-Term Dynamics of Jovian Synchrotron Radiation", Journal of Geophysical Research: Space Physics **123**, 9508–9516 (2018).

[48] M. Horanyi, T. E. Cravens, and J. H. Waite, "The precipitation of energetic heavy ions into the upper atmosphere of Jupiter", Journal of Geophysical Research **93**, 7251 (1988).

[49] R. B. Horne, R. M. Thorne, S. A. Glauert, J. Douglas Menietti, Y. Y. Shprits, and D. A. Gurnett, "Gyro-resonant electron acceleration at Jupiter", Nature Physics **4**, 301–304 (2008).

[50] F. Jansen, D. Lumb, B. Altieri, J. Clavel, M. Ehle, C. Erd, C. Gabriel, M. Guainazzi, P. Gondoin, R. Much, R. Munoz, M. Santos, N. Schartel, D. Texier, and G. Vacanti, "XMM-Newton observatory - I. The spacecraft and operations", Astronomy & Astrophysics **365**, L1–L6 (2001).

[51] R. E. Johnson, *Energetic Charged-Particle Interactions with Atmospheres and Surfaces* (Springer Science & Business Media, Mar. 13, 2013), 235 pp.

[52] Y. Katoh, F. Tsuchiya, Y. Miyoshi, A. Morioka, H. Misawa, R. Ujiie, W. S. Kurth, A. T. Tomás, and N. Krupp, "Whistler mode chorus enhancements in association with energetic electron signatures in the Jovian magnetosphere", Journal of Geophysical Research: Space Physics **116** (2011).

[53] Y. Katoh and Y. Omura, "Relativistic particle acceleration in the process of whistler-mode chorus wave generation", Geophysical Research Letters **34** (2007).

[54] R. L. Kelley, K. Mitsuda, C. A. Allen, P. Arsenovic, M. D. Audley, T. G. Bialas, K. R. Boyce, R. F. Boyle, S. R. Breon, G. V. Brown, J. Cottam, M. J. DiPirro, R. Fujimoto, T. Furusho, K. C. Gendreau, G. G. Gochar, O. Gonzalez, M. Hirabayashi, S. S. Holt, H. Inoue, M. Ishida, Y. Ishisaki, C. S. Jones, R. Keski-Kuha, C. A. Kilbourne, D. McCammon, U. Morita, S. H. Moseley, B. Mott, K. Narasaki, Y. Ogawara, T. Ohashi, N. Ota, J. S. Panek, F. S. Porter, A. Serlemitsos, P. J. Shirron, G. A. Sneiderman, A. E. Szymkowiak, Y. Takei, J. L. Tveekrem, S. M. Volz, M. Yamamoto, and N. Y. Yamasaki, "The Suzaku High Resolution X-Ray Spectrometer", Publications of the Astronomical Society of Japan **59**, S77–S112 (2007).

[55] V. Kharchenko, A. Bhardwaj, A. Dalgarno, D. R. Schultz, and P. C. Stancil, "Modeling spectra of the north and south Jovian X-ray auroras", Journal of Geophysical Research: Space Physics **113** (2008).

[56] K. K. Khurana, M. G. Kivelson, V. Vasyliunas M., N. Krupp, J. Woch, A. Lagg, B. H. Mauk, and W. S. Kurth, "The Configuration of Jupiter's Magnetosphere", in *Jupiter: the planet, satellites, and magnetosphere, F. Bagenal, T. E. Dowing and W. B. McKinnon (ed.)* (2004).

[57] M. Klein, S. Bolton, S. Gulkis, M. Janssen, S. Levin, J. Roller, and R. McLeod, "Cassini - Jupiter microwave observing campaign: DSN and GAVRT observations of jovian synchrotron radio emission", in *Planetary Radio Emissions V*, edited by H. Rucker, M. Kaiser, and Y. Leblanc (Austrian Academy of Science Press, Austria, 2001), pp.221–228.

[58] K. Koyama, H. Tsunemi, T. Dotani, M. W. Bautz, K. Hayashida, T. G. Tsuru, H. Matsumoto, Y. Ogawara, G. R. Ricker, J. Doty, S. E. Kissel, R. Foster, H. Nakajima, H. Yamaguchi, H. Mori, M. Sakano, K. Hamaguchi, M. Nishiuchi, E. Miyata, K. Torii, M. Namiki, S. Katsuda, D. Matsuura, T. Miyauchi, N. Anabuki, N. Tawa, M. Ozaki, H. Murakami, Y. Maeda, Y. Ichikawa, G. Y. Prigozhin, E. A. Boughan, B. LaMarr, E. D. Miller, B. E. Burke, J. A. Gregory, A. Pillsbury, A. Bamba, J. S. Hiraga, A. Senda, H. Katayama, S. Kitamoto, M. Tsujimoto, T. Kohmura, Y. Tsuboi, and H. Awaki, "X-Ray Imaging Spectrometer (XIS) on Board Suzaku", Publications of the Astronomical Society of Japan **59**, S23–S33 (2007).

[59] D. Krankowsky, P. Lämmerzahl, I. Herrwerth, J. Woweries, P. Eberhardt, U. Dolder, U. Herrmann, W. Schulte, J. J. Berthelier, J. M. Illiano, R. R. Hodges, and J. H. Hoffman, "In situ gas and ion measurements at comet Halley", Nature **321**, 326–329 (1986).

[60] V. A. Krasnopolsky, J. B. Greenwood, and P. C. Stancil, "X-Ray and extreme ultraviolet emissions from comets", Space Science Reviews **113**, 271–374 (2004).

[61] S. M. Krimigis, "A post-Voyager view of Jupiter's magnetosphere", Endeavour **5**, 50–60 (1981).

[62] A. Kushino, Y. Ishisaki, U. Morita, N. Y. Yamasaki, M. Ishida, T. Ohashi, and Y. Ueda, "Study of the X-Ray Background Spectrum and Its Large-Scale Fluctuation with ASCA", Publications of the Astronomical Society of Japan **54**, 327–352 (2002).

[63] R. Lallement, "The heliospheric soft X-ray emission pattern during the ROSAT survey: Inferences on Local Bubble hot gas", Astronomy & Astrophysics **418**, 143–150 (2004).

[64] R. B. Leighton, R. W. Noyes, and G. W. Simon, "Velocity Fields in the Solar Atmosphere. I. Preliminary Report.", The Astrophysical Journal **135**, 474 (1962).

[65] C. M. Lisse, T. E. Cravens, and K. Dennerl, "X-Ray and Extreme Ultraviolet Emission from Comets", in *Comets II, M.C. Festou, H.U. Keller, H.A. Weaver (ed.)* (University of Arizona Press, 2004), p. 14.

[66] C. M. Lisse, K. Dennerl, J. Englhauser, M. Harden, F. E. Marshall, M. J. Mumma, R. Petre, J. P. Pye, M. J. Ricketts, J. Schmitt, J. Trümper, and R. G. West, "Discovery of X-ray and Extreme Ultraviolet Emission from Comet C/Hyakutake 1996 B2", Science **274**, 205–209 (1996).

[67] C. M. Lisse, K. Dennerl, J. Englhauser, J. Trümper, F. E. Marshall, R. Petre, A. Valinia, B. J. Kellett, and R. Bingham, "X-Ray Emission From Comet Hale - Bopp", Earth, Moon, and Planets **77**, 283–291 (1997).

[68] D. Lumb, "EPIC BACKGROUND FILES XMM-SOC-CAL-TN-0016 issue 2.0", 15 (2002).

[69] R. J. MacDowall, M. L. Kaiser, M. D. Desch, W. M. Farrell, R. A. Hess, and R. G. Stone, "Quasiperiodic Jovian Radio bursts: observations from the Ulysses Radio and Plasma Wave Experiment", Planetary and Space Science, Special Issue: Ulysses Flyby of Jupiter **41**, 1059–1072 (1993).

[70] A. N. Maurellis, T. E. Cravens, G. R. Gladstone, J. H. Waite, and L. W. Acton, "Jovian X-ray emission from solar X-ray scattering", Geophysical Research Letters **27**, 1339–1342 (2000).

[71] C. E. McIlwain, "Coordinates for mapping the distribution of magnetically trapped particles", Journal of Geophysical Research (1896-1977) **66**, 3681–3691 (1961).

[72] A. E. Metzger, D. A. Gilman, J. L. Luthey, K. C. Hurley, H. W. Schnopper, F. D. Seward, and J. D. Sullivan, "The detection of X rays from Jupiter", Journal of Geophysical Research **88**, 7731 (1983).

[73] R. Mewe, "Ionization of Hot Plasmas", in *Physical Processes in Hot Cosmic Plasmas*, edited by W. Brinkmann, A. C. Fabian, and F. Giovannelli, NATO ASI Series (Springer Netherlands, Dordrecht, 1990), pp. 39–65.

[74] K. Mitsuda, M. Bautz, H. Inoue, R. L. Kelley, K. Koyama, H. Kunieda, K. Makishima, Y. Ogawara, R. Petre, T. Takahashi, H. Tsunemi, N. E. White, N. Anabuki, L. Angelini, K. Arnaud, H. Awaki, A. Bamba, K. Boyce, G. V. Brown, K.-W. Chan, J. Cottam, T. Dotani, J. Doty, K. Ebisawa, Y. Ezoe, A. C. Fabian, E. Figueroa, R. Fujimoto, Y. Fukazawa, T. Furusho, A. Furuzawa, K. Gendreau, R. E. Griffiths, Y. Haba, K. Hamaguchi, I. Harrus, G. Hasinger, I. Hatsukade, K. Hayashida, P. J. Henry, J. S. Hiraga, S. S. Holt, A. Hornschemeier, J. P. Hughes, U. Hwang, M. Ishida, Y. Ishisaki, N. Isobe, M. Itoh, N. Iyomoto, S. M. Kahn, T. Kamae, H. Katagiri, J. Kataoka, H. Katayama, N. Kawai, C. Kilbourne, K. Kinugasa, S. Kissel, S. Kitamoto, M. Kohama, T. Kohmura, M. Kokubun, T. Kotani, J. Kotoku, A. Kubota, G. M. Madejski, Y. Maeda, F. Makino, A. Markowitz, C. Matsumoto, H. Matsumoto, M. Matsuoka, K. Matsushita, D. McCammon, T. Mihara, K. Misaki, E. Miyata, T. Mizuno, K. Mori, H. Mori, M. Morii, H. Moseley, K. Mukai, H. Murakami, T. Murakami, R. Mushotzky, F. Nagase, M. Namiki, H. Negoro, K. Nakazawa, J. A. Nousek, T. Okajima, y. ogasaka, T. Ohashi, T. Oshima, N. Ota, M. Ozaki, H. Ozawa, A. N. Parmar, W. D. Pence, F. S. Porter, J. N. Reeves, G. R. Ricker, I. Sakurai, W. T. Sanders, A. Senda, P. Serlemitsos, R. Shibata, Y. Soong, R. Smith, M. Suzuki, A. E. Szymkowiak, H. Takahashi, T. Tamagawa, K. Tamura, T. Tamura, Y. Tanaka, M. Tashiro, Y.

Tawara, Y. Terada, Y. Terashima, H. Tomida, K. Torii, Y. Tsuboi, M. Tsujimoto, T. G. Tsuru, M. J. L. Turner, Y. Ueda, S. Ueno, M. Ueno, S. Uno, Y. Urata, S. Watanabe, N. Yamamoto, K. Yamaoka, N. Y. Yamasaki, K. Yamashita, M. Yamauchi, S. Yamauchi, T. Yaqoob, D. Yonetoku, and A. Yoshida, "The X-Ray Observatory Suzaku", Publications of the Astronomical Society of Japan **59**, S1–S7 (2007).

[75] Y. Miyoshi, H. Misawa, A. Morioka, T. Kondo, Y. Koyama, and J. Nakajima, "Observation of short-term variation of Jupiter's synchrotron radiation", Geophysical Research Letters **26**, 9–12 (1999).

[76] Y. Miyoshi, A. Morioka, H. Misawa, T. Obara, T. Nagai, and Y. Kasahara, "Rebuilding process of the outer radiation belt during the 3 November 1993 magnetic storm: NOAA and Exos-D observations", Journal of Geophysical Research: Space Physics **108**, SMP 3-1-SMP 3–15 (2003).

[77] M. Numazawa, Y. Ezoe, K. Ishikawa, T. Ohashi, Y. Miyoshi, T. Kimura, Y. Uchiyama, D. Shiota, and G. Branduardi-Raymont, "Suzaku observation of Jupiter's X-rays around solar maximum", Publications of the Astronomical Society of Japan **71**, 93(1–9) (2019).

[78] Y. Omura, Y. Katoh, and D. Summers, "Theory and simulation of the generation of whistler-mode chorus", Journal of Geophysical Research: Space Physics (2008).

[79] E. N. Parker, "Dynamical theory of the solar wind", Space Science Reviews **4**, 666–708 (1965).

[80] D. Porquet, M. Arnaud, and A. Decourchelle, "Impacts of a power-law non-thermal electron tail on the ionization and recombination rates", Astronomy & Astrophysics **373**, 1110–1124 (2001).

[81] J. A. Ratcliffe and L. R. O. Storey, "An investigation of whistling atmospherics", Philosophical Transactions of the Royal Society of London. Series A, Mathematical and Physical Sciences **246**, 113–141 (1953).

[82] J. H. Rogers, *The Giant Planet Jupiter* (Cambridge University Press, July 20, 1995), 472 pp.

[83] G. B. Rybicki and A. P. Lightman, *Radiative processes in astrophysics*, Physics Textbook, OCLC: 255501661 (Wiley, Weinheim, 2004), 382 pp.

[84] O. Santolík, D. A. Gurnett, and J. S. Pickett, "Multipoint investigation of the source region of storm-time chorus", Annales Geophysicae **22**, 2555–2563 (2004).

[85] D. Santos-Costa, S. J. Bolton, R. M. Thorne, Y. Miyoshi, and S. M. Levin, "Investigating the origins of the Jovian decimetric emission's variability", Journal of Geophysical Research: Space Physics **113**, A01204 (2008).

[86] J. Saur, D. F. Strobel, F. M. Neubauer, and M. E. Summers, "The ion mass loading rate at Io", Icarus **163**, 456–468 (2003).

[87] A. Schardt and C. Goertz, "High-Energy Particles", (1983).

[88] R. W. Schunk and A. F. Nagy, *Ionospheres: Physics, Plasma Physics, and Chemistry* (Cambridge University Press, Cambridge, 2000).

[89] N. A. Schwadron and T. E. Cravens, "Implications of Solar Wind Composition for Cometary X-Rays", The Astrophysical Journal **544**, 558 (2000).

[90] P. J. Serlemitsos, Y. Soong, K.-W. Chan, T. Okajima, J. P. Lehan, Y. Maeda, K. Itoh, H. Mori, R. Iizuka, A. Itoh, H. Inoue, S. Okada, Y. Yokoyama, Y. Itoh, M. Ebara, R. Nakamura, K. Suzuki, M. Ishida, A. Hayakawa, C. Inoue, S. Okuma, R. Kubota, M. Suzuki, T. Osawa, K. Yamashita, H. Kunieda, Y. Tawara, Y. Ogasaka, A. Furuzawa, K. Tamura, R. Shibata, Y. Haba, M. Naitou, and K. Misaki, "The X-Ray Telescope onboard Suzaku", Publications of the Astronomical Society of Japan **59**, S9–S21 (2007).

[91] A. Sicard and S. Bourdarie, "Physical Electron Belt Model from Jupiter's surface to the orbit of Europa: JOVIAN RADIATION BELT MODEL", Journal of Geophysical Research: Space Physics **109** (2004).

[92] R. P. Singhal, S. C. Chakravarty, A. Bhardwaj, and B. Prasad, "Energetic electron precipitation in Jupiter's upper atmosphere", Journal of Geophysical Research: Planets **97**, 18245–18256 (1992).

[93] R. M. Sloanaker, "Apparent temperature of Jupiter at a wave length of 10 cm.", The Astronomical Journal **64**, 346 (1959).

[94] E. J. Smith, L. Davis, and D. E. Jones, "Jupiter's magnetic field and magnetosphere", IAU Colloq. 30: Jupiter: Studies of the Interior, Atmosp here, Magnetosphere and Satellites, 788 (1976).

[95] W. H. Smyth, "Energy escape rate of neutrals from Io and the implications for local magnetospheric interactions", Journal of Geophysical Research: Space Physics **103**, 11941–11950 (1998).

[96] R. von Steiger, N. A. Schwadron, L. A. Fisk, J. Geiss, G. Gloeckler, S. Hefti, B. Wilken, R. R. Wimmer-Schweingruber, and T. H. Zurbuchen, "Composition of quasi-stationary solar wind flows from Ulysses/Solar Wind Ion Composition Spectrometer", Journal of Geophysical Research: Space Physics **105**, 27217–27238 (2000).

[97] T. Takahashi, K. Abe, M. Endo, Y. Endo, Y. Ezoe, Y. Fukazawa, M. Hamaya, S. Hirakuri, S. Hong, M. Horii, H. Inoue, N. Isobe, T. Itoh, N. Iyomoto, T. Kamae, D. Kasama, J. Kataoka, H. Kato, M. Kawaharada, N. Kawano, K. Kawashima, S. Kawasoe, T. Kishishita, T. Kitaguchi, Y. Kobayashi, M. Kokubun, J. Kotoku, M. Kouda, A. Kubota, Y. Kuroda, G. Madejski, K. Makishima, K. Masukawa, Y. Matsumoto, T. Mitani, R. Miyawaki, T. Mizuno, K. Mori, M. Mori, M. Murashima, T. Murakami, K. Nakazawa, H. Niko, M. Nomachi, Y. Okada, M. Ohno, K. Oonuki, N. Ota, H. Ozawa, G. Sato, S. Shinoda, M. Sugiho, M. Suzuki, K. Taguchi, H. Takahashi, I. Takahashi, S. Takeda, K.-i. Tamura, T. Tamura, T. Tanaka, C. Tanihata, M. Tashiro, Y. Terada, S. Tominaga, Y. Uchiyama, S. Watanabe, K. Yamaoka, T. Yanagida, and D. Yonetoku, "Hard X-Ray Detector (HXD) on Board Suzaku", Publications of the Astronomical Society of Japan **59**, S35–S51 (2007).

[98] M. Tashiro, H. Maejima, K. Toda, R. Kelley, L. Reichenthal, J. Lobell, R. Petre, M. Guainazzi, E. Costantini, M. Edison, R. Fujimoto, M. Grim, K. Hayashida, J.-W. den Herder, Y. Ishisaki, S. Paltani, K. Matsushita, K. Mori, G. Sneiderman, Y. Takei, Y. Terada, H. Tomida, H. Akamatsu, L. Angelini, Y. Arai, H. Awaki, L. Babyk, A. Bamba, P. Barfknecht, K. Barnstable, T. Bialas, B. Blagojevic, J. Bonafede, C. Brambora, L. Brenneman, G. Brown, K. Brown, L. Burns, E. Canavan, T. Carnahan, M. Chiao, B. Comber, L. Corrales, C. de Vries, J. Dercksen, M. Diaz-Trigo, T. Dillard, M. DiPirro, C. Done, T. Dotani, K. Ebisawa, M. Eckart, T. Enoto, Y. Ezoe, C. Ferrigno, Y. Fukazawa, Y. Fujita, A. Furuzawa, L. Gallo, S. Graham, L. Gu, K. Hagino, K. Hamaguchi, I. Hatsukade, D. Hawes, T. Hayashi, C. Hegarty, N. Hell, J. Hiraga, E. Hodges-Kluck, M. Holland, A. Hornschemeier, A. Hoshino, Y. Ichinohe, R. Iizuka, K. Ishibashi, M. Ishida, K. Ishikawa, K. Ishimura, B. James, T. Kallman, E. Kara, S. Katsuda, S. Kenyon, C. Kilbourne, M. Kimball, T. Kitaguti, S. Kitamoto, S. Kobayashi, T. Kohmura, S. Koyama, A. Kubota, M. Leutenegger, T. Lockard, M. Loewenstein, Y. Maeda, L. Marbley, M. Markevitch, H. Matsumoto, K. Matsuzaki, D. McCammon, B. McNamara, J. Miko, E. Miller, J. Miller, K. Minesugi, I. Mitsuishi, T. Mizuno, H. Mori, K. Mukai, H. Murakami, R. Mushotzky, H. Nakajima, H. Nakamura, S. Nakashima, K. Nakazawa, C. Natsukari, K. Nigo, Y. Nishioka, K. Nobukawa, M. Nobukawa, H. Noda, H. Odaka, M. Ogawa, T. Ohashi, M. Ohno, M. Ohta, T. Okajima, A. Okamoto, M. Onizuka, N. Ota, M. Ozaki, P. Plucinsky, F. S. Porter, K. Pottschmidt, K. Sato, R. Sato, M. Sawada, H. Seta, K. Shelton, Y. Shibano, M. Shida, M. Shidatsu, P. Shirron, A. Simionescu, R. Smith, K. Someya, Y. Soong, Y. Suagawara, A. Szymkowiak, H. Takahashi, T. Tamagawa, T. Tamura, T. Tanaka, Y. Terashima, Y. Tsuboi, M. Tsujimoto, H. Tsunemi, T. Tsuru, H. Uchida, H. Uchiyama, Y. Ueda, S. Uno, T. Walsh, S. Watanabe, B. Williams, R. Wolfs, M. Wright, S. Yamada, H. Yamaguchi, K. Yamaoka, N. Yamasaki, S. Yamauchi, M. Yamauchi, K. Yanagase, T. Yaqoob, S. Yasuda, N. Yoshioka, J. Zabala, and Z. Irina, "Concept of the X-ray Astronomy Recovery Mission", in Space Telescopes and Instrumentation 2018: Ultraviolet to Gamma Ray, Vol. 10699 (July 6, 2018), p. 1069922.

[99] V. Tatischeff, "X- and Gamma-Ray Line Emission Processes", EAS Publications Series **7**, 79–79 (2003).

[100] Y. Uchiyama, Y. Maeda, M. Ebara, R. Fujimoto, Y. Ishisaki, M. Ishida, R. Iizuka, M. Ushio, H. Inoue, S. Okada, H. Mori, and M. Ozaki, "Restoring the Suzaku Source Position Accuracy and Point-Spread function", Publications of the Astronomical Society of Japan **60**, S35–S41 (2008).

[101] J. H. Waite Jr., F. Bagenal, F. Seward, C. Na, G. R. Gladstone, T. E. Cravens, K. C. Hurley, J. T. Clarke, R. Elsner, and S. A. Stern, "ROSAT observations of the Jupiter aurora", Journal of Geophysical Research: Space Physics **99**, 14799–14809 (1994).

[102] J. H. Waite Jr., J. T. Clarke, T. E. Cravens, and C. M. Hammond, "The Jovian aurora: Electron or ion precipitation?", Journal of Geophysical Research: Space Physics **93**, 7244–7250 (1988).

[103] J. H. Waite Jr., T. E. Cravens, J. Kozyra, A. F. Nagy, S. K. Atreya, and R. H. Chen, "Electron precipitation and related aeronomy of the Jovian thermosphere and ionosphere", Journal of Geophysical Research: Space Physics **88**, 6143–6163 (1983).

[104] J. H. Waite Jr., G. R. Gladstone, W. S. Lewis, P. Drossart, T. E. Cravens, A. N. Maurellis, B. H. Mauk, and S. Miller, "Equatorial X-ray Emissions: Implications for Jupiter's High Exospheric Temperatures", Science **276**, 104–108 (1997).

[105] B. J. Wargelin, M. Markevitch, M. Juda, V. Kharchenko, R. Edgar, and A. Dalgarno, "ChandraObservations of the "Dark" Moon and Geocoronal Solar Wind Charge Transfer", The Astrophysical Journal **607**, 596–610 (2004).

[106] V. Zabalza, "Naima: a Python package for inference of particle distribution properties from nonthermal spectra", in Proceedings of The 34th International Cosmic Ray Conference — PoS(ICRC2015) (Aug. 18, 2016), p. 922.

[107] H. Zirin, "Astrophysics of the sun", Cambridge and New York, Cambridge University Press, 1988, 440 p. (1988).

Acknowledgements

Six years have passed since I hit the gates of Astrophysics. In the last six years, I have had countless knowledge (maybe countable yet), endless curiosity, and priceless blessing, and lost a little bit of strength and youth. Looking back on the years, I think it was a series of setbacks. I often threw in the towel (or the spoon in Japanese idiom), but picked "it" up each time. I wouldn't have been able to write this paper without my teachers, co-walkers, friends, and family. I am deeply grateful to all the people.

My research life was opened with one-to-one lessons in "practical" Astrophysics with Dr. Yuichiro Ezoe. Ezoe-sensei considerably assisted me to lay the groundwork for my researches of both analyses and experiments. I am somewhat confident in my research skills transmitted directly from him and looking forward to improving them as my own from now on. I would like to express my sincere gratitude to Ezoe-sensei for his kind and generous guidance as my supervisor and a chief examiner in this Ph.D. thesis. I also owe a very important debt to the thesis committee members, Dr. Yoshitaka Ishisaki, Prof. Kuniaki Masai, and Prof. Yasunobu Uchiyama. Their helpful comments allowed me to raise the quality of this thesis. I have to take this opportunity to express my thanks to other members in my laboratory at Tokyo Metropolitan University (TMU). I had thought of Prof. Takaya Ohashi as just a drinking buddy, but now I profoundly respect him. I was deeply moved that my (too) poor English grammar and physical contexts of this thesis were reformed via Ohashi-sensei's "magical" rehabilitation process. I often consulted with Dr. Shinya Yamada about a lot of topics, Astronomy basics, useful tips, Python codings, job hunting, etc. Without Yamada-san's encouragement, my heart would have been broken. I would like to show my appreciation to Secretary Yuko Kawakami and the office of the Department of Physics. Thanks to their good management, I have done my research, especially, paperwork smoothly. Kawakami-san often cooked us delicious meals at our small parties, which is a wonderful memory for me. My research at TMU has been supported by many other people: Prof. Manabu Ishida, Dr. Yoshitomo Maeda, and Dr. Ryo Iizuka for experiments of X-ray telescopes, Prof. Yoshiaki Kanamori and Dr. Kohei Morishita for fabrications of X-ray telescopes, Prof. Yoshizumi Miyoshi, Dr. Daikou Shiota, and Dr. Tomoki Kimura for discussion about Jovian X-rays, and Prof. Graziella Branduardi-Raymont for gentle acceptance during my stay in the U.K. and subsequent continuous guidance. Also, I am gratefully thankful for all my co-workers at TMU, Kumi Ishikawa, Tomohiro Ogawa, Masahiro Ikuta, Toshiki Sato, Saori Konami, Magnus Axelsson, Kasumi Nakamura, Sho Kurashima, Gensei Kuromaru, Shota Suzuki, and all my dependable juniors. This research was also supported by Grant-in-Aid for Japan Society for the Promotion of Science (JSPS) Fellows Grant Number JP17J05475.

Of course, I must not forget to say "thank you" to my family from the bottom of my heart. Their deep affection always helped me to keep trying. I am feeling relieved to meet their expectation while writing the last page of this thesis. Finally, my heartfelt appreciation goes to my girlfriend, for all her love and encouragement, and all my mirthful friends, too. The time I spent at TMU gave me "a small spaceship" named *Wisdom.* Now, I want to say to myself, *"Let's go on the spaceship and see the unknown stars!"*